



**HAL**  
open science

# Etude physique et technologique d'architectures de transistors MOS à nanofils

Kiichi Tachi

► **To cite this version:**

Kiichi Tachi. Etude physique et technologique d'architectures de transistors MOS à nanofils. Micro et nanotechnologies/Microélectronique. Université de Grenoble, 2011. Français. NNT : 2011GRENT084 . tel-00721968

**HAL Id: tel-00721968**

**<https://theses.hal.science/tel-00721968>**

Submitted on 31 Jul 2012

**HAL** is a multi-disciplinary open access archive for the deposit and dissemination of scientific research documents, whether they are published or not. The documents may come from teaching and research institutions in France or abroad, or from public or private research centers.

L'archive ouverte pluridisciplinaire **HAL**, est destinée au dépôt et à la diffusion de documents scientifiques de niveau recherche, publiés ou non, émanant des établissements d'enseignement et de recherche français ou étrangers, des laboratoires publics ou privés.

## THÈSE

Pour obtenir le grade de

## DOCTEUR DE L'UNIVERSITÉ DE GRENOBLE

Spécialité : **Micro et Nano Electronique**

Arrêté ministériel : 7 août 2006

Présentée par

**Kiichi TACHI**

Thèse dirigée par **Sorin CRISTOLOVEANU** et  
codirigée par **Thomas ERNST**

préparée au sein des **Laboratoires LETI et IMEP-LAHC**  
dans l'**École Doctorale EEATS**

# Étude physique et technologique d'architectures de transistors MOS à nanofils

Thèse soutenue publiquement le **8 Juillet 2011**,  
devant le jury composé de :

**M. Olivier BONNAUD**

Professeur, Université de Rennes (Président, Rapporteur)

**M. Matteo VALENZA**

Professeur, Université de Montpellier (Rapporteur)

**M. Hiroshi IWAI**

Professeur, Tokyo Institute of Technology (Membre)

**M. Alexander ZASLAVSKY**

Professeur, Brown University, USA (Membre)

**M. Thomas ERNST**

Ingénieur Recherche, CEA-LETI (Membre)

**M. Sorin CRISTOLOVEANU**

Directeur de Recherche CNRS (Membre)



## ABSTRACT

Vertically-stacked silicon nanowire MOSFETs (SNWTs) were experimentally investigated as one of the possible solutions to achieve both high speed, low power consumption in combination with high integration capabilities for future LSI applications. To evaluate the potentials, analyze and improve the performance of these devices, source/drain series resistance for thick source/drain region were studied. Carrier transport mechanisms and the controllability of threshold voltage for vertically-stacked SNWTs with separated gates were also investigated.

The influence of *in situ* doped SEG source/drain was examined for vertically-stacked channel MOSFETs. A large enhancement, by a factor of 2 in the drive current, was obtained when *in situ* doped SEG process was adopted. Detailed parameter extraction from the electrical measurements showed the  $R_{SD}$  values can be reduced by 90 and 75% for *n*- and *p*-FETs, respectively, when *in situ* doped SEG is reinforced by adding ion implantation. On the other hand, by combining the ion implantation to SEG process,  $V_T$  roll-off characteristics and the effective mobility behavior are slightly degraded. Mobility analysis revealed an increase in the Coulomb scattering with  $L_G$  scaling, indicating the diffusion of dopant atoms from S/D regions. Further improvements in the performance can be sought by optimizing the S/D activation annealing step.

In order to enhance the performance of the vertically-stacked nanowire MOSFETs, the carrier transport limiting components caused by short channel effects were assessed. The optimization of drive currents will have to take into account specific effects to vertically-stacked SNWTs. In particular, the use of SiGe sacrificial layer to make vertically-stacked channels cause large mobility degradation due to the surface roughness, resulted from the damage of plasma etching. This leads to the poor ballisticity in the short channel SNWTs. Hydrogen annealing was shown to be advantageous for improving the surface-roughness limited mobility. Charge pumping measurements, however, revealed that circular-shaped SNWTs, which are formed by annealing, have a higher interface trap density ( $D_{it}$ ) than rectangular ones, leading to

low-field mobility degradation. This high  $D_{it}$  could be caused by the continuously-varying surface orientation. The resulting additional coulomb scattering could partly explain the quite low mobility in 5 nm diameter SNWTs together with the already known transport limitations in NWs.

In addition, the vertically-stacked SNWTs with independent gates by internal spacers between the nanowires to control threshold voltage (named  $\Phi$ -FETs), were evaluated.  $\Phi$ -FETs demonstrated excellent  $V_T$  controllability due to inter-gate coupling effects. Numerical simulations to optimize  $\Phi$ -FETs structures show that when the spacer width is reduced, the DIBL value can be lowered by a factor of 2 compared to independent-gate FinFETs with the same silicon width. The superior scaling of  $\Phi$ -FETs with narrow spacer results from a better electrostatic control which also attenuates the inter-gate coupling.

Overall it was shown that using vertical stack structure can increase the drive current density while allowing for better threshold voltage controllability. As for the performance benchmark, nanowires with a diameter of 10 nm, showed the most acceptable balance between mobility, short channel effect. However, to further improve the device performance, process induced surface damage of nanowires must be mitigated.

## ACKNOWLEDGEMENTS

This study has been done in CEA-LETI, Minatec for two years and three months. I am very grateful to so many people for their help and support given to me. Without their help, this thesis would not have been possible.

First of all, I would like to express my sincere gratitude to my supervisor Professor Sorin Cristoloveanu, for his inspiring guidance and constant encouragement throughout this work. I gave him quite a lot of trouble and worry. I really don't know how to thank you. I'll never forget your kindness.

I am also grateful to my boss Dr. Thomas Ernst of CEA-LETI for everything you have done for me. His vast knowledge and strong technical expertise have helped me in getting an excellent background in the semiconductor device technology, identifying the opportunities in this field and preparing for the challenges. I am thankful for the rewarding learning experience that his mentorship has produced.

I am also grateful to Dr. Simon Deleonibus, Dr. Olivier Faynot of CEA-LETI, and Professor Hiroshi Iwai and Associate Professor Kuniyuki Kakushima of Tokyo Institute of Technology for their guidance, encouragement and continuous support throughout my research.

Special thanks go to the members of "team nanowire" Alex, Nathalie, Sylvain, Stephan, Christian V, Cecilia, Emile, Paul-Henry, Virginie, and Marie-Emmanuelle for their support and friendship. I would also like to thank my research colleagues for a lot of help. Mere words are not enough to express the gratitude I feel for them.

I would like to thank all people I met in France. I spent great and wonderful days in Grenoble.

This work was partially performed as part of the IBM-STMicroelectronics-CEA-LETI Development Alliance.

## *Acknowledgements*

---

*Acknowledgements*

---

*To my family for their kind support  
and encouragement throughout my life.*

*Merci beaucoup!*

## *Acknowledgements*

---



# CONTENTS

	<i>Page</i>
<i>List of Tables</i>	xi
<i>List of Figures</i>	xiii
<i>Symbols and Abbreviations</i>	xxii
<b>1 Introduction – MOSFET Scaling –</b>	<b>1</b>
1.1 MOSFET Downsizing	3
1.1.1 Basic CMOS Operation	
1.1.2 MOSFET Scaling	
1.1.3 CMOS Performance Indexes	
1.2 Short Channel MOSFET	18
1.2.1 Short Channel Effects	
1.2.2 Source/Drain Series Resistance in Short-Channel MOSFET	
1.2.3 Carrier Transport Mechanisms in Short-Channel MOSFET	
1.3 Key Technologies to Improve MOSFET Performance	30
1.3.1 Gate-All-Around Silicon Nanowire MOSFET	
1.3.2 Vertically-Stacked Channel MOSFET	
1.4 Purpose and Contents of This Study	39
1.5 References	43

<b>2</b>	<b>Vertically-Stacked Channel MOSFET Fabrication</b>	<b>49</b>
2.1	Silicon-On-Nothing Technology	51
2.2	Key Steps	52
2.2.1	High- $\kappa$ /Metal Gate Stacks	
2.2.2	SiGe Epitaxy and Etching	
2.3	Process Step Overview for Multi-Channel MOSFET	55
2.4	Process Step Overview for Vertically-Stacked Nanowire MOSFET	57
2.5	Conclusions	61
2.6	References	62
 <b>3</b>	 <b>Electrical Characterization Methods</b>	 <b>65</b>
3.1	Introduction	67
3.2	$Y$ -function Method	67
3.3	Split $C$ - $V$ Method	72
3.4	Mobility Limiting Components	75
3.5	Charge Pumping Method	78
3.6	Low-frequency Noise Measurement	81
3.7	Conclusions	82
3.8	References	82
 <b>4</b>	 <b>Source/Drain Doping Techniques for Vertically-Stacked Channel Structure</b>	 <b>85</b>
4.1	Introduction	87
4.2	Experimental Conditions	88
4.3	Electrical Characteristics	88
4.3.1	$I$ - $V$ Characteristics	
4.3.2	Source/Drain Series Resistance Evaluation	
4.3.3	Carrier Mobility Evaluation	
4.3.4	Gate Length Scaling	
4.4	Conclusions	97

4.5	References	98
<b>5</b>	<b>Carrier Transport Properties of Vertically-Stacked Nanowire MOSFETs</b>	<b>101</b>
5.1	Introduction	104
5.2	Electrical Characteristics	104
5.2.1	<i>I-V</i> Characteristics	
5.2.2	Transport Limiting Velocity	
5.2.3	Carrier Mobility Evaluation	
5.2.4	Mobility Limiting Factors	
5.3	Impact on Plasma Etching of SiGe Sacrificial layers	118
5.3.1	One-Leveled Nanowire MOSFET Fabrication	
5.3.2	Carrier Mobility Evaluation	
5.4	Effect of Hydrogen Annealing	122
5.4.1	Cross-Sectional Shape	
5.4.2	Carrier Mobility Evaluation	
5.4.3	Interface Trap density	
5.5	SiGe Nanowire MOSFET	128
5.5.1	Device Fabrication Process	
5.5.2	<i>I-V</i> Characteristics	
5.5.3	Carrier Mobility Evaluation	
5.5.4	Noise Measurement	
5.6	Conclusions	131
5.7	References	131
<b>6</b>	<b>Threshold Voltage Control of Vertically-Stacked Nanowire MOSFETs</b>	<b>135</b>
6.1	Introduction	137
6.1.1	Threshold Voltage Control by Independent-Gate FinFET	
6.1.2	Vertically-Stacked Nanowire Transistor with Independent Gates	
6.2	Optimization of Device Dimensions	140

6.3	Conclusions	146
6.4	References	146
<b>7</b>	<b>Conclusions</b>	<b>149</b>
7.1	Summary	151
7.2	Conclusions and Perspectives	153
	<i>Résumé du travail de thèse en Français</i>	<b>155</b>
	<i>Publications and Presentations</i>	<b>165</b>
	<i>Awards</i>	<b>173</b>

# LIST OF TABLES

## Chapter 1 Introduction – MOSFET scaling –

<i>Table 1.1 Constant-field scaling and generalized scaling of MOSFET device and circuit parameters.</i>	10
<i>Table 1.2 Key device features of Intel 32 nm logic technology.</i>	31
<i>Table 1.3 Natural length in devices with different geometries.</i>	35

## Chapter 2 Vertically-Stacked Channel MOSFET Fabrication

<i>Table 2.1 Process description of anisotropic etching of SiGe/Si superlattice.</i>	53
<i>Table 2.2 Nanowire width with various definitions and surface gain factor <math>W_{eff}/W_{Top}</math>.</i>	60

## Chapter 3 Electrical characterization methods

<i>Table 3.1 Lists of effective mass and valley degeneracy of silicon on (100), (110), and (111) surfaces.</i>	75
--	----

## Chapter 4 Source/Drain Doping Techniques for Vertically-Stacked Channel Structure

<i>Table 4.1 Doping scheme</i>	88
--------------------------------	----

Chapter 5 Carrier Transport Properties of Vertically-Stacked Nanowire MOSFETs

*Table 5.1 Device parameters for vertically-stacked silicon nanowire n- and p-MOSFET with sub-50-nm- $L_{eff}$  and 15-nm- $W_{Top}$ . The on-currents  $I_{ON}$  are extracted at  $V_G - V_T = 0.7$  and  $-0.7$  V for n- and p-MOSFETs, respectively. The off-currents  $I_{OFF}$  are extracted at  $V_G - V_T = -0.3$  and  $0.3$  V for n- and p-MOSFETs, respectively.*

# LIST OF FIGURES

## Chapter 1 Introduction – MOSFET scaling –

- Figure 1.1 (a) Number of transistors in Intel's microprocessor chips, (b) Average transistor price by year, (c) Clock speed of Intel's microprocessor. 3
- Figure 1.2 Three-dimensional view of basic CMOS structure.  $V_G$  is gate voltage,  $V_S$  is source voltage,  $V_D$  is drain voltage,  $L_G$  is gate length,  $t_{ox}$  is gate oxide thickness,  $N_a$  is acceptor impurity density,  $N_d$  is donor impurity density,  $x_j$  is junction depth 4
- Figure 1.3 Three regions of a MOSFET operation in the  $V_{DS}$ - $V_G$  plane. 5
- Figure 1.4 Typical  $I_{DS}$ - $V_G$  characteristics of an nMOSFET at high drain voltages. The same current is plotted on both linear scale (a) and logarithmic scale (b). 6
- Figure 1.5 (a) Circuit diagram of CMOS inverter. (b) Charge and (c) discharge equivalent circuits. 8
- Figure 1.6 Principles of MOSFET constant-electric-field scaling. 9
- Figure 1.7 CVI performance metric. 12
- Figure 1.8 Equivalent circuit with wiring capacitance. 13
- Figure 1.9 (a) Operation of a CMOS inverter in inverter chain. (b)  $I_{DS}$ - $V_{DS}$  curve and trajectories with and without a degraded DIBL for nMOSFET. 14
- Figure 1.10 Layout of a CMOS inverter based on lambda-based design rules. 15
- Figure 1.11 Sources of leakage current increase as the technology causes gate lengths to shrink. Data from ITRS 17
- Figure 1.12 (a) Leakage current components in a nMOSFET, (b)  $I_D$ - $V_G$  curves with and without leakage currents.  $I_{subth0}$  is the initial subthreshold current, while  $\Delta I_{subth}$  is the added current due to the short-channel effects. 17

Figure 1.13	Schematic diagram of the charge-sharing model. The dashed lines indicate the boundary of the gate and source–drain depletion regions. The arrows represent electric field lines that originate from a positive charge and terminate on a negative charge. The dotted lines partition the depletion charge and form the two sides of the trapezoid.	19
Figure 1.14	Surface potential lowering due to the short-channel effects: (a) a long-channel MOSFET, (b) a short-channel MOSFET at low drain bias, (c) a short-channel MOSFET at high drain bias.	21
Figure 1.15	Subthreshold swing calculated by using MASTAR MOSFET modeling software: $N_a=10^{18} \text{ cm}^{-3}$ , $x_j=30 \text{ nm}$ , $t_{ox}= 1.3 \text{ nm}$ , $V_{DD}= 1.2 \text{ V}$ , $W=1 \mu\text{m}$ .	21
Figure 1.16	DIBL calculated by using MASTAR MOSFET modeling software: $N_a=10^{18} \text{ cm}^{-3}$ , $x_j=30 \text{ nm}$ , $t_{ox}= 1.3 \text{ nm}$ , $V_{DD}= 1.2 \text{ V}$ , $W=1 \mu\text{m}$ .	22
Figure 1.17	$V_T$ roll-off calculated by using MASTAR MOSFET modeling software: $N_a=10^{18} \text{ cm}^{-3}$ , $x_j=30 \text{ nm}$ , $t_{ox}= 1.3 \text{ nm}$ , $V_{DD}= 1.2 \text{ V}$ , $W=1 \mu\text{m}$ .	23
Figure 1.18	Off-current increase due to the short-channel effects.	24
Figure 1.19	Equivalent circuit of MOSFET with source and drain resistance.	24
Figure 1.20	On-currents as a function of source/drain series resistance. All plots are calculated by using MASTAR MOSFET modeling software: $N_a=10^{18} \text{ cm}^{-3}$ , $t_{ox}= 1.3 \text{ nm}$ , $V_{DD}= 1.2 \text{ V}$ , $L_G=50 \text{ nm}$ , $W=1 \mu\text{m}$ .	25
Figure 1.21	On-current lowering ratio of $R_{SD}= 500 \Omega \cdot \mu\text{m}$ to $100 \Omega \cdot \mu\text{m}$ as a function of gate length. All plots are calculated by using MASTAR MOSFET modeling software: $N_a=10^{18} \text{ cm}^{-3}$ , $t_{ox}= 1.3 \text{ nm}$ , $V_{DD}= 1.2 \text{ V}$ , $W=1 \mu\text{m}$ .	26
Figure 1.22	Schematic diagrams of carrier transport models to determine $I_{ON}$ . (a) Conventional transport model. (b) Quasi-ballistic transport model. (c) Full-ballistic transport model.	27
Figure 1.23	Channel potential profiles under conditions of carrier mobility $\mu$ and velocity $v$ . (a) Linear region. (b) Saturation region.	27
Figure 1.24	Velocity–field relationship for electrons ( $n=2$ ) and holes ( $n=1$ ) by the empirical form inserted. The critical field $E_c = v_{sat}/\mu$ .	28
Figure 1.25	$L_G$ dependence of velocity with $\mu$ as parameter.	30
Figure 1.26	Cross section of Intel’s NMOS and PMOS with 4th generation strained silicon, 2nd generation high- $\kappa$ /metal gate, and raised S/D regions for 32 nm technology.	31
Figure 1.27	Cross-section of a planar FDSOI MOSFET.	33



Figure 1.28	Various SOI device: (a) Single gate SOI FET, (b) double gate planar SOI FET, (c) double gate non-planar FinFET, (d) tri-gate FET, (e) quadruple-gate (or gate-all-around) FET, and gate-all-around (or surrounding gate) FET (nanowire FET).	33
Figure 1.29	Illustration of electric field lines from drain of different device types: (a) bulk, (b) FD SOI, and (c) double gate (DG).	34
Figure 1.30	Maximum allowed Si thickness and device width vs. gate length to avoid short-channel effects in single-, double- and quadruple-gate SOI MOSFETs.	35
Figure 1.31	Comparison of DIBL of elliptical GAA SNWTs (width $W = 6.8$ nm and height $H = 9.5$ nm) and single-gate ETSOI FETs (SOI thickness $t_{si} = 8$ nm) with similar body dimensions.	35
Figure 1.32	MOSFET layout; (a) planar MOSFET, (b) GAA SNWT with multi-finger, and (c) cross-section of GAA SNWT.	36
Figure 1.33	Normalized current of a rectangular GAA SNWT as a function of multi-finger pitch width. $W_{NW} = W_{pitch}/2$ . The top interface mobility is $300$ cm <sup>2</sup> /Vs and sidewall mobility is $150$ cm <sup>2</sup> /Vs.	37
Figure 1.34	Normalized current of a rectangular GAA SNWT as a function of space between nanowires. $H_{NW} = 10$ nm. The top interface mobility is $300$ cm <sup>2</sup> /Vs and sidewall mobility is $150$ cm <sup>2</sup> /Vs.	38
Figure 1.35	Structure of vertically-stacked GAA SNWT(a) and its cross-section (b)	39
Figure 1.36	Normalized current of a rectangular GAA SNWT as a function of staking level of nanowires. $H_{NW} = 10$ nm. $W_{space} = 30$ nm. The top interface mobility is $300$ cm <sup>2</sup> /Vs and sidewall mobility is $150$ cm <sup>2</sup> /Vs.	39
Figure 1.37	Outline of each chapter in this thesis.	41

## Chapter 2 Vertically-Stacked Channel MOSFET Fabrication

Figure 2.1	Fabrication process of the SON MOSFET: (a) epitaxy of SiGe and Si layers on isolated bulk wafer; (b) conventional CMOS process steps until formation of the nitride spacers; (c) formation of the shallow trenches in the S/D regions and formation of the tunnel under the Si film; (d) filling the tunnel with oxide (optional step); (e) selective epitaxy of S/D regions, implantation and RTA.	51
Figure 2.2	(Si/SiGe) $\times$ $n$ superlattice on SOI used to pre-define the channel thickness.	52
Figure 2.3	Cross-section (a) and top view (b) SEM images of the Si/SiGe superlattice with the etched SiGe sacrificial layers.	54
Figure 2.4	Cross-sectional TEM image of vertically-stacked silicon nanowire with high- $\kappa$ /metal gate.	54

Figure 2.5	<i>MCFET fabrication process overview.</i>	56
Figure 2.6	<i>Fabricated multi-channel FET along (a) channel length and (b) width direction. (c) is the enlarged image of the gate stack.</i>	56
Figure 2.7	<i>Vertically-stacked nanowire MOSFET fabrication process overview.</i>	57
Figure 2.8	<i>Fabricated vertically-stacked silicon nanowires: (a) a top-view SEM image, (b) a cross-section TEM image.</i>	58
Figure 2.9	<i>(a) Top-view SEM images of silicon nanowires after HfO<sub>2</sub> deposition with width <math>W_{SEM} = 16, 26, \text{ and } 36 \text{ nm}</math>. (b) Variation of nanowire width in a 200-nm-wafer. The variations are less than <math>\pm 1.5 \text{ nm}</math>. The thickness of HfO<sub>2</sub> on side walls (3nm x 2) is included in the values of <math>W_{SEM}</math>. <math>W_m</math> is the mask width.</i>	59
Figure 2.10	<i>Cross-sectional TEM images of vertically-stacked silicon nanowire MOSFET with top-view width <math>W_{Top} = 10, 15, 20 \text{ and } 30 \text{ nm}</math>.</i>	59
Figure 2.11	<i>(a) Cross-sectional TEM image of vertically-stacked silicon nanowire MOSFET with top-view width <math>W_{Top} = 5 \text{ nm}</math>. (b) Enlarged image of 5-nm-diameter nanowire.</i>	60
Figure 2.12	<i>Top-view (a) and cross-section (b) of SEM images of vertically-stacked silicon nanowire MOSFET with mask length <math>L_m = 40, 100, \text{ and } 600 \text{ nm}</math>.</i>	61

### Chapter 3 Electrical Characterization Methods

Figure 3.1	<i>Y-function as a function of the gate voltage. The device used is n-type vertically-stacked SNWT with <math>L_m = 100 \text{ nm}</math> and <math>W_{NW} = 15 \text{ nm}</math>.</i>	69
Figure 3.2	<i>Extraction of <math>\Theta_{I_{eff}}</math>. The device used is n-type vertically-stacked SNWT with <math>L_m = 85 \text{ nm}</math> and <math>W_{NW} = 15 \text{ nm}</math>.</i>	70
Figure 3.3	<i>(a) <math>I_{DS} - V_G</math> and (b) <math>g_m - V_G</math> curves comparisons between the measured data and the fitted model.</i>	70
Figure 3.4	<i>(a) <math>R_{SD}</math>, <math>\Theta_I</math>, and (b) <math>L_{eff}</math> extraction.</i>	71
Figure 3.5	<i>Flow chart of the extraction procedure.</i>	71
Figure 3.6	<i>Configuration for (a) gate-to-channel, (b) gate-to-substrate capacitance measurement for split C-V measurement.</i>	73
Figure 3.7	<i><math>C_{GC} - V_G</math> curves with and without correction of parasitic capacitances. The devices used are n-type vertically-stacked SNWT with various gate lengths.</i>	74
Figure 3.8	<i>Comparison of effective mobility extracted by split C-V, double <math>L_m</math> method, and from parameters extracted by Y-function method. The measured device is the stacked SNWTs with <math>W_{NW} = 15 \text{ nm}</math> and <math>L_{eff} = 242 \text{ nm}</math>.</i>	74

Figure 3.9	Electron and hole mobilities in the inversion layers with the substrate orientations.	76
Figure 3.10	Schematic diagram of mobility limiting components as a function of inversion charge density at low and high temperature.	78
Figure 3.11	Electron mobility on (100) as a function of effective field. The dots are experimental results in ref [3.21] with substrate acceptor concentration dependence. The lines are the limited mobilities calculated by Matthiessen's rule.	78
Figure 3.12	Schematics of the experimental setup used for CP; a trapezoidal pulse is applied to the gate and CP current is measured on the P+ contact.	79
Figure 3.13	(Color online) Energy range scanned by temperature modulation from 20 K to 400 K (bold line) or by rise/fall time modulation (dashed line), as calculated from Eqs. (3.24) for Si. Insert: Schematic of the physical mechanism involved during CP measurement. The electron and hole emission levels $E_{em}$ can be scanned by changing temperature $T$ and/or the rise of fall time $t_{rf}$ .	80

Chapter 4 Source/Drain Doping Techniques for Vertically-Stacked Channel Structure

Figure 4.1	On-off relations of (a) n- and (b) p-MCFETs.	89
Figure 4.2	$V_T$ roll-off characteristics of MCFETs with $L_G$ scaling.	90
Figure 4.3	On-current dependency on the gate length for (a) n- and (b) p-MCFETs.	90
Figure 4.4	Transconductance of the (a) n- and (b) p-MCFETs. Solid lines represent the fitted model.	91
Figure 4.5	$\Theta_{1eff}$ vs. $\beta$ curves of the fabricated (a) n- and (b) p-MCFETs.	91
Figure 4.6	$C_{GC}$ characteristics with various $L_G$ for (a) n- and (b) p-MCFETs.	92
Figure 4.7	$\mu_{eff}$ of the MCFETS with different $L_G$ of 570 and 70 nm.	93
Figure 4.8	Estimated $\mu_0$ on $L_G$ scaling.	94
Figure 4.9	Summary of the extracted $\alpha_\mu$ and $\mu_{max}$ with reported values for planar FETs.	95
Figure 4.10	$I_{ON}$ - $I_{OFF}$ characteristics with several channel sizes for nMCFET (a) and pFET (b).	96
Figure 4.11	$I_D$ - $V_G$ (a) and $I_D$ - $V_D$ (b) characteristics for the scaled MCFETs.	97

Chapter 5 Carrier Transport Properties of Vertically-Stacked Nanowire MOSFETs

Figure 5.1	Threshold voltage as a function of effective gate length for vertically- stacked silicon nanowire n- and p-MOSFET with 15-nm- $W_{Top}$ .	105
Figure 5.2	Subthreshold slope as a function of effective gate length for vertically- stacked silicon nanowire n- and p-MOSFET with 15-nm- $W_{Top}$ .	105
Figure 5.3	DIBL as a function of effective gate length for vertically-stacked silicon nanowire n- and p-MOSFET with 15-nm- $W_{Top}$ .	106
Figure 5.4	$I_{ON}-I_{OFF}$ characteristics of vertically-stacked silicon nanowire n- and p-MOSFET with 15-nm- $W_{Top}$ .	106
Figure 5.5	$I_D-V_D$ characteristics of vertically-stacked silicon nanowire n- and p-MOSFET with sub-50-nm- $L_{eff}$ and 15-nm- $W_{Top}$ .	107
Figure 5.6	$I_D-V_G$ characteristics of vertically-stacked silicon nanowire n- and p-MOSFET with sub-50-nm- $L_{eff}$ and 15-nm- $W_{Top}$ .	108
Figure 5.7	DIBL comparison of GAA SNWTs from this work and other published results.	109
Figure 5.8	$I_{ON}$ comparison of GAA SNWTs from this work and other published results. (a) $I_{ON}$ are normalized by top-view width of nanowires $W_{Top}$ , (b) $I_{ON}$ are normalized by total effective surface of nanowires $W_{eff}$ .	109
Figure 5.9	Saturation current density (a) and linear current density (b) as a function of effective gate length for vertically-stacked silicon nanowire n- and p-MOSFET with 15-nm- $W_{Top}$ . The currents are normalized by top-view width $W_{Top}$ (left y-axis) and effective total width $W_{eff}$ (right y-axis).	110
Figure 5.10	Temperature dependence of saturated electron drift velocity.	111
Figure 5.11	Injection velocity of a nMOSFET on (100) plane as a function of inversion charge density at 300 and 77 K.	111
Figure 5.12	Temperature dependence of $I_D-V_G$ characteristics for vertically-stacked SNWTs.	112
Figure 5.13	Temperature dependence of extracted limiting velocity $v_{lim}$ . Theoretical dependence of saturation velocity $v_{sat}$ from [5.13] and injection velocity $v_{inj}$ from [5.14] are given. The $v_{lim}$ were extracted by the equations in the right table [5.9], where $F_{1/2}$ is Fermi-Dirac integral.	112
Figure 5.14	Schematic image of nanowire MOSFET (a) and its cross-section (b). Varying ratio of (100) width to (110) width, (c) varying size, (d) varying radius of curvature at the corners.	114
Figure 5.15	Rectangular-shaped nanowire mobility as a function of $W_{(100)}$ -to- $W_{(110)}$ ratio. The average mobility is $m_{ave}=(\mu_{(100)}W_{(100)}+\mu_{(110)}W_{(110)})/(W_{(100)}+W_{(110)})$ , where $\mu_{(100)}$ and $\mu_{(110)}$ are the mobilities on (100) and (110) surfaces, respectively.	114

Figure 5.16	Calculated profiles of electron density across the cross section of silicon nanowires with $W_{(110)}=18$ nm, and $W_{(100)}= 7$ and 22 nm.	115
Figure 5.17	Temperature dependence of effective electron mobility in vertically-stacked silicon nanowire FET (a) and in fully-depleted SOI-FET (b).	116
Figure 5.18	Temperature dependence of effective hole mobility in vertically-stacked silicon nanowire FET.	116
Figure 5.19	(a) Temperature dependence of effective mobility at high inversion charge density ( $N_{INV}=10^{13}$ cm <sup>-2</sup> ). (b) Schematic diagram of mobility limiting components at low temperature.	117
Figure 5.20	Temperature dependence of phonon-limited mobility at high inversion charge density ( $N_{INV}=10^{13}$ cm <sup>-2</sup> ) for vertically-stacked silicon nanowire MOSFETs.	117
Figure 5.21	Mobility limiting components for electron (a) and hole for vertically- stacked silicon nanowire MOSFETs at 300 K.	117
Figure 5.22	Temperature dependence of effective mobility at low inversion charge density ( $N_{INV}=2 \times 10^{12}$ cm <sup>-2</sup> ).	118
Figure 5.23	Atomic force microscopy images of silicon surface after isotropic SiGe dry etching (a) and the reference sample without the etching (b).	119
Figure 5.24	Root mean square (RMS) values as a function of isotropic SiGe dry etching.	119
Figure 5.25	Brief process flow of 1-level silicon nanowire MOSFET.	120
Figure 5.26	Gate-all-around 1-level silicon nanowire MOSFETs fabricated without SiGe epitaxy and selective etching.	120
Figure 5.27	Electron mobility comparisons between 1-leveled and vertically-stacked silicon nanowire MOSFET at 300 K (a) and 5 K (b).	121
Figure 5.28	Temperature dependence of effective mobility at high inversion charge density ( $N_{INV}=10^{13}$ cm <sup>-2</sup> ) for 1-leveled and vertically-stacked silicon nanowire MOSFET.	121
Figure 5.29	Mobility limiting components comparison at high inversion charge density between 1-leveled and vertically-stacked silicon nanowire MOSFETs at 300 K.	122
Figure 5.30	Temperature dependence of effective mobility at low inversion charge density ( $N_{INV}=2 \times 10^{12}$ cm <sup>-2</sup> ).	122
Figure 5.31	Cross-sectional TEM images of silicon nanowire (a) without and (b) with hydrogen annealing at 750 °C for two minutes.	123
Figure 5.32	Electron mobility comparison of 1-leveled silicon nanowire MOSFETs between with and without hydrogen annealing. The measurement temperatures are 300 K (a) and 5 K (b).	124

Figure 5.33	Temperature dependence of effective mobility at high inversion charge density ( $N_{INV}=10^{13} \text{ cm}^{-2}$ ) for 1-leveled nanowire MOSFET with and without $\text{H}_2$ anneal.	124
Figure 5.34	Temperature dependence of effective mobility at low inversion charge density ( $N_{INV}=2 \times 10^{12} \text{ cm}^{-2}$ ).	124
Figure 5.35	Electron mobility comparison of vertically-stacked silicon nanowire MOSFETs between with and without hydrogen annealing.	125
Figure 5.36	Charge pumping currents $I_{cp}$ obtained base voltage sweep on nanowire gated-diode with $L_G = 240 \text{ nm}$ and $W_{NW}/H_{NW} = 20 \text{ nm}/15 \text{ nm}$ . The currents are normalized by $W_{eff}$ obtained from TEM images.	126
Figure 5.37	Charge pumping currents $I_{cp}$ as a function of frequency $f$ .	127
Figure 5.38	Interface trap density as a function of energy for vertically-stacked nanowires with (a) and without (b) hydrogen annealing, and planar SOI devices (c) with the same gate stack (3 nm $\text{HfO}_2$ ALD/10 nm TiN CVD). The profile is obtained by scanning temperature from 300 K down to 25 K by 25 K steps. The bold line represents the mean value of $D_{it}(E)$ . The dashed line is the directly measured mean value of interface trap density over the full energy range at 300 K which evidence the lower density of interface traps in the middle of the gap.	127
Figure 5.39	(a) Cross-sectional TEM micrographs of 3D-stacked compressively(c)- strained SiGe NWTs, (b) enlarged images of c-strained SiGe NW, (c) top view of bended c-strained SiGe NWs with $L_{NW}=600\text{nm}$ , (d) top view of c-strained SiGe NWs with $L_{NW}=250\text{nm}$ , and (e) top view of un-strained SiGe NWs with $L_{NW}=600\text{nm}$ . Short length SiGe NWs are straight, this whatever their strain state.	128
Figure 5.40	$I_{ON}/I_{OFF}$ characteristics of Si, c-strained and un-strained SiGe NWs normalized by the number of wires. The total NW surface $W_{total}$ is estimated from the cross-sectional TEM images. The $W_{NW}$ of all NWs is $\sim 20\text{nm}$ .	129
Figure 5.41	Threshold voltage of Si, c-strained and un-strained SiGe NWs as a function of gate length. The $W_{NW}$ of all NWs are $\sim 20\text{nm}$ .	129
Figure 5.42	Effective hole mobility of Si, c-strained and un-strained SiGe NWs. The $W_{NW}$ of all NWs are $\sim 20\text{nm}$ .	130
Figure 5.43	Low-frequency noise of Si and c-strained SiGe NWs. Inserted figure is a comparison of oxide trap density ( $N_t$ ). $L_G$ and $W_{NW}$ are $\sim 290\text{nm}$ and $\sim 20\text{nm}$ , respectively.	130

Chapter 6 Threshold Voltage Control of Vertically-Stacked Nanowire MOSFETs

Figure 6.1	Cross-sectional TEM image of the independent-gate FinFET fabricated by the resist etch back process.	137
Figure 6.2	$\Phi$ -FET scheme.	139
Figure 6.3	Schematic fabrication sequence of $\Phi$ -FET.	139
Figure 6.4	Cross-sectional TEM pictures of $\Phi$ -FET (3 stacked nanowires). Left: 25s SiN isotropic etching Right: 28s SiN isotropic etching.	139
Figure 6.5	Experimental $I_d$ - $V_{g1}$ characteristics at various $V_{g2}$ for n-channel $\Phi$ -FET. The gate length and channel width are 550 nm and 25 nm, respectively.	140
Figure 6.6	$I_{on}$ - $I_{off}$ characteristics comparison between $\Phi$ -FET and IG-FinFET.	140
Figure 6.7	Simulated inversion charge density in a $\Phi$ FET for (a) one gate activated (single drive mode) and (b) two gates activated (double drive mode).	142
Figure 6.8	Schematic illustration of a SNWT with boundary conditions.	143
Figure 6.9	Potential along the channel for a long and short-channel transistor.	143
Figure 6.10	Simplified Poisson equation resolution for long-channel with C.F. for short channel is compared to the drift-diffusion model.	143
Figure 6.11	DIBL versus coupling factor: Silicon width ( $W_{Si}$ ) dependence.	145
Figure 6.12	DIBL versus coupling factor: Spacer width ( $T_{Si}$ ) dependence.	145
Figure 6.13	DIBL versus coupling factor: Spacer width ( $W_{sp}$ ) dependence.	145
Figure 6.14	Lateral gates can screen narrow silicon body from the other gate influence.	146

Chapter 7 Conclusions

Figure 7.1	Performance benchmark with published SNWT data from other gropes. (a) DIBL versus gate length, (b) $I_{ON}/W_{TOP}$ versus gate length, and (c) $I_{ON}/W_{eff}$ versus gate length.	151
Figure 7.2	Cross-sectional TEM image of the 19 period superlattice with 19 nm $Si_{0.8}Ge_{0.2}$ and 32 nm of Si [fabricated by J.M. Hartmann in CEA-Leti].	154

## LIST OF SYMBOLS AND ABBREVIATIONS

---

### A

AFM	Atomic Force Microscopy
ALD	Atomic Layer Deposition
$\alpha_{\mu}$	Mobility degradation factor

---

### B

BEOL	Back-End-Of-the-Line
BOX	Buried Oxide
$\beta$	Gain factor of the transistor

---

### C

CMOS	Complementary MOS
CMP	Chemical Mechanical Polishing
$C$	Capacitance [F]
$C_{dm}$	Maximum depletion-layer capacitance per area [F/cm <sup>2</sup> ]
$C_{ox}$	Gate oxide capacitance per area [F/cm <sup>2</sup> ]



*List of symbols and abbreviations*

---

$C_{in}$	Input capacitance of the next stage or stages [F]
$C_{out}$	Output capacitance of the switching inverter [F]
$C_{wire}$	Wiring capacitance [F]
$C_G$	Gate capacitance [F]
$C_{GC}$	Gate-to-channel capacitance [F]
$C_L$	Load capacitance [F]
$C_{L(W)}$	Load capacitance depending on gate width [F]

---

## **D**

DG	Double gate
DIBL	Drain-induced barrier lowering
$D_{it}$	Interface trap density

---

## **E, $\epsilon$**

EI	Electrostatic integrity
EOT	Equivalent oxide thickness
$E_{eff}$	Transverse effective electric field [V/cm]
$E_g$	Band gap [eV]
$E_{lateral}$	Lateral electric field [V/cm]
$E_F$	Fermi energy [eV]
$E_s$	Electric field near source edge [V/cm]
$\epsilon_0$	Vacuum permittivity [8.85 x 10 <sup>-14</sup> F/cm]
$\epsilon_s$	Semiconductor permittivity [Si: 1.04 x 10 <sup>-12</sup> F/cm]
$\epsilon_{ox}$	Silicon-dioxide permittivity [3.45 x 10 <sup>-13</sup> F/cm]
$\epsilon_r$	Relative permittivity

---

## **F**

FDSOI	Fully-depleted SOI
$f$	Frequency [Hz]

$f_{clk}$	Clock frequency
$\Phi_B$	Potential barrier [eV]
$\Phi_{MS}$	Work-function difference between metal and silicon [eV]

---

## **G**

GIDL	Gate-Induced Drain Leakage
GAA	Gate-All-Around
$g_m$	Transconductance [S]

---

## **H**

HM	Hard Mask
HP	High Performance logic
HTO	High-Temperature Oxide
$H_{fin}$	Fin height [cm]
$H_{NW}$	Nanowire height [cm]
$\eta_F$	Reduced Fermi energy [eV]

---

## **I**

IG	Independent-Gate
I/I	Ion Implantation
$I_{Dlin}$	Drain current at low drain voltage [A]
$I_{Dsat}$	Saturation current [A]
$I_{DS}$	Drain-to-source current [A]
$I_{ON}$	On-state current [A]
$I_{OFF}$	Off-state current [A]
$I_N$	nMOSFET drain current in a CMOS inverter [A]
$I_P$	pMOSFET drain current in a CMOS inverter [A]
$I_{GIDL}$	Gate-induced drain leakage current [A]
$I_{cp}$	Charge pumping current [A]

## *List of symbols and abbreviations*

---

$I_{leak}$	Total leakage current including gate and junction leakages [A]
$I_{gate}$	Gate leakage current [A]
$I_{subth}$	Subthreshold current [A]
$I_{Tr}$	Transistor current corresponding to the threshold voltage [A]

---

## **J**

$J_G$	Gate leakage current density [A/cm <sup>2</sup> ]
-------	---

---

## **K, $\kappa$**

$k$	Boltzmann constant [=8.617 x 10 <sup>-5</sup> eV/K]
$\kappa$	Scaling factor, Relative dielectric constant

---

## **L**

LOP	Low Operating Power logic
LSTP	Low Standby Power logic
LSI	Large-Scale Integrated circuit
$L_G$	Physical gate length [cm]
$L_{eff}$	Electrical channel length [cm]
$L_{ov}$	Gate overlap length [cm]
$L_m$	Mask gate length [cm]
$\lambda$	Backscattering mean free path of carriers [cm]
$\lambda$	Natural length [cm]
$l$	Critical length of scattering [cm]

---

## **M, $\mu$**

MBCFET	Multi-Bridge Channel MOSFET
MCFET	Multi-Channel MOSFET
MOSFET	Metal-Oxide-Silicon Field-Effect-Transistor
$m$	Body-effect coefficient

*List of symbols and abbreviations*

---

$m^*$	Carrier effective conduction mass
$\mu_{eff}$	Effective mobility [ $\text{cm}^2/\text{V}\cdot\text{s}$ ]
$\mu_s$	Mobility near source edge [ $\text{cm}^2/\text{V}\cdot\text{s}$ ]
$\mu_{ph}$	Phonon limited mobility [ $\text{cm}^2/\text{V}\cdot\text{s}$ ]
$\mu_{sr}$	Surface-roughness limited mobility [ $\text{cm}^2/\text{V}\cdot\text{s}$ ]
$\mu_{cb}$	Coulomb limited mobility [ $\text{cm}^2/\text{V}\cdot\text{s}$ ]
$\mu_0$	Low-field mobility [ $\text{cm}^2/\text{V}\cdot\text{s}$ ]

---

## **N**

$N_{INV}$	Inversion charge density [ $\text{cm}^{-2}$ ]
$N_{INV}^{source}$	Inversion charge density near source edge [ $\text{cm}^{-2}$ ]
$N_a$	Acceptor impurity concentration [ $\text{cm}^{-3}$ ]
$N_d$	Donor impurity concentration [ $\text{cm}^{-3}$ ]
$N_t$	Oxide trap density

---

## **O**

## **P**

## **Q**

$q$	Unit electronic charge [C]
$Q_i$	Inversion charge per unit gate area [ $\text{C}/\text{cm}^2$ ]
$Q_B$	Total gate depletion charge [C]
$Q_{inv}$	Inversion charge [C]
$\theta_{eff}$	Mobility reduction factor
$\theta_1$	First order mobility reduction coefficient
$\theta_2$	Second mobility reduction coefficient

---

## **R**

RMS	Root Mean Square
RP-CVD	Reduced-Pressure Chemical Vapor Deposition
$R_{SD}$	Source/drain series resistance
$R_S$	Source resistance
$R_D$	Drain resistance
$r$	Backscattering rate near-source region

---

## **S**

SEG	Selective Epitaxial Growth
SEM	Scanning Electron Microscopy
SNM	Static Noise Margin
SNWT	Silicon NanoWire field-effect Transistor
SOI	Silicon-On-Insulator
SON	Silicon-On-Nothing
SRAM	Static Random Access Memory
STI	Shallow Trench Isolation
$S_Y$	Y-function slope
SS	Subthreshold swing [V/decade]

---

## **T, $\tau$**

TEM	Transmission electron microscopy
$T$	Temperature [K]
$T_{dep}$	Thickness of depletion layer
$t_{ox}$	Gate oxide thickness [cm]
$t_{Si}$	Silicon thickness [cm]
$t_r$	Rising time [s]
$t_f$	Falling time [s]

$\tau$	Average time between two collisions [s]
$\tau_n$	nMOSFET pull-down delay [s]
$\tau_p$	pMOSFET pull-up delay [s]

---

## U

---

## V

VDT	Voltage-Doing Transformation
$V_T$	Threshold voltage [V]
$V_{DD}$	Power-supply voltage [V]
$V_G$	Gate voltage [V]
$V_S$	Source voltage [V]
$V_D$	Drain voltage [V]
$V_{DS}$	Source–drain voltage [V]
$V_{Dsat}$	Drain saturation voltage [V]
$V_{in}$	Input voltage [V]
$V_{out}$	Output voltage [V]
$V_{fb}$	Flat-band voltage [V]
$V_{base}$	Gate pulse base level [V]
$V_{Tlong}$	Threshold voltage in a long-channel device [V]
$V_{bi}$	Built-in voltage [V]
$V_{thermal}$	Thermal voltage ( $= kT/q$ ) [V]
$v_s$	Average carrier velocity near the source edge [cm/s]
$v_{sat}$	Saturation velocity [cm/s]
$v_{\theta}$	Ballistic velocity of carriers [cm/s]
$v_{inj}$	Injection carrier velocity at the top of the barrier near the source edge [cm/s]

---

## **W**

$W$	Gate width [cm]
$W_d$	Depletion-layer depth [cm]
$W_{dm}$	Maximum depletion-layer depth [cm]
$W_{space}$	Lateral space between nanowires for multi-finger [cm]
$W_{pitch}$	Nanowire Pitch for multi-finger [cm]
$W_{NW}$	Nanowire width [cm]
$W_{fin}$	Fin width [cm]
$W_m$	Mask gate width [cm]
$W_{TOT}$	Total gate width [cm]
$W_{Top}$	Top-view width [cm]
$W_{sp}$	Spacer width [cm]

---

## **X**

$x_j$	Source/drain junction depth [cm]
-------	----------------------------------

---

## **Y, $\psi$**

$\psi_B$	Difference between Fermi level and intrinsic level [eV]
$\psi_S$	Surface potential [eV]

---

## **Z**

$\mathfrak{S}_n$	Fermi integral of the $n$ th order
------------------	------------------------------------

---

# **CHAPTER 1**

---

## *INTRODUCTION – MOSFET SCALING –*

---

Silicon-based large-scale integrated circuits (LSIs) have been rapidly developed in the past 40 years with an unprecedented growth of the semiconductor industry, bringing an enormous impact on the way people work and live. This evolution is owed to the continued downsizing of Metal-Oxide-Silicon Field-Effect-Transistors (MOSFETs). Recently, however, the conventional miniaturization has caused various problems such as threshold voltage roll-off, subthreshold leakage, gate leakage, etc.

In this chapter, firstly, the conventional scaling method and the basic operation of MOSFET are described. Then the specific features of short-channel MOSFETs are considered. The latter half of this chapter covers the proposed solutions and challenges to continue the scaling toward purpose of this thesis.

---



# CHAPTER 1 CONTENTS

## **1 Introduction – MOSFET Scaling –**

### 1.1 MOSFET Downsizing

#### 1.1.1 Basic CMOS Operation

#### 1.1.2 MOSFET Scaling

#### 1.1.3 CMOS Performance Indexes

### 1.2 Short Channel MOSFET

#### 1.2.1 Short Channel Effects

#### 1.2.2 Source/Drain Series Resistance in Short-Channel MOSFET

#### 1.2.3 Carrier Transport Mechanisms in Short-Channel MOSFET

### 1.3 Key Technologies to Improve MOSFET Performance

#### 1.3.1 Gate-All-Around Silicon Nanowire MOSFET

#### 1.3.2 Vertically-Stacked Channel MOSFET

### 1.4 Purpose and Contents of This Study

### 1.5 References

## 1.1 MOSFET DOWNSIZING

Since the invention of the CMOS (complementary MOS) in 1963, for which both  $n$ -channel and  $p$ -channel transistors are constructed simultaneously on the same substrate, the number of devices on a chip has increased thanks to MOSFET downsizing in accordance with Moore’s Law. The latter was proposed by Gordon E. Moore in 1965 [1.1]. His prediction states that the number of transistors per chip will double about every two years. That has happened fairly regularly up to now as shown in Figure 1.1 (a) [1.2]. In addition, the average transistor price has decreased markedly over the past four decades (Figure 1.1 (b)) [1.3]. Increasing transistor budgets and decreasing average price per transistor opened up the possibility for high-speed designs that were not technologically or economically feasible before (Figure 1.1 (c)) [1.2]. The speed improvements have been achieved by MOSFET scaling. In this section, the basic MOSFET operation principle and the scaling rule are described.

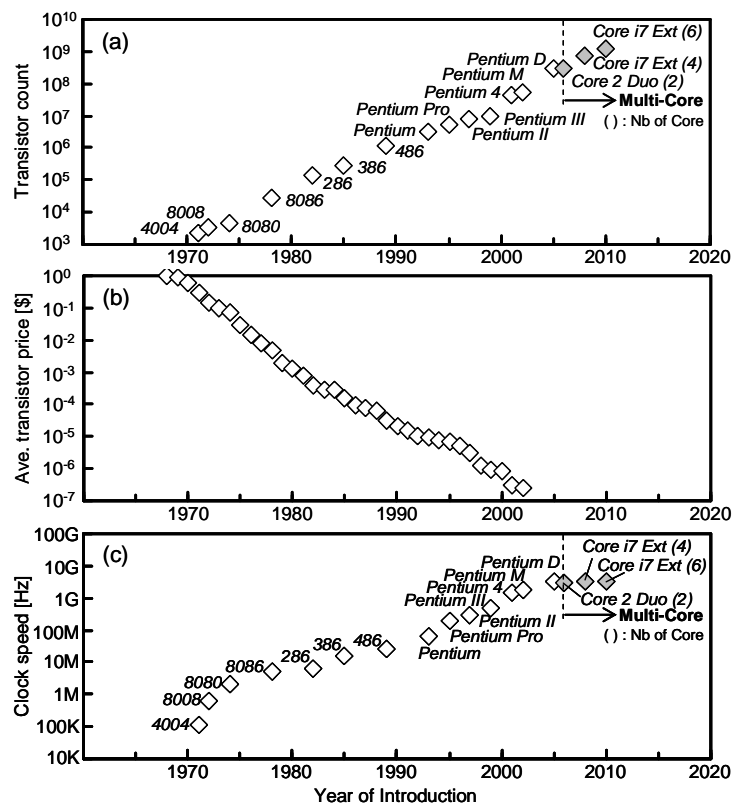


Figure 1.1 (a) Number of transistors in Intel’s microprocessor chips, (b) Average transistor price by year, (c) Clock speed of Intel’s microprocessor [1.2, 1.3].

### 1.1.1 Basic CMOS Operation

A schematic three-dimensional illustration of conventional CMOS transistors of the year early 2000 or earlier, consisting of an n-channel MOSFET (nMOSFET) and a p-channel MOSFET (pMOSFET) integrated on the same chip, is shown in Figure 1.2. The MOSFET is a four-terminal device where *gate*, *source*, *drain* and *substrate* or *body* are the considered electrodes. The nMOSFET consists of a p-type silicon (Si) substrate for which n+ regions, the source and the drain, are formed (e.g., by ion implantation). The gate electrode is usually made of heavily doped polysilicon (poly-Si) and is insulated from the substrate by a thin silicon dioxide (SiO<sub>2</sub>) films, the gate oxide. The SiO<sub>2</sub> film is usually formed by a thermal oxidation of the silicon substrate. The surface region under the gate oxide between the source and the drain is called the *channel* region and is critical for current conduction in a MOSFET. One of the main reasons for the successful development of the MOSFET technology is the nature of the SiO<sub>2</sub> film which is stable thermally and with a high quality interface with the Si channel. To obtain a low resistive contact, metal silicide is formed on the polysilicon gate as well as on the source and the drain diffusion regions. A MOSFET is surrounded by a thick oxide called the field oxide to isolate it from the adjacent devices. The key physical parameters are the gate length ( $L_G$ ), the gate width ( $W$ ), the source/drain junction depth ( $x_j$ ), the gate oxide thickness ( $t_{ox}$ ), and the channel dopant atoms concentration ( $N_a, N_d$ ).

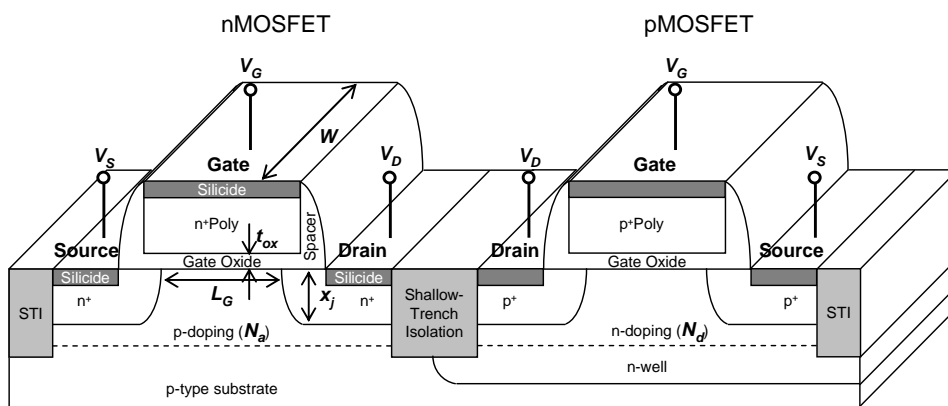


Figure 1.2 Three-dimensional view of a basic CMOS structure.  $V_G$  is the gate voltage,  $V_S$  is the source voltage,  $V_D$  is the drain voltage,  $L_G$  is the gate length,  $t_{ox}$  is the gate oxide thickness,  $N_a$  is the acceptor impurity density,  $N_d$  is the donor impurity density,  $x_j$  is the junction depth

### ■ Drain–Source Current Model

In a MOSFET device, an inversion charge layer at the silicon–gate oxide interface acts as a conducting channel. For example, for a bulk nMOSFET, the substrate will be made in  $p$ -type silicon and the inversion charge will consist of electrons that form a conducting channel between the  $n^+$  source and drain regions. The onset of the strong inversion regime is defined in terms of a threshold voltage ( $V_T$ ) being applied to the gate electrode relative to the other terminals. Depending on the gate voltage ( $V_G$ ) and source–drain voltage ( $V_{DS}$ ), a MOSFET can be biased in one of the three regions: linear region, saturation region, and subthreshold region, as shown in Figure 1.3.

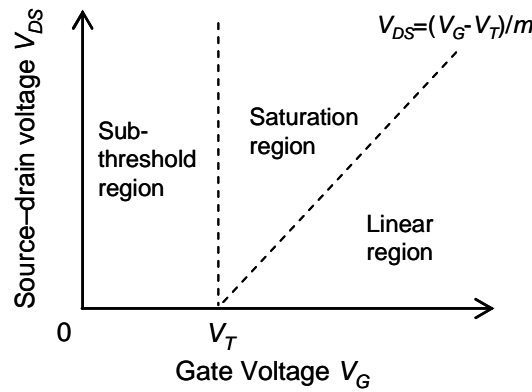


Figure 1.3 The three operating regions of a MOSFET operation in the  $V_{DS}$ – $V_G$  plane [1.4].

In the following, the drain–source current ( $I_{DS}$ ) model for long-channel MOSFETs is described. One key assumption is the *gradual–channel approximation*, which assumes that the transverse electric field in the channel is much larger than the longitudinal field, that is one-dimensional. This allows us to express  $I_{DS}$  as [1.4]

$$I_{DS} = \mu_{eff} \frac{W}{L_G} \int_0^{V_{DS}} (-Q_i(V)) dV, \quad (1.1)$$

where  $\mu_{eff}$  is the carriers effective mobility and  $Q_i$  is the inversion charge per unit of channel area. The drain–source current based on the gradual–channel approximation is valid for most of the  $V_{DS}$  regions except beyond saturation voltage ( $V_{DSat}$ ). Beyond  $V_{DSat}$ ,  $I_{DS}$  stays constant at a saturation value ( $I_{DSat}$ ), independent of  $V_{DS}$ . In addition, the use of

the *charge-sheet model*, which assumes that the inversion layer is a charge sheet as zero thickness, allows us to simply express the  $I_{DS}$  in each  $V_{DS}$  region as the following equations:

$$I_{DS} = \mu_{eff} C_{ox} \frac{W}{L_G} (V_G - V_T) V_{DS} \quad \text{for } V_{DS} \leq V_G - V_T \text{ (linear region)} \quad (1.2)$$

$$I_{Dsat} = \mu_{eff} C_{ox} \frac{W}{L_G} \frac{(V_G - V_T)^2}{2m} \quad \text{for } V_{DS} > V_{Dsat} \text{ (saturation region)} \quad (1.3)$$

where  $C_{ox}$  ( $= \epsilon_{ox}/t_{ox}$ ) is the gate oxide capacitance per area,  $\epsilon_{ox}$  is the gate oxide permittivity,  $m$  is the body-effect coefficient related to doping concentration and oxide thickness.

When the gate bias is below the threshold voltage and the semiconductor is in weak inversion or depletion, the corresponding drain current is called the subthreshold current. The subthreshold region tells how sharply the current drops with gate bias. Figure 1.4 shows schematic  $I_{DS} - V_G$  curves of nMOSFETs.  $I_{DS}$  at  $V_G = 0$  and  $V_{DS} = V_{DD}$  is equivalent to the off-state current ( $I_{OFF}$ ), while  $I_{DS}$  at  $V_G = V_{DS} = V_{DD}$  is equivalent the on-state currents ( $I_{ON}$ ). Here,  $V_{DD}$  is the power-supply voltage. The transition from one state to another defines the  $V_T$  of the MOSFET. In Figure 1.4 (a),  $I_{DS}$  on a linear scale appears to approach zero immediately below the threshold voltage. On a logarithmic scale, however, it is seen that the descending  $I_{DS}$  remains at significant levels for several tenths of a volt below  $V_T$  (Figure 1.4 (b)).

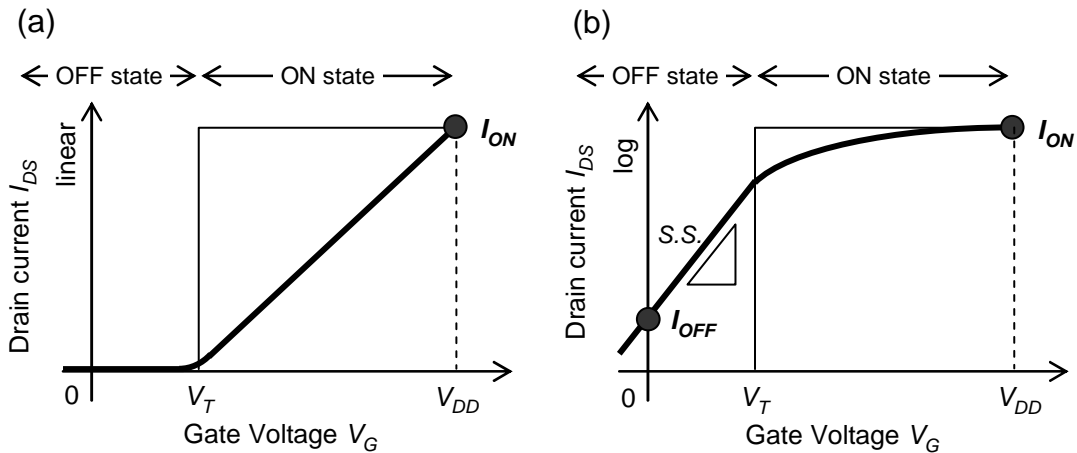


Figure 1.4 Typical  $I_{DS} - V_G$  characteristics of an nMOSFET at high drain voltages. The same current is plotted on both linear scale (a) and logarithmic scale (b).

In general, the current density in a semiconductor can be expressed by the sum of the drift current density and the diffusion current. In weak inversion and depletion mode, however, electron charge is small and thus, the drift current is low. The drain current is dominated by diffusion. Therefore, the inversion charge density ( $N_{INV}$ ) does not drop to zero abruptly. One can write the subthreshold current ( $I_{subth}$ ) a function of  $V_G$  as

$$I_{subth} = \mu_{eff} C_{ox} \frac{W}{L_G} (m-1) \left( \frac{kT}{q} \right)^2 e^{q(V_G - V_T)/mkT} (1 - e^{-qV_{DS}/kT}) \quad (\text{subthreshold region}), \quad (1.4)$$

where  $q$  is electronic charge,  $k$  is the Boltzmann constant, and  $T$  is temperature. The subthreshold current is independent of the drain voltage once  $V_{DS}$  is larger than a few  $kT/q$ , as would be expected for a diffusion-dominated current transport. The current dependence with the gate voltage, on the other hand, is exponential. The subthreshold behaviors are primarily determined by fabrication technology considerations. The parameter to quantify how sharply the MOSFET is turned off by the gate voltage is called the subthreshold swing ( $SS$ ), defined as the gate-voltage change needed to induce a drain-current change of one order of magnitude. The  $SS$  thus can be written as

$$SS = \left( \frac{d \log_{10} I_{DS}}{dV_G} \right) = \ln(10) \frac{kT}{q} \left( 1 + \frac{C_{dm}}{C_{ox}} \right), \quad (1.5)$$

where  $C_{dm}$  is the maximum depletion-layer capacitance per area.

## ■ CMOS Inverter

The most basic component of digital static CMOS circuits is a CMOS inverter, which is composed by an nMOSFET and a pMOSFET as shown in Figure 1.5 (a). The source terminal of the nMOSFET is grounded, while the one of the pMOSFET is connected to  $V_{DD}$ . The gates of the two MOSFETs are connected as the input node, and the drains are connected as the output node. Here,  $C_L$  in Figure 1.5 is a lumped load capacitance of the output node (including the output capacitance  $C_{out}$  of the switching inverter, the input capacitance  $C_{in}$  of the next stage or stages it drives, and the wiring capacitance  $C_{wire}$ ). The current through the pMOSFET ( $I_P > 0$ ) flows from  $V_{DD}$  into the output node and tends to charge up the node voltage toward  $V_{DD}$  (i.e., pull-up), while the current through the nMOSFET ( $I_N > 0$ ) flows out of the output node into the ground and

tends to discharge the node voltage to zero (i.e., pull-down) as shown in Figure 1.5 (b) and (c). In such a system, the complementary nature of n- and pMOSFETs allows one and only one MOSFET to be conducting in one of the two stable states. Since only one of the MOSFETs is “on” in the steady state, there is little static current or static power dissipation. In principle, the power dissipation occurs only during switching transients when a charging or discharging current is flowing through the circuit [1.4].

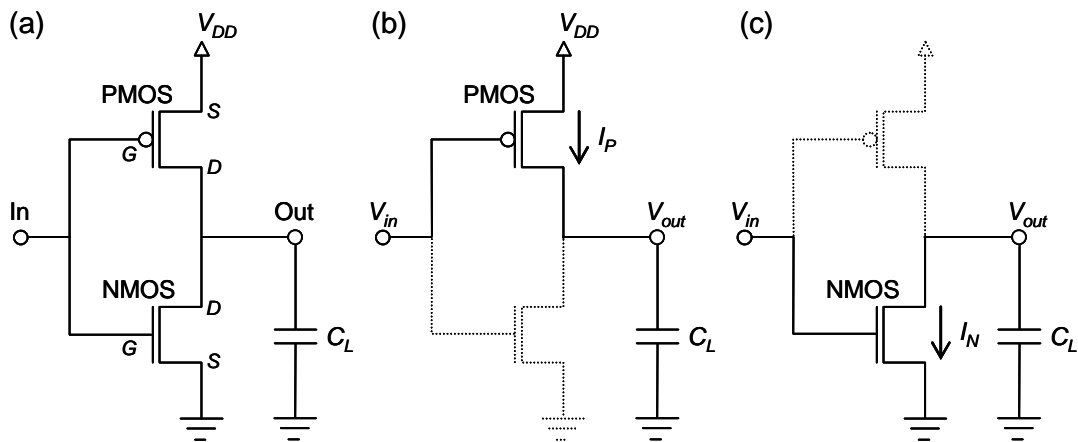


Figure 1.5 (a) Circuit diagram of CMOS inverter. (b) Charge and (c) discharge equivalent circuits.

### 1.1.2 MOSFET Scaling

A CMOS technology performance is basically evaluated by three indexes: its *switching speed*, *power consumption*, and *integration density*. These indexes have been successfully increased in the past 40 years. This progress has been achieved on the basis of MOSFET scaling rule. As the channel length decreases, the depletion width ( $W_d$ ) around the source and drain becomes comparable to the channel length. This will cause high short-channel effects (as described in detail in Section 1.2). Because the short-channel effects complicate device operation and degrade device performance, these effects should be minimized so that a physical short-channel device can preserve the electrical long-channel behavior. The most-ideal scaling rule to avoid the short-channel effects is simply to reduce proportionally all device dimensions (both horizontal and vertical), the operating voltages and to increase channel doping level by

the same factor ( $\kappa > 1$ ) as shown in Figure 1.6, so that the electric field remains unchanged and the depletion width of the source and drain is reduced. This scaling is called “constant-field scaling” proposed by R. Dennard in 1974 [1.5]. The scaling rule is summarized in Table 1.1. In the scaled MOSFETs, the current equations (1.2, 1.3) can be rewritten as

$$I'_{DS} = \mu_{eff} \frac{\epsilon_0 \epsilon_{ox}}{(t_{ox}/\kappa)} \frac{W/\kappa}{L_G/\kappa} \left( \frac{V_G - V_T - mV_{DS}/2}{\kappa} \right) (V_{DS}/\kappa) = \frac{I_{DS}}{\kappa} \quad (\text{linear region}) \quad (1.6)$$

$$I'_{DS} = \mu_{eff} \frac{\epsilon_0 \epsilon_{ox}}{(t_{ox}/\kappa)} \frac{W/\kappa}{L_G/\kappa} \left( \frac{V_G - V_T}{\kappa} \right)^2 / 2m = \frac{I_{DS}}{\kappa}. \quad (\text{saturation region}) \quad (1.7)$$

Since the current is reduced by the factor  $\kappa$ , the channel current per unit of channel width is unchanged by scaling. This is consistent with the same sheet density of carriers moving at the same velocity. As a result, the switching speed, the power consumption, and the integration density are improved by factor of  $\kappa$ ,  $1/\kappa^2$ , and  $\kappa^2$ , respectively.

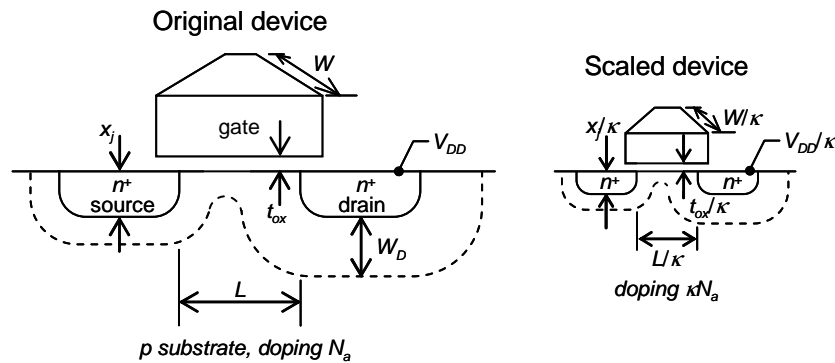


Figure 1.6 Principles of MOSFET constant-electric-field scaling.

In reality, partly because of the unwillingness to depart from the standardized voltage levels of the previous generation, the power-supply voltage was seldom scaled in proportion to channel length. Even though constant-field scaling provides a basic guideline to the design of scaled MOSFETs, the requirement of reducing the voltage by the same factor as the device physical dimension is too hard. Moreover, there are several factors that scale neither with the physical dimensions nor with the operating voltage. The primary reason for the nonscaling effects that neither the thermal voltage ( $V_{thermal} = kT/q$ ) nor the silicon band gap ( $E_g$ ) changes with scaling. Because of the



exponential dependence of subthreshold current (see the equation (1.4)), the threshold voltage cannot be scaled down significantly without causing a substantial increase in the off-current. In fact, even if the threshold voltage is held unchanged, the off-current per device still increases by a factor  $\kappa$  (from the  $C_{ox}$  factor) when the physical dimensions are scaled down by  $\kappa$ . Note that the  $SS$  factor remains essentially the same since  $SS$  is proportional to  $1+C_{dm}/C_{ox}$  (see the equation (1.5)) and both capacitances are scaled up by the same factor  $\kappa$ . In addition, the process difficulties for aggressively scaled MOSFETs also limit the scaling. With the practical limitations, other scaling rules have been proposed, including constant-voltage scaling and generalized scaling [1.4]. This allows the various device parameters to be adjusted independently as long as the overall behavior is preserved. These nonideal factors, which hinder constant-field scaling, result in some form of a penalty as shown in Table 1.1, especially power consumption. Therefore, it is important to understand how factors affect the performance of a CMOS LSI chip in order to obtain an optimized device structure.

*Table 1.1 Constant-field scaling and generalized scaling of MOSFET device and circuit parameters [1.4].*

	Device and Circuit Parameters	Multiplicative Factor ( $\kappa > 1$ )	
		Constant-field Scaling	Generalized Scaling
Scaling assumptions	Device dimensions ( $t_{ox}$ , $L$ , $W$ , $x_j$ )	$1/\kappa$	$1/\kappa$
	Doping concentration ( $N_a$ , $N_d$ )	$\kappa$	$\alpha\kappa$
	Voltage ( $V$ )	$1/\kappa$	$\alpha/\kappa$
Derived scaling behavior of device parameters	Electric field ( $E$ )	1	$\alpha$
	Carrier velocity ( $v$ )	1	$\alpha$ 1
	Depletion-layer width ( $W_d$ )	$1/\kappa$	$1/\kappa$
	Capacitance ( $C = \epsilon A/t$ )	$1/\kappa$	$1/\kappa$
	Inversion/layer charge density ( $Q_i$ )	1	$\alpha$
	Current, drift ( $I$ )	$1/\kappa$	$\alpha^2/\kappa$ $\alpha/\kappa$
Derived scaling behavior of circuit parameters	Circuit delay time ( $\tau \sim CV/I$ )	$1/\kappa$	$1/\alpha\kappa$ $1/\kappa$
	Power dissipation per circuit ( $P \sim VI$ )	$1/\kappa^2$	$\alpha^3/\kappa^2$ $\alpha^2/\kappa^2$
	Power/delay product per circuit ( $P\tau$ )	$1/\kappa^3$	$\alpha^2/\kappa^3$
	Circuit density ( $\propto I/A$ )	$\kappa^2$	$\kappa^2$
	Power density ( $P/A$ )	1	$\alpha^3$

### 1.1.3 CMOS Performance Indexes

The need for low power devices was a major driving force behind the development of CMOS technologies. As a result, CMOS devices are best known for low power consumption due to the unique characteristic of very low standby power. This enables higher integration levels and makes them the technology of choice for most LSI applications. However, continuing aggressive scaling of MOSFETs and the resulting circuit density growth lead inevitably to a further increase of power consumption of CMOS integrated circuits recently. Therefore, for optimizing the performance, simply knowing that CMOS devices may use less power than equivalent devices from other technologies does not help much. It is necessary to understand the relationship between switching characteristics, integration density, and power dissipation in terms of MOSFET dimensions.

#### ■ Switching Characteristics

A realistic benchmarking of the switching delay for CMOS circuits is essential to quantify technology requirements in order to continue its historical scaling trend. In the research stage, it is important to establish the connection of the device-level targets with circuit-level performance. In 1995, M. Bohr has proposed a MOSFET speed metric as an approximated gate delay [1.6]. This metric assumes a transistor circuit as shown in Figure 1.7. This circuit can be easily imagined from Figure 1.5 (b) or (c). Transistor A and B are identical. The gate delay is defined as the time it takes node C to make a voltage swing equal to  $V_{DD}$ . The only capacitance on node C is the gate capacitance  $C_G$  of transistor B, which is defined as gate area times gate oxide capacitance per unit area ( $C_{ox}$ ). It is important to note that physical gate length  $L_G$  as opposed to electrical channel length  $L_{eff}$  is used to calculate  $C_G$  because  $L_G$  will include both channel and overlap capacitance. The on-state drive current  $I_{ON}$  of transistor A charges or discharges this capacitor. The gate delay can thus be approximated by the equation:

$$\tau \approx \frac{C_G \times V_{DD}}{I_{ON}}. \quad (1.8)$$

Historically, this expression (1.8) has been widely used as a benchmark of the

MOSFET speed [1.7]. This is because one can easily quantify the relative performance without fabricating a circuit. The only information needed from a MOSFET to estimate its  $CV/I$  gate delay is  $V_{DD}$ ,  $L_G$ ,  $I_{ON}$ , and  $C_{ox}$ . The equation (1.8) can be rewritten by using the equation (1.3):

$$\tau \approx \frac{(C_{ox}WL_G) \times V_{DD}}{\mu_{eff} C_{ox} \frac{W}{L_{eff}} \frac{(V_{DD} - V_T)^\alpha}{2m}} = (L_{eff} + 2L_{ov})L_{eff} \frac{2m}{\mu_{eff}} \frac{V_{DD}}{(V_{DD} - V_T)^\alpha}, \quad (1.9)$$

where  $L_{ov}$  is the gate overlap length and the power of  $\alpha$  ( $1 < \alpha < 2$ ) indicates the degree of velocity saturation in short-channel MOSFETs. It is clear that the gate delay is strongly depends on the gate length. This is a reason that  $I_{ON}$  enhancement as a function of the gate length is often used as a metric of a MOSFET speed. Note that this gate delay is independent on the gate width because both  $C_G$  and  $I_{ON}$  are linearly proportional to the gate width.

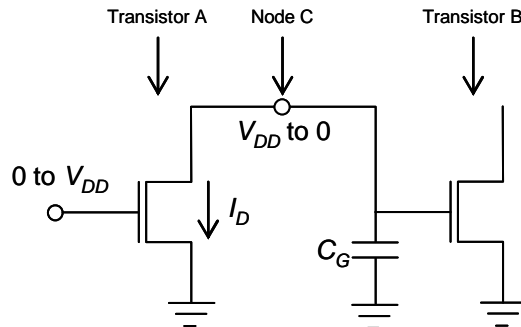


Figure 1.7  $CV/I$  performance metric [1.6].

However, in actual CMOS circuits, the load capacitance is not so simple. The difference between the geometrical dependences of each capacitance source leads to the gate delay estimation error. Here we discuss an effect of the gate width independent components. When the gate capacitance in the equation (1.8) is replaced by a lumped load capacitance  $C_L$ , the equivalent circuit can be modified as shown in Figure 1.8. The load capacitance can be separated into three major components.

1. The output capacitance  $C_{out}$  that results from the drain diffusion of the driving transistor A.
2. The input capacitance  $C_{in}$  that is the gate capacitance of the transistor B being

driven by the transistor A, including the intrinsic and the overlap components.

3. The wiring capacitance  $C_{wire}$  that results from interconnects to the gates being driven.

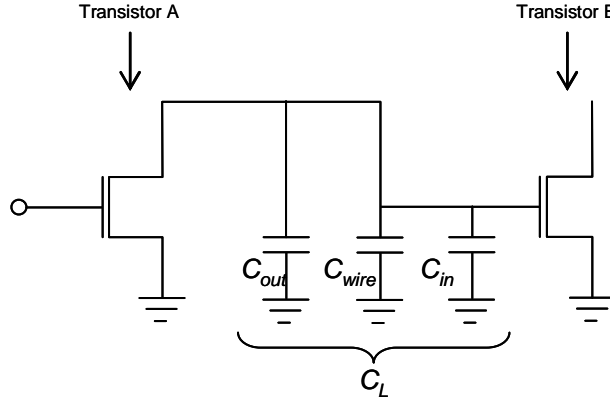


Figure 1.8 Equivalent circuit with wiring capacitance.

In general, the output of a transistor may drive more than one stage. In that case, the fan-out  $FO$  is 2, 3, ..., which means that each inverter in the chain is driving 2, 3, ... stages in parallel. The lumped load capacitance  $C_L$  thus can be written by

$$C_L = C_{out} + C_{wire} + C_{in} \times FO. \quad (1.9)$$

Here  $C_{out}$  and  $C_{in}$  are linearly proportional to the gate width, while  $C_{wire}$  is independent on that. The gate delay of the equation (1.8) then can be rewritten by the equation (1.9):

$$\begin{aligned} \tau &\approx \frac{C_L \times V_{DD}}{I_{ON}} = \frac{(C_{out} + C_{wire} + C_{in} \times FO) \times V_{DD}}{I_{ON}} \\ &= \frac{(C_{out} + C_{in} \times FO) \times V_{DD}}{I_{ON}} + \frac{C_{wire} \times V_{DD}}{I_{ON}} \\ &= \frac{C_L(W) \times V_{DD}}{I_{ON}} + \frac{C_{wire} \times V_{DD}}{I_{ON}}, \end{aligned} \quad (1.10)$$

where  $C_L(W)$  is the gate width dependent capacitance, which consists of the p-n junction capacitance and the gate capacitance including the intrinsic and overlap components. Since both  $C_L(W)$  and  $I_{ON}$  are linearly proportional to the gate width, the gate width effect is canceled out in the first term. On the other hand, the second term depends on the gate width. As the gate width increases, the delay decreases. However, the reduction

in the delay must be traded off against the increased area (and power) when the width is increased.

Moreover, accuracy of the  $CV/I$  metric in approximating delay time is degraded as device scaling progresses [1.8–1.11]. The problem of the  $CV/I$  metric is that the MOSFETs in a real CMOS logic gate chain usually do not operate at the bias point ( $V_{GS} = V_{DS} = V_{DD}$ ) which gives  $I_{ON}$  because an inverter is driven by output from a previous stage whose waveform has a finite rise or fall time associated with it as shown in Figure 1.9. The peak current is typically 80–90% of maximum on-current  $I_{ON}$  at  $V_G = V_{DS} = V_{DD}$ . The exact percentage depends on the detailed device parameters such as mobility, velocity saturation, short-channel effects and series resistance. In particular, the contribution of drain-induced barrier lowering (DIBL) due to the short-channel effects has been pointed out as shown in Figure 1.9 (b) [1.8–1.11]. The difference of  $I_{DS}$ - $V_{DS}$  curves between with and without a degraded DIBL results in different bias-point trajectories during switching. Though  $I_{ON}$  is kept at the same level, the inverter chain built by devices with the degraded DIBL switches at a lower speed. To evaluate of the delay of a short-channel MOSFET, it is important to consider both the current level and the DIBL.

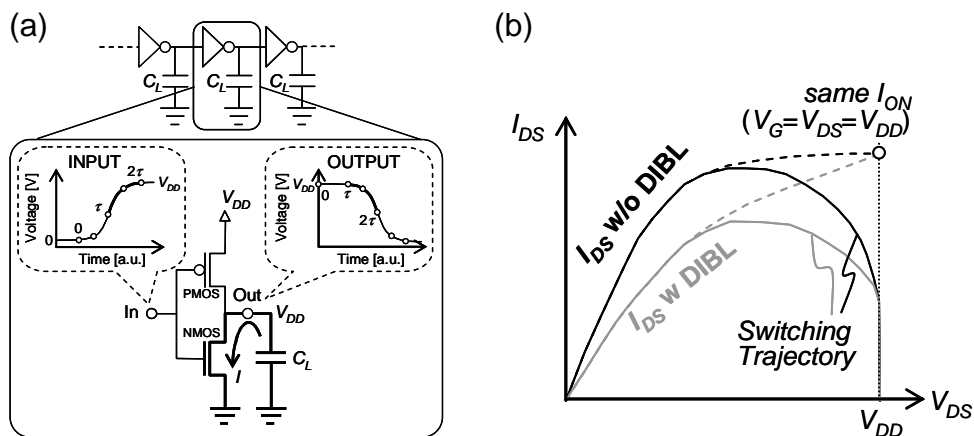


Figure 1.9 (a) Operation of a CMOS inverter in inverter chain. (b)  $I_{DS}$ - $V_{DS}$  curve and trajectories with and without a degraded DIBL for nMOSFET [1.11].

■ **Integration density**

Integration density means that what number of MOSFETs is fabricated on a chip. As shown in Figure 1.1 (a), the number has been dramatically increased in the last forty years thanks to MOSFET area down-scaling. Figure 1.10 shows a sample layout of a CMOS inverter based on lambda-based design rules [1. 15]. The lambda unit is fixed to half of the minimum available lithography of the technology, typically the minimum gate length ( $L_G=2\lambda$ ). The layout clearly shows that the source/drain active area occupies a large area in a MOSFET, which is determined by the source/drain length and the gate width. The former is limited by the feature size of the process technology used (e.g. contact size, space between contact and gate poly). The latter depends on the carrier mobility ratio between n- and pMOSFET and the current level needed. Regarding the integration density, the key consideration is how to obtain a high current level with a smaller gate width as the feature size is fixed.

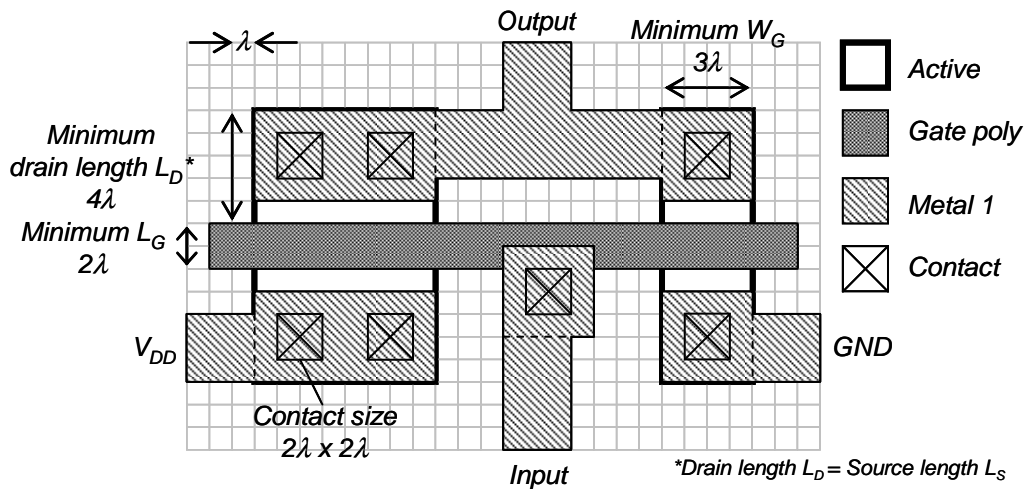


Figure 1.10 Layout of a CMOS inverter based on lambda-based design rules [1. 15]

■ **Power Consumption**

There are three major sources of power consumption in digital CMOS circuits which are summarized in the following equation [1.12]:

$$\begin{aligned}
 P_{consum} &= P_{switching} + P_{short-circuit} + P_{leakage} \\
 &= \alpha f_{clk} C_L V_{DD}^2 + I_{sc} V_{DD} + I_{leak} V_{DD}
 \end{aligned}
 \tag{1.11}$$

The first term represents the switching component of dynamic power, where  $C_L$  is the load capacitance,  $f_{clk}$  is the clock frequency, and  $\alpha$  is the node transition activity factor (the average number of times the node makes a power consuming transition in one clock period). The second term is due to the direct-path short circuit current,  $I_{sc}$ , which arises when both the n- and pMOSFET are simultaneously active, conducting current directly from supply to ground. Finally, the leakage component of static power is negligible in principle. This is one of the primary advantages of CMOS system. CMOS circuits do not dissipate power if they are not switching.

However, the continuing MOSFET scaling and the resulting circuit density growth has led to unacceptable level of static power consumption recently. Figure 1.11 shows the power consumption for CMOS logic circuits. As MOSFETs get smaller with each new process technologies, their channel lengths become shorter and the static power consumption increases over the dynamic power consumption. Nowadays, reduction of the static power consumption has become a major challenge for deep submicron CMOS. Total static power consumption can be obtained as

$$P_{static} (= P_{leakage}) = n \sum I_{leak} \times V_{DD} = n(I_{subth} + I_{gate} + I_{GIDL}) \times V_{DD}, \quad (1.12)$$

where  $n$  is the number of transistors in the off-state,  $I_{gate}$  is the gate tunneling current, and  $I_{GIDL}$  is the gate-induced drain leakage (GIDL) current. The leakage currents can be divided in to three main groups:  $I_{subth}$ ,  $I_{gate}$ , and  $I_{GIDL}$ . The increase of  $I_{subth}$  is due to the nonscaling effects and short-channel effects (see in Section 1.2). The increase of  $I_{gate}$  is due to the aggressively scaled  $t_{ox}$  which causes exponential increase of the tunneling current when the  $t_{ox}$  is scaled down to less than 2 nm as shown in Figure 1.11. This gate leakage can be reduced by replacing the gate silicon dioxide ( $\text{SiO}_2$ ) by a high- $\kappa$  material. Practically, high- $\kappa$  technology has been introduced in the 45 nm process technology microprocessor since 2007 by Intel Corporation [1.13]. The  $I_{GIDL}$  is caused by band-to-band tunneling in the gate-to-drain overlap region when a large gate-to-drain voltage is applied, which force the band bending to be larger than the silicon band gap. Lightly doped drain (LDD) structure has been studied as a solution for the GIDL [1.14, 1.15]. Figure 1.12 shows the summary of leakage current components. Actually, the

off-state leakage currents become more and more problematic in a scaled MOSFET (as explained in detail in Section 1.2).

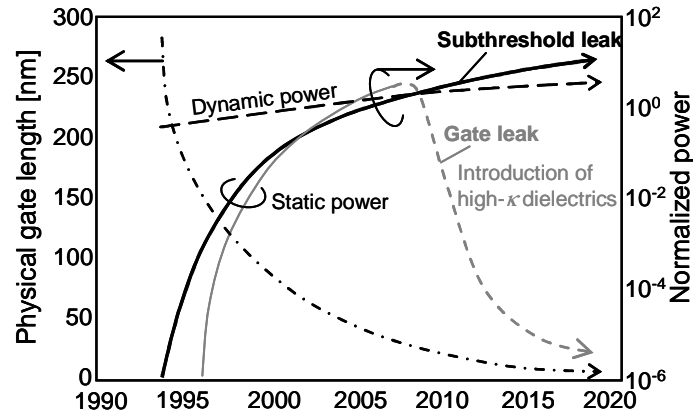


Figure 1.11 Sources of leakage current increase as the technology causes gate lengths to shrink. Data from ITRS [1.6]

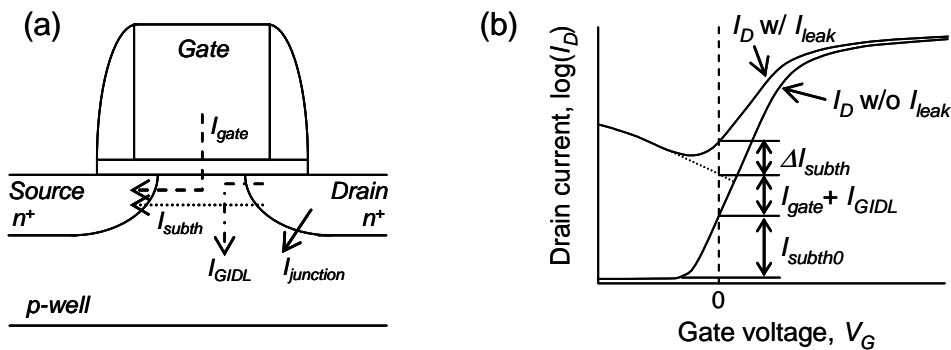


Figure 1.12 (a) Leakage current components in a nMOSFET, (b)  $I_D$ - $V_G$  curves with and without leakage currents.  $I_{subth0}$  is the initial subthreshold current, while  $\Delta I_{subth}$  is the added current due to the short-channel effects.

In this section, we discussed the basic MOSFET operation, the scaling method, and the CMOS performance indexes. CMOS LSI has been developed owing to the diminishing size of MOSFET. Especially, the impact of the gate length and width on CMOS performances was discussed in the latter half. To improve the whole performance, we have to consider the switching characteristics, the integration density,



and the power dissipation at a same time. The diminishing gate length contributes the gate delay reduction, while causes the power dissipation increase due to the short-channel effects. On the other hand, the diminishing gate width can reduce device area leading to a higher integration density, while causing the gate delay increase if the gate width independent capacitances are not negligible. To make the most of the geometrical effects, the key issues will be summarized to the following two points:

1. How can we suppress the short-channel effects?
2. How can we increase the effective gate width in a given layout area?

In the next section, we will discuss the short-channel effects in detail.

## **1.2 SHORT-CHANNEL MOSFET**

Short-channel MOSFETs differ in many important aspects from long-channel devices. This section covers the features of short-channel devices that especially are important for current MOSFETs.

### **1.2.1 Short-Channel Effects**

The key difference between a short-channel and a long-channel MOSFET is that the field pattern in the depletion region of a short-channel MOSFET is two-dimensional. In other words, the gradual-channel approximation breaks down for short-channel devices. The two-dimensional field pattern arises from the proximity of the source and drain regions. The source-drain distance is comparable to the MOS depletion width in the vertical direction, and the source-drain potential has a strong effect on the band bending over a significant portion of the device. This phenomenon will cause the device parameter changes which can be summarized as follows: (1)  $V_T$  roll-off, (2) subthreshold swing degradation, and (3) DIBL degradation.

#### **■ Threshold voltage roll-off**

One way to describe it is to consider the net charge (ionized acceptors or donors) in the depletion region of the device. The field lines terminating on these fixed charges

originate either from the gate or from the source and drain. This is referred to as the charge-sharing model as shown in Figure 1.13 [1.4]. At a low drain voltage, only the field lines terminating on the depletion charges within the trapezoidal region are assumed to originate from the gate. The rest of the field lines originate either from the source or from the drain. Total charge within the trapezoidal region,  $Q'_B \propto W_{dm} \times (L + L')/2$ , is proportionally less than the total gate depletion charge,  $Q_B \propto W_{dm} \times L$ , in the long-channel case. As a result, it takes a lower gate voltage to reach the threshold condition of a short-channel device,

$$V_T = V_{fb} + 2\psi_B + \frac{Q'_B}{WLC_{ox}}, \quad (1.13)$$

Where  $W_{dm}$  is the maximum depletion-layer depth,  $V_{fb}$  is the flat-band voltage, and  $\psi_B$  is the difference between Fermi level and intrinsic level. Note that the horizontal depletion-layer widths  $y_S$  and  $y_D$ , are smaller than the vertical depletion-layer widths  $W_S$ , and  $W_D$ , respectively, because the transverse field strongly influences the potential distribution at the surface. Even though a simple, analytical expression for the threshold voltage can be obtained from the charge-sharing model, the division of depletion charge between the gate and the source and drain is somewhere arbitrary.

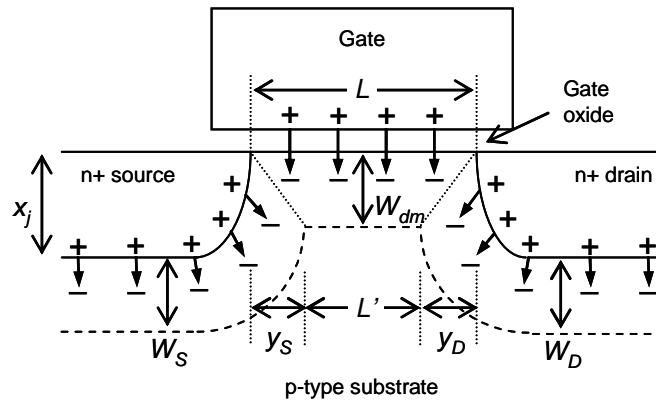


Figure 1.13 Schematic diagram of the charge-sharing model. The dashed lines indicate the boundary of the gate and source–drain depletion regions. The arrows represent electric field lines that originate from a positive charge and terminate on a negative charge. The dotted lines partition the depletion charge and form the two sides of the trapezoid.

The voltage-doing transformation (VDT) has been proposed to replace the influence of the lateral drain–source field by an equivalent reduction in the channel doping concentration [1.17, 1.18]. On the basis of this model, the threshold voltage roll-off can be written as follows:

$$SCE \equiv |\Delta V_T| = 0.64 \frac{\epsilon_s}{\epsilon_{ox}} EI \times \Phi_D \quad (1.14)$$

where

$$EI = \left( 1 + \frac{x_j^2}{L_{eff}^2} \right) \frac{t_{ox}}{L_{eff}} \frac{W_{dm}}{L_{eff}} \quad (1.15)$$

is the Electrostatic Integrity for planar bulk MOSFET,  $\epsilon_s$  is the semiconductor permittivity, and  $\epsilon_{ox}$  is the oxide permittivity. The VDT was proven to be successful in describing the  $V_T$  roll-off for all CMOS technologies from CMOS 1.2  $\mu\text{m}$  down to CMOS 65 nm based on a comparison to numerical simulations and experimental data.

#### ■ Subthreshold swing degradation

The physics of the short-channel effect can be understood from a different angle by considering the potential barrier at the surface between the source and drain, as shown in Figure 1.14. Under off conditions, this potential barrier prevents electron current from flowing to the drain. The surface potential is mainly controlled by the gate voltage. When the gate voltage is below the threshold voltage, there are only a limited number of electrons injected from the source over the barrier and collected by the drain (subthreshold current). In the long-channel case, the potential barrier is flat over most part of the channel. Source and drain fields only affect the very ends of the channel. As the channel length is shortened, however, the source and drain fields penetrate deeply into the middle of the channel, which lowers the potential barrier between the source and drain as shown in Figure 1.14 (b). The region of maximum potential barrier shrinks to a single point near the center of the channel. This causes a substantial increase of the subthreshold current.

Here the equation 1.5 for the subthreshold swing for long-channel devices, which comes from the direct derivation of the drain current expression, can be rewritten as a

function of the surface potential  $\psi_s$ ,

$$S.S. = \frac{kT}{q} \ln(10) \cdot \left( \frac{\partial V_G}{\partial \psi_s} \right) = \frac{kT}{q} \ln(10) \cdot \left( 1 + \frac{1}{C_{ox}} \frac{\partial Q_B}{\partial \psi_s} \right), \quad (1.16)$$

It is clear that the potential barrier lowering in short-channel device will have an impact on subthreshold swing. On the basis of the VDT model, the subthreshold swing behavior with the gate length can be rewritten as follows [1.18]:

$$S.S. = \frac{kT}{q} \ln(10) \cdot \left[ 1 + \frac{1}{C_{ox}} \frac{\partial Q_B}{\partial \psi_s} + \frac{\epsilon_s}{\epsilon_{ox}} \frac{t_{ox}}{L_{eff}} \frac{x_j}{L_{eff}} \left( 1 + \frac{3}{4} \frac{W_{dm}}{L_{eff}} \right) \sqrt{1 + 2 \frac{V_{DS}}{\Phi_D}} \right]. \quad (1.17)$$

Figure 1.15 shows the subthreshold swing calculated by using the MASTAR MOSFET modeling software based on the VDT model [1.19]. It is clear that the subthreshold swing increases as decreasing the gate length.

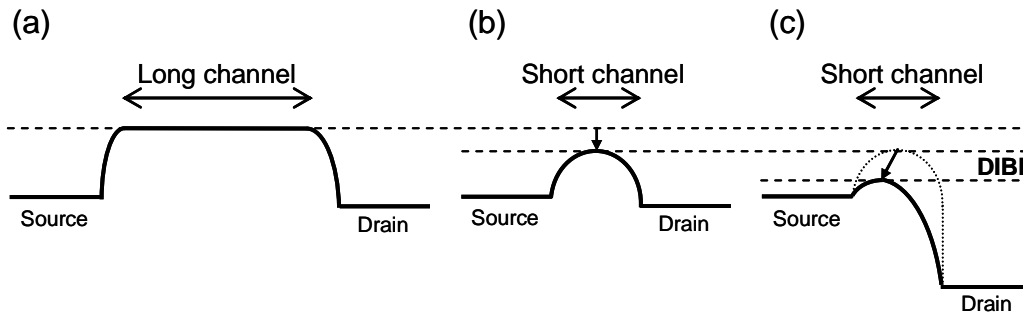


Figure 1.14 Surface potential lowering due to the short-channel effects: (a) a long-channel MOSFET, (b) a short-channel MOSFET at low drain bias, (c) a short-channel MOSFET at high drain bias.

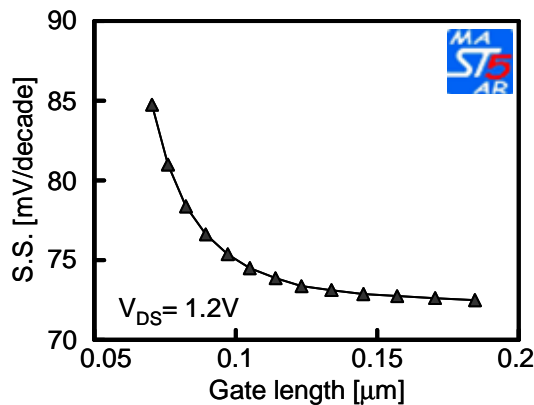


Figure 1.15 Subthreshold swing calculated by using MASTAR MOSFET modeling software [1.19]:  $N_a = 10^{18} \text{ cm}^{-3}$ ,  $x_j = 30 \text{ nm}$ ,  $t_{ox} = 1.3 \text{ nm}$ ,  $V_{DD} = 1.2 \text{ V}$ ,  $W = 1 \mu\text{m}$ .

■ **Drain-induced barrier lowering**

When a high drain voltage is applied to a short-channel device, the barrier height is lowered even more, and the point of maximum barrier also shifts toward the source end as shown in Figure 1.14 (c). The lowering of the source barrier causes an injection of extra carriers, thereby increasing the current substantially. As a result, the threshold voltage decreases. This effect is referred to as drain-induced barrier lowering (DIBL). On the basis of the VDT model, the DIBL behavior can be rewritten as follows [1.18]:

$$DIBL = 0.80 \frac{\epsilon_s}{\epsilon_{ox}} EI \times V_{DS} . \quad (1.18)$$

Figure 1.15 shows the DIBL calculated by using MASTAR MOSFET modeling software based on the VDT model [1.19]. The DIBL increases in short-channel MOSFET as well as the subthreshold swing.

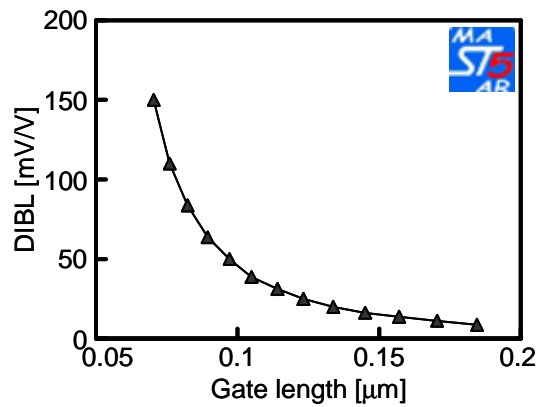


Figure 1.16 DIBL calculated by using MASTAR MOSFET modeling software [1.19]:  $N_a=10^{18} \text{ cm}^{-3}$ ,  $x_j=30 \text{ nm}$ ,  $t_{ox}= 1.3 \text{ nm}$ ,  $V_{DD}= 1.2 \text{ V}$ ,  $W=1 \mu\text{m}$ .

Consequently, the threshold voltage for a short-channel device can be rewritten as follows:

$$V_T = V_{Tlong} - SCE - DIBL , \quad (1.19)$$

where  $V_{Tlong}$  is the threshold voltage in a long-channel device. Figure 1.17 shows the threshold roll-off calculated by using MASTAR MOSFET modeling software based on the VDT model [1.19].

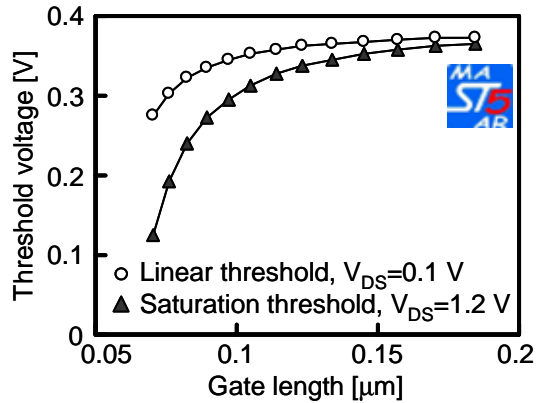


Figure 1.17  $V_T$  roll-off calculated by using MASTAR MOSFET modeling software [1.19]:  $N_a=10^{18} \text{ cm}^{-3}$ ,  $x_j=30 \text{ nm}$ ,  $t_{ox}=1.3 \text{ nm}$ ,  $V_{DD}=1.2 \text{ V}$ ,  $W=1 \mu\text{m}$ .

Here, we should reconsider the static power consumption in short-channel CMOS logic gates. The increase of off-state current is the sum of these short-channel effects as shown in Figure 1.18. The subthreshold current for a short-channel device can be rewritten as follows [1.18]:

$$\text{Log}(I_{subth}) = \text{Log}(I_{Tr}) - (V_{Tlong} - SCE - DIBL) / SS, \quad (1.20)$$

where  $I_{Tr}$  is the transistor current corresponding to the threshold voltage. With gate length and threshold voltage scaled down the subthreshold leakage current increases exponentially. In order to suppress the increase, it is clear that we have to avoid increasing the three factors: SCE, DIBL, and  $SS$ . Now, we can easily understand which physical parameters are important from the equations 1.14, 1.15, 1.17, and 1.18;  $t_{ox}/L_{eff}$ ,  $x_j/L_{eff}$ , and  $W_{dm}/L_{eff}$ . Thinning of gate oxide was one of the easiest solutions technologically. Until now, aggressive scaling of the gate oxide ( $\text{SiO}_2$ ) thickness thus has continued. However, this resulted in rapid increase of the tunneling current when the gate oxide thickness is scaled down to less than 2 nm as shown in Figure 1.11. This gate leakage can be reduced by replacing gate silicon dioxide ( $\text{SiO}_2$ ) by a high- $\kappa$  material. To form shallow junctions, the use of Silicon-On-Insulator (SOI) wafer is one of the most effective solutions. The source/drain junction depth in SOI thin body device is terminated by the buried oxide. Moreover, the thin body thickness can limit the maximum depletion-layer depth. These devices will be discussed in section 1.4.

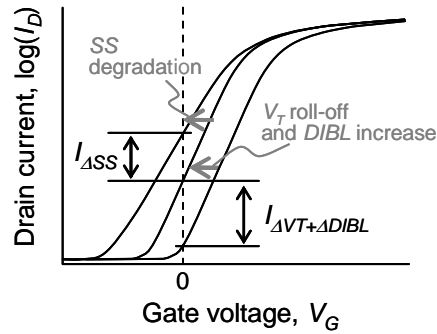


Figure 1.18 Off-current increase due to the short-channel effects.

### 1.2.2 Source/Drain Series Resistance in Short-Channel MOSFET

In the discussion of MOSFET current thus far, it was assumed that the source and drain regions were perfectly conducting. In reality, as the current flows from the channel to the terminal contact, there is a voltage drop in the source and drain regions due to the finite silicon receptivity and metal contact resistance as shown in Figure 1.19.

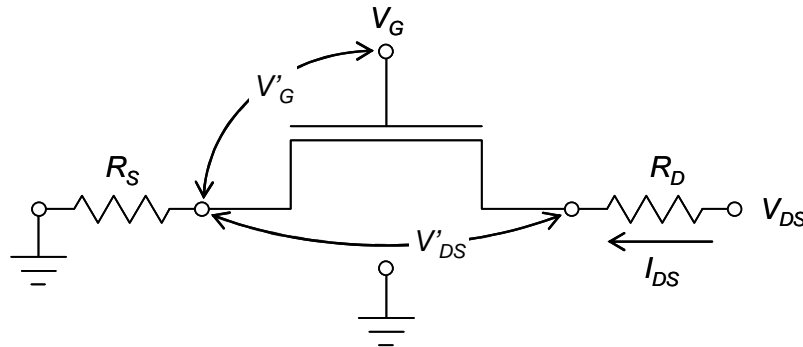


Figure 1.19 Equivalent circuit of MOSFET with source and drain resistance [1.4].

In a long-channel device, the source–drain parasitic resistance is negligible compared with the channel resistance. In a short channel device, however, the source–drain series resistance can be an appreciable fraction of the channel resistance and can therefore cause significant current degradation. The most severe current degradation by series resistance occurs in the linear region (Low  $V_{DS}$ ) when the gate voltage is high because the MOSFET channel resistance is the lowest under such bias conditions. The MOSFET current in the saturation region is least affected by the resistance degradation of

source–drain voltage,  $I_{DS}$  is essentially independent of  $V_{DS}$  in saturation. The saturation current is only affected through gate–source voltage degradation by voltage drop between the source contact and the source end of the channel [1.4]:

$$V'_G = V_G - R_S I_{DS} . \quad (1.21)$$

In aggressively scaled MOSFETs, however, the saturation current degradation becomes more and more problematic. Figures 1.20 and 1.21 show the on-current degradations due to the source/drain series resistance. This degradation implies that further improvements in  $I_{ON}$  by shortening the gate length cannot be expected when the channel resistance becomes comparable to the source and drain resistance. Nowadays, the source/drain series resistance is a major concern for the MOSFET scaling. Shallow junctions in the source/drain regions are needed to minimize the short-channel effects as discussed in subsection 1.2.1. ITRS predicts that source/drain extension junction depth below sub-50 nm CMOS will be scaled further down around 10 nm to maintain acceptable short channel performance, but this may lead to a high series resistance problem [1.7, 1.20]. In other words, further down-scaling without improvement of  $I_{ON}$  is meaningless even if short-channel effects are completely suppressed by introducing shallow junction technologies (e.g. source/drain extension, SOI wafer, etc.). It is important to design MOSFET structure effective in suppression of both short-channel effects and source/drain resistance.

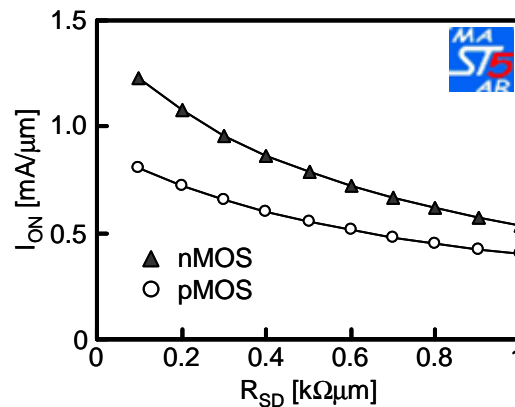


Figure 1.20 On-currents as a function of source/drain series resistance. All plots are calculated by using MASTAR MOSFET modeling software [1.19]:  $N_a=10^{18}cm^{-3}$ ,  $t_{ox}=1.3$  nm,  $V_{DD}=1.2$  V,  $L_G=50$  nm,  $W=1\mu m$ .



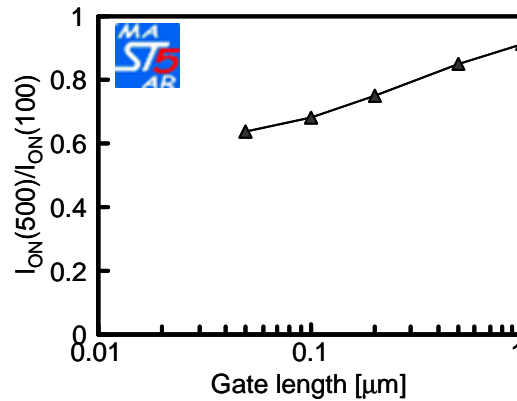


Figure 1.21 On-current lowering ratio of  $R_{SD} = 500 \Omega \cdot \mu\text{m}$  to  $100 \Omega \cdot \mu\text{m}$  as a function of gate length. All plots are calculated by using MASTAR MOSFET modeling software [1.19]:  $N_a = 10^{18} \text{cm}^{-3}$ ,  $t_{ox} = 1.3 \text{nm}$ ,  $V_{DD} = 1.2 \text{V}$ ,  $W = 1 \mu\text{m}$ .

### 1.2.3 Carrier Transport Mechanisms in Short-Channel MOSFET

In short channel devices, the short-channel effects become problematic. On the other hand, carrier transport also has gate length dependence. Precise understanding of correlation between low-lateral-field mobility and high-lateral field velocity, which is more directly related to on-current, is important. In analyzing the carrier transport mechanisms depending on the gate length, we go back to the general equation of the saturation current. We start with the generalized form

$$I_{ON} \approx WqN_{INV}^{source} \cdot v_s \quad (1.22)$$

where  $q$  is the elemental charge,  $N_{INV}^{source}$  is the inversion charge density near the source edge, and  $v_s$  is the average carrier velocity near the source edge [1.21]. While  $qN_{INV}$  is simply determined by the maximum value at the source as  $C_{ox}(V_G - V_T)$ , the determination mechanism of  $v_s$  is dependent on the gate length. So the only critical parameter is  $v_s$ . Figure 1.22 shows the schematic diagrams of carrier transport models to determine  $I_{ON}$ . In long-channel MOSFETs, the carrier mobility  $\mu$  is the solely important factor in determining the velocity  $v$ . The  $v$ - $\mu$  relationship is given by  $v = \mu * E_{lateral}$ , where  $E_{lateral}$  is the lateral electric field, as shown in Figure 1.23. However, the linear  $v$ - $\mu$  relationship breaks down when the gate length becomes shorter. As the lateral

electric field is increased, the average carrier velocity and the average carrier energy increase as well. When the carrier energy increases beyond the optical phonon energy, the probability of emitting an optical phonon increases abruptly. This mechanism causes the carrier velocity to saturate with increasing electric field as shown in Figure 1.24 [1.22, 1.23]. As velocity saturation phenomenon begins to occur,  $\mu$  dependence of  $v$  becomes weaker. As far as carrier scattering events in the channels sufficiently occur and the stationary transport dominate the carrier transport, the carrier transport model as shown in Figure 1.22 (a) basically holds even under the existence of velocity saturation.

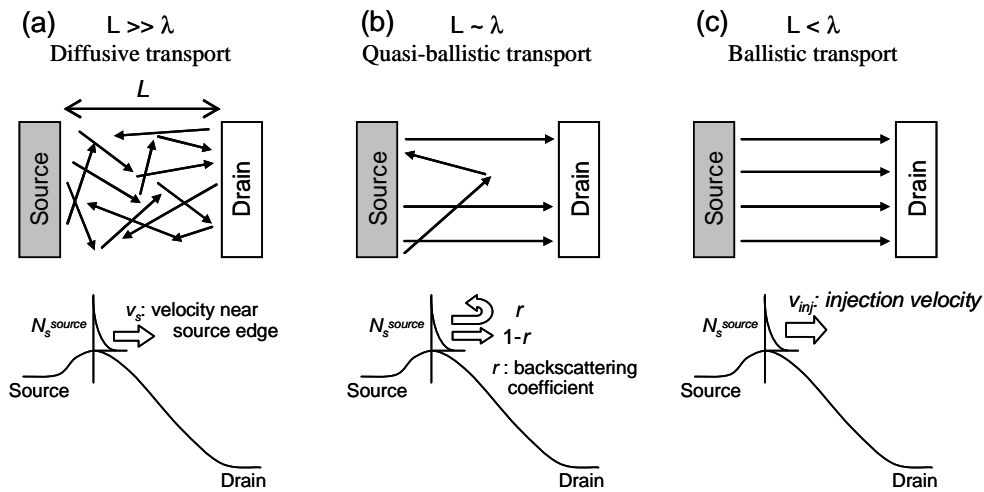


Figure 1.22 Schematic diagrams of carrier transport models to determine  $I_{ON}$ . (a) Conventional transport model. (b) Quasi-ballistic transport model. (c) Full-ballistic transport model [1.24, 1.25].

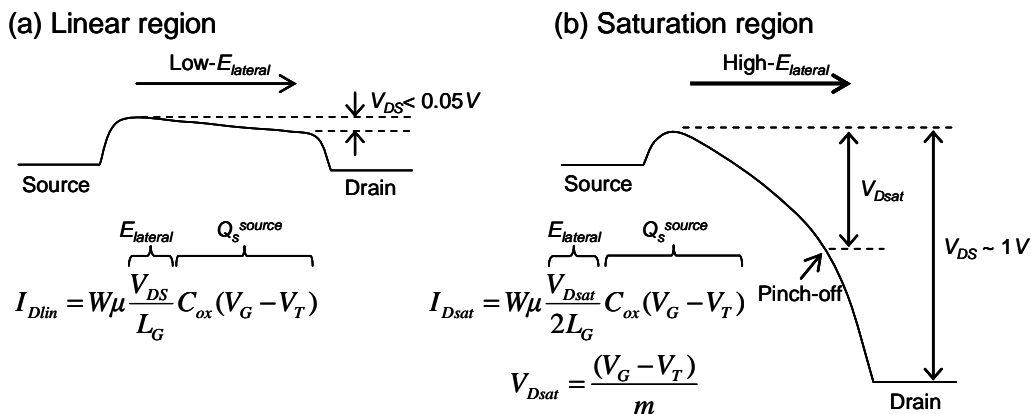


Figure 1.23 Channel potential profiles under conditions of carrier mobility  $\mu$  and velocity  $v$ . (a) Linear region. (b) Saturation region.

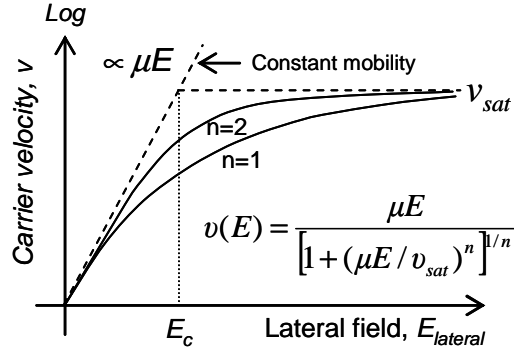


Figure 1.24 Velocity–field relationship for electrons ( $n=2$ ) and holes ( $n=1$ ) by the empirical form inserted [1.22]. The critical field  $E_c = v_{sat}/\mu$ .

As the channel length becomes shorter, nonstationary transport becomes more dominant, where sufficient numbers of scattering events do not occur inside the channels. This situation, as shown in Figure 1.22 (b), has been formulated as quasi-ballistic transport by Lundstrom *et al.* [1.21]:

$$I_{ON} = qN_{INV}^{source} \cdot v_{inj} \cdot \frac{1-r}{1+r}, \quad (1.23)$$

where  $v_{inj}$  is the injection velocity at the top of the barrier near the source edge, and  $r$  is the backscattering rate near-source region. The fraction  $r$  of the carriers are scattered back to the source, as shown in Figure 1.22 (b). Hence the effective velocity of carriers at the barrier, called virtual source velocity, is determined by this fraction. Lundstrom’s theory uses assumption that only scattering events that take place in the vicinity of the virtual source are responsible for backscattering of carriers to the source. Once a carrier passes the point where the potential has dropped by  $kT/q$  from the barrier top, the probability of return to the source is negligible. Hence, the  $r$  depends on the ration between the backscattering mean free path of carriers,  $\lambda$ , and the distance over which the potential drops by the thermal voltage, the so-called critical length of scattering,  $l$ :

$$r = \frac{l}{l + \lambda}. \quad (1.24)$$

The notion of mobility in short-channel devices, where the scattering mean free path is comparable to the channel length, is subject of controversy. However, a

phenomenological mobility can always be extracted at low  $V_{DS}$ . Assuming that the mobility is constant across the channel and that the carriers at the top of the barrier are in a near-equilibrium condition, Rahman related this mobility to the backscattering mean free path by matching the low  $V_{DS}$  drift-diffusion equation with the MOSFET scattering model [1.22]:

$$\lambda = \left( \frac{2\mu}{v_\theta} \frac{kT}{q} \right) \frac{\mathfrak{S}_0(\eta_F)}{\mathfrak{S}_{-1}(\eta_F)}, \quad (1.25)$$

where  $v_\theta$  is the ballistic velocity of carriers which in the non-degenerate limit is equal to the thermal velocity,  $\eta_F = (E_F - \varepsilon)/kT$  is the reduced Fermi energy,  $\varepsilon$  is the minimum band energy, and  $\mathfrak{S}_n$  is the Fermi integral of the  $n$ th order. This equation (1.25) means that in order for the ballistic efficiency to increase, the low-field mobility should be increased. Since  $r$  is related to  $\mu$ , the enhancement of mobility can be still important in increasing  $I_{ON}$  under quasi-ballistic transport regime.

Furthermore, when channel length becomes much shorter, probably down to less than 10 nm in Si MOSFETs, and no carrier-scattering events occur inside the channel, the carrier transport is dominated by full ballistic transport, as shown in Figure 1.22(c). Here,  $I_{ON}$  in MOSFETs under this ballistic transport, which have also been formulated by Natori [1.24], is simply represented by

$$I_{ON} = qN_s^{source} \cdot v_{inj}. \quad (1.26)$$

Thus the enhancement of  $v_{inj}$  is necessary to increase  $I_{ON}$  of ballistic MOSFETs, while the carrier mobility loses its meaning.

Recently, the  $v$ - $L_G$  relationships have been experimentally investigated in order to clarify the effectiveness of  $\mu$  enhancement to improve  $I_{ON}$  [1.27]. Figure 1.25 shows the experimental results of  $L_G$  dependence of velocity. It was found the velocity is not completely saturated even below  $L_G = 50$  nm and still increases with a slope of  $L_G^{-0.45}$ . This can be attributed to the velocity overshoot phenomenon near the source edge due to contribution of quasi-ballistic carriers. Note that the mobility enhancement is still effective at  $L_G = 30$  nm.

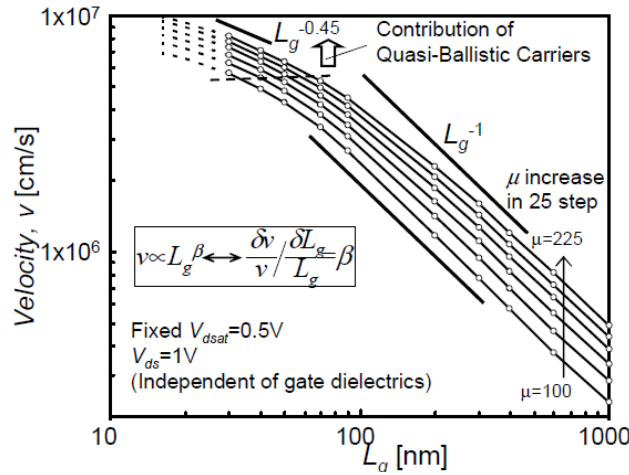


Figure 1.25  $L_G$  dependence of velocity with  $\mu$  as parameter [1.27].

In this section, we discussed several effects in short-channel MOSFETs. To suppress the off leakage current caused by the short channel effects, the minimization of  $t_{ox}$ ,  $x_j$ , and  $W_{dm}$  is effective. However, the shallow junction leads to  $I_{ON}$  degradation due to the high source/drain series resistance. To avoid this trade-off, it is important to design MOSFET structure effective in suppression of both short-channel effects and source/drain resistance. Moreover, although  $\mu$  dependence of  $v$  becomes weaker in short-channel MOSFETs, the  $\mu$  enhancement can be still important in increasing  $I_{ON}$  under quasi-ballistic transport regime.

### 1.3 KEY TECHNOLOGIES TO IMPROVE MOSFET PERFORMANCE

This section introduces some solutions and challenges to continue the scaling, which is the purpose of this thesis. First, we consider a leading edge of CMOS technology. Figure 1.26 shows cross section of n- and pMOSFETs for 32 nm technology fabricated by Intel Corporation in 2009 [1.28]. The key device features are summarized in Table 1.2. The foundation of the 32 nm process technology is the second generation high- $\kappa$ /metal gate MOSFET to suppress the short-channel effects without increasing gate leakage. The equivalent oxide thickness (EOT) of the high- $\kappa$  dielectric has been

reduced from 1.0 nm on 45 nm to 0.9 nm on the 32 nm process while gate length has been reduced to 30 nm. Using a replacement metal gate flow, that is a gate-last process, enables stress enhancement techniques to be in place before removing the poly gate from the transistor. This 32 nm technology also uses 4<sup>th</sup> generation SiGe strained silicon for pMOSFET resulting in linear drive current exceeding nMOSFET. Moreover, the raised S/D regions and 2<sup>nd</sup> generation trench contacts technologies enables reduced S/D access resistance.

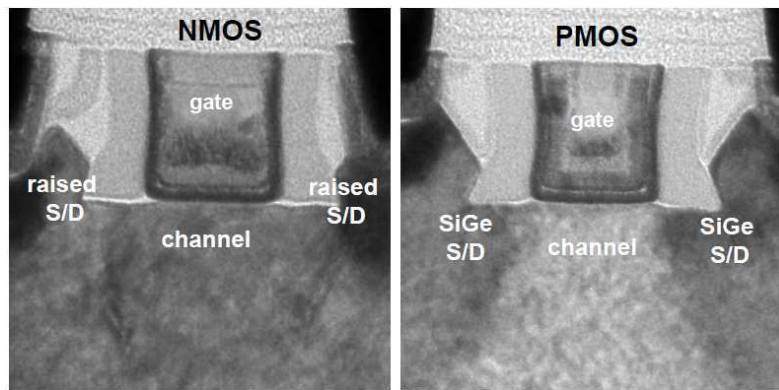


Figure 1.26 Cross section of Intel's NMOS and PMOS with 4th generation strained silicon, 2nd generation high- $\kappa$ /metal gate, and raised S/D regions for 32 nm technology [1.28].

Table 1.2 Key device features of Intel 32 nm logic technology [1.28].

	NMOS	PMOS	
			<ul style="list-style-type: none"> <li>❑ 30 nm gate length with 112.5 nm contacted gate pitch</li> </ul>
$L_G$ [nm]	30	30	<ul style="list-style-type: none"> <li>❑ 2<sup>nd</sup> generation high-<math>\kappa</math>/metal gate                             <ul style="list-style-type: none"> <li>✓ 0.9 nm EOT</li> <li>✓ Replacement metal gate approach                                     <ul style="list-style-type: none"> <li>- Enables stress enhancement techniques</li> </ul> </li> <li>✓ Replacement high-k approach                                     <ul style="list-style-type: none"> <li>- Improved performance</li> </ul> </li> </ul> </li> </ul>
EOT [nm]	0.9	0.9	
$I_{Dsat}$ [mA/mm] $V_{GS}=V_{DS}=1.0V$	1.62	1.37	<ul style="list-style-type: none"> <li>❑ 4<sup>th</sup> generation SiGe strained silicon PMOS device                             <ul style="list-style-type: none"> <li>✓ Increased Ge concentration</li> <li>✓ Closer proximity to channel for enhanced mobility</li> </ul> </li> </ul>
$I_{Dlin}$ [mA/mm] $V_{GS}=1.0V$ $V_{DS}=0.05V$	0.231	0.240	
$I_{OFF}$ [nA/mm]	100	100	<ul style="list-style-type: none"> <li>❑ Raised NMOS S/D region                             <ul style="list-style-type: none"> <li>✓ Improved external resistance</li> </ul> </li> </ul>
$V_{Tsat}$ [V]	0.115	-0.18	
DIBL [mV/V]	~200	~200	<ul style="list-style-type: none"> <li>❑ 2<sup>nd</sup> generation trench contacts                             <ul style="list-style-type: none"> <li>✓ Reduced contact resistance</li> <li>✓ Used as local interconnects</li> </ul> </li> </ul>
SS [mV/dec]	~100	~100	

These technologies are introduced along with the performance enhancement strategies mentioned above. Note that most of these technologies are needed due to the short-channel effects. For a given short channel characteristic and constant  $I_{OFF}$ , the gate length scaling increases the threshold voltage which degrades the transistor drive current. The improvement in drive current owing to the shorter gate length is offset by the reduction in overdrive voltage ( $V_G - V_T$ ). Therefore, mobility enhancement becomes a key engineering factor with minimal impact on the leakage. Moreover, suppression of the short-channel effects demands rapid development of high- $\kappa$ /metal gate technology to minimize EOT and the raised S/D technology to obtain low S/D resistance with shallow junction as well as several channel doping technologies. In addition, increasing the impurity concentration in the channel region is also necessary to suppress the short-channel effects. However, this causes a degradation of the carrier mobility due to impurity scattering, which result in obstruction to increase the drive current [1.29]. Moreover, random dopant fluctuation in such short channel results in variation of the threshold voltage [1.30]. To continuously improve CMOS performance, comprehensive reforms of the CMOS scaling strategy will be required to achieve high immunity against short-channel effects.

### **1.3.1 Gate-All-Around Silicon Nanowire MOSFET**

Fully-depleted (FD) silicon-on-insulator (SOI) MOSFETs are considered as possible successors for bulk MOSFETs because their thin body dimensions provide geometric electrostatic confinement for controlling short-channel effects as well as less stringent requirements of EOT scaling over conventional bulk Si. Figure 1.27 shows a typical planar FDSOI MOSFET structure. The thin layer of silicon is separated from buried oxide (BOX) film, thus electrically isolating the devices from the underlying silicon substrate. In this structure, the source and drain junction capacitances are almost entirely eliminated. Here FD structure means that the silicon body film is thin enough that the entire film is depleted before the threshold condition is reached. An important merit of SOI technology is that it provides the cornerstone for new FD device structures such as multi-gate MOSFETs, which includes more than one gate into a single device as

shown in Figure 1.28 [1.32].

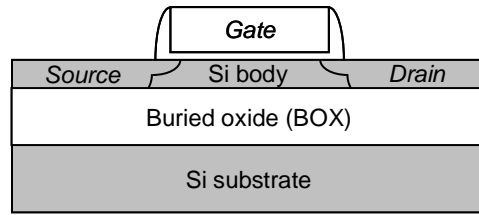


Figure 1.27 Cross-section of a planar FDSOI MOSFET.

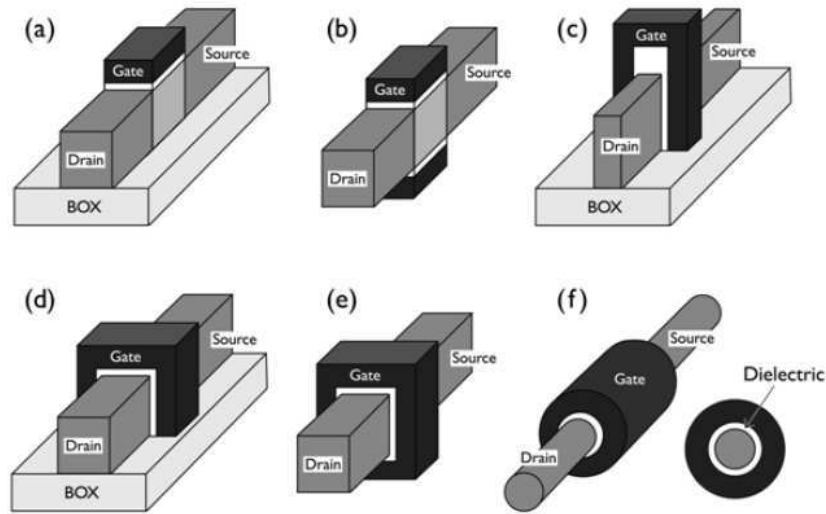


Figure 1.28 Various SOI device: (a) Single gate SOI FET, (b) double gate planar SOI FET, (c) double gate non-planar FinFET, (d) tri-gate FET, (e) quadruple-gate (or gate-all-around) FET, and gate-all-around (or surrounding gate) FET (nanowire FET).

Figure 1.29 displays the electric field lines from the drain in different MOSFET structures. More is the penetration of field lines from the drain towards the source, greater is the interference of the drain against the function of the gate. The conventional MOSFET geometry, shown in Figure 1.29 (a), can hardly be scaled down because of strong permeation of the field lines towards the source. The behavior of FDSOI structure of Figure 1.29 (b) is not encouraging (until the buried oxide is very thin) because the buried oxide does not terminate the drain field lines. Only in the double-gate (DG) MOSFET structure shown in Figure 1.29 (c), the field lines are not able to reach near the source [1.31]. Hence the effect of the drain field on the channel is minimized providing far superior scalability.



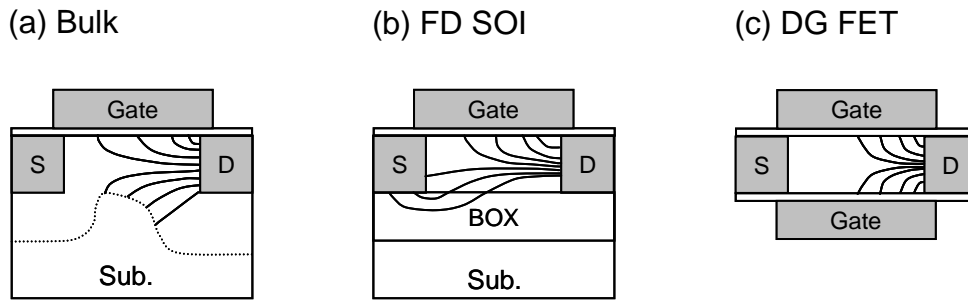


Figure 1.29 Illustration of electric field lines from drain of different device types: (a) bulk, (b) FD SOI, and (c) double gate (DG).

Yan *et al.* proposed a unique scaling theory for double-gate SOI MOSFETs as a design guideline [1.33]. According to their theory, the device should be designed maintaining

$$\alpha = \frac{L_{eff}}{2\lambda}, \quad (1.27)$$

where  $\lambda$  is the so-called natural length which governs the influence of lateral field on the channel potential and depends on device geometry and boundary conditions. This natural length is an easy guide for choosing device structure and parameters, and has simple physical meaning that a small natural length corresponds to superb short channel effect immunity. Table 1.3 shows the natural length for different gate configurations [1.32]. Here a small  $\alpha$  gives degraded short-channel effect immunity. For instance, to achieve  $SS < 75$  mV/decade and  $DIBL < 50$  mV/V,  $\alpha$  needs to be larger than 2.2 for all devices when the gate oxide is 2 nm and the channel doping concentration is  $1 \times 10^{18} \text{cm}^{-3}$  [1.34]. Figure 1.30 shows the maximum allowed silicon film thickness (and device width in a four-gate device with  $W = t_{si}$ ) to avoid short-channel effects [1.35]. As a consequence, gate-all-around (GAA) silicon nanowire MOSFETs (SNWTs) have the best short-channel effect immunity among all the FDSOI architectures for the same body dimensions. The experimental data reported by Bangsaruntip *et al.* also shows better short-channel immunity for GAA SNWTs than that of FDSOI by as shown in Figure 1.31 [1.36].

Table 1.3 Natural length in devices with different geometries [1.32].

Single gate	$\lambda_1 = \sqrt{\frac{\epsilon_{si} t_{si} t_{ox}}{\epsilon_{ox}}}$
Double gate	$\lambda_2 = \sqrt{\frac{\epsilon_{si} t_{si} t_{ox}}{2\epsilon_{ox}}}$
Quadruple gate (square section)	$\lambda_4 \cong \sqrt{\frac{\epsilon_{si} t_{si} t_{ox}}{4\epsilon_{ox}}}$
Surrounding gate (circular section)	$\lambda_o \cong \sqrt{\frac{2\epsilon_{si} t_{si}^2 \ln(1 + 2t_{ox}/t_{si})}{16\epsilon_{ox}} + \epsilon_{ox} t_{si}^2}$

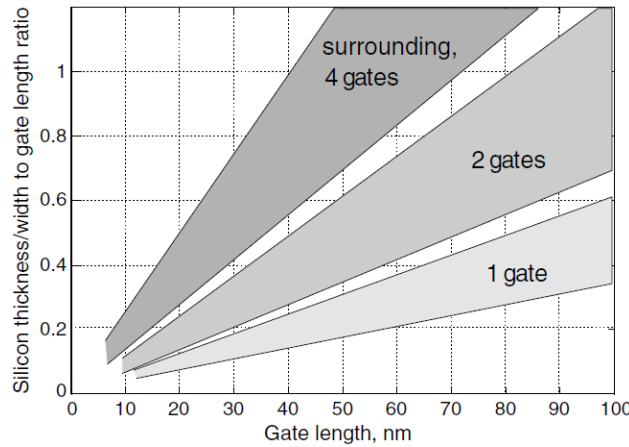


Figure 1.30 Maximum allowed Si thickness and device width vs. gate length to avoid short-channel effects in single-, double- and quadruple-gate SOI MOSFETs [1.35].

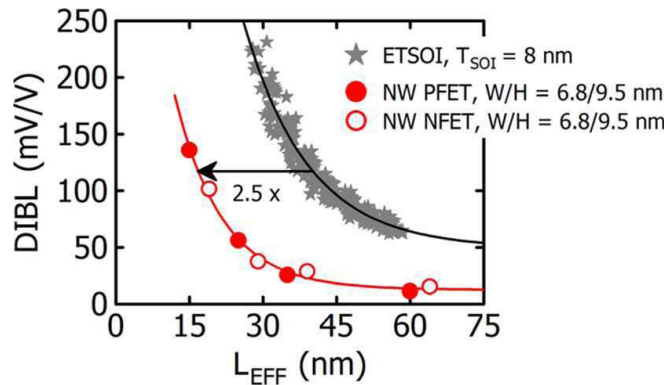


Figure 1.31 Comparison of DIBL of elliptical GAA SNWTs (width  $W = 6.8$  nm and height  $H = 9.5$  nm) and single-gate ETSOI FETs (SOI thickness  $t_{si} = 8$  nm) with similar body dimensions. [1.36].

### 1.3.2 Vertically-Stacked Channel MOSFET

In a GAA SNWT, the current drive is essentially equal to the sum of the currents flowing along all the interfaces covered by the gate electrode [1.32]. To drive large currents, multi-finger pattern are needed as shown in Figure 1.32. When an ideal current transport (without corner effect, volume inversion effect, and so on) are considered in rectangular GAA SNWT, the current level depends on the width  $W_{NW}$  and height  $H_{NW}$ , of a nanowire, the top and bottom surface mobility  $\mu_{top}$ , the side surface mobility  $\mu_{side}$ , and the number of the nanowires for given layout area. The on-current in GAA SNWT with multi-finger are given by

$$I_{ON}^{nanowire} = n \times (2W_{NW}\mu_{top} + 2H_{NW}\mu_{side}) \frac{C_{ox}}{L_{eff}} \frac{(V_{DD} - V_T)^\alpha}{2m}, \quad (1.28)$$

where  $n$  is the number of the nanowires and the power of  $\alpha$  ( $1 < \alpha < 2$ ) indicates the degree of velocity saturation in short-channel MOSFETs. Considering a nanowire pitch  $W_{pitch}$ , the current per unit device width is given by

$$\frac{I_{ON}^{nanowire}}{W_{pitch}} = \frac{I_{ON}^{planar}}{W} \cdot \frac{2W_{NW}\mu_{top} + 2H_{NW}\mu_{side}}{\mu_{top}W_{pitch}}, \quad (1.29)$$

where  $I_{ON}^{planar}$  is the current in the single-gate, planar MOSFET occupying the same area as the multi-finger device as shown in Figure 1.32.

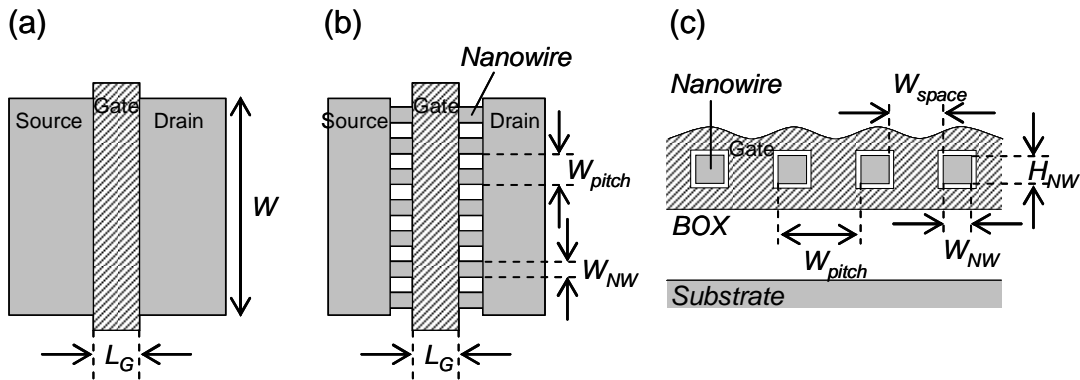


Figure 1.32 MOSFET layout; (a) planar MOSFET, (b) GAA SNWT with multi-finger, and (c) cross-section of GAA SNWT.

To evaluate the benefit of the multi finger layout, the current of GAA SNWT per layout surface normalized to planar MOSFET are calculated with several dimensions.

Here we assume the nanowire direction of  $\langle 110 \rangle$ , the top surface orientation of (100), and the sidewall surface orientation of (110). The values of the electron mobility for (100) and (110) used thus are  $300 \text{ cm}^2/\text{Vs}$  and  $150 \text{ cm}^2/\text{Vs}$ , respectively. Figure 1.33 shows its nanowire pitch dependence. The nanowire width  $W_{NW}$  is equal to a half of the pitch width. Because of that, the currents of GAA SNWT approach to the planar one as increase the pitch. If the cross section of the nanowire is square ( $W_{NW} = H_{NW}$ ), the current is independent on the pitch, and we have  $I_{ON}^{nanowire} = 1.5x I_{ON}^{planar}$ . In actual case, since each nanowires are wrapped by the gate dielectrics and the space between them must be filled by gate metal, the space between nanowires  $W_{space}$  may need at least 15 nm. In that case, the diminishing cross-section to obtain the better short-channel effect immunity is traded off against the current density gain. When the space is equal to 15 nm, there is no gain of the current density for GAA SNWT with  $W_{NW} = 5 \text{ nm}$  and  $H_{NW} = 10 \text{ nm}$  to the planar one, for instance.

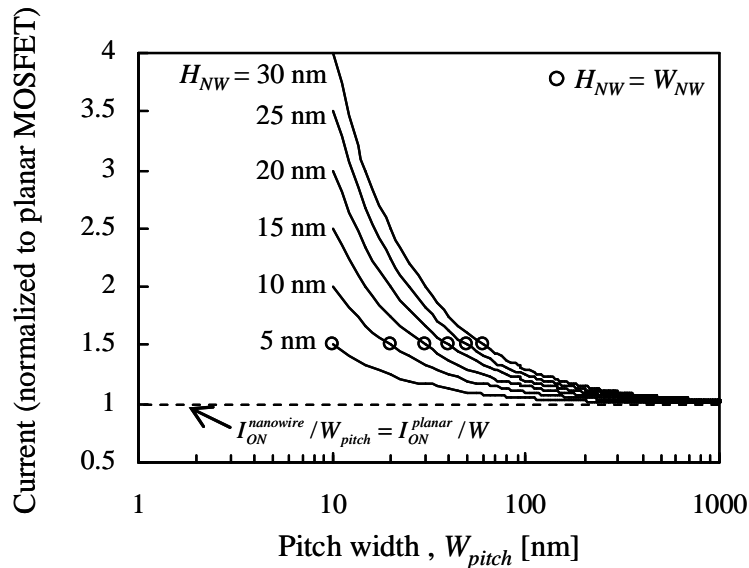


Figure 1.33 Normalized current of a rectangular GAA n-SNWT as a function of multi-finger pitch width.  $W_{NW} = W_{pitch}/2$ . The top interface mobility is  $300 \text{ cm}^2/\text{Vs}$  and sidewall mobility is  $150 \text{ cm}^2/\text{Vs}$ .

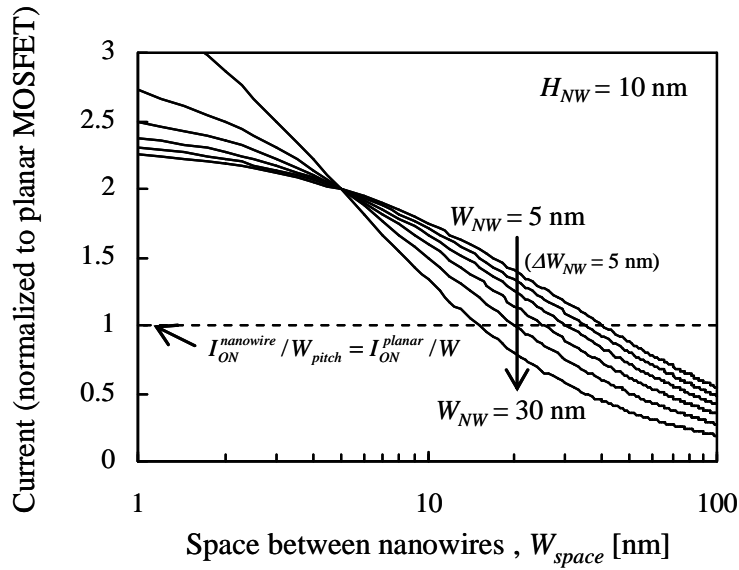


Figure 1.34 Normalized current of a rectangular GAA SNWT as a function of space between nanowires.  $H_{NW}=10$  nm. The top interface mobility is  $300$   $\text{cm}^2/\text{Vs}$  and sidewall mobility is  $150$   $\text{cm}^2/\text{Vs}$ .

To obtain larger current density per a given layout with a high immunity against the short-channel effects, the vertical integration of nanowires is effective as shown in Figure 1.35. In this structure, the current density can be proportionally increased to the stacking level (three levels in the case of Figure 1.35) without the layout surface area penalty as seen in Figure 1.36. This structure enables to achieve both a high integration density and low power dissipation. Note that since this current increment is due to the effective surface enlargement, the intrinsic gate delay cannot be directly reduced as discussed in Subsection 1.13. The propagation delay, however, can be improved as the interconnect capacitance becomes larger [1.37]. The suppressed short channel effects are also effective to reach the ideal switching trajectory.

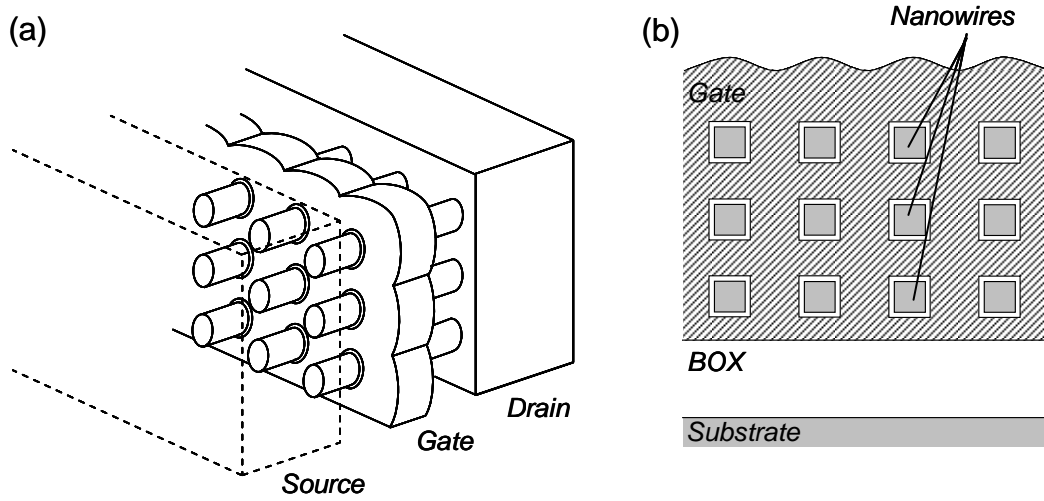


Figure 1.35 Structure of vertically-stacked GAA SNWT(a) and its cross-section (b)

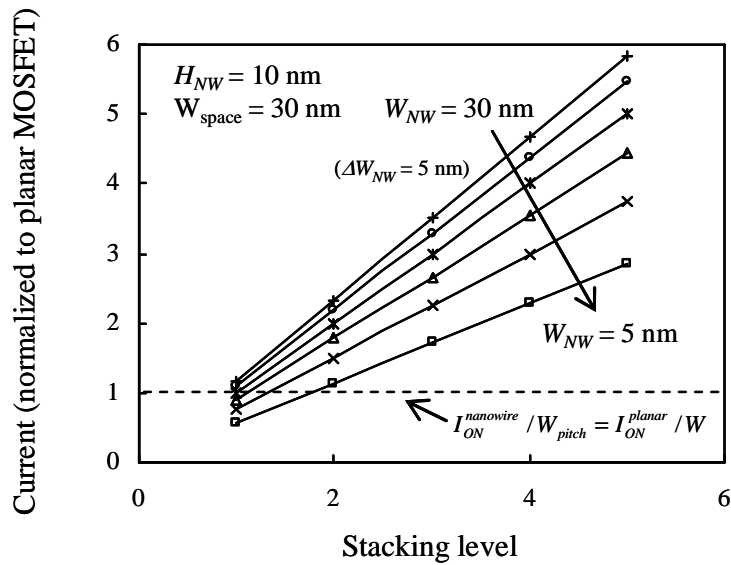


Figure 1.36 Normalized current of a rectangular GAA SNWT as a function of staking level of nanowires.  $H_{NW}=10$  nm.  $W_{space}=30$  nm. The top interface mobility is  $300$   $cm^2/Vs$  and sidewall mobility is  $150$   $cm^2/Vs$ .

## 1.4 PURPOSE AND CONTENTS OF THIS STUDY

The operation speed and integration density of a microprocessor chip have doubled every two or three years in line with Moore’s law. For each generation, in order

to achieve the target performance, prospective problems were analyzed in detail and solved by introducing new technologies. Looking back at the history, it seems that many problems result from the short-channel effects. Now we are faced with the critical issue of power dissipation due to subthreshold leakage. This power dissipation, which surpasses dynamic power consumption, can no longer be ignored. Therefore comprehensive reform of the CMOS scaling strategies is required to continuously improve speed, integration density, and power dissipation of LSI all at the same time.

The purpose of this thesis thus is to characterize vertically-stacked GAA SNWT as one of the most promising MOSFETs for future CMOS circuits. The superior immunity to short-channel effects and the high integration density can be straightforwardly expected from this structure. However, the body dimensions must be considered with drive current enhancement. In addition, it is possible that the thick source/drain regions of the vertically-stacked channel MOSFET need special treatments in the fabrication process to obtain low access resistance. As other critical issue in this type of three dimensional devices, body bias techniques are not available for power management of digital circuits. Thus the studies are classified into three issues:

- How do we achieve low access resistance with uniform doping profile in the thick source/drain regions?
- How are the carrier transport properties of vertically-stacked nanowire channels?
- How can we realize the controllability and flexibility of the threshold voltage?

Figure 1.37 shows the outline of this thesis. First, the basic device fabrication process of vertically-stacked channel structure is presented and specific technological issues are evidenced in Chapter 2. Next, the electrical characterization methods are described in detail in Chapter 3. Chapter 4 covers the studies source/drain resistance reduction technique for thick source/drain regions in vertically-stacked channel devices. Chapter 5 covers the carrier transport properties of vertically-stacked GAA SNWTs in detail, especially the dimension effects and the impacts on the fabrication process. Chapter 6 covers the studies of the threshold voltage tuning technique by the independently separated gates. The studies referred to in each chapter were done in

order to achieve CMOSFET with high performance, high integration density, and low power dissipation for future generation. Details are as follows.

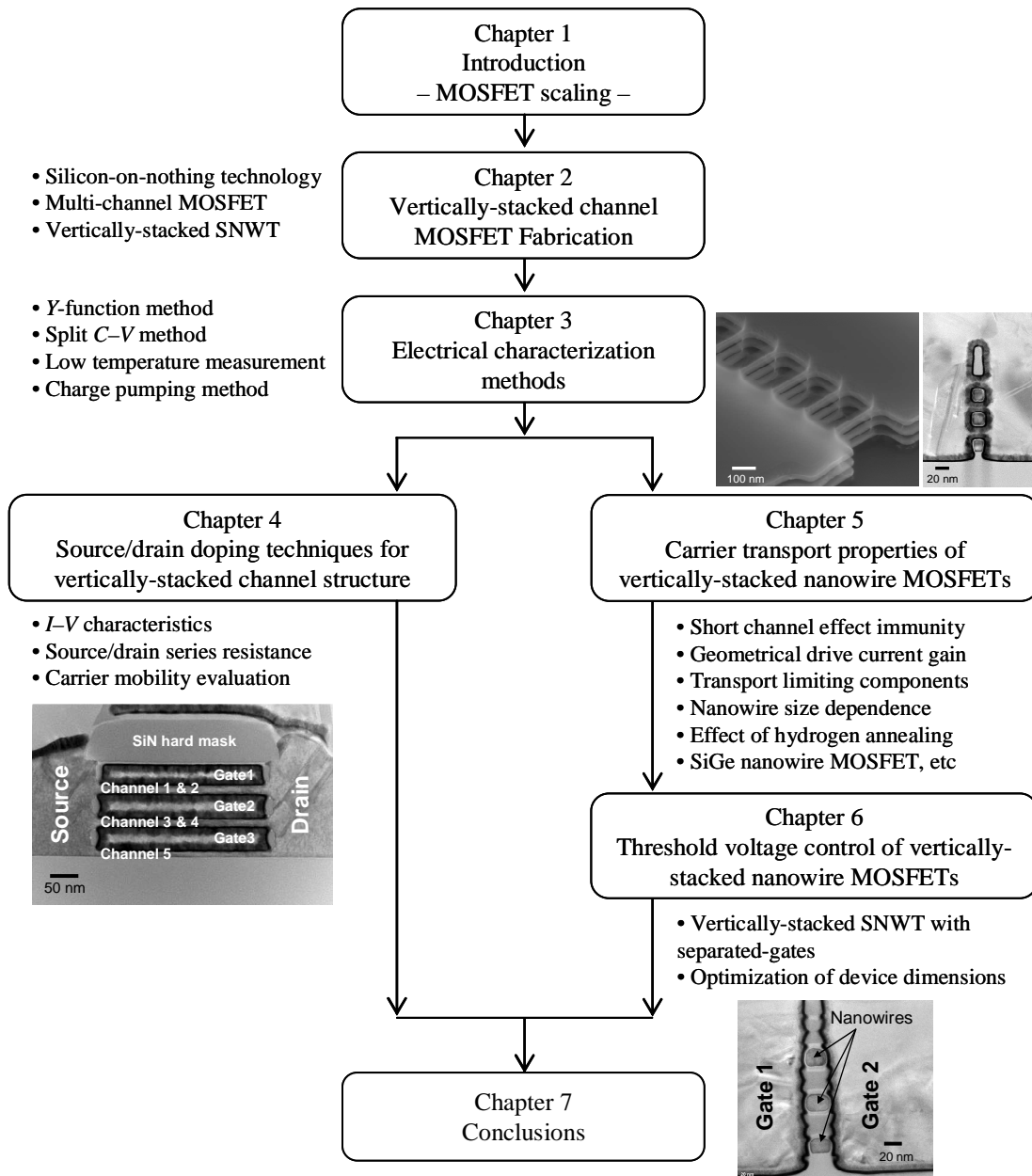


Figure 1.37 Outline of each chapter in this thesis.



**a) Source/drain doping techniques for vertically-stacked channel structure (Chapter 4)**

The reduction of parasitic access resistances serially connected at source and drain region of MOSFETS are one of the challenging technology to meet the performance required in the roadmap as discussed in Chapter 1. The voltage drops at the resistances reduces the applied voltages at the drain and gate electrodes in the transistors, resulting in the decrease in the overdrive voltage to lower the on-current. These resistances also cause degradation in the time constant, commonly referred as RC delay, to lower the switching speed. Therefore, as the channel resistance reduces with the scaling in the gate length, the parasitic series resistance should be further reduced not to increase its proportion in the total resistance at on-state. In addition, the vertically-stacked channel structure suffers from the uniformity of the doping profile due to the thick source/drain regions.

In Chapter 4, a novel process to decrease the resistivity of the source and drain regions is presented using *in situ* doped selective epitaxial growth in combination with conventional ion-implantation as a novel process for source and drain formation. The effect of source and drain formation process on the series resistance and carrier mobility will be discussed through electrical characteristics.

**b) Carrier transport properties of vertically-stacked nanowire MOSFETs (Chapter 5)**

Recently, short channel GAA SNWTs have been successfully fabricated with diameter of less than 10 nm using several top-down CMOS compatible processes [1.38–1.40]; they showed excellent short-channel effects immunity. On the other hand, transport property degradation in SNWTs was also reported by several groups [1.41–1.43]. However, the mobility behavior when the width is reduced has been remained unclear. Carrier transport in nanowire is commonly discussed in terms of two main mechanisms; one is one-dimension transport model, and the other is a facet-dominated transport model. The former can be adapted to sub-10 nm diameter, and the latter to more than 20 nm one. In the range of between them, the mixed transport properties are expected. The range of between them is production-friendly,

provided that the short-channel effects under aggressively scaled gate length are suppressed, while carrier transport model becomes complicate due to the mixed properties.

In Chapter 5, carrier transport limiting components for vertically-stacked GAA SNWTs will be discussed in detail to obtain better performance with suppressing short channel effects.

***c) Threshold voltage control of vertically-stacked nanowire MOSFETs (Chapter 6)***

Another issue for the vertically-stacked SNWTs is how to control the threshold voltage. For various CMOS applications and power management, it is important to achieve controllable and flexible threshold voltage in a transistor. As one of the possible techniques for three-dimensional devices, separated-gate structures have been proposed [1.44, 1.45]. In Chapter 5, the possibility of the flexible threshold voltage for vertically-stacked GAA SNWTs with separated gate will be discussed.

Finally, in Chapter 7, the results obtained in these studies are summarized and conclusions are presented. The perspective of vertically-stacked GAA SNWTs for future LSI applications is described.

## **1.5 REFERENCE**

- [1.1] G. E. Moore, “Cramming more components onto integrated circuits,” *Electronics*, Vol. 38, No. 8, 1965.
- [1.2] Data source: <http://www.intel.com/technology/timeline.pdf>
- [1.3] G. E. Moore, “No Exponential is Forever: But “Forever” Can be Delayed!,” in *ISSCC Tech. Dig.*, Feb. 2003, vol.1, pp.20–23.
- [1.4] Y. Taur and T. H. Ning, *Fundamental of Modern VLSI Devices*, 2<sup>nd</sup> edition, Cambridge University Press, 2009.
- [1.5] R. H. Dennard, F. H. Gaensslen, H-N, Yu, V. L. Rideout, E. Bassous, and A. R. LeBlanc, "Design of ion-implanted MOSFET's with very small physical

- dimensions," *IEEE J. Solid-State Circuits*, vol. SC-9, no. 5, pp. 256–268, 1974.
- [1.6] M. Bohr, "MOS Transistor: Scaling and Performance Trends," *Semiconductor International*, vol. 18, no. 6, pp.75–80.
- [1.7] International Technology Roadmap for Semiconductors (ITRS): <http://www.itrs.net/reports.html>
- [1.8] M. H. Na, E. J. Nowak, W. Haensch, and J. Cai, "The effective drive current in CMOS inverters," in *IEDM Tech. Dig.*, 2002, pp. 121–124.
- [1.9] E. Yoshida, Y. Momiyama, M. Miyamoto, T. Saiki, M. Kojima, S. Satoh, and T. Sugii," Performance Boost using a New Device Design Methodology Based on Characteristic Current for Low-Power CMOS," in *IEDM Tech. Dig.*, 2006, pp. 195–198.
- [1.10] L. Wei, F. Boeuf, D. Antoniadis, T. Skotnicki, and H.-S. P. Wong, "Exploration of Device Design Space to Meet Circuit Speed Targeting 22nm and Beyond," in extended abstracts of SSDM, 2009, pp.808–809.
- [1.11] T. Skotnicki and F. Boeuf, "How Can High Mobility Channel Materials Boost or Degrade Performance in Advanced CMOS," in *VLSI Tech. Dig.*, 2010, pp. 153–154.
- [1.12] T. Sakurai, "Perspectives of power-aware electronics (Plenary)," in *Proc. ISSCC Dig. Tech. Papers*, 2003, pp. 26–29.
- [1.13] K. Mistry, C. Allen, C. Auth, B. Beattie, D. Bergstrom, M. Bost, M. Brazier, M. Buehler, A. Cappellani, R. Chau, C.-H. Choi, G. Ding, K. Fischer, T. Ghani, R. Grover, W. Han, D. Hanken, M. Hattendorf, J. He, J. Hicks, R. Huessner, D. Ingerly, P. Jain, R. James, L. Jong, S. Joshi, C. Kenyon, K. Kuhn, K. Lee, H. Liu, J. Maiz, B. McIntyre, P. Moon, J. Neiryneck, S. Pae, C. Parker, D. Parsons, C. Prasad, L. Pipes, M. Prince, P. Ranade, T. Reynolds, J. Sandford, L. Shifren, J. Sebastian, J. Seiple, D. Simon, S. Sivakumar, P. Smith, C. Thomas, T. T roeger, P. Vandervoorn, S. Williams, and K. Zawadzki, "A 45nm Logic Technology with High-k+Metal Gate Transistors, Strained Silicon, 9 Cu Interconnect Layers, 193nm Dry Patterning, and 100% Pb-free Packaging," in *IEDM Tech. Dig.*, 2007, pp. 247–250.

- [1.14] S. A. Parke, J.E. Moon, H. C. Wann, P. K. Ko, and C. Hu, “Design for suppression of gate-induced drain leakage in LDD MOSFET’s using a quasi-two-dimensional analytical model,” *IEEE Trans. Electron Devices*, vol. 39, no. 7, pp. 1694–1703, 1992.
- [1.15] K. Tanaka, K. Takeuchi, and M. Hane, ”Practical FinFET designe considering GIDL for LSTP (Low Standby Power) devices,” in *IEDM Tech. Dig.*, 2005, pp. 980–983.
- [1.16] Scalable CMOS (SCMOS) Design Rules (Based on *MOSIS* design: <http://www.mosis.com/> )
- [1.17] T. Skotnicki, G. Merckel, and T. Pedron, “The voltage-doping transformation: A new approach to the modeling of MOSFET short-channel effects,” *IEEE Electron Device Lett.*, vol. 9, no. 3, pp. 109–112, 1988.
- [1.18] T. Skotnicki, C. F.-Beranger, C. Gallon, F. Boeuf, S. Monfray, F. Payet, A. Pouydebasque, M. Szczap, A. Farcy, F. Arnaud, S. Clerc, M. Sellier, A. Cathignol, J.-P. Schoellkopf, E. Perea, R. Ferrant, and H. Mingam, “Innovative Materials, Devices, and CMOS Technologies for Low-Power Mobile Multimedia,” *IEEE Trans. Electron Devices*, vol. 55, no. 1, pp. 96–130, 2008.
- [1.19] *MASTAR4 Code and User Guide*. Available: <http://www.itrs.net/models.html>
- [1.20] S. Thompson, P. Packan, T. Ghani, M. Stettler, M. Alavi, I. Post, S. Tyagi, S. Ahmed, S. Yang, and M.Bohr, ”Source/Drain extension scaling for 0.1mm and below channel length MOSFETs,” in *Proc. Symp. VLSI Tech.*, 1998, pp. 132–133.
- [1.21] M. Lundstrom and Z. Ren, “Essential physics of carrier transport in nanoscale MOSFETs,” *IEEE Trans. Electron Devices*, vol. 49, no. 1, pp. 133–141, 2002.
- [1.22] S. M. Sze and Kwok K. Ng, *Physics of Semiconductor Devices*, 3<sup>rd</sup> edition, John Wiley & Sons, Inc., Hoboken, New Jersey, 2007.
- [1.23] M. Saitoh and K. Uchida, “Universal relationship between low-field mobility and high-field carrier velocity in high- $\kappa$  and SiO<sub>2</sub> gate dielectric MOSFETs,” in *IEDM Tech. Dig.*, 2006, pp. 261–264.
- [1.24] K. Natori, “Ballistic metal–oxide–semiconductor field effect transistor,” *J. Appl.*

- Phys.*, vol. 76, no. 8, pp. 4879–4890, Oct. 1994.
- [1.25] S. Takagi, T. Irisawa, T. Tezuka, T. Numata, S. Nakaharai, N. Hirashita, Y. Moriyama, K. Usuda, E. Toyoda, S. Dissanayake, M. Shichijo, R. Nakane, S. Sugahara, M. Takenaka, and N. Sugiyama, “Carrier-Transport-Enhanced Channel CMOS for Improved Power Consumption and Performance, ” *IEEE Trans. Electron Devices*, vol. 55, no. 1, pp. 21–38, 2008.
- [1.26] A. Rahaman and M. S. Lundstrom, “A compact scattering model for the nanoscale double gate MOSFET,” *IEEE Trans. Electron Devices*, vol. 49, no. 3, pp. 481–489, 2002.
- [1.27] K. Tatsumura, M. Goto, S. Kawanaka, and A. Kinoshita, “Correlation between low-field mobility and high-field carrier velocity in quasi-ballistic-transport MISFETs scaled down to  $L_g=30$  nm,” in *IEDM Tech. Dig.*, 2009, pp. 465–468.
- [1.28] P. Packan, S. Akbar, M. Armstrong, D. Bergstrom, M. Brazier, H. Deshpande, K. Dev, G. Ding, T. Ghani, O. Golonzka, W. Han, J. He, R. Heussner, R. James, J. Jopling, C. Kenyon, S-H. Lee, M. Liu, S. Lodha, B. Mattis, A. Murthy, L. Neiberg, J. Neiryneck, S. Pae, C. Parker, L. Pipes, J. Sebastian, J. Seiple, B. Sell, A. Sharma, S. Sivakumar, B. Song, A. St. Amour, K. Tone, T. Troeger, C. Weber, K. Zhang, Y. Luo, S. Natarajan, “High Performance 32nm Logic Technology Featuring 2nd Generation High-k + Metal Gate Transistors,” in *IEDM Tech. Dig.*, 2009, pp. 659–662.
- [1.29] S. Takagi, A. Toriumi, M. Iwase, and H. Tango, “On the Universality of Inversion Layer Mobility in Si MOSFET’s: Part I–Effects of Substrate Impurity Concentration,” *IEEE Trans. Electron Devices*, vol. 41, no. 12, pp. 2357–2362, Dec. 1994.
- [1.30] K. Nishinohara, N. Shygyo, and T. Wada, “Effects of microscopic fluctuations in dopant distributions on MOSFET threshold voltage,” *IEEE Trans. Electron Devices*, vol. 39, no. 3, pp. 634–639, Mar. 1992.
- [1.31] T. Ernst, R. Ritzenthaler, O. Faynot, and S. Cristoloveanu, “A model of fringing field in short-channel planar and triple-gate SOI MOSFETs,” *IEEE Trans. Electron Devices*, vol. 54, no. 6, pp. 1366–1375, June. 2007.

- [1.32] J. P. Coling, “Multi-gate SOI MOSFETs,” *Microelectronic Engineering*, vol. 84, pp. 2071–2076, 2007.
- [1.33] R.-H. Yan, A. Ourmazd, and L. F. Lee, “Scaling the Si MOSFET: from bulk to SOI to bulk,” *IEEE Trans. Electron Devices*, vol. 39, no. 7, pp. 1704–1710, July 1992.
- [1.34] C.-W. Lee, S.-R.-N. Yun, C.-G. Yu, J.-T. Park, J.P. Colinge, “Device design guidelines for nano-scale MuGFETs,” *Solid-State Electronics*, vol. 51, pp. 505–510, 2007.
- [1.35] J. P. Coling, “Multiple-gate SOI MOSFETs,” *Solid-State Electronics*, vol. 48, pp. 897–905, 2004.
- [1.36] S. Bangsaruntip, G. M. Cohen, A. Majumdar, and J. W. Sleight, “Univesality of short-channel effects in undoped-body silicon nanowire MOSFETs,” *IEEE Electron Device Lett.* vol. 31, no. 9, pp. 903–905, Sept. 2010.
- [1.37] E. Bernard, T. Ernst, B. Guillaumot, N. Vulliet, T.C. Lim, O. Rozeau, F. Danneville, T. Skotnicki, S. Deleonibus, O. Faynot, “Novel internal spacers 50nm gate length Multi-Channel MOSFET (MCFET) with TiN/HfO<sub>2</sub> gate stack”, *IEEE Electron Device Letters*, Vol. 30, No. 2, pp. 148–151, 2009.
- [1.38] S. Bangsaruntip, G.M. Cohen, A. Majumdar, Y. Zhang, S. U. Engelmann, N. C. M. Fuller, L. M. Gignac, S. Mittal, J. S. Newbury, M. Guillorn, T. Barwicz, L. Sekaric, M. M. Frank, and J. W. Sleight, “High performance and highly uniform gate-all-around silicon nanowire MOSFETs with wire size dependent scaling,” in *IEDM Tech. Dig.*, 2009, pp. 297–300.
- [1.39] M. Li, K.H. Yeo, S.D. Suk, Y.Y. Yeoh, D.-W. Kim, T.Y. Chung, K. S. Oh, and W.-S. Lee, “Sub-10 nm gate-all-around CMOS nanowire transistors on bulk Si substrate,” in *VLSI Tech. Dig.*, 2009, pp. 94–95.
- [1.40] G. Bidal, F. Boeuf, S. Denorme, N. Loubet, J.L. Huguenin, P. Perreau, D. Fleury, F. Leverd, S. Lagrasta, S. Barnola, T. Salvetat, B. Orlando, R. Beneyton, L. Clement, R. Pantel, S. Monfray, G. Ghibaudo, and T. Skotnicki, “High velocity Si-nanodot: a candidate for SRAM applications at 16 nm node and below,” in *VLSI Tech. Dig.*, 2009, pp. 240–241.

- [1.41] S. D. Suk, M. Li, Y. Y. Yeoh, K. H. Yeo, K. H. Cho, I. K. Ku, H. Cho, W. J. Jang, D.-W. Kim, D. Park, and W.-S. Lee, “Investigation of nanowire size dependency on TSNWFET,” in *IEDM Tech. Dig.*, 2007, pp. 891–894.
- [1.42] M. Saitoh, Y. Nakabayashi, H. Itokawa<sup>1</sup>, M. Murano, I. Mizushima<sup>1</sup>, K. Uchida, and T. Numata, “Short-Channel Performance and Mobility Analysis of <110>- and <100>-Oriented Tri-Gate Nanowire MOSFETs with Raised Source/Drain Extensions,” in *VLSI Tech. Dig.*, 2010, pp. 169–170.
- [1.43] J. Chen, T. Saraya, K. Miyaji, K. Shimizu, and T. Hiramoto, “Experimental Study of Mobility in [110]- and [100]-Directed Multiple Silicon Nanowire GAA MOSFETs on (100) SOI,” in *VLSI Tech. Dig.*, 2008, pp. 32–33.
- [1.44] Y. X. Liu, M. Masahara, K. Ishii, T. Tsutsumi, T. Sekigawa, H. Takahima, H. Yamauchi and E. Suzuki, “Flexible Threshold Voltage FinFETs with Independent Double Gates and an Ideal Rectangular Cross- Section Si-Fin Channel”, in *IEDM Tech. Dig.*, 2003, pp. 986–989.
- [1.45] C. Dupré, A. Hubert, S. Bécu, M. Jublot, V. Maffini-Alvaro, C. Vizioz, F. Aussenac, C. Arvet, S. Barnola, J.-M. Hartmann, G. Garnier, F. Allain, J.-P. Colonna, M. Rivoire, L. Baud, S. Pauliac, V. Loup, T. Chevolleau, P. Rivallin, B. Guillaumot, G. Ghibaud, O. Faynot, T. Ernst, and S. Deleonibus, “ 15nm-diameter 3D Stacked Nanowires with Independent Gate Operation: □FET,” in *IEDM Tech. Dig.*, 2008, pp. 749–752.

# **CHAPTER 2**

---

## ***VERTICALLY- STACKED CHANNEL MOSFETS FABRICATION***

---

Vertically-stacked channel structure has been derived from Silicon-On-Nothing Technology and Gate-All-Around concepts. The use of sacrificial SiGe layers enables silicon channel to be piled up. In this chapter, the fabrication process will be described. Vertically-stacked channels with uniformly-deposited high- $\kappa$ /metal gate will be demonstrated.

---



# CHAPTER 2 CONTENTS

## **2 Vertically-Stacked Channel MOSFET Fabrication**

- 2.1 Silicon-On-Nothing Technology
- 2.2 Key Steps
  - 2.2.1 SiGe Epitaxy and Etching
  - 2.2.2 High- $\kappa$ /Metal Gate Stacks
- 2.3 Process Step Overview for Multi-Channel MOSFET
- 2.4 Process Step Overview for Vertically-Stacked Nanowire MOSFET
- 2.5 Conclusions
- 2.6 References

## 2.1 SILICON-ON-NOTHING TECHNOLOGY

Silicon-On-Nothing (SON) architecture have been proposed allowing extremely thin buried oxides and Silicon films to be fabricated and thereby better resisting to short-channel effects [2.1–2.3]. The process is based on the use of a sacrificial SiGe layer that is selectively removed versus the silicon as shown in Fig. 2.1. The tunnel under the silicon film is then filled with the oxide. Silicon film and buried oxide are defined by epitaxy that opens access to extremely thin and high crystalline quality films. Extensions are physically limited by the silicon film thickness preserving a good control of shorts channel effects. In the same time, source and drain remain in continuity with the substrate, limiting self-heating and lowering  $R_{SD}$ . The use of thin buried oxide allows the control of the fringing field. Moreover, this architecture is co-integrable with bulk one, aspecific gate work-function is provided for bulk and thin films [2.3].

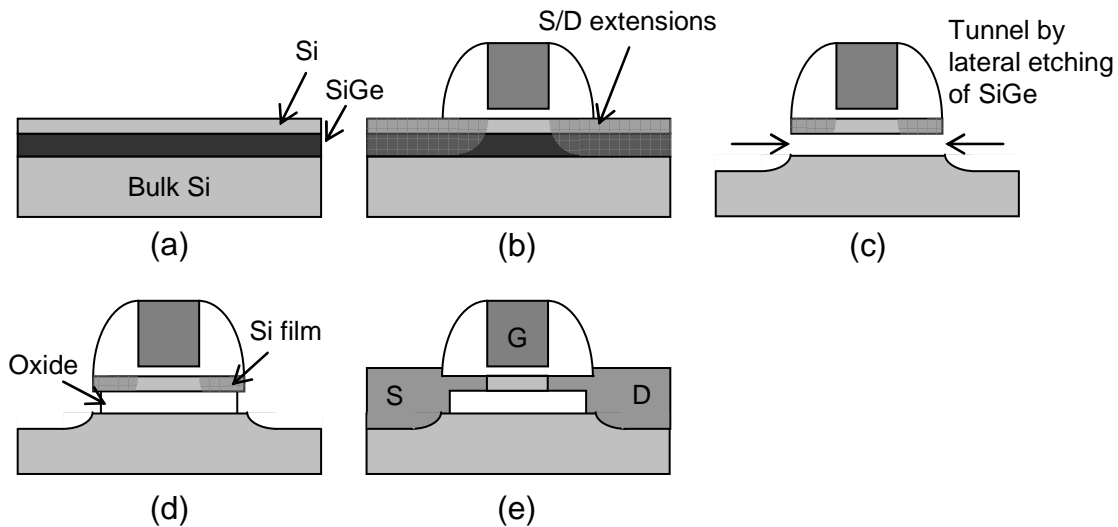


*Figure 2.1 Fabrication process of the SON MOSFET: (a) epitaxy of SiGe and Si layers on isolated bulk wafer; (b) conventional CMOS process steps until formation of the nitride spacers; (c) formation of the shallow trenches in the S/D regions and formation of the tunnel under the Si film; (d) filling the tunnel with oxide (optional step); (e) selective epitaxy of S/D regions, implantation and RTA.*

Vertically-stacked channel structure has been derived from SON and GAA concepts. The use of sacrificial SiGe layers enables silicon channel to be piled up. In this study, two types of stacked channel MOSFETs were fabricated; one is multi-channel MOSFET (MCFET), another is vertically-stacked silicon nanowire MOSFET (vertically-stacked SNWT).

## 2.2 KEY STEPS

In the processes of two type of vertically-stacked channel MOSFETs, the following technologies were commonly used as key technologies.

### 2.2.1 SiGe Epitaxy and Etching

#### ■ $\text{Si}_{0.8}\text{Ge}_{0.2}/\text{Si}$ superlattice epitaxial growth

$\text{Si}_{0.8}\text{Ge}_{0.2}/\text{Si}$  epitaxial growth is processed in the Epi Centura Reduced-Pressure Chemical Vapor Deposition (RP-CVD) industrial cluster tool [2.4]. The Si layers are grown at  $700^\circ\text{C}$  and the SiGe ones at  $650^\circ\text{C}$ . Such a low growth temperature enables to grow quite thick layers without any elastic relaxation of the strain through the formation of surface undulations [2.1]. Pure dichlorosilane ( $\text{SiH}_2\text{Cl}_2$ ) is used as the source of Si and germane ( $\text{GeH}_4$ ) diluted at 2% in  $\text{H}_2$  as the source of Ge. The number of vertically aligned channels is determined by that of the grown SiGe/Si layers and is practically limited by the possible superlattice relaxation due to the compressively strained SiGe layers. Figure 2.2 shows the grown Si /  $\text{Si}_{0.8}\text{Ge}_{0.2}$  superlattice on SOI. Highly regular and defect free superlattices are obtained.

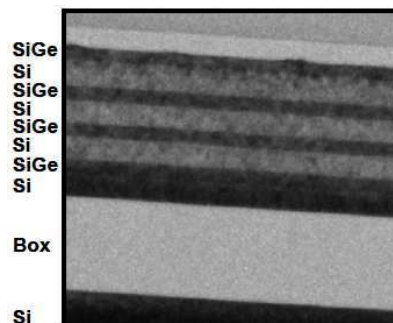


Figure 2.2  $(\text{Si}/\text{SiGe}) \times n$  superlattice on SOI used to pre-define the channel thickness.

■ **Anisotropic plasma etching of Si<sub>0.8</sub>Ge<sub>0.2</sub>/Si superlattice**

A hybrid lithography with Deep UV (248nm wavelength) (equipment: ASM 300) and ebeam (equipment: LEICA VB6HR) was used to define the initial photo-resist patterns. The whole stack with Si<sub>3</sub>N<sub>4</sub>/SiO<sub>2</sub> Hard Mask (HM) is etched in an applied material reactor (Applied Material Centura tool). The etching process is divided into five steps as seen in Table 2.1.

*Table 2.1 Process description of anisotropic etching of SiGe/Si superlattice.*

Step description	Plasma chemistry	Step type
Resist trimming (optional)	Cl <sub>2</sub> /O <sub>2</sub>	Adjusted Time
Resist cure (optional)	HBr	Time= 60s
Oxide hard mask etch	CF <sub>4</sub> /CH <sub>2</sub> F <sub>2</sub> /He	Time=15s
Hard Mask etch	CF <sub>4</sub> /CH <sub>2</sub> F <sub>2</sub> /O <sub>2</sub> /He	Endpoint
Si/SiGe multilayer main etch	Cl <sub>2</sub> /HBr/O <sub>2</sub>	Endpoint + over etch

■ **Si<sub>0.8</sub>Ge<sub>0.2</sub> layers selectively removal**

This step is performed with pure CF<sub>4</sub> plasma at high pressure and low microwave power in a remote plasma chamber (CDE by Shibaura). With such a process, a selectivity of about 60:1 (SiGe towards Si) is achieved [2.5]. The phenomenon of selectivity towards Si is based on the competition between the creation of GeF<sub>4</sub> and SiF<sub>4</sub> during etching. SiGe is preferentially etched because Ge-Si bonds are weaker than the Si-Si ones (2.12eV vs. 2.31eV). The etching rate depends on the Ge concentration of the SiGe layers. The critical point of this process is the adjustment of the tunnel etching time. It must be long enough to remove all the SiGe present in the tunnel but not too much to avoid any consumption of the silicon channels in the case of MCFETs. Figure 2.3 shows the SEM images of the Si/SiGe superlattice with the etched SiGe sacrificial layers. The optimal etching time is obtained when all the SiGe has been removed resulting in a totally open tunnel. On the other hand, the consumption of the silicon in vertically-stacked SNWTs can be used to control the nanowire diameter.

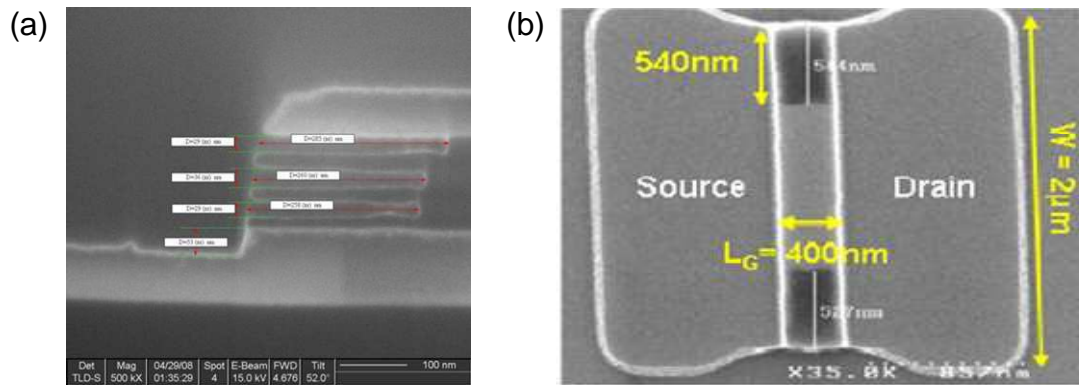


Figure 2.3 Cross-section (a) and top view (b) SEM images of the Si/SiGe superlattice with the etched SiGe sacrificial layers.

## 2.2.2 High- $\kappa$ /Metal Gate Stacks

High- $\kappa$  dielectrics and metal gate are strongly required to achieve small EOT with low gate leakage current density. HfO<sub>2</sub> dielectrics and TiN metal has been chosen as a gate stack for both n- and p-MOSFET. 3 nm of HfO<sub>2</sub> and 10 nm of TiN are deposited in the tunnels by uniform deposition methods of Atomic Layer Deposition (ALD) and Chemical Vapor Deposition (CVD), respectively. The thick n<sup>+</sup> polysilicon layers (CVD) are used to fill in the cavities and connect the vertically-stacked gates. Figure 2.4 shows cross-sectional TEM image of silicon nanowire with 3nm-thick-HfO<sub>2</sub> and 10nm-thick-TiN gate stack. A SiO<sub>2</sub>-like interfacial layer was observed. This layer is grown by the thermal process after the gate deposition. The resulting equivalent oxide thickness (EOT) is ~1.7 nm for this device.

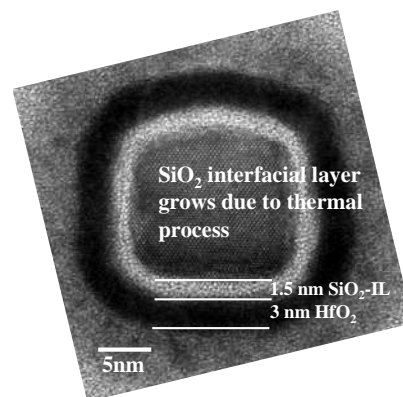


Figure 2.4 Cross-sectional TEM image of vertically-stacked silicon nanowire with high- $\kappa$ /metal gate.

## **2.3 PROCESS STEP OVERVIEW FOR MULTI-CHANNEL MOSFET**

The fabrication process of MCFETs, which is based on the principles developed for Silicon-On-Nothing FETs, has been developed by Bernard [2.2–2.3, 2.6]. Figure 2.5 shows an overview of the MCFET process flow. First, a (25-nm-Si and 30-nm-Si<sub>0.8</sub>Ge<sub>0.2</sub>) superlattice structure was epitaxially grown on a 20-nm thick SOI substrate (step 1). The grown Si layers will be used as channels for MCFETs. 5nm of high-temperature oxide (HTO) and 80nm of silicon nitride (Si<sub>3</sub>N<sub>4</sub>) are deposited as a hard mask on the top of the stack. After a gate photolithography, the superlattice is then anisotropically etched down to the bottom SOI layer (step 2). Since  $L_G$  is defined at this etching step, a vertical etching profile is an important requirement for this technology in order to suppress the variability of the  $L_G$  among the stacked Si channels. To introduce internal spacers, the SiGe layers are partially etched selectively to the Si ones (step 2.1). The depth of the SiGe recess determines the thickness of the future internal spacers. Then, HTO and Si<sub>3</sub>N<sub>4</sub> layers are deposited in the cavities with a thickness ratio optimized for the following spacers etch (step 2.2 and 2.3). An anisotropic/isotropic etch sequence of the deposited dielectrics allows one to access the silicon layers for further S/D epitaxy (step 2.4). After the wet cleaning to remove entirely the dielectrics on the sides of silicon layers, crystalline Si S/D was selectively grown with a natural “flat” shape induced by the presence of the internal spacers (step 3). The S/D were then ion-implanted. The channel width was defined by the active-area patterning and etching, giving access to the SiGe layers. The SiGe layers are then selectively removed using pure CF<sub>4</sub> at high pressure and low microwave power in a remote plasma tool. The high- $k$ /metal gate stack (HfO<sub>2</sub>/TiN/n<sup>+</sup> poly-Si) was deposited in the obtained cavities. A second gate etch is subsequently carried out followed by the formation of external silicon nitride spacers to avoid any short-cut between the gate and the S/D. After the dopant activation anneal, the top of S/D are silicided (with nickel) to reduce the series resistances, followed by a standard back-end-of-the-line (BEOL) process (for contacts and interconnections).

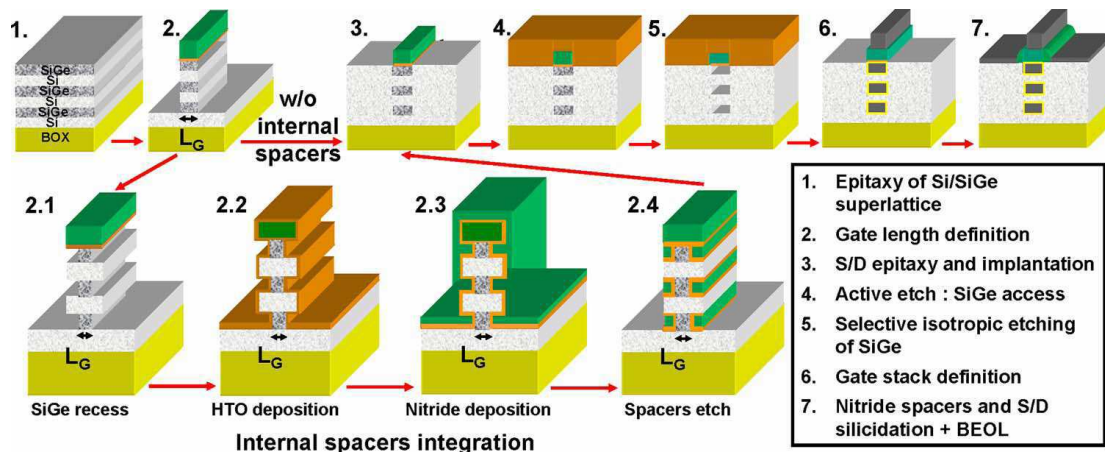


Figure 2.5 MCFET fabrication process overview [2.2].

Figure 2.6 shows the cross-sectional TEM images of the fabricated MCFETs along the Si channel and width direction. Here, two SiGe/Si alternating layers, resulting in five Si channels in parallel, were designed for fabrication. Channels 1 and 2 are activated at the top and bottom interfaces of the superior silicon island, whereas channels 3 and 4 have similar formations within the intermediate Si island. Channel 5 is responsible for conduction as the top of the original Si film. The sixth possible channel, which can be activated at the bottom of the Si film by substrate (back-gate) biasing, is not investigated in this work [see ref 2.7]. The resulting channel thickness was 10 nm for all channels. The electrically-measured EOT in inversion was  $\sim 2.5$  nm. The gate lengths of the MCFETs range from 500 to 70 nm.

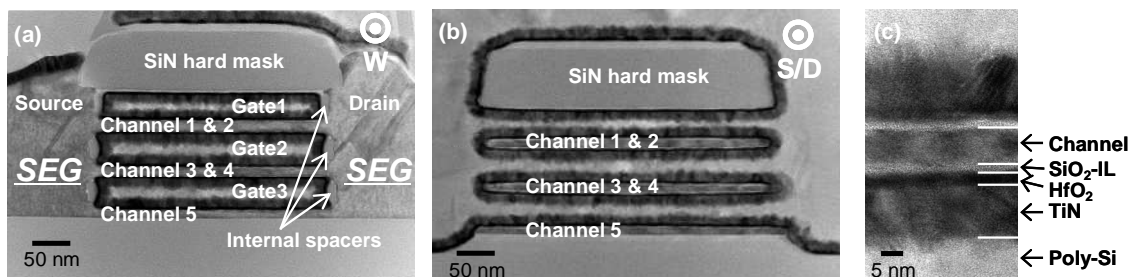
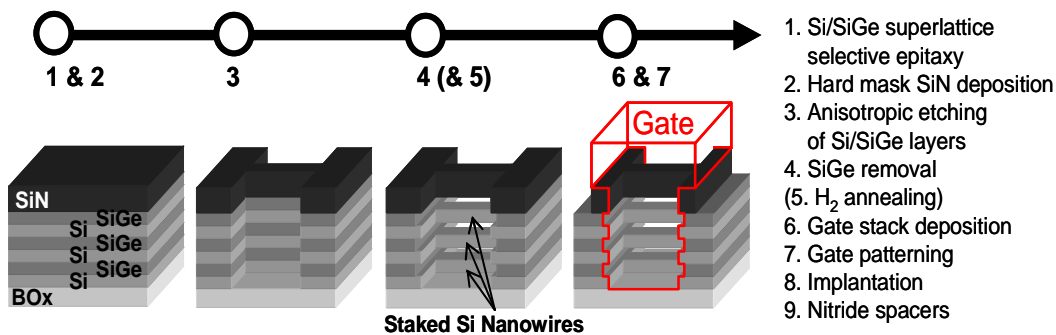


Figure 2.6 Fabricated multi-channel FET along (a) channel length and (b) width direction. (c) is the enlarged image of the gate stack.

## 2.4 PROCESS STEP OVERVIEW FOR VERTICALLY-STACKED NANOWIRE MOSFET

Figure 2.7 illustrates briefly the process flow for making vertically stacked silicon nanowire MOSFET [2.8, 2.9]. First, a (30-nm Si / 30-nm Si<sub>0.8</sub>Ge<sub>0.2</sub>)x3 superlattice was epitaxially grown on (100) SOI substrate (step1). 5nm of HTO and 40nm of Si<sub>3</sub>N<sub>4</sub> are deposited as a hard mask on the top of the stack (step 2). Hybrid DUV/ebeam-lithography and resist trimming were combined to define narrow lines. A damascene process was used: cavities were patterned thanks to anisotropic dry plasma etching of the superlattice (step 3). SiGe layers between Si ones were then etched isotropically (step 4). Optionally, an hydrogen annealing process (at 750 °C and 20 Torr for 2 min) was applied to obtained circular cross-sectional shape of nanowires (step 5). The obtained cavities were then filled with the gate stack (HfO<sub>2</sub>/TiN/N<sup>+</sup> poly-Si) (step 6). The gate length is thus defined by the cavity length. Chemical Mechanical Polishing (CMP) of poly-silicon and the thick HTO hard mask deposition for S/D implantation were carried out followed by the gate patterning (step 7). After gate etching, S/D implantation, spacers formation, and the dopant activation anneal were performed. The nickel silicide was formed on the top of Source / Drain area. The fabrication ended with a standard BEOL process.



*Figure 2.7 Vertically-stacked nanowire MOSFET fabrication process overview [2.5].*

Figure 2.8 shows their cross-sectional TEM image and SEM image. We successfully fabricated narrow nanowires by using e-beam lithography and isotropic plasma etching of SiGe sacrificial layers. Good uniformity of the nanowires in a



200-mm-wafer has been also achieved as shown in Figure 2.9. The width ( $W_{NW}$ ) of rectangular shape nanowire ranges from 5 nm up to 30 nm and the height ( $H_{NW}$ ) is 15 nm as seen in Figure 2.10 and Figure 2.11. The smallest nanowire with 5-nm- $W_{NW}$  was formed by self-limited oxidation and  $H_2$  annealing. Thanks to the vertically-stacked channel structures, large surface gains ( $W_{eff}/W_{Top}$ ) have been achieved as summarized in Table 2.2. Superior on-state currents per surface unit can be achieved in those devices.

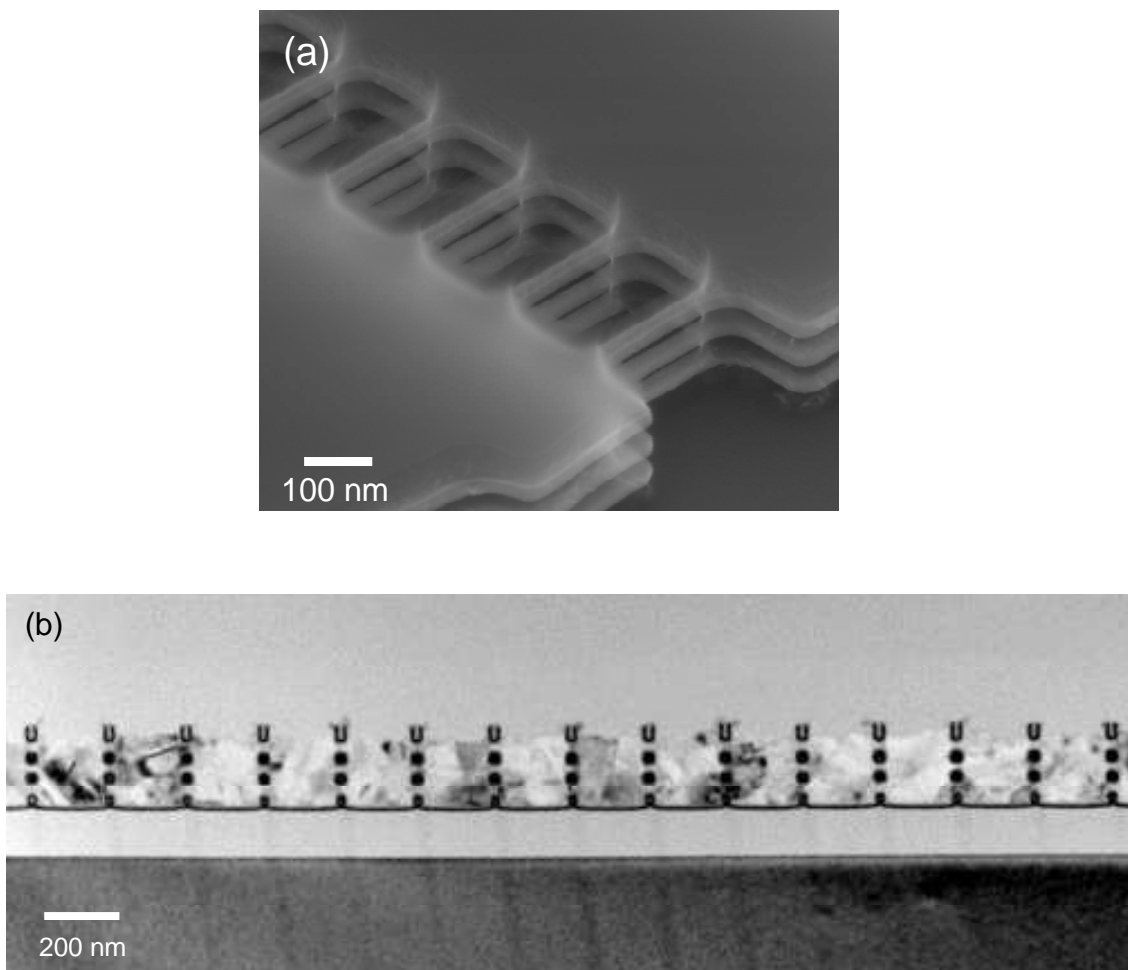


*Figure 2.8 Fabricated vertically-stacked silicon nanowires: (a) a top-view SEM image, (b) a cross-section TEM image.*

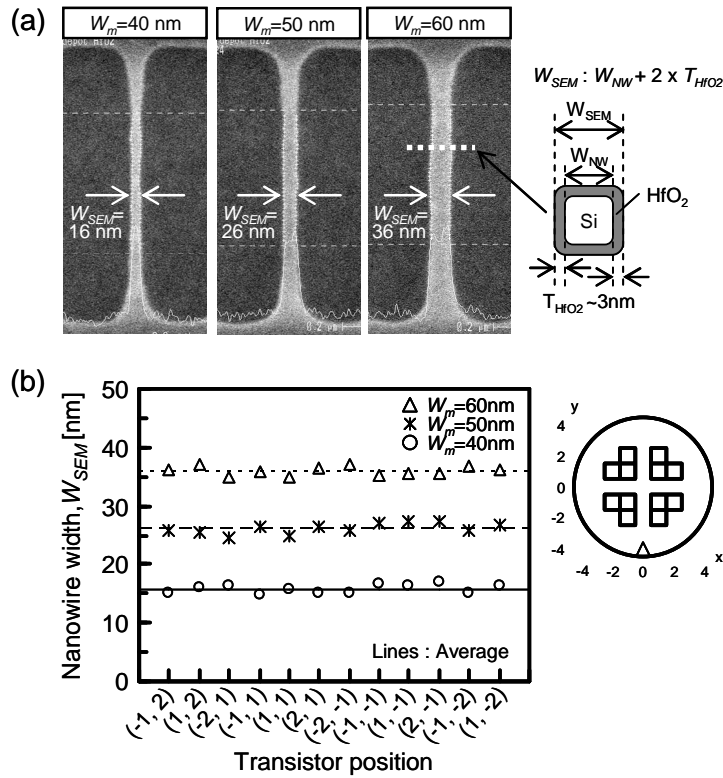


Figure 2.9 (a) Top-view SEM images of silicon nanowires after  $HfO_2$  deposition with width  $W_{SEM} = 16, 26,$  and  $36$  nm. (b) Variation of nanowire width in a 200-nm-wafer. The variations are less than  $\pm 1.5$  nm. The thickness of  $HfO_2$  on side walls ( $3\text{nm} \times 2$ ) is included in the values of  $W_{SEM}$ .  $W_m$  is the mask width.

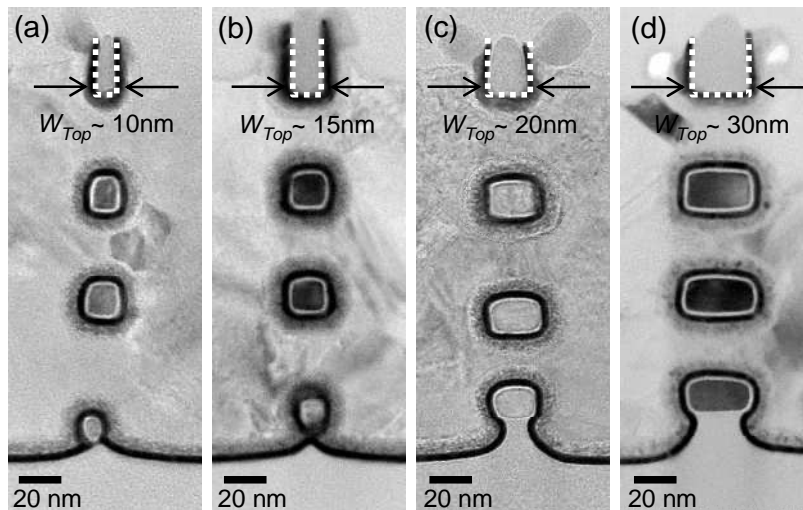


Figure 2.10 Cross-sectional TEM images of vertically-stacked silicon nanowire MOSFET with top-view width  $W_{Top} = 10, 15, 20$  and  $30$  nm.

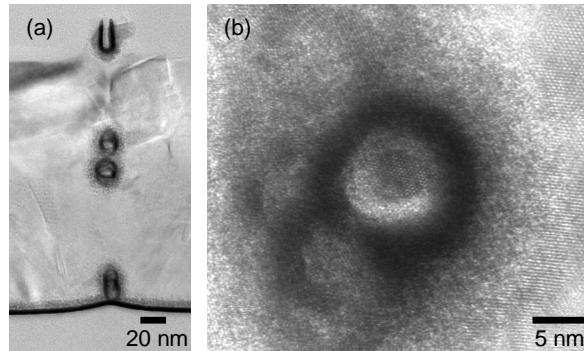
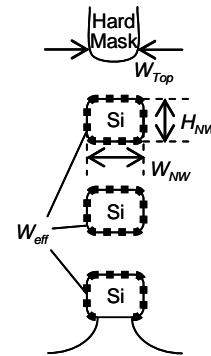


Figure 2.11 (a) Cross-sectional TEM image of vertically-stacked silicon nanowire MOSFET with top-view width  $W_{Top} = 5$  nm. (b) Enlarged image of 5-nm-diameter nanowire.

Table 2.2 Nanowire width with various definitions and surface gain factor  $W_{eff}/W_{Top}$ .

$W_m$ [nm]	40	45	50	60
$W_{Top}$ [nm]	10	15	20	30
Max. $W_{NW}/H_{NW}$ [nm]	11/14	15/14	21/15	32/15
$W_{eff}$ [nm]	102	130	171	227
$W_{eff}/W_{Top}$	10.2	8.7	8.5	7.6



The nanowires are [110]-oriented and horizontally arrayed with 50 or 10 parallel wires. The physical wire lengths ( $L_{NW}$ ) are in the 42 – 607 nm range as shown in Figure 2.12. Effective gate length ( $L_{eff}$ ) and source/drain resistance ( $R_{SD}$ ) were extracted thanks to the Y-function-based technique as shown in Chapter 3. Differences between  $L_{NW}$  and  $L_{eff}$  were less than 10 nm. This means that the source/drain implantation and activation annealing are well-controlled. The resulting  $R_{SD}$  are 159  $\Omega \cdot \mu\text{m}$  for NMOS and 161  $\Omega \cdot \mu\text{m}$  for PMOS.

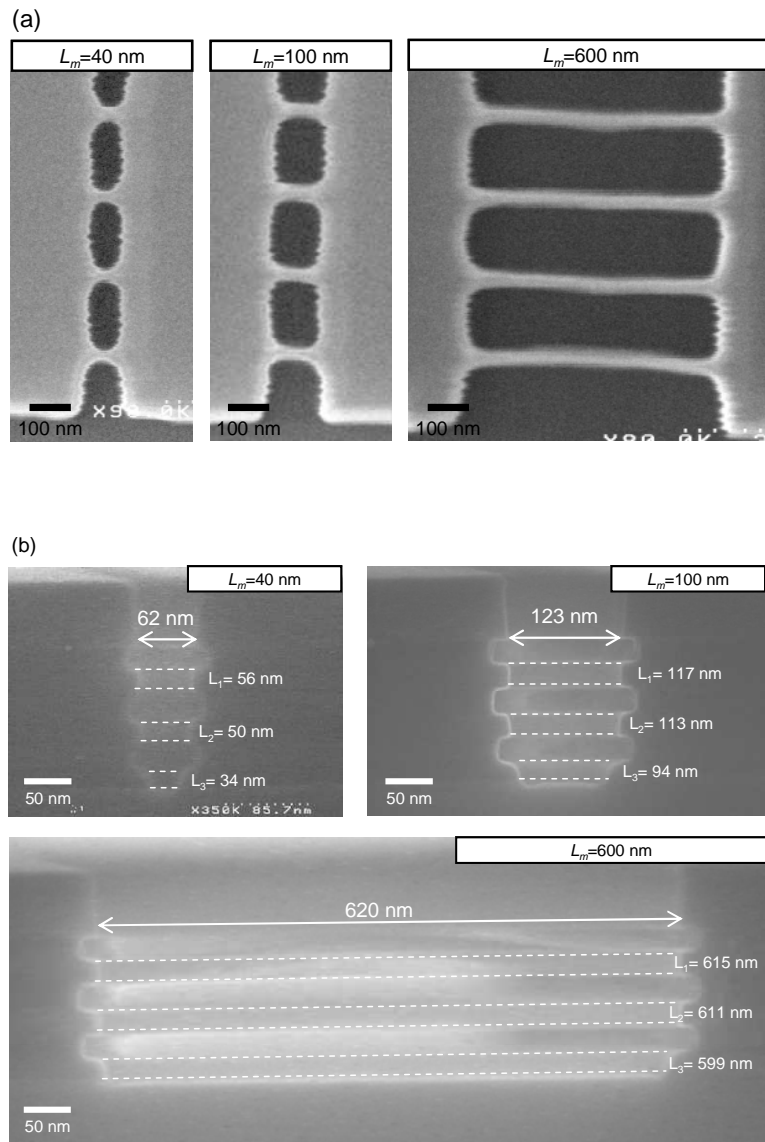


Figure 2.12 Top-view (a) and cross-section (b) of SEM images of vertically-stacked silicon nanowire MOSFET with mask length  $L_m = 40, 100, \text{ and } 600$  nm.

## 2.5 CONCLUSIONS

In this chapter, the fabrication process of the vertically-stacked channel MOSFETs were described. The use of sacrificial SiGe layers enables silicon channel to be piled up. The gate stacks were uniformly surrounded owing to ALD and CVD process.

## 2.6 REFERENCES

- [2.1] A.J. Pidduck, D.J. Robbins, A.G. Cullis, W.Y. Leong, A.M. Pitt, “Evolution of surface morphology and strain during SiGe epitaxy”, *Thin Solid Films*, Vol. 222, Issue 1-2, pp. 78-84, 1992.
- [2.2] E. Bernard, T. Ernst, B. Guillaumot, N. Vulliet, T.C. Lim, O. Rozeau, F. Danneville, T. Skotnicki, S. Deleonibus, O. Faynot, “Novel internal spacers 50nm gate length Multi-Channel MOSFET (MCFET) with TiN/HfO<sub>2</sub> gate stack”, *IEEE Electron Device Letters*, Vol. 30, No. 2, pp. 148–151, 2009.
- [2.3] E. Bernard, T. Ernst, B. Guillaumot, N. Vulliet, P. Coronel, T. Skotnicki, S. Deleonibus, O. Faynot, “Multi-Channel Field Effect Transistors (MCFET) - Part I: Electrical performances and current gain analysis”, *IEEE Transactions on Electron Devices*, Vol. 56, No. 6, pp. 1243–1251, 2009.
- [2.4] J.M. Hartmann, M. Py, P.H. Morel, T. Ernst, N. Vulliet, B. Previtali and J.P. Barnes, “Cyclic Deposition / Etch processes for the formation of Si raised sources and drains in advanced MOSFETs,” *ECS Trans.*, Vol. 33, No. 6, pp. 391–407, 2010.
- [2.5] S. Borel, C. Arvet, J. Bilde, S. Harrison, D. Louis, “Isotropic etching of SiGe alloys with high selectivity to similar materials”, *Microelectronic Engineering*, Vol. 73–74, pp. 301–305, 2004.
- [2.6] E. Bernard, T. Ernst, B. Guillaumot, N. Vulliet, P. Coronel, T. Skotnicki, S. Deleonibus, O. Faynot, “Multi-Channel MOSFET (MCFET) structures - Part II : Analysis of the gate stack and the series resistances influence on the performances”, *IEEE Transactions on Electronic Devices*, Vol. 56, No. 6, pp. 1252–1261, 2009.
- [2.7] C. Dupre, T. Ernst, E. Bernard, B. Guillaumot, N. Vulliet, P. Coronel, T. Skotnicki, S. Cristoloveanu, G. Ghibardo, S. Deleonibus, “A Mobility Extraction Method for 3D Multi- Channel MOSFET”, *Proceedings of ESSDERC*, pp. 230-233, 2008.
- [2.8] C. Dupré, A. Hubert, S. Bécu, M. Jublot, V. Maffini-Alvaro, C. Vizioz, F. Aussenac, C. Arvet, S. Barnola, J.-M. Hartmann, G. Garnier, F. Allain, J.-P. Colonna, M. Rivoire, L. Baud, S. Pauliac, V. Loup, T. Chevolleau, P. Rivallin, B.

Guillaumot, G. Ghibaudo, O. Faynot, T. Ernst, and S. Deleonibus, “15nm-diameter 3D Stacked Nanowires with Independent Gate Operation:  $\Phi$ FET,” in *IEDM Tech. Dig.*, 2008, pp. 749–752.

- [2.9] K. Tachi, M. Casse, D. Jang, C. Dupré, A. Hubert, N. Vulliet, V. Maffini-Alvaro, C. Vizios, C. Carabasse, V. Delaye, J. M. Hartmann, G. Ghibaudo, H. Iwai, S. Cristoloveanu, O. Faynot, and T. Ernst, “Relationship between mobility and high- $k$  interface properties in advanced Si and SiGe nanowires,” in *IEDM Tech. Dig.*, pp.313–316, 2009, Baltimore, US.



# **CHAPTER 3**

## *ELECTRICAL CHARACTERIZATION METHODS*



# CHAPTER 3 CONTENTS

## **3 Electrical Characterization Methods**

- 3.1 Introduction
- 3.2  $Y$ -function Method
- 3.3 Split  $C$ - $V$  Method
- 3.4 Mobility Limiting Components
- 3.5 Charge Pumping Method
- 3.6 Low-frequency Noise Measurement
- 3.7 Conclusions
- 3.8 References

### **3.1 INTRODUCTION**

In short-channel MOSFETs, it is important to design MOSFET structure effective in suppression of both short-channel effects and source/drain resistance. Moreover, although  $\mu$  dependence of  $v$  becomes weaker in short-channel MOSFETs, the  $\mu$  enhancement can be still important in increasing  $I_{ON}$  under quasi-ballistic transport regime as explained in Chapter 1. To analyze the performances of the vertically-stacked channel architectures, it is necessary to accurately extract its intrinsic parameters such as the threshold voltage, the effective gate length, the series resistances, and the carrier mobility. Although many techniques have been developed during the past decades [3.1–3.9], only few of them remain reliable for aggressively-scaled MOSFETs have been applied. Especially, the mobility decrease with the channel length downscaling is often problematic [3.10–3.11]. In this study, we basically use two methods. One is Y-function-based techniques [3.1–3.5] which rely on the low field drain current model (BSIM3v3-like [3.12]) and does not require any assumption about the  $\mu$  (L) behavior. This method enables us to simply and correctly extract the device parameters. The other method is split  $C$ – $V$  method to analyze the effective mobility in the inversion layer [3.13–3.16]. Indeed, parasitic effects and coexistence of a couple of carrier scattering mechanisms make the accurate analysis of the mobility difficult. In this study, the effective mobility is evaluated by combining these two methods. Then the carrier scattering components in the nanowires are investigated from the viewpoint of the validity of the Matthiessen’s rule.

### **3.2 Y-FUNCTION METHOD**

Y-function has been first introduced by Ghibaudo *et al.* to provide an easy and reliable way to extract the device parameters [3.1], then completed by including a quadratic mobility attenuation factor. Y-function-based method is based on the combined exploitation of the  $I_{DS}$ – $V_G$  and  $g_m$ – $V_G$  curves. The MOSFET parameter extraction is performed within the strong inversion regime of the MOSFET linear

region and, therefore, relies on the following equations [3.4]:

$$\frac{V_{DS}}{I_{DS}} = \frac{V_{DS}}{I_{DS0}} + R_{SD}, \quad (3.1)$$

$$I_{DS0} = \frac{W_{TOT}}{L_{eff}} \mu_{eff} C_{ox} (V_G - V_T - V_D / 2) V_{DS}, \quad (3.2)$$

$$\mu_{eff} = \frac{\mu_0}{1 + \Theta_1 (V_G - V_T - V_D / 2) + \Theta_2 (V_G - V_T - V_D / 2)^2}, \quad (3.3)$$

$$\beta \equiv \frac{\mu_0 W_{TOT} C_{ox}}{L_{eff}}, \quad (3.4)$$

$$g_m \equiv \frac{\partial I_{DS}}{\partial V_G}, \quad (3.5)$$

$$Y \equiv \frac{I_{DS}}{\sqrt{g_m}} = \sqrt{\frac{\beta V_D}{1 - \Theta_2 (V_G - V_T - V_D / 2)^2}} (V_G - V_T - V_D / 2), \quad (3.6)$$

$$\Theta_{1eff} = \Theta_1 + \beta R_{SD}, \quad (3.7)$$

where  $I_{DS0}$  is intrinsic value of  $I_{DS}$  (i.e. at  $V_{DS}$ , without  $R_{SD}$  influence),  $\mu_0$  is the low-field mobility,  $\Theta_1$  and  $\Theta_2$  are the first- and second- order mobility attenuation factors.  $\Theta_{1eff}$  represents the mobility limitation caused by phonon scattering and includes the  $R_{SD}$ . These equations are valid in strong inversion. The drain current  $I_{DS}$  and transconductance  $g_m$  then can be rewritten by the following equation:

$$I_{DS} = \frac{\beta V_D (V_G - V_T - V_D / 2)}{1 + \Theta_{1eff} (V_G - V_T - V_D / 2) + \Theta_2 (V_G - V_T - V_D / 2)^2}, \quad (3.8)$$

$$g_m = \frac{\beta V_D \{1 - \Theta_2 (V_G - V_T - V_D / 2)^2\}}{\{1 + \Theta_{1eff} (V_G - V_T - V_D / 2) + \Theta_2 (V_G - V_T - V_D / 2)^2\}^2}. \quad (3.9)$$

In the strong inversion regime, the Y-function varies linearly with the gate voltage when  $\Theta_2$ -effect (i.e. the surface roughness effect) is negligible.  $V_T$  can then be obtained by the extrapolation of the linear part of the curve (intercept with the X-axis).  $\beta$  can be extracted from the Y-slope. Unfortunately, the Y-function calculated from the complete model (including  $\Theta_2$ -effect) takes a non-linear form (3.6). This non-linearity causes strong uncertainties on and  $\beta$  extraction. This problem has been noticed by several researchers [3.2–3.5]. Tanaka *et. al.* introduced a corrective factor ( $\Phi$ ) to suppress the

and linearize the Y-function for performing a straightforward extraction [3.4]:

$$F(Y, \Phi) \equiv \frac{1}{\sqrt{1/Y^2 + \Phi}} = \sqrt{\beta V_D} (V_G - V_T - V_D / 2), \quad (3.10)$$

$$\Phi = \Theta_2 / \beta V_D. \quad (3.11)$$

Therefore by finding  $\Phi$  which satisfied that  $F(Y, \Phi)$  is linear to  $V_G$  of  $dF(Y, \Phi)/dV_G$  is constant, we can extract  $\Phi$ . Figure 3.1 shows an example of  $\Phi$  extraction. Since effect of  $\Phi$  on  $F(Y, \Phi)$  is monotonic, we can straightforwardly and robustly solve it. Following it, the parameter  $\beta$ ,  $\Theta_2$ , and  $V_T$  are extracted by linear regression curve. To calculate  $\Theta_{1eff}$ , the effective mobility attenuation function  $\Theta_{eff}$  is defined from the equation (3.8) as,

$$\Theta_{eff} = \frac{\beta V_D}{I_{DS}} - \frac{1}{(V_G - V_T - V_D / 2)} = \Theta_{1eff} + \Theta_2 (V_G - V_T - V_D / 2). \quad (3.12)$$

Figure 3.2 shows the  $\Theta_{eff}$  as a function of gate voltage. A good linear relation with  $V_G$  is obtained. The  $\Theta_{1eff}$  can be extracted from the intercept of  $\Theta_{eff}(V_G)$  with the Y-axis. In addition, the slope enables the validation of the  $\Theta_2$  extracted from the equation (3.11). The modeled  $I_{DS}-V_G$  and  $g_m-V_G$  curves then are obtained from the equations (3.8) and (3.9) by using the extracted factors ( $\beta$ ,  $\Theta_{1eff}$ ,  $\Theta_2$ , and  $V_T$ ). Figure 3.3 shows the  $I_D$  and  $g_m$  curves comparisons between the measured data and the fitted model, showing that a fairly nice modeling has been achieved. The model is then well adapted even for short channel MOSFET devices ( $L_G < 100\text{nm}$ ).

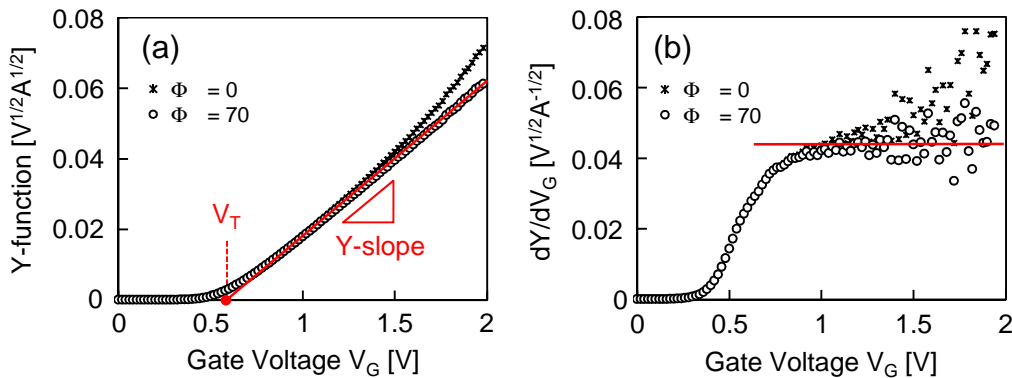


Figure 3.1 Y-function as a function of the gate voltage. The device used is n-type vertically-stacked SNWT with  $L_m=100\text{ nm}$  and  $W_{NW}=15\text{ nm}$ .

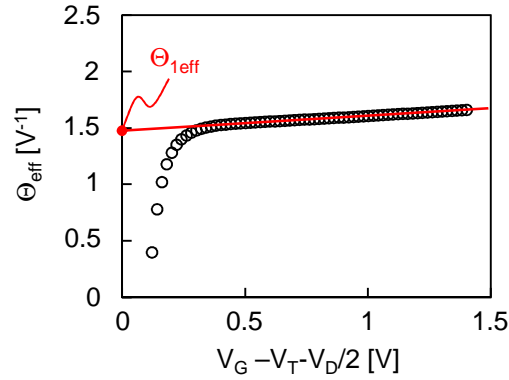


Figure 3.2 Extraction of  $\Theta_{1eff}$ . The device used is n-type vertically-stacked SNWT with  $L_m=85$  nm and  $W_{NW}=15$  nm.

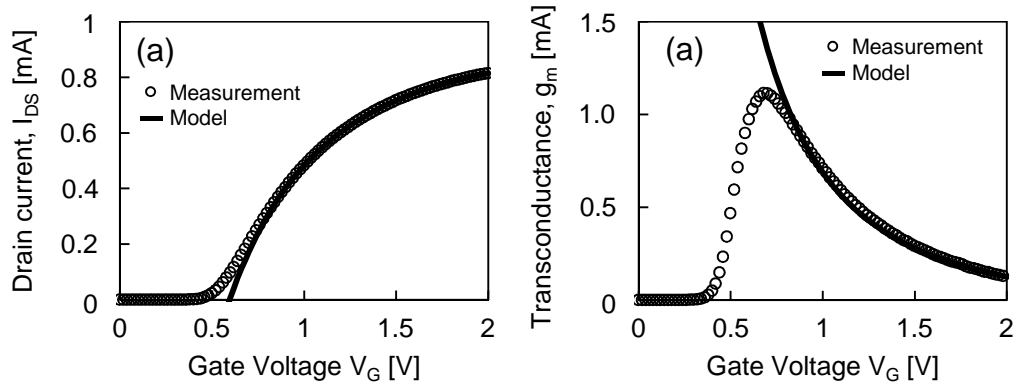


Figure 3.3 (a)  $I_{DS}-V_G$  and (b)  $g_m-V_G$  curves comparisons between the measured data and the fitted model.

By using the obtained parameters ( $\beta$ ,  $\Theta_{1eff}$ ,  $\Theta_2$ , and  $V_T$ ), we can extract  $R_{SD}$ ,  $L_{eff}$ , and  $\mu_{eff}$ .

The parameter extraction is performed by the four steps:

- (1) we extract  $\beta$ ,  $\Theta_{1eff}$ ,  $\Theta_2$ , and  $V_T$  in each  $L_G$  as above.
- (2) we extract  $R_{SD}$  by plotting  $\Theta_{1eff}-\beta$  among all  $L_G$  as shown in Figure 3.4 (a). Note that errors in  $L_G$  and  $L_G$ -dependent  $\mu_0$  never affect the extracted  $R_{SD}$  value.
- (3) we extracted  $L_{eff}$  by plotting  $1/\beta-L_m$  as shown in Figure 3.4 (b).
- (4) we finally can extract  $\mu_{eff}$  as a function of  $V_G$  by using all the parameters extracted and  $C_{OX}$  measured by split  $C-V$  method.

The flow chart is shown in Figure 3.5. Note that total gate width  $W_{TOT}$  is not needed to

extract the mobility because  $\beta$  (Eq.3.4) can be rewritten by using the measured capacitance  $C_m$  without any normalization as following

$$\beta \equiv \mu_0 \frac{W_{TOT}}{L_{eff}} C_{OX} = \mu_0 \frac{W_{TOT}}{L_{eff}} \left( \frac{C_m}{W_{TOT} L_{eff}} \right) = \mu_0 \frac{C_m}{L_{eff}^2} \quad (3.13)$$

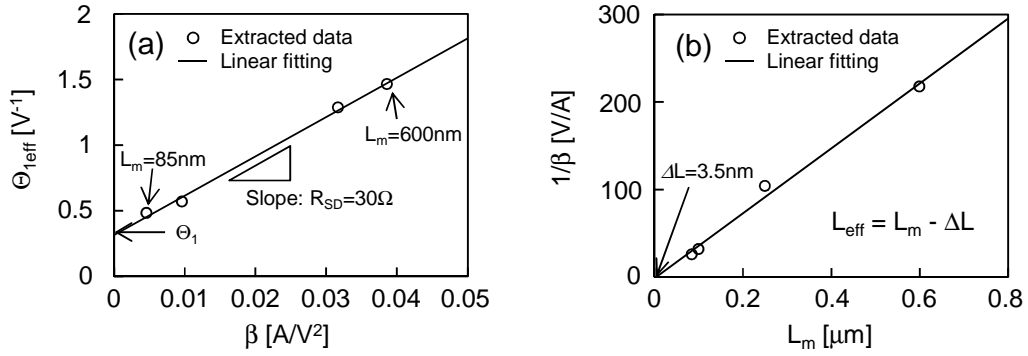


Figure 3.4 (a)  $R_{SD}$ ,  $\Theta_1$ , and (b)  $L_{eff}$  extraction.

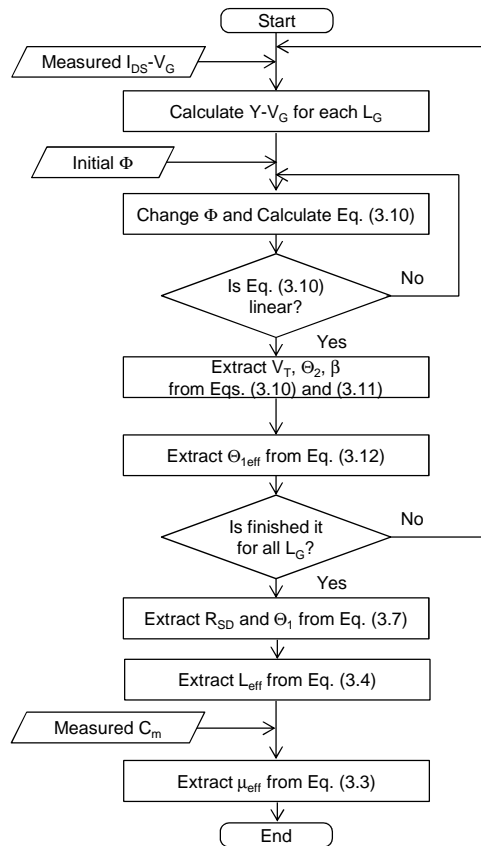


Figure 3.5 Flow chart of the extraction procedure.

### 3.3 SPLIT C–V METHOD

This method is based on the combination of two capacitance measurements and one current–voltage measurement in order to obtain the effective mobility  $\mu_{eff}$  as a function of the inversion charge density  $Q_{INV}$  or the effective electric field  $E_{eff}$ .

The drain current  $I_{DS}$  is a combination drift and diffusion currents. At low drain voltage of typically 10–100mV, the channel charge is uniform from source to drain, allowing the diffusive current to be ignorable. The drain current then can be simply written by

$$I_D = \frac{W_{TOT}}{L_{eff}} \mu_{eff} Q_{INV} V_{DS} \cdot \quad (3.14)$$

which can be written:

$$\mu_{eff} = \frac{g_d L_{eff}}{W_{TOT} Q_{INV}}, \quad (3.15)$$

where the drain conductance  $g_d$  is defined as:

$$g_d = \left. \frac{\partial I_D}{\partial V_{DS}} \right|_{V_{GS}} = const. \quad (3.16)$$

The inversion charge  $Q_{INV}$  can be directly determined from the gate-to-channel capacitance  $C_{GC}$ , according to:

$$Q_{INV}(V_G) = \frac{1}{L_{eff} W_{TOT}} \int_{-\infty}^{V_G} C_{GC}(V_G) dV_G \cdot \quad (3.17)$$

Then  $C_{GC}$  is measured using the connection of Figure 3.6 (a). The capacitance meter is connected between (i) the grounded substrate and (ii) the gate and the source/drain electrodes connected together. Setup in Figure 3.6 (b) is used to measure the gate-to-substrate capacitance  $C_{GB}$ . The connected source-drain is grounded during  $C_{GB}$  measurement. This measurement determines a bulk charge density  $Q_B$  according to the following equation

$$Q_B(V_G) = \frac{1}{L_{eff} W_{TOT}} \int_{V_{FB}}^{V_G} C_{GB}(V_G) dV_G \cdot \quad (3.18)$$

Then the effective vertical electric field can be calculated by using both  $Q_{INV}$  and  $Q_B$  as

the following equation

$$E_{eff} = \frac{Q_B + \eta Q_{INV}}{\epsilon_{Si} \epsilon_0}, \quad (3.18)$$

where  $\eta$  is an empiric parameter equal to 1/2 for electrons and to 1/3 for holes. Note that, on SOI substrate,  $C_{GB}$  measurement cannot be performed due to the presence of the BOX. But for ultra-thin films transistors on SOI with undoped channels and thick BOX (which is the case of our transistors), the depletion charge is negligible compared to the inversion charge and the effective field is solely determined from the inversion charge.

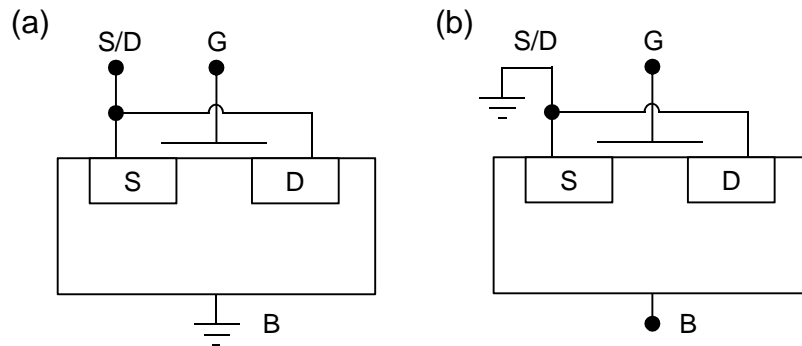


*Figure 3.6 Configuration for (a) gate-to-channel, (b) gate-to-substrate capacitance measurement for split C–V measurement [3.17]*

The split C–V method is applicable to short channel devices, only if: the drain current is corrected by the series resistances, the capacitances are corrected from the parasitic capacitances, and the effective gate length is correctly extracted [3.15-3.16]. In order to accurately evaluate the mobility, the effective mobility was extracted by split C–V method with both parasitic capacitance and  $R_{SD}$  corrections. The parasitic capacitance, independent of the gate length, can thus be removed by the following equation

$$C_{GC2}^{intrinsic} = \frac{C_{GC2} - C_{GC1}}{L_2 - L_1} L_2, \quad (3.18)$$

where  $L_1$  and  $L_2$  are the effective gate length,  $C_{GC2}^{intrinsic}$  is the intrinsic gate-to-channel capacitance for the transistor with  $L_2$ . The use of two close gate length is needed for avoiding too large threshold voltage mismatch between the two corresponding devices.



Figure 3.7 shows typical  $C_{GC}$ - $V_G$  curves with and without correction of parasitic capacitances.

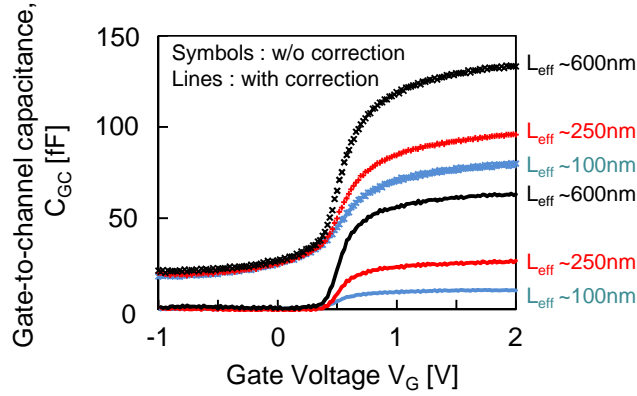


Figure 3.7  $C_{GC}$ - $V_G$  curves with and without correction of parasitic capacitances. The devices used are n-type vertically-stacked SNWT with various gate lengths.

To correct the drain current by the  $R_{SD}$  influence, we used the  $R_{SD}$  value extracted by the Y-function method. Note that when the equation (3.17) is substituted to the equation (3.15),  $W_{TOT}$  is canceled out. As a consequence, to extract the effective mobility, we only need the measured  $I_D$ - $V_G$  and  $C_{GC}$ - $V_G$ , and the  $L_{eff}$ , and  $R_{SD}$  extracted by Y-function method. Figure 3.8 shows the validity of the extraction. A good agreement when compared to other techniques was achieved.

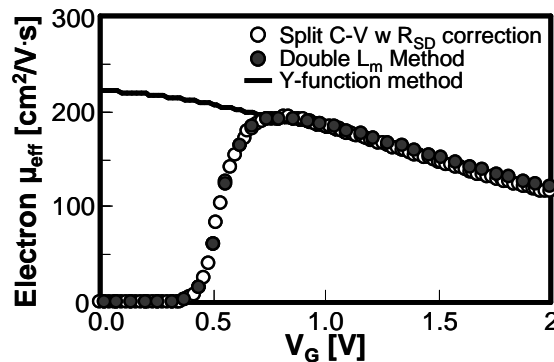


Figure 3.8 Comparison of effective mobility extracted by split C-V, double  $L_m$  method [3.16], and from parameters extracted by Y-function method. The measured device is the stacked SNWTs with  $W_{NW}=15$  nm and  $L_{eff}=242$  nm. The device with  $L_{eff}=592$  nm was also used for double  $L_m$  method.

### 3.4 MOBILITY LIMITING COMPONENTS

Mobility describes carrier motion in a material or a device under the influence of an electric field and is expressed as the carrier velocity per unit electric field. It is a function of the carrier effective conduction mass  $m^*$  and of the average time between two collisions  $\tau$ .

$$\mu = \frac{q\tau}{m^*}. \quad (3.18)$$

One of the important factors which predominate in the mobility expression is the effective mass of the charge carriers in the inversion layer. The effective mass leads to the substantial surface-orientation dependence of the subband structures. Table 3.1 shows the values of the effective mass and the valley degeneracy of Si on the three main surface orientations, (100), (110), and (111) [3.18]. The anisotropy of the effective mass in silicon makes necessary the appropriate choice of the surface orientation for an optimum design of the effective mass. It is well recognized that the twofold valleys on a (100) Si surface is one of the optimum surface orientation in Si, because  $m_x$  and  $m_z$  becomes the minimum (transverse mass  $m_t$ ) and the maximum (longitudinal mass,  $m_l$ ) values of Si, respectively. Figure 3.9 shows a sample of the experimental results of the effective mobility on (100), (110), and (111) surfaces. In general, the electron mobility is highest on <110>/<100> substrate while hole mobility is highest <110>/<110> substrate.

*Table 3.1 Lists of effective mass and valley degeneracy of silicon on (100), (110), and (111) surfaces.*

unit: m0	surface orientation	channel direction	1st ladder				2nd ladder					
			$m_x$	$m_y$	$m_z$	$n_v$	$m_x$	$m_y$	$m_z$	$n_v$		
Si	(100)	<001>	0.19	0.19	0.916	2	0.19	0.916	0.19	2		
		<011>					0.916	0.19				
		<011>					0.315	0.315			4	
	(110)	<001>	0.19	0.553	0.315	4	0.916	0.19	0.19	2		
		<110>	0.553	0.19			0.19	0.916			2	
	(111)	<110>		0.412	0.232	0.258	4					
				0.19	0.674							2
				0.232	0.412							4
				0.674	0.19							2

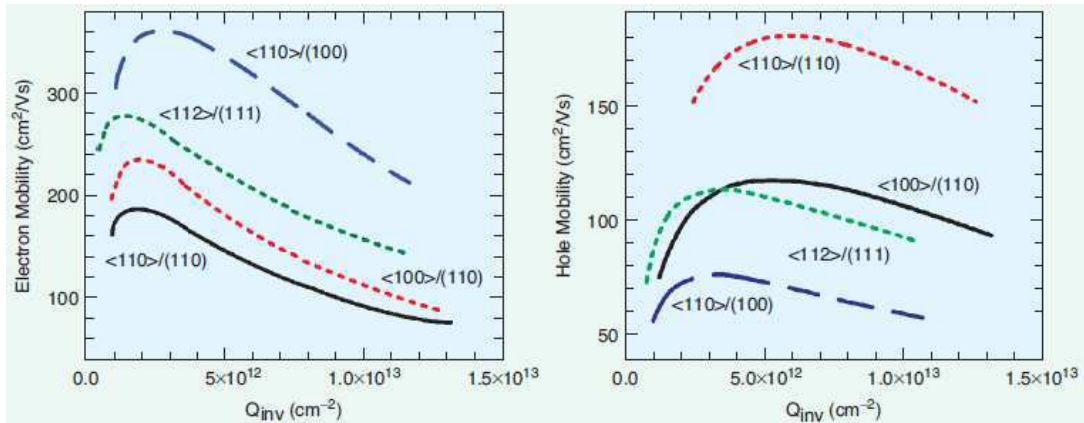


Figure 3.9 Electron and hole mobilities in the inversion layers with the substrate orientations. (data from ref. [3.19]).

Moreover, the carriers in the inversion layer are scattered according to several mechanisms. Each scattering mechanism is associated with a mobility component. According to the Mathiessen’s rule the net mobility  $\mu$  depends on the various mobility components as [3.17]

$$\frac{1}{\mu} = \frac{1}{\mu_1} + \frac{1}{\mu_2} + \dots, \quad (3.19)$$

and the lowest mobility component dominates. The scattering mechanisms are *lattice* or *phonon scattering* and *ionized impurity scattering*. The location of the carriers near the oxide-semiconductor interface introduces additional scattering mechanisms like *Coulomb scattering* from oxide charges and interface states, as well as *surface roughness scattering*, reducing the MOSFET mobility below the bulk mobility. Since these scattering mechanisms show the different transverse-field-dependence and temperature-dependence, the mobility limiting components can be analyzed by plotting it as a function of the transverse field or the inversion charge density, and the measurement temperature.

### ■ Phonon Scattering

Phonons are pseudo-particles associated to the crystalline network vibrations. When the temperature is below 100K, acoustic phonons are dominant. For higher

temperatures, between 100K and 400K, optic phonons are predominant. The phonon limited mobility is given by

$$\mu_{ph} \propto \frac{E_{eff}^{-1/3}}{T^\beta}, \quad (3.20)$$

where  $\beta$  value, between 1 and 1.75, is dependent on the surface orientation [3.20].

### ■ Coulomb Scattering

Coulomb interactions are induced by any mobile or fixed charge in the channel (impurities) or close to it (oxide charges). They are predominant at low temperature and low electric field (weak inversion). In strong inversion, the coulomb scattering is screened due to the high carrier density. The Coulombian limited mobility is expressed as

$$\mu_{cb} \propto E_{eff} T. \quad (3.21)$$

### ■ Surface Roughness Scattering

The oxide/silicon interface roughness induces carrier scattering. This scattering does not depend on the temperature. It is predominant at high electric effective field, when the carriers are close to the interface. The surface roughness limited mobility is given by

$$\mu_{sr} \propto E_{eff}^{-2}. \quad (3.22)$$

Figure 3.10 shows a schematic diagram of mobility limiting components. At low effective field, the electron mobility is limited by the Coulombian interactions (impurities and interfaces charges). When the effective field is increased, the mobility becomes independent on the doping level according to a universal curve as shown in Figure 3.11 [3.21]. In this region, the mobility is limited by the phonons and surface roughness interactions. When the temperature is low below 100 K, the phonon interactions can be ignored. Then we can extract the surface-roughness-limited mobility at high effective field of inversion charge density.

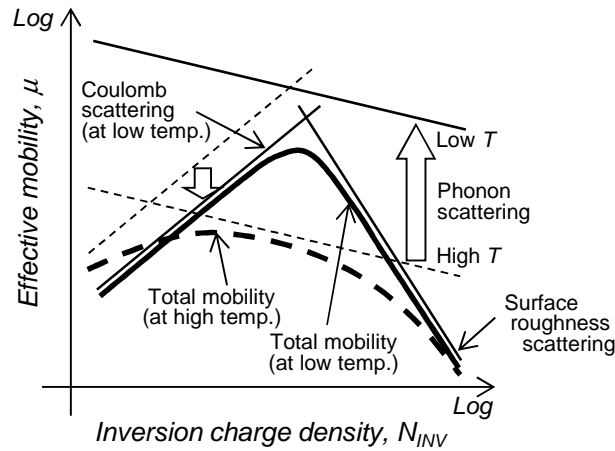


Figure 3.10 Schematic diagram of mobility limiting components as a function of inversion charge density at low and high temperature.

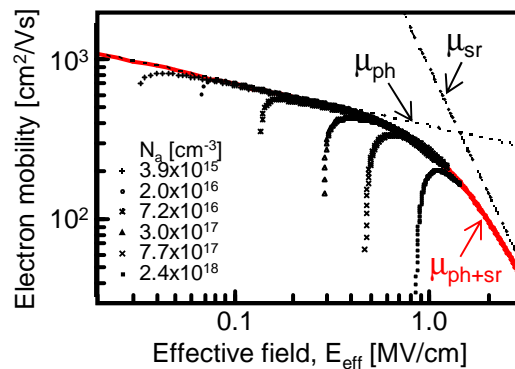


Figure 3.11 Electron mobility on (100) as a function of effective field. The dots are experimental results in ref [3.21] with substrate acceptor concentration dependence. The lines are the limited mobilities calculated by Matthiessen's rule.

### 3.5 CHARGE PUMPING METHOD

Whereas the quality of the thermal SiO<sub>2</sub> oxide in conventional SiO<sub>2</sub> / poly-silicon MOSFETs was rather well controlled, the introduction of new materials in the gate stack (such as high-k oxides, metallic gate, nitrided oxide...) has a strong impact on the quality and their electrical characteristics. In this study, we have investigated the combined effect of advanced structures such as SNWTs, with HfO<sub>2</sub>/TiN gate stack, on the channel/oxide interface quality by using the charge pumping (CP) technique in

specific P-i-N nanowire structures as shown in Figure 3.12 [3.22].

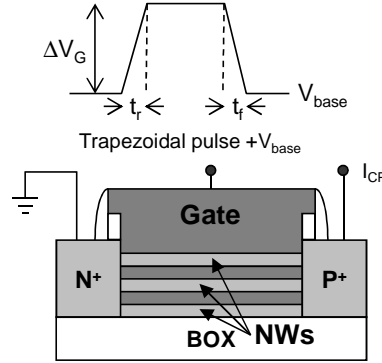


Figure 3.12 Schematics of the experimental setup used for CP; a trapezoidal pulse is applied to the gate and CP current is measured on the P+ contact.

In the CP technique, a trapezoidal voltage pulse is applied to the transistor gate (Figure 3.12) which alternatively fills the interface traps with electrons and holes, thereby causing a recombination current,  $I_{CP}$ , to flow in the P<sup>+</sup> and N<sup>+</sup> regions of the gated diode. By varying the base level  $V_{base}$  from accumulation to inversion, with a constant amplitude  $\Delta V_G$  greater than the value of the band gap ( $\Delta V_G = 1.3$  eV is used here), the measured  $I_{CP}$  has a typical “hat” shape. The maximum of the two-level CP current can be expressed as

$$I_{CP} = qfA \int_{E_{em,h}}^{E_{em,e}} D_{it}(E) dE, \quad (3.23)$$

where  $A$  is the gate area, and  $q$  the electron charge. The integration is done between the hole and the electron emission levels  $E_{em,h}$  and  $E_{em,e}$ . Those energy levels are given by

$$E_{em,h} = E_i + k_B T \ln \left( v_{th} n_i \sigma_p \frac{|V_{FB} - V_T|}{\Delta V_G} t_r \right),$$

$$E_{em,e} = E_i + k_B T \ln \left( v_{th} n_i \sigma_n \frac{|V_{FB} - V_T|}{\Delta V_G} t_f \right). \quad (3.24)$$

where  $E_i$  is the intrinsic Fermi level,  $v_{th}$  the thermal velocity of carriers,  $n_i$  the intrinsic carrier density, and  $\sigma_{n,p}$  the capture cross-section of electrons or holes. Equation (3.23) shows a linear relation between  $I_{CP}$  and frequency  $f$ . This simple relation allows to measure the mean value  $D_{it}$  integrated over the band gap by sweeping the frequency of

the pulsed signal  $D_{it} = 1/qA\Delta E_{em}dI_{CP}/df$ . According to Eqs. (3.24), the emission levels can be modulated by varying either the fall or rise time, or the temperature. In particular, varying  $t_r$  while keeping  $t_f$  constant, and reversely, allows to extract the  $D_{it}$  energy profile in the forbidden band gap using

$$D_{it}(E_{em}) = \frac{1}{qAfk_B T} \frac{dI_{CP}}{d \ln t_{f,r}}, \quad (3.25)$$

where  $t_{r,f}$  is the rise or fall time depending on the energy range scanned within the band gap. Finally, changing the temperature allows to scan a broader range of energy. Low temperatures down to 25 K give thus access to the energy distribution close to the conduction and the valence band of Si in a typical  $\pm(0.58-0.3)$  eV energy range (Figure 3.13). Notice that the energy band gap of the Si increases at low temperature, reaching 1.17 eV at 25 K. The value of the capture cross-section  $\sigma_{n,p}$  is hard to determine experimentally. However, an error on this parameter only results in a shift in the energy axis (limited to 120 meV for  $\sigma_{n,p} = 10^{-15}-10^{-17}$  cm<sup>2</sup>) and does not change our results in a significant way. In the following we have chosen a constant value equal to  $10^{-16}$  cm<sup>2</sup>, which is a physically acceptable value. Finally, due to the derivative used in Eq. (3.25), and for the small geometries of the measured devices, the measurement sensitivity of this spectroscopic CP technique is around  $10^{11}$  eV<sup>-1</sup> cm<sup>-2</sup>.

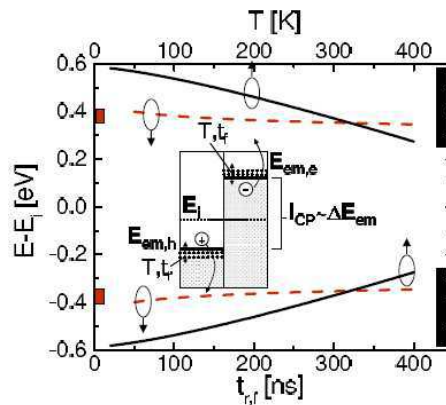


Figure 3.13 (Color online) Energy range scanned by temperature modulation from 20 K to 400 K (bold line) or by rise/fall time modulation (dashed line), as calculated from Eqs. (3.24) for Si. Insert: Schematic of the physical mechanism involved during CP measurement. The electron and hole emission levels  $E_{em}$  can be scanned by changing temperature  $T$  and/or the rise of fall time  $t_{r,f}$ .

### 3.6 LOW-FREQUENCY NOISE MEASUREMENT

Low-frequency (LF) noise is a powerful technique to characterize the electronic devices, providing relevant information about the defect density in the active regions. Very few studies have been dedicated to LF noise in Si nanowires. In this study, we investigate the LF noise in vertically-stacked SNWTs [3.23]. The LF noise measurements were performed between 10 Hz and 10 kHz at  $V_{DS}=50$  mV. They show typical  $1/f$  spectra for both devices. It is well known that, in electronic devices, the  $1/f$  noise can mainly be interpreted by following two approaches:

- (I) The carrier number fluctuation (CNF) model, originally proposed by McWhorter. In this model, the trapping/release of charge carriers near the dielectric/semiconductor interface causes modulation of the flat-band voltage, and by turn, of the drain current. This model can be extended to include the correlated mobility fluctuations (CNF+CMF), such that the normalized drain current noise reads,

$$\frac{S_{ID}}{I_D^2} = \left( 1 + \alpha \cdot \mu_{eff} \cdot C_{OX} \frac{I_D}{g_m} \right) \times S_{VFB} \times \left( \frac{g_m}{I_D} \right)^2, \quad (3.26)$$

where  $S_{ID}$  is the current noise power spectral density ( $A^2/Hz$ ),  $\alpha$  the Coulomb scattering parameter (Vs/C), , and  $S_{VFB}$  the flat-band voltage power spectral density. The  $S_{VFB}$  is associated with the interface charge fluctuations and is given by,

$$S_{VFB} = \frac{q^2 kT \lambda N_t}{f W L C_{OX}^2}, \quad (3.27)$$

where  $\lambda$  is the oxide tunneling distance and  $N_t$  the volume trap density ( $cm^{-3}eV^{-1}$ ). Thus, the CNF model is particularly sensitive to the quality of dielectric/channel interface, especially in the presence of high- $\kappa$  dielectric and metal gate stacks.

- (II) The Hooge mobility fluctuation model (HMF) is based on the assumption that the carrier mobility fluctuates by the interactions with phonons, as in conventional conductors or semiconductors. It can be expressed through a phenomenological parameter,  $\alpha_H$



$$\frac{S_{ID}}{I_D^2} = \frac{q\alpha_H}{fWLQ_i} \approx \frac{1}{I_D}, \quad (3.28)$$

where  $Q_i$  is the inversion charge density per unit area ( $\text{C}/\text{cm}^2$ ) and  $\alpha_H$  ( $=10^{-3}$ – $10^{-6}$ ) is the Hooge parameter.

### 3.7 CONCLUSIONS

In this chapter, the two electrical characterization methods were described. The calculated  $I$ – $V$  curve with parameters extraction by the Y-function method was well fitted to the measured data for various device dimensions, showing the validity of the method. Finally, a good agreement between the effective mobility values when compared between Y-function method and split  $C$ – $V$  technique was achieved. In addition, each mobility-limiting-component can be analyzed by plotting its transverse field and temperature dependence. The CP method and LF noise technique were described as the electrical evaluation techniques of the interface quality on nanowires.

### 3.8 REFERENCES

- [3.1] G. Ghibaudo, “New method for the extraction of MOSFET parameters,” *IEE Electronics Letters*, vol. 24, pp. 543–545, Apr. 1988.
- [3.2] C. Mourrain, B. Cretu, G. Ghibaudo *et al.*, “New method for parameter extraction in deep submicrometer MOSFETs,” in *Proc. IEEE Int. Conf. Microelectronic Test Structures (ICMTS’00)*, Monterey, USA, Mar. 2000, pp. 181–186.
- [3.3] T. Tanaka, “Novel extraction method for size-dependent mobility based on BSIM3-like compact model,” *Japanese Journal of Applied Physics*, vol. 44, pp. 2424–2427, 2005.
- [3.4] T. Tanaka, “Novel parameter extraction method for low field drain current of nano-scaled MOSFETs,” in *Proc. IEEE Int. Conf. Microelectronic Test Structures (ICMTS’07)*, Tokyo, Japan, Mar. 2007, pp. 265–267.

- [3.5] D. Fleury, A. Cros, H. Brut, and G. Ghibaudo, "New Y-function-based methodology for accurate extraction of electrical parameter on nano-scaled MOSFETs," in *Proc. IEEE Int. Conf. Microelectronic Test Structures (ICMETS'08)*, Edinburgh, UK, Mar. 2008, pp. 160–165.
- [3.6] Y. Taur, D. Zicherman, D. Lombardi *et al.*, "A new 'shift and ratio' method for MOSFET channel-length extraction," *IEEE Electron Device Lett.*, vol. 13, pp. 267–269, May 1992.
- [3.7] H. Katto, "Device parameter extraction in the linear region of MOSFET's," *IEEE Trans. Electron Devices*, vol. 18, pp. 408–410, Sep. 1997.
- [3.8] B. Cretu, T. Boutchacha, G. Ghibaudo *et al.*, "New ratio method for effective channel length and threshold voltage extraction in MOS transistors," *IEEE Electron Device Lett.*, vol. 37, pp. 717–719, May 2001.
- [3.9] H. Brut, A. Juge, and G. Ghibaudo, "New approach for the extraction of gate voltage dependent series resistance and channel length reduction in CMOS transistors," in *Proc. IEEE Int. Conf. Microelectronic Test Structures (ICMETS'97)*, Monterey, USA, Mar. 1997, pp. 188–193.
- [3.10] A. Cros, K. Romanjek, D. Fleury *et al.*, "Unexpected mobility degradation for very short devices : A new challenge for CMOS scaling," in *Proc. IEEE IEDM Tech. Dig.*, San Francisco, USA, Dec. 2006, pp.663–666.
- [3.11] G. Bidal, D. Fleury, G. Ghibaudo, F. Boeuf, and T. Skotnicki, "Guidelines for MOSFET Device Optimization accounting for L-dependent Mobility Degradation," in *IEEE Silicon Nanoelectronics Workshop*, Jun. 2009, pp. 5–6.
- [3.12] Y. Cheng, M.-C. Jeng, S. Liu *et al.*, "A physical and scalable I-V model in BSIM3v3 for analog/digital circuit simulation," *IEEE Trans. Electron Devices*, vol. 44, pp. 277–287, Feb. 1997.
- [3.13] J. Koomen, "Investigation of the MOST channel conductance in weak inversion," *Solid State Electron.*, vol. 16, pp. 801–810, 1973.
- [3.14] C. Sodini, T. Ekstedt, and J. Moll, "Charge accumulation and mobility in thin dielectric MOS transistors," *Solid State Electron.*, vol. 25, pp. 833–841, 1982.
- [3.15] K. Romanjek, F. Andrieu, T. Ernst, and G. Ghibaudo, "Improved split C-V

- method for effective mobility extraction in sub-0.1  $\mu\text{m}$  Si MOSFETs,” *IEEE Electron Device Lett.*, vol. 25, no. 8, pp. 583–585, Aug. 2004.
- [3.16] A. Toriumi, K. Kita, and H. Irie, “Novel approach to MOS inversion layer mobility characterization with advanced split C-V and hall factor analyses,” in *Proc. IEEE IEDM Tech. Dig.*, San Francisco, USA, Dec. 2006, pp.671–674.
- [3.17] D. K. Schroder, *Semiconductor material and device characterization*, John Willy & Son, 3<sup>rd</sup> Edition, pp. 489-494 (2006).
- [3.18] S. Takagi, T. Irisawa, T. Tezuka, T. Numata, S. Nakaharai, N. Hirashita, Y. Moriyama, K. Usuda, E. Toyoda, S. Dissanayake, M. Shichijo, R. Nakane, S. Sugahara, M. Takenaka, and N. Sugiyama, “Carrier-Transport-Enhanced Channel CMOS for Improved Power Consumption and Performance,” *IEEE Trans. Electron Devices*, vol. 55, no. 1, pp. 21–38, Jan. 2008.
- [3.19] C. W. Liu, S. Maikap, and C.-Y. Yu, “Mobility-enhancement technologies,” *IEEE Circuit & Devices Magazine*, pp. 21–36, May/June, 2005.
- [3.20] S. Takagi, A. Toriumi, M. Iwase, and H. Tango, “On the Universality of Inversion Layer Mobility in Si MOSFET’s: Part II–Effects of Surface Orientation,” *IEEE Trans. Electron Devices*, vol. 41, no. 12, pp. 2363–2368, Dec. 1994.
- [3.21] S. Takagi, A. Toriumi, M. Iwase, and H. Tango, “On the Universality of Inversion Layer Mobility in Si MOSFET’s: Part I–Effects of Substrate Impurity Concentrations,” *IEEE Trans. Electron Devices*, vol. 41, no. 12, pp. 2357–2362, Dec. 1994.
- [3.22] M. Cassé, K. Tachi, S. Thiele, and T. Ernst, “Spectroscopic charge pumping in Si nanowire transistors with a high-k/metal gate,” *Appl. Phys. Lett.*, vol. 96, no. 12, 123506, Mar. 2010.
- [3.23] D. Jang, J. W. Lee, K. Tachi, L. Montes, T. Ernst, G. T. Kim, and G. Ghibaudo, “Low-frequency noise in strained SiGe core-shell nanowire p-channel field effect transistors,” *Appl. Phys. Lett.*, vol. 97, no. 7, 073505, 2010.

# **CHAPTER 4**

## ***SOURCE/DRAIN DOPING TECHNIQUES FOR VERTICALLY-STACKED CHANNEL STRUCTURE***

# CHAPTER 4 CONTENTS

## 4 Source/Drain Doping Techniques for Vertically-Stacked Channel Structure

4.1 Introduction

4.2 Experimental Conditions

4.3 Electrical Characteristics

4.3.1  $I$ - $V$  Characteristics

4.3.2 Source/Drain Series Resistance Evaluation

4.3.3 Carrier Mobility Evaluation

4.3.4 Gate Length Scaling

4.4 Conclusions

4.5 References

## **4.1 INTRODUCTION**

The reduction of parasitic access resistances serially connected at source and drain region of MOSFETS are one of the challenging technology in order to meet the performance required in the roadmap as discussed in Chapter 1. The voltage drops at the resistances reduces the applied voltages at the drain and gate electrodes in the transistors, resulting in the decrease in the overdrive voltage to lower the on-current. These resistances also cause degradation in the time constant, commonly referred as RC delay, which lower the switching speed. Therefore, as the channel resistance reduces with the scaling in the gate length, the parasitic series resistance should be further reduced not to increase its proportion in the total resistance at on-state.

MOSFETs with 3 dimensional channels (e.g. Fin FETs) severely suffer from the parasitic access resistance with scaling, as the cross-sectional area at the entrance from the source to channel becomes smaller compared to the surface used for conduction. Therefore, novel processes dedicated for 3 dimensional FETs should be implemented. The aim of such approaches is to modify the shape of the source and drain region in order to reduce the current density or to further reduce the resistivity of the wiring. One example of such process is selective epitaxy growth process to elevate the source and drain region to reduce the current density. Since the growth is selectively done only on Si surfaces, the source and drain regions can be modified without any short circuit to other electrodes. One of the concerns is the excess growth of the source and drain regions results in the increase in the gate to drain capacitances, to lower the switching speed. The later process includes recoil ion-implantation, plasma doping and refractory metal silicide technologies; those techniques are aggressively under research.

As with vertically stacked multi channel devices [4.1–4.3], the later approach to reduce the resistivity of the source and drain region should be done as the source and drain regions are already grown to access to the channels. Therefore, a further increase in the doping concentration with higher activation ratio at source and drain regions are mandatory. In terms of the gate to drain capacitances, the use of oxide spacers with lower k-values between gate and drain regions are reported to be effective and a

reduction in the intrinsic  $CV/I$  delay by 39 % has been achieved [4.1].

In this chapter, a novel process to decrease the resistivity of the source and drain regions of MCFET is presented using *in situ* doped selective epitaxial growth in combination with conventional ion-implantation (I/I) as a novel process for source and drain formation. The effect of source and drain formation process on the series resistance and carrier mobility will be discussed through electrical characteristics.

## 4.2 EXPERIMENTAL CONDITIONS

Three types of MCFETs with different S/D doping schemes, listed in Table 4.1, were investigated. For control MCFET samples, arsenic ions were implanted to the un-doped selective epitaxial growth (SEG) S/D (with a thickness of 200 nm) with a dose of  $10^{15}$  cm<sup>-2</sup> of at 50 keV for *n*-MCFETs. For *p*-MCFETS, boron fluoride ions were implanted with a dose of  $10^{15}$  cm<sup>-2</sup> at 40 keV. For sample A, the source and drain regions were *in situ* doped during the SEG step. The dopant atoms ( $\sim 2 \times 10^{19}$  cm<sup>-3</sup>) for the *in situ* doped SEG were phosphorus and boron for *n*- and *p*-MCFETs, respectively. For sample B, in situ doped SEG was combined with I/I.

*Table 4. 1 Doping scheme*

	Un-doped SEG	<i>In situ</i> doped SEG	Ion implantation (I/I)
Control	✓		✓
Process A		✓	
Process B		✓	✓

## 4.3 ELECTRICAL CHARACTERISTICS

### 4.3.1 $I-V$ Characteristics

Drive current (at  $|V_G - V_T| = 0.9$  V and  $|V_D| = 1.2$  V) against standby current (at  $|V_G - V_T| = 0.3$  V and  $|V_D| = 1.2$  V) for MCFETs with a  $L_G = 70$  nm is shown in Figure 4.1.

The currents were normalized by the top-view width. A large enhancement in the drive current with process A and B respectively, can be obtained with *in situ* doped SEG process compared to the control MCFET. This improvement applies for both *n*- and *p*-MCFETs. The mean drive currents of 2.4 and 1.2 mA/ $\mu$ m are achieved for *n*- and *p*-MCFETs with process B, respectively. These high current densities are due to the *in situ* doped SEG combined with I/I and 3-D configuration of vertically-stacked channels.

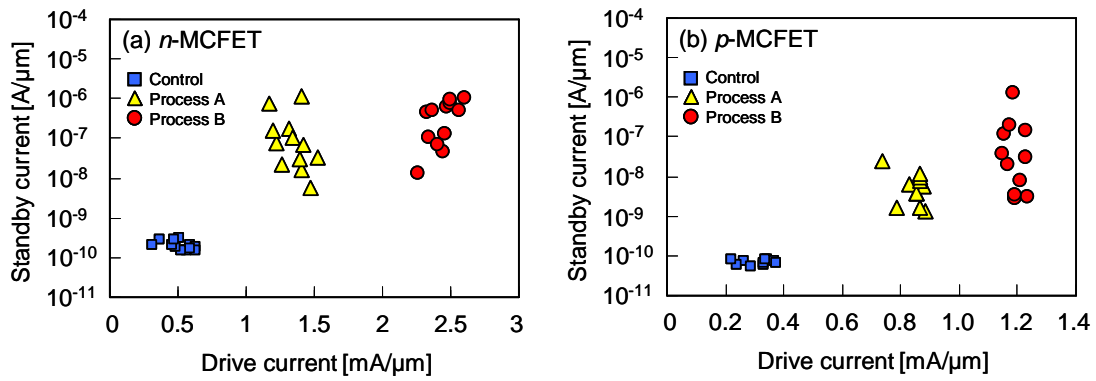


Figure 4.1 On-off relations of (a) *n*- and (b) *p*-MCFETs.

Although the variability in the drive current for *n*- and *p*-MCFET showed little dependence within the same process conditions, the standby currents tend to scatter and the mean value slightly increases with process A and B. The reason of the variability increase in the standby current might be originated from the residual defect in the *in situ* doped SEG. These defects, commonly observed in highly doped silicon, produce generation centers which degrade the on/off junction property.

The threshold voltage dependence on the  $L_G$  is shown in Figure 4.2. Enhanced roll-off properties were observed with sample A and B, where *in situ* doped SEG was adopted. This suggests the influence of the dopant diffusion which lowers the abruptness of the junction.

The dependence of the on-current per a unit width ( $\mu$ m) on the  $L_G$ , for both *n*- and *p*-MCFETs, is shown in Figure 4.3. Here, the total width ( $W_{TOT}$ ) of the channels was used for the normalization. The  $I_{ON}(L_G)$  dependence clearly demonstrates the scaling potential achieved with *in situ* SEG process compared to those with the control



MCFETs. Especially one can see the merits of process B, which enables further enhancement in the  $I_{ON}$  when  $L_G$  is scaled down below 100 nm.

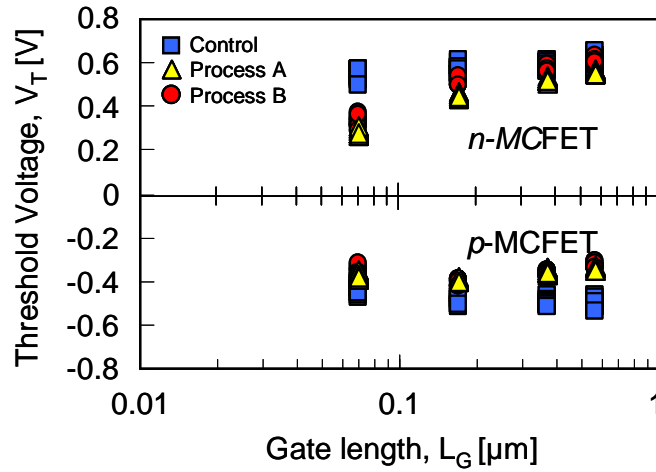


Figure 4.2 Threshold voltage roll-off characteristics of MCFETs with  $L_G$  scaling.

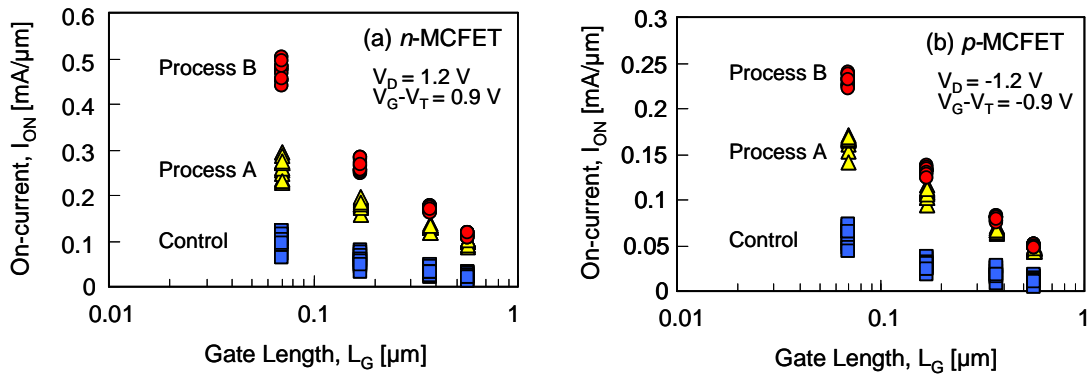


Figure 4.3 On-current dependency on the gate length for (a)  $n$ - and (b)  $p$ - MCFETs.

### 4.3.2 Source/Drain Series Resistance Evaluation

The access resistance values are evaluated through electrical measurements of the transistors by Y-function based methods (see Chapter 3). Figure 4.4 shows typical modeling results of the transconductance of multi channel FETs with different  $L_G$ . One can confirm a fairly nice modeling with the above equations.

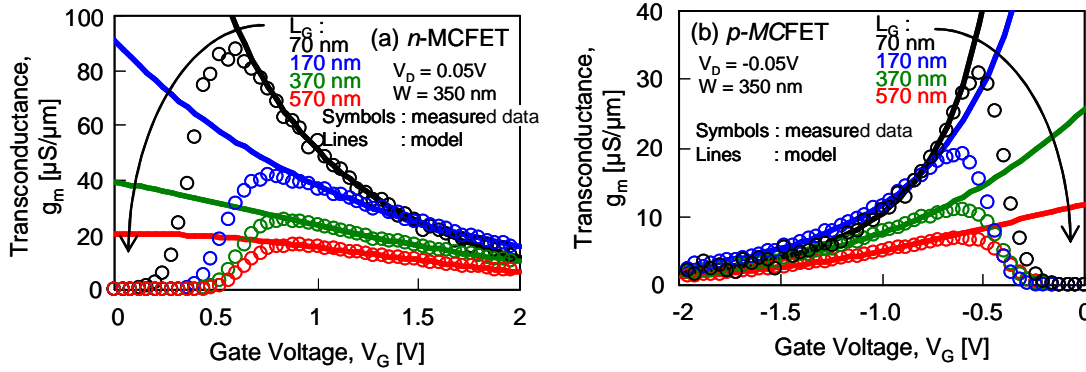


Figure 4.4 Transconductance of the (a) *n*- and (b) *p*-MCFETs. Solid lines represent the fitted model.

$R_{SD}$  can be extracted from the slope in the relation between  $\Theta_{I_{eff}}$  and  $\beta$  as is shown in Figure 4.5. The good linearity in  $\Theta_{I_{eff}}$  vs.  $\beta$  curves, for all the  $L_G$  down to 70 nm, indicates that  $R_{SD}$  is identical among different  $L_G$ . The extracted values of  $R_{SD}$  normalized for a unit channel width ( $\mu\text{m}$ ), for the control sample and MCFETs with process A and B were 4.5, 3.6 and 0.4  $\text{k}\Omega\text{-}\mu\text{m}$  for *n*-MCFET and 5.2, 3.2 and 1.2  $\text{k}\Omega\text{-}\mu\text{m}$  for *p*-MCFET, respectively. Note the remarkable  $R_{SD}$  reduction which has been successfully obtained by combining in situ doped SEG with I/I for both *n*- and *p*-MCFETs (process B). The relatively large  $R_{SD}$  in the control sample may be attributed to un-optimized doping profile in un-doped SEG, so that ion implantation with multiple acceleration energy appears to be necessary.

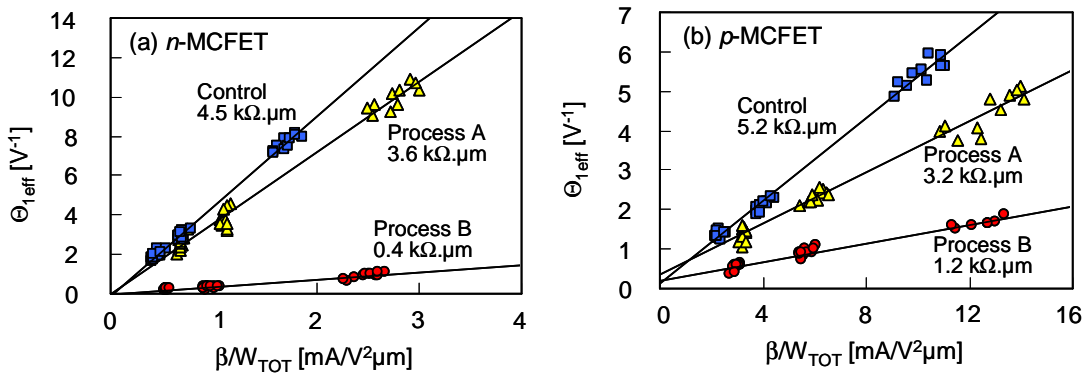


Figure 4.5  $\Theta_{I_{eff}}$  vs.  $\beta$  curves of the fabricated (a) *n*- and (b) *p*-MCFETs.

On the other hand, *in situ* doped SEG process facilitates and improves the processing of vertically aligned MCFETs S/D-channel junctions. The additional I/I into *in situ* doped SEG further reduces the  $R_{SD}$  by 90 % and 60% for n- and p-MCFET, respectively. The origin of the reduction is still unclear, however, for n-MCFET the better positioning and uniformity of the doped S/D and the high solubility of implanted arsenic atoms in silicon compared to that of phosphorus atoms may increase the activation rate, leading to a decrease in  $R_{SD}$ .

### 4.3.3 Carrier Mobility Evaluation

Besides the  $R_{SD}$  values, the effect of junction formation process affects the effective mobility  $\mu_{eff}$  in the channel, in particular when neutral defects are formed during I/I steps [4.4]. A degraded  $\mu_{eff}$  is commonly observed for small  $L_G$ . We here investigate the  $\mu_{eff}$  of the MCFETs and compared the influence of the junction formation process.

The  $\mu_{eff}$  was extracted by a modified split C-V method in order to exclude the parasitic capacitance, which may become dominant in scaled  $L_G$ . Figure 4.6 shows examples of gate-to-channel capacitances  $C_{GC}$  ( $V_G$ ) curves of the MCFETs with process A and B, indicating that the parasitic capacitances were identical among different  $L_G$ , so that the inversion carrier density can be extracted.

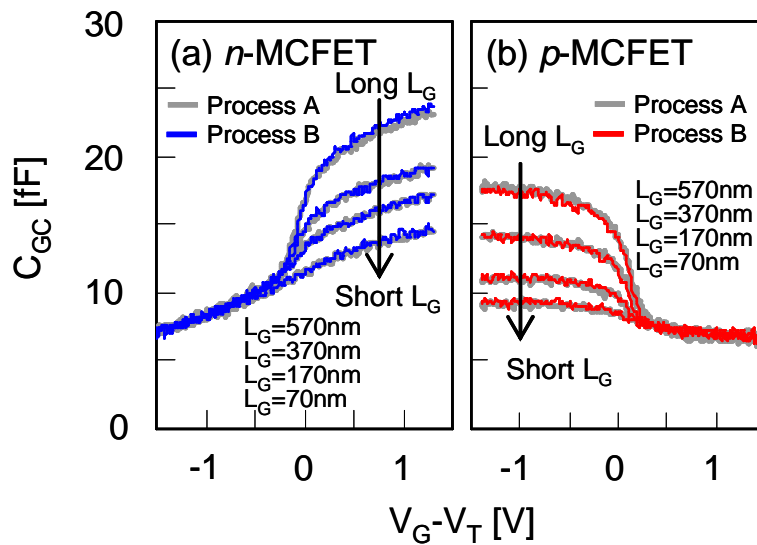


Figure 4.6  $C_{GC}$  characteristics with various  $L_G$  for (a) n- and (b) p-MCFETs.

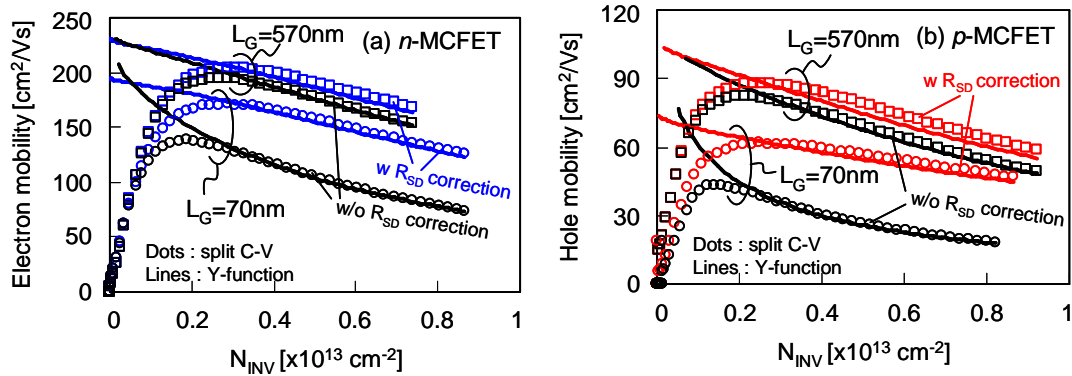


Figure 4.7  $\mu_{eff}$  of the MCFETs with different  $L_G$  of 570 and 70 nm.

Additionally,  $R_{SD}$  correction for  $\mu_{eff}$  extraction is necessary as the output conductance is strongly degraded by the parasitic resistance. Figure 4.7 (a) and (b) show the  $\mu_{eff}$  of  $n$ - and  $p$ -MCFETs of  $L_G=70$  and 570 nm with process B with and without RSD correction, respectively. The contribution of  $R_{SD}$  on the  $\mu_{eff}$  is obviously more prominent when the  $L_G$  is scaled, as the ratio of the  $R_{SD}$  to the total resistance increases. The  $\mu_{eff}$  calculated by Y-function method agrees well with the  $\mu_{eff}$  extracted by split C–V method in the region of high carrier density, confirming the correctness of the extracted  $\mu_{eff}$ . Process A results in slightly higher mobility values, as illustrated in Figure 4.7.

One can observe a degraded  $\mu_{eff}$  with smaller  $L_G$  for both  $n$ - and  $p$ -MCFETs even after  $R_{SD}$  correction. This fact implies the existence of another mechanism degrading the  $\mu_{eff}$  in the direction of channel. Figure 4.8 compares the low-field mobility  $\mu_0$  values in MCFETs with process B and C. A distinct degradation in the  $\mu_0$  with  $L_G$  scaling can be observed for both  $n$ - and  $p$ -MCFETs. Using the model proposed by Bidal *et al.*[4.5], a  $L_G$ -dependent limiting mobility,  $\mu_0(L_G)$ , can be postulated as

$$\frac{1}{\mu_0(L)} = \frac{1}{\mu_{max}} + \frac{\alpha_\mu}{L_G}, \quad (3.7)$$

where  $\mu_{max}$  and  $\alpha_\mu$  are the maximum mobility in long channel MCFETs and the mobility degradation factor, respectively. Using this model with the two fitting parameters,  $\mu_0$  at further scaled  $L_G$  can be predicted as shown in Figure 4.8. The mean  $\mu_{max}$  showed smaller values with process B compared to those with process A, suggesting the

influence of I/I.

On the other hand, the  $\alpha_\mu$  values were found to be similar in the range of 0.09~0.10 and 0.22~0.24 nm-Vs/cm<sup>2</sup> for *n*- and *p*-MCFETs, respectively. Therefore, the degraded  $\mu_{eff}$  in the low carrier density region can be considered to be originated by Coulomb scattering from the dopant atoms diffusion from S/D regions induced by I/I B-type process. Indeed the  $V_T$  roll-off characteristics on  $L_G$  shown in Figure 4.2 revealed slightly changed characteristics for both *n*- and *p*-MCFETs, supporting the possibility of an enhanced dopant diffusion. Moreover, the threading dislocation patterns observed in the TEM images shown in Figure 2.3 suggest an enhanced diffusion of dopant atoms, typically reported as 100 times higher, through the defects which reduces the abruptness of channel and S/D regions [4.6].

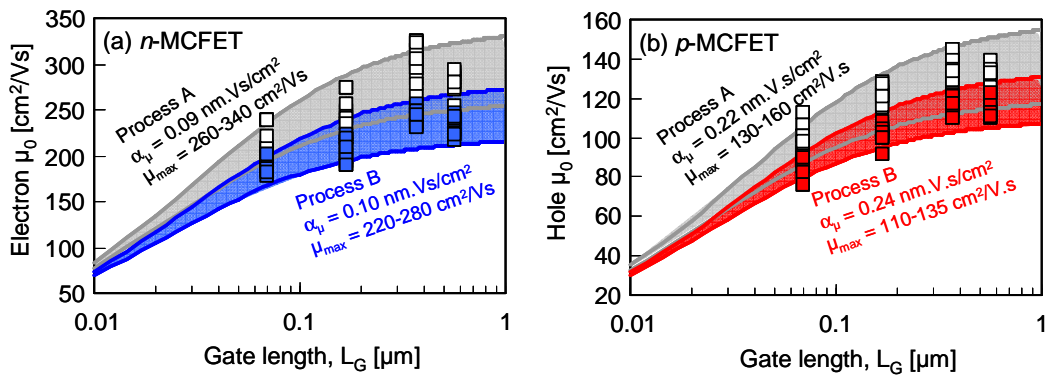


Figure 4.8 Estimated  $\mu_0$  on  $L_G$  scaling.

The values of the  $\alpha_\mu$  and  $\mu_{max}$  for MCFETs are summarized with reported values for planar FETs in Figure 4.9. The MCFETs with in situ SEG process show 2 and 3 times higher values in  $\alpha_\mu$  than the ballistic limit ( $\alpha_{\mu,bal}$ ), for *n*- and *p*-MCFETs, respectively. This deviation indicates the presence of Coulomb scattering in the channel which can also be inferred from the lower  $\mu_{max}$  value compared to other devices. The message is that, although in situ doped SEG process is useful for  $R_{SD}$  reduction, further process optimization in the dopant activation step is needed in order to suppress the diffusion of dopant atoms in to the channel.

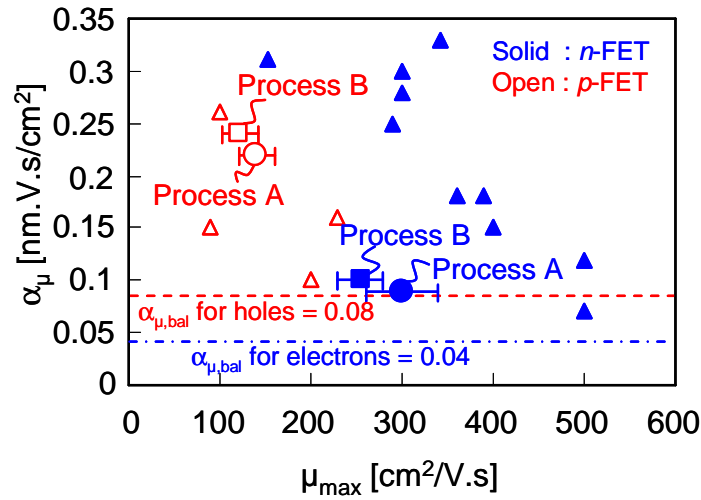


Figure 4.9 Summary of the extracted  $\alpha_{\mu}$  and  $\mu_{max}$  with reported values for planar FETs [4.5].

#### 4.3.4 Gate Length Scaling

Using the extracted  $\alpha_{\mu}$  and  $\mu_{max}$ , one can estimate the  $\mu_0$  value of the MCFETs with further scaled  $L_G$ . From Figure 4.8,  $\mu_0$  with  $L_G$  scaling can be estimated.  $\mu_0$  showed further reduction at scaled  $L_G$ , even considering the variability. The difference of  $\mu_0$  becomes smaller between the process A and B. This estimation indicates that the electrical influence of the diffused dopants from the source and drain region can be neglected as large portion of ballistic limited mobility dominates at these  $L_G$  regions.

Here we examine the global MCFETs down-scaling, including short-channel effects. The  $I_{OFF}$  behavior, when normalized by a common threshold voltage  $V_T$ , reflects the subthreshold properties such as DIBL and SS (not the  $V_T$  roll-off, however). Figure 4.10 shows the  $I_{ON}$ - $I_{OFF}$  characteristics of  $n$ - and  $p$ -MCFET with several  $L_G$  and  $W$ . The currents were normalized by the total channel surface  $W_{total}$  ( $W_{total} = W \times 5ch. + T_{Si} \times 6side-ch.$ ). When reducing  $L_G$  down to 70 nm,  $I_{OFF}$  increases progressively due to the enhanced DIBL, while the SS value remains constant at  $\sim 70$  mV/decade for nFET and  $\sim 75$  mV/decade for pFET. MCFETs with  $L_G$  smaller than 70 nm have degraded subthreshold properties without the expected  $I_{ON}$  enhancement. This kind of degradation can be suppressed by adding the lateral gates electrostatic control through  $W$  down-scaling [4.7]. Drive current gains of 14 % for nFET and 20 % for pFET were

observed when  $W$  was reduced from 350 nm down to 100 nm. We measured in the meantime an improved mobility  $\mu_0$  of 11 % and 18 % for nFET and pFET, respectively. This suggests that  $W$  down-scaling may reduce the  $L_G$  dependent mobility degradation. Additional investigation is needed in order to obtain a physical explanation of this phenomenon which is compatible with volume inversion.

Lastly, we present the scaled MCFETs characteristics with the process C. Figure 4.11 shows  $I_D-V_G$  and  $I_D-V_D$  characteristics associated to 50-nm- $L_G$  80-nm- $W$  nMCFET and 40-nm- $L_G$  and 70-nm- $W$  pMCFET. We obtained extremely high  $I_{ON}$ -currents of 4.1 mA/ $\mu\text{m}$  for nFET and a record 2.7 mA/ $\mu\text{m}$  for pFET at  $V_{DD} = 1.2$  V. These values are obtained thanks to the 3D configuration of the vertically stacked channels and the enhanced impact of lateral conduction with small gate width. However,  $I_{OFF}$  is still high due to the non-optimized threshold voltage on those samples. When normalized at  $V_{OFF}+V_{DD}$ , the  $I_{ON}$ -currents are 3.3 mA/ $\mu\text{m}$  for nFET and 2.0 mA/ $\mu\text{m}$  for pFET. When normalized by  $W_{total}$ , the  $I_{ON}$ -currents at  $V_{OFF}+V_{DD}$  for n- and p-FET are 538  $\mu\text{A}/\mu\text{m}$  and 396 $\mu\text{A}/\mu\text{m}$ , respectively. These normalized  $I_{ON}$  values are comparable to planar fully depleted – SOIFETs when using the same (unoptimized) gate stack [4.8].

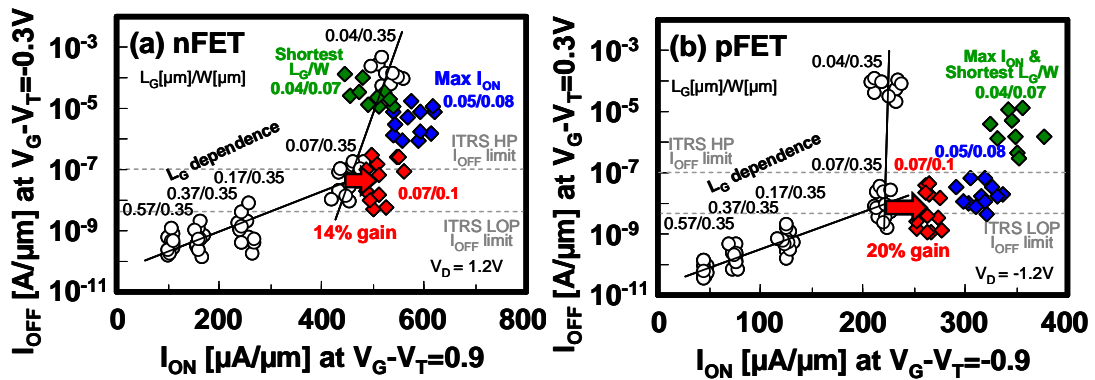


Figure 4.10  $I_{ON}$ - $I_{OFF}$  characteristics with several channel sizes for nMCFET (a) and pFET (b).

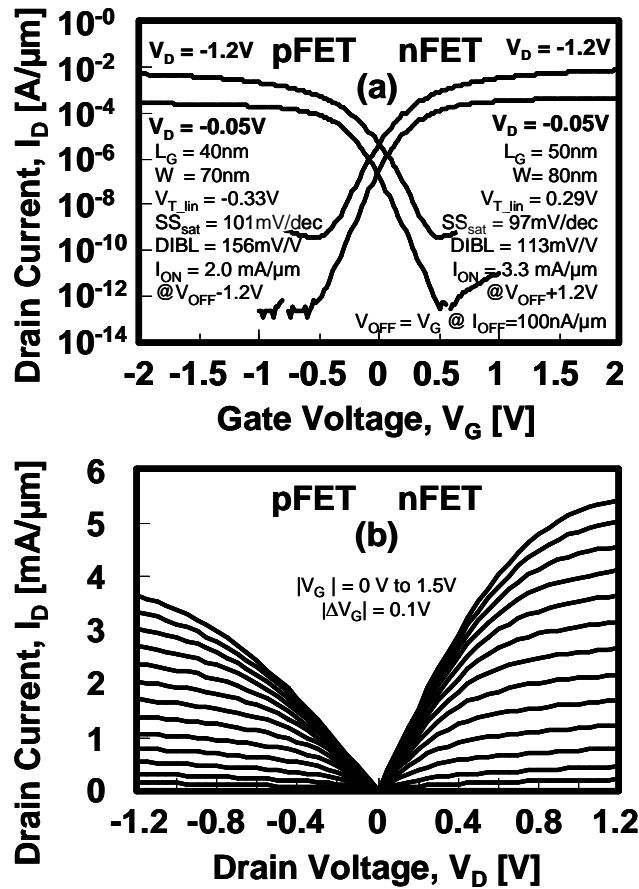


Figure 4.11  $I_D$ - $V_G$  (a) and  $I_D$ - $V_D$  (b) characteristics for the scaled MCFETs.

## 4.4 CONCLUSIONS

The influence of in situ doped SEG source and drain has been examined for vertically aligned MCFETs. A large enhancement, by a factor of 2 in the drive current, can be obtained when in situ doped SEG process is adopted. Detailed parameter extraction from the electrical measurements shows that the  $R_{SD}$  values can be reduced by 90 and 75% for  $n$ - and  $p$ -MCFETs, respectively, when in situ doped SEG is reinforced by adding ion implantation. On the other hand,  $V_T$  roll-off characteristics and the effective mobility behavior are slightly degraded, especially when ion implantation is combined to the SEG process. Mobility analysis has revealed an increase in the Coulomb scattering with  $L_G$  scaling, indicating the diffusion of dopant atoms from S/D regions. These results indicate an avenue to further improve the performance by optimizing the S/D activation annealing step.



## 4.5 REFERENCES

- [4.1] E. Bernard T. Ernst, B. Guillaumot, N. Vulliet, T. C. Lim, O. Rozeau. F. Danneville, P. Coronel, T. Skotnicki, S. Deleonibus, O. Faynot, First Internal Spacers' Introduction in Record High  $I_{ON}/I_{OFF}$  TiN/HfO<sub>2</sub> Gate Multichannel MOSFET Satisfying Both High-Performance and Low Standby Power Requirements, *IEEE Elec. Dev. Lett.*, 30 (2) (2009) pp. 148–151.
- [4.2] S.-Y. Lee, E.-J. Yoon, D.-S. Shin, S.-M. Kim, S.-D. Suk, M.-S. Kim, D.-W. Kim, D. Park, K. Kim and B.-il Ryu, Sub-25nm Single-Metal Gate CMOS Multi-Bridge-Channel MOSFET (MBCFET) for High Performance and Low Power Application, Tech. Dig. Symp. VLSI Tech. (2005) pp. 154–155.
- [4.3] K. Tachi, N. Vulliet, S. Barraud, B. Guillaumot, V. Maffini-Alvaro, C. Vizioz, C. Arvet, Y. Campidelli, P. Gautier, J.M. Hartmann, T. Skotnicki, S. Cristoloveanu, H. Iwai, O. Faynot and T. Ernst, "3D Source/Drain Doping Optimization in Multi-Channel MOSFET," 40th European Solid-State Device Research Conference (ESSDERC), pp. 368, 2010, Spain.
- [4.4] C. Dupre, P. F. Fazzini, T. Ernst, F. Cristiano, A. Claverie, J.-M. Hartmann, F. Andrieu, O. Faynot, P. Rivallin, J.-P. Barnes, G. Ghibaudo, S. Cristoloveanu and S. Deleonibus, "Carrier Mobility degradation due to High Dose Implantation Impact in Ultra-Thin Unstrained and Strained Silicon On Insulator Films", *Journal of Applied Physics*, vol. 102, p. 104505, 2007.
- [4.5] G. Bidal, D. Fleury, G. Ghibaudo, F. Boeuf, and T. Skotnicki, Guidelines for MOSFET Device Optimization accounting for L-dependent Mobility Degradation, *IEEE Silicon Nanoelectronics Workshop*, (2009) pp. 5–6.
- [4.6] K. Inoue, F. Yano, A. Nishida, T. Tsunomura, T. Toyama, Y. Nagai and M. Hasegawa, Three dimensional characterization of dopant distribution in polycrystalline silicon by laser-assisted atom probe, *Appl. Phys. Lett.* 93 (2008) 133507.
- [4.7] E. Bernard *et al.*, "Novel integration process and performances analysis of Low Standby Power (LSTP) 3D multi-channel CMOSFET (MCFET) on SOI with

metal / high-K gate stack," in *VLSI Symp. Tech. Dig.*, 2008, pp. 16-17, 17–19.

- [4.8] F. Andrieu *et al.*, "Comparative scalability of PVD and CVD TiN on HfO<sub>2</sub> as a metal gate stack for FDSOI CMOSFET down to 25 nm gate length and width," in *IEDM Tech. Dig.*, 2006, pp. 641–644.



# **CHAPTER 5**

## ***CARRIER TRANSPORT PROPERTIES OF VERTICALLY- STACKED NANOWIRE MOSFETS***

# CHAPTER 5 CONTENTS

## **5 Carrier Transport Properties of Vertically-Stacked Nanowire MOSFETs**

- 5.1 Introduction
- 5.2 Electrical Characteristics
  - 5.2.1  $I$ - $V$  Characteristics
  - 5.2.2 Transport Limiting Velocity
  - 5.2.3 Carrier Mobility Evaluation
  - 5.2.4 Mobility Limiting Factors
- 5.3 Impact on Plasma Etching of SiGe Sacrificial layers
  - 5.3.1 One-Levelled Nanowire MOSFET Fabrication
  - 5.3.2 Carrier Mobility Evaluation
- 5.4 Effect of Hydrogen Annealing
  - 5.4.1 Cross-Sectional Shape
  - 5.4.2 Carrier Mobility Evaluation
  - 5.4.3 Interface Trap density
- 5.5 SiGe Nanowire MOSFET
  - 5.5.1 Device Fabrication Process
  - 5.5.2  $I$ - $V$  Characteristics
  - 5.5.3 Carrier Mobility Evaluation

5.5.4 Noise Measurement

5.6 Conclusions

5.7 References

## **5.1 INTRODUCTION**

To achieve devices with both high speed and low power consumption for future LSI applications, GAA SNWTs are one of the promising candidates because of their strong short-channel effect immunity. Moreover, to increase the drive current per unit area with the higher integration density, vertical stacking of NWs enables the use more available silicon surface per device as shown in Chapter 1. Recently, short channel GAA-SNWTs have been successfully fabricated with diameter of less than 10 nm using several top-down CMOS compatible processes; they successfully suppress the short-channel effects [5.1-5.3]. On the other hand, transport property degradation in SNWTs was also reported by several groups [5.4-5.6]. However, the mobility behavior when the width is reduced has been remained unclear. Carrier transport in SNW is commonly discussed in terms of two main mechanisms; one is one-dimension (1-D) transport model, and the other is a facet-dominated transport model. The former can be adapted to sub-10 nm diameter, and the latter to larger one. From the fabrication process viewpoints, (dispersion, yield rate), a larger diameter is production friendly, provided that the short-channel effects under aggressively scaled gate length are suppressed.

In this chapter, carrier transport limiting components for vertically-stacked nanowire MOSFETs will be discussed to obtain better performance with suppressing short channel effects.

## **5.2 ELECTRICAL CHARACTERISTICS**

### **5.2.1 $I$ - $V$ Characteristics**

In this subsection, we discuss basic electrical characteristics of vertically-stacked SNWTs by comparing the scaled planar CMOS [5.7] and the reported SNWTs [5.1-5.3]. Figures 5.1–5.4 detail the electrical characteristics of our vertically-stacked SNWTs with 15-nm- $W_{Top}$ . Its cross-sectional TEM image is shown in Figure 2.10 (b). Mid-gap metal gates lead to normally-off MOSFETs with a centered threshold voltage as shown in Figure 5.1. Nearly ideal subthreshold slope and very low DIBL can be kept down to

$L_{eff}$  of 32 nm for nSNWTs, while these characteristics are degraded in pMOSFETs. This kind of pSNWTs degradation has been observed in several experimental data [5.2, 5.4]. As a result,  $I_{OFF}$  for pSNWT increases in sub-50 nm of  $L_{eff}$  as shown in Figure 5.4. On the other hand, there is no degradation of  $I_{OFF}$  for nSNWTs.

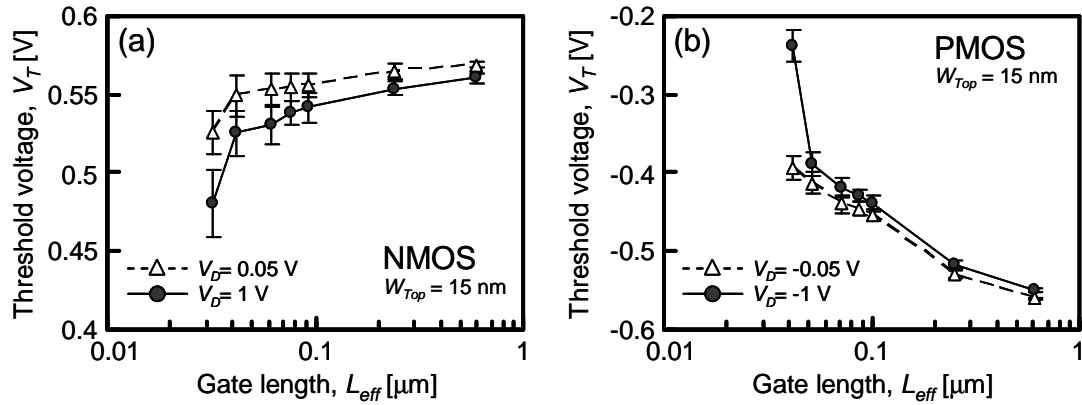


Figure 5.1 Threshold voltage as a function of effective gate length for vertically-stacked silicon nanowire n- and p-MOSFET with 15-nm- $W_{Top}$ .

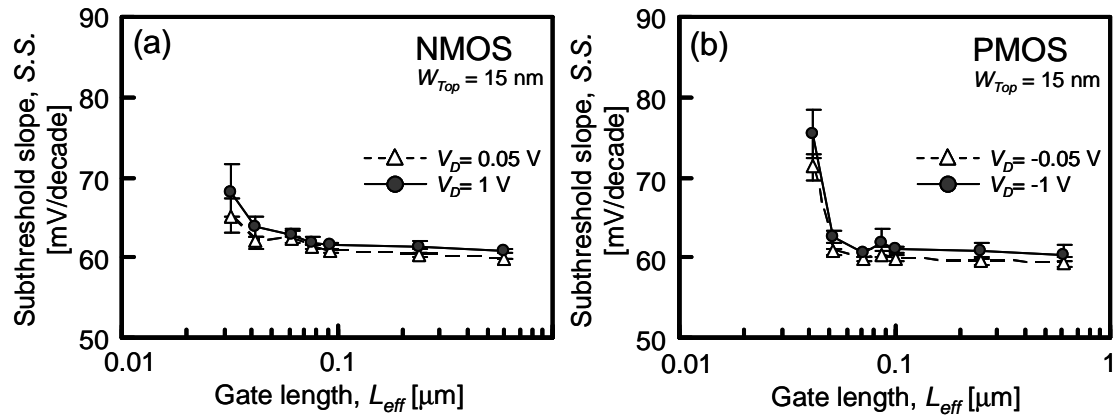


Figure 5.2 Subthreshold slope as a function of effective gate length for vertically-stacked silicon nanowire n- and p-MOSFET with 15-nm- $W_{Top}$ .



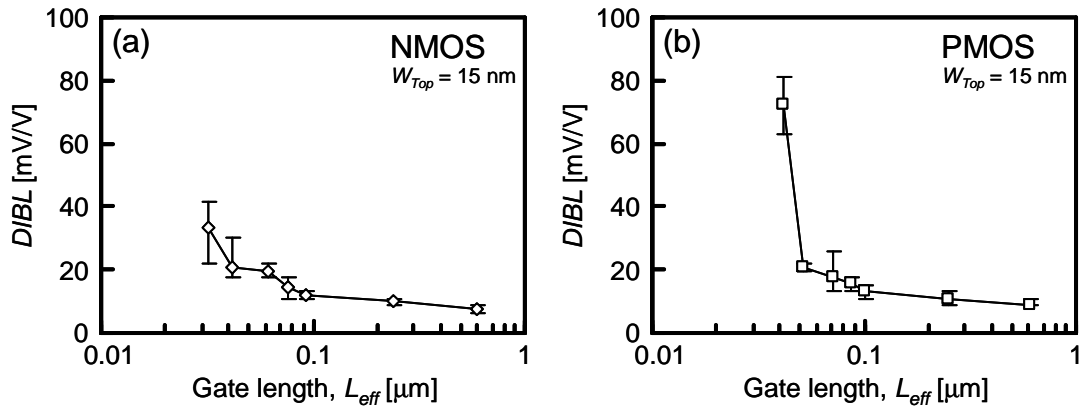


Figure 5.3 DIBL as a function of effective gate length for vertically-stacked silicon nanowire n- and p-MOSFET with 15-nm- $W_{Top}$ .

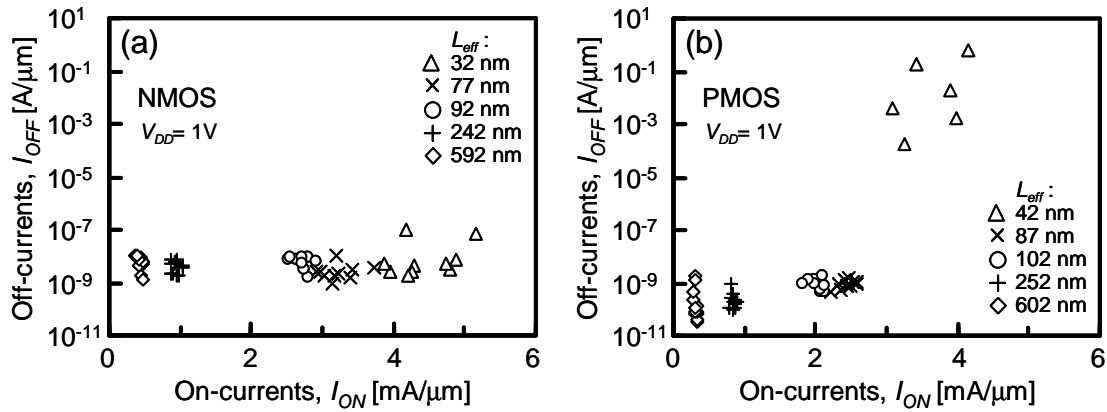


Figure 5.4  $I_{ON}$ - $I_{OFF}$  characteristics of vertically-stacked silicon nanowire n- and p-MOSFET with 15-nm- $W_{Top}$ .

The measured  $I_D$ - $V_D$  (Figure 5.6) and  $I_D$ - $V_G$  (Figure 5.7) characteristics for our best devices of vertically-stacked 15 nm width SNWTs with 32 nm of  $L_{eff}$  for nMOSFET and 42 nm for pMOSFET show well-behaved characteristics.  $I_D$ - $V_G$  curves exhibit an excellent subthreshold slope (64 mV/dec for nMOSFET and 74 mV/dec for pMOSFET) and very low DIBL (32mV/V for nMOSFET and 62 mV/V for pMOSFET). On-currents  $I_{ON}$  (normalized by total circumference) of 840  $\mu\text{A}/\mu\text{m}$  and 540  $\mu\text{A}/\mu\text{m}$  with  $I_{OFF}$  of 4 nA/ $\mu\text{m}$  and 96 nA/ $\mu\text{m}$  are obtained for n- and pMOSFET, respectively. When the currents are normalized by top-view width, the  $I_{ON}$  is 7.2 mA/ $\mu\text{m}$  for nMOSFET and 4.7 mA/ $\mu\text{m}$  for pMOSFET. The obtained device performances are

summarized in Table 5.1. Figure 5.7 shows the comparison of *DIBL* from this work and other published results. It is clear that our vertically-stacked SNWTs show excellent short-channel effects immunity compared to the planar bulk High Performance (HP) MOSFETs as well as that of the other 1-level GAA SNWTs. Figure 5.8 shows the comparisons of  $I_{ON}$  from this work and the other published results. It is clear that the  $I_{ON}$  are higher than the others when the currents are normalized by top-view width. This is due to the vertically stacked structure, showing the interest of 3-D devices to increase current density for a given layout. When the currents are normalized by the total effective surface of channels as shown in Figure 5.8 (b), we can consider the carrier transport properties. Although our results are smaller current levels due to the longer gate length, they are on  $1/L$  line. Figure 5.9 shows drain currents as a function of  $L_{eff}$ . Gate length scaling is still effective down to sub-50 nm  $L_{eff}$ . Further enhancement of the currents can be expected if the gate length is diminished below 30 nm.

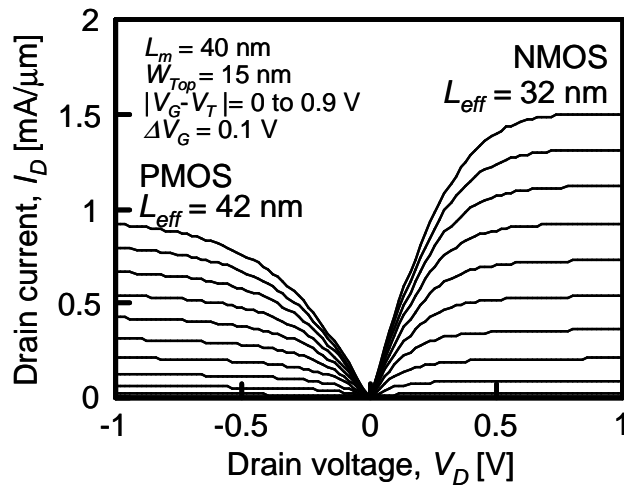


Figure 5.5  $I_D$ - $V_D$  characteristics of vertically-stacked silicon nanowire *n*- and *p*-MOSFET with sub-50-nm- $L_{eff}$  and 15-nm- $W_{Top}$ .

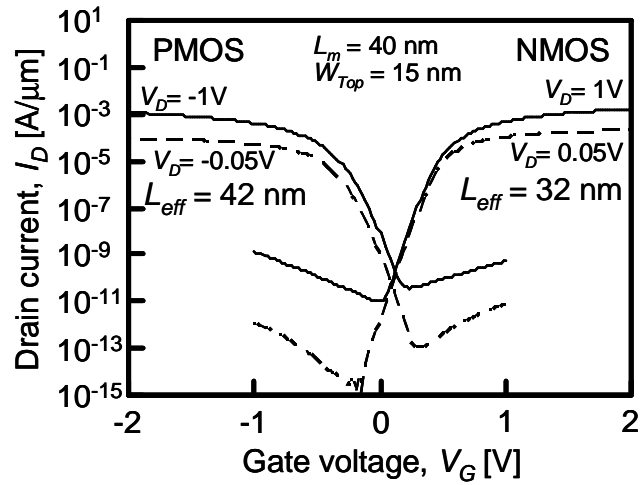


Figure 5.6  $I_D$ - $V_G$  characteristics of vertically-stacked silicon nanowire  $n$ - and  $p$ -MOSFET with sub-50-nm- $L_{eff}$  and 15-nm- $W_{Top}$ .

Table 5.1 Device parameters for vertically-stacked silicon nanowire  $n$ - and  $p$ -MOSFET with sub-50-nm- $L_{eff}$  and 15-nm- $W_{Top}$ . The on-currents  $I_{ON}$  are extracted at  $V_G - V_T = 0.7$  and  $-0.7$  V for  $n$ - and  $p$ -MOSFETs, respectively. The off-currents  $I_{OFF}$  are extracted at  $V_G - V_T = -0.3$  and  $0.3$  V for  $n$ - and  $p$ -MOSFETs, respectively.

	NMOS	PMOS
NW cross-section	3-level-stacking	
Max $W_{NW}/H_{NW}$	15nm/14nm	
$L_m$ [nm]	40	
$L_{eff}$ [nm]	32	42
$EOT$ [nm]	1.7	1.7
$V_{DD}$ [V]	1	1
$I_{ON}/W_{eff}$ [mA/mm]	840	540
$I_{ON}/W_{Top}$ [mA/mm]	7.2	4.7
$I_{ON}/I_{OFF}$	$\sim 2 \times 10^5$	$\sim 6 \times 10^3$
$V_{Tsat}$ [V]	0.50	-0.37
$DIBL$ [mV/V]	32	63
$S.S._{sat}$ [mV/dec]	64	73

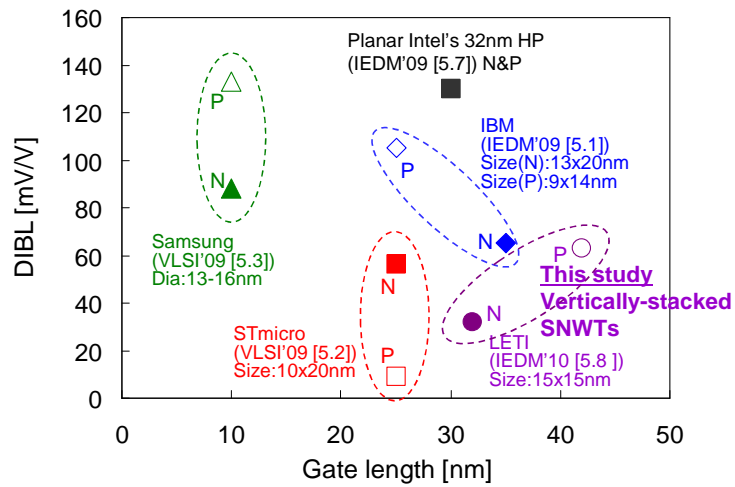


Figure 5.7 DIBL comparison of GAA SNWTs from this work and other published results.

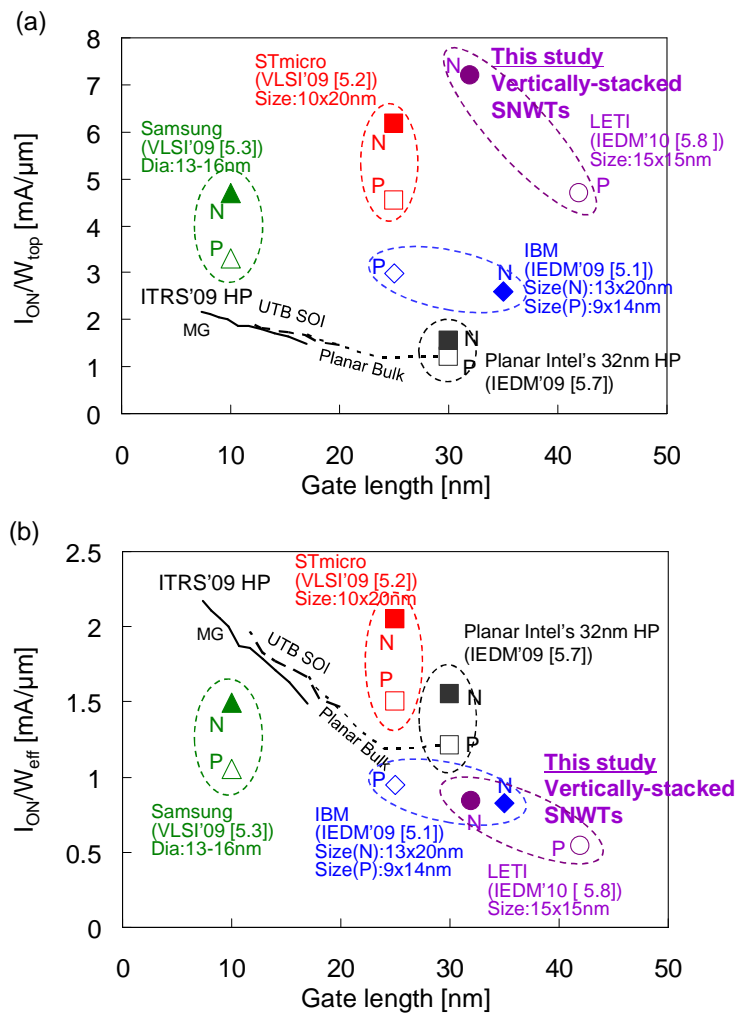


Figure 5.8  $I_{ON}$  comparison of GAA SNWTs from this work and other published results. (a)  $I_{ON}$  are normalized by top-view width of nanowires  $W_{Top}$ , (b)  $I_{ON}$  are normalized by total effective surface of nanowires  $W_{eff}$ .

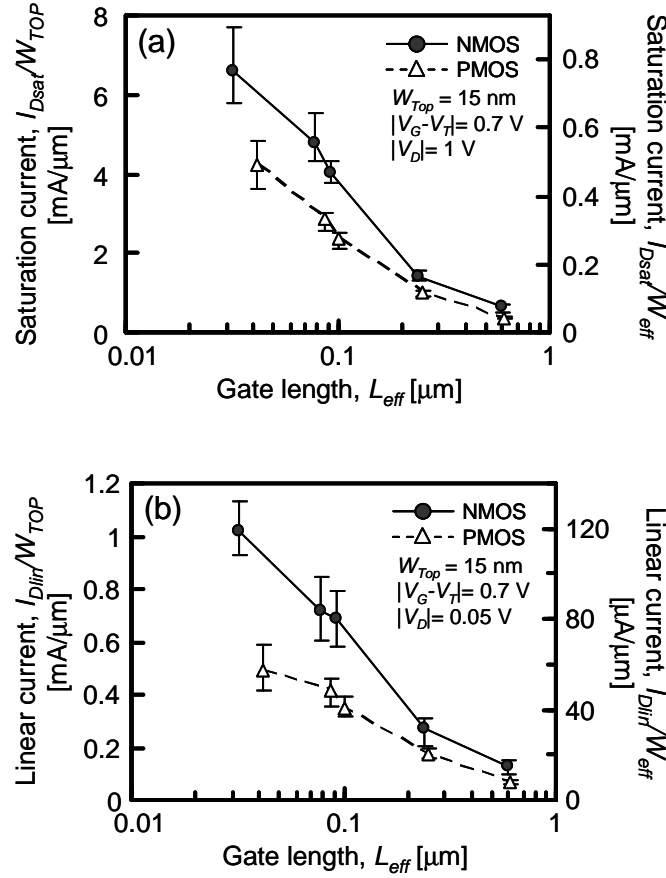


Figure 5.9 Saturation current density (a) and linear current density (b) as a function of effective gate length for vertically-stacked silicon nanowire n- and p-MOSFET with 15-nm- $W_{Top}$ . The currents are normalized by top-view width  $W_{Top}$  (left y-axis) and effective total width  $W_{eff}$  (right y-axis).

## 5.2.2 Transport Limiting Velocity

In this subsection, we discuss carrier transport limiting mechanisms in the short-channel vertically-stacked SNWTs in detail.

In thermal equilibrium conditions, carriers can be injected from the source reservoir to the channel with a thermal velocity. The part ( $r$ ) of injected carriers can be elastically backscattered towards the source, whereas the  $(1-r)$  part propagates towards the drain. Therefore, the effective source injection velocity ( $v_{inj}$ ) is smaller than thermal velocity. In the linear regime (small lateral field), the injection velocity, resulting from forwarded and backscattered fluxes and given by the ratio  $(1-r)/(1+r)$ , will be the only limitation of the total drain current, this being called the quasi-ballistic transport as

described in Subsection 1.2.3. However for high lateral electric field, saturation velocity  $v_{sat}$  resulting from optical phonon-electron interactions may constitute a stronger limitation than injection velocity. Therefore, whatever the conduction regime (linear or on-state), there exists a certain limiting velocity that can be expressed as:  $v_{lim} = \min(v_{sat}, v_{inj})$ . This simple reasoning gives ground for a unification of all transport mechanisms, within one universal and continuous drain current model that is a kind of the Matthiessen's rule [5.9]. Since  $v_{sat}$  and  $v_{inj}$  have very close values, it is difficult to identify the true limiting mechanism. Fortunately, the temperature dependences of  $v_{sat}$  and  $v_{inj}$  are opposed as shown in Figures 5.10 and 5.11, and thus they can reveal the limiting mechanism.

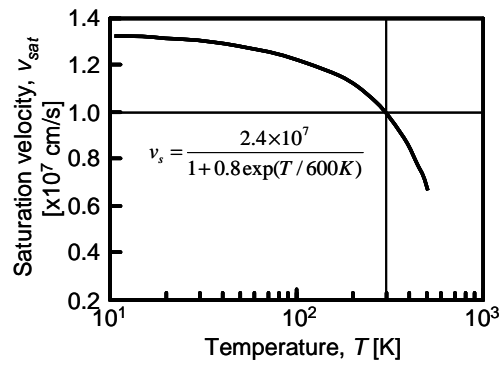


Figure 5.10 Temperature dependence of saturated electron drift velocity [5.10].

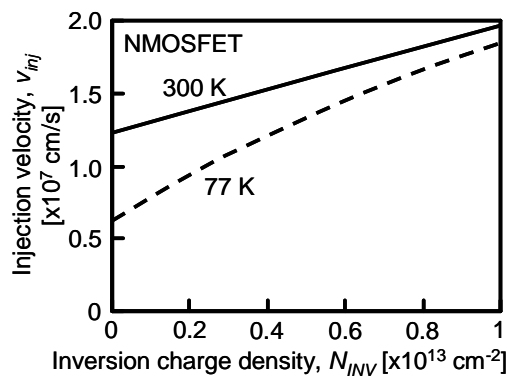


Figure 5.11 Injection velocity of a nMOSFET on (100) plane as a function of inversion charge density at 300 and 77 K. [5.11].

Thanks to the temperature dependence of both saturation velocity and injection velocity, the nature of the transport can be evidenced by plotting the temperature

dependence of the limiting velocity. The temperature dependence of  $I_D$ - $V_G$  curves for the vertically-stacked nSNWT with  $L_{eff}$  of 32 nm is shown in Figure 5.12. The temperature range for measurements varies from 5 to 300 K. The threshold voltage decreases with temperature, while the sub-threshold slope increases. These changes in  $V_T$  and  $SS$  with temperature are mainly due to band gap changes and are consistent with the theory. Figure 5.13 shows temperature dependence of  $v_{lim}$ . It is clear that the vertically-stacked nSNWTs are almost exclusively  $v_{sat}$  limited. This result implies a high backscattering rate and the presence of strong scattering components.

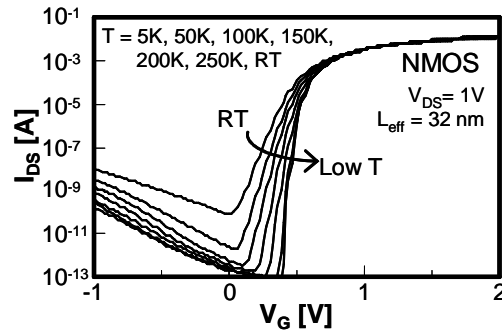


Figure 5.12 Temperature dependence of  $I_D$ - $V_G$  characteristics for vertically-stacked SNWTs.

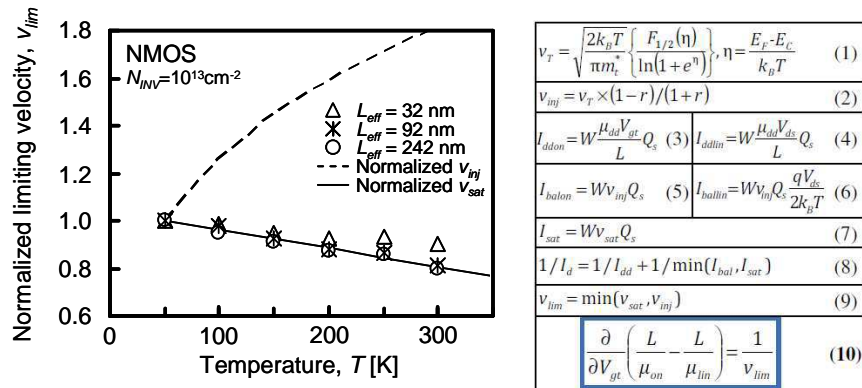


Figure 5.13 Temperature dependence of extracted limiting velocity  $v_{lim}$ . Theoretical dependence of saturation velocity  $v_{sat}$  from [5.13] and injection velocity  $v_{inj}$  from [5.14] are given. The  $v_{lim}$  were extracted by the equations in the right table [5.9], where  $F_{1/2}$  is Fermi-Dirac integral.

### **5.2.3 Carrier Mobility Evaluation**

The carrier scattering components can be identified by analyzing the effective mobility behaviors in long-channel MOSFETs as explained in Chapter 3. Before discussing the experimental results, we consider possible factors of mobility limitations in silicon nanowire. Figure 5.14 shows possible mobility limiting factors intrinsically for SNWTs. In general, the carrier mobility in two-dimensional (2-D) transport for planar MOSFET strongly depends on its surface orientations due to the effective mass difference as shown in Chapter 3. The electrons mobility on (100)-surface is about two times as high as that on (110)-surface, while the holes mobility behavior is opposite. The rectangular nanowires directed to  $\langle 110 \rangle$  have two oriented surfaces, that is, (100)-surface for the top and bottom channels and (110)-surface for the side channels. In that case, as shrinking the wire width, that is, the (100)-surface, it is expected that the electron mobility decreases, while the hole mobility increase as shown in Figures 5.14 (b) and 5.15. Moreover, in silicon nanowire with less than 10 nm in diameter, carrier transport will become one-dimension (1-D). In that case, it is expected that carrier limiting components show different behaviors from two-dimensional transport as shown in Figure 5.14 (c). In addition, as nanowire width decreases, transport property at the corners for rectangular shaped nanowires becomes dominant. The carriers at the corners could possibly behave like one-dimensional transport depending radius of curvature as shown in Figure 5.14 (d) and 5.16. The experimentally extracted mobility is represented as an outcome of all or parts of these effects. Moreover the outcome is more complicated when extrinsic degradation factors are added.

In this study, mobility limiting components in the vertically-stacked SNWTs will be investigated in detail by observing temperature dependence and inversion charge density dependence on the mobility.



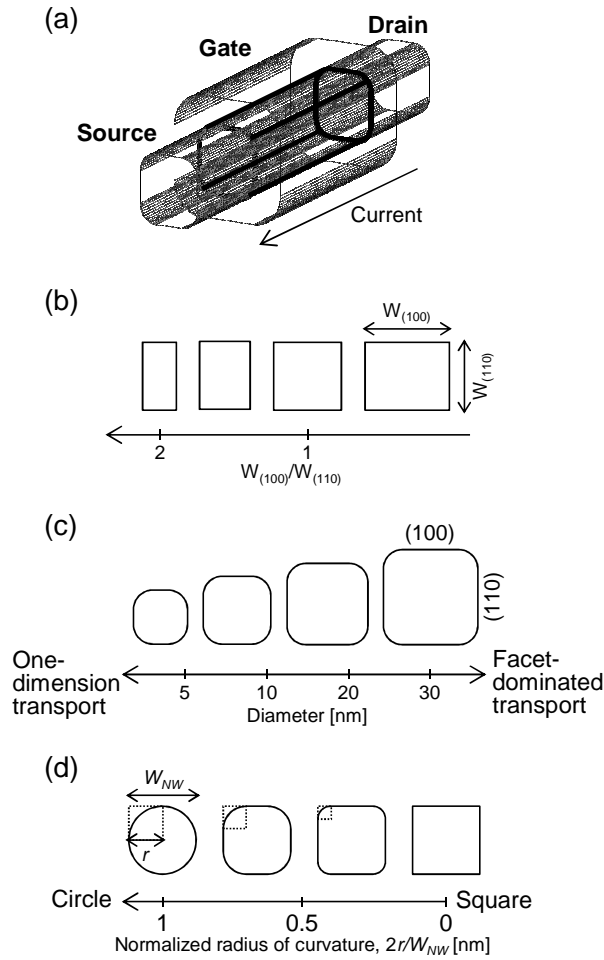


Figure 5.14 Schematic image of nanowire MOSFET (a) and its cross-section (b). Varying ratio of (100) width to (110) width, (c) varying size, (d) varying radius of curvature at the corners.

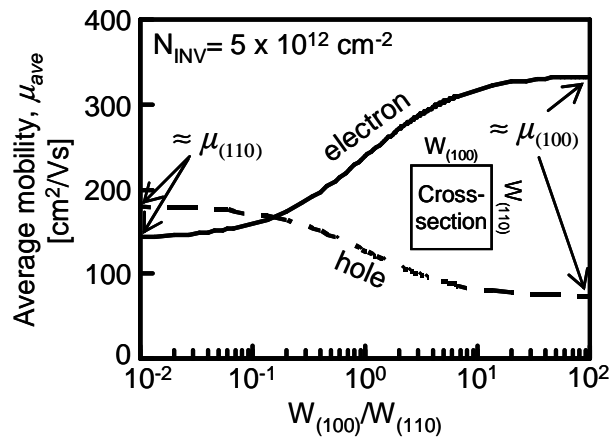


Figure 5.15 Rectangular-shaped nanowire mobility as a function of  $W_{(100)}$ -to-  $W_{(110)}$  ratio. The average mobility is  $\mu_{ave} = (\mu_{(100)}W_{(100)} + \mu_{(110)}W_{(110)}) / (W_{(100)} + W_{(110)})$ , where  $\mu_{(100)}$  and  $\mu_{(110)}$  are the mobilities on (100) and (110) surfaces, respectively.

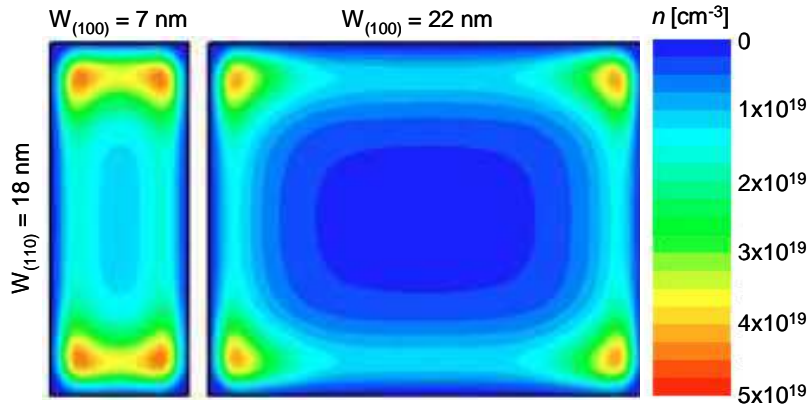


Figure 5.16 Calculated profiles of electron density across the cross section of silicon nanowires with  $W_{(110)}=18$  nm, and  $W_{(100)}= 7$  and 22 nm [5.15].

Figures 5.17 (a) show effective mobility for electrons as a function of inversion charge density at different temperatures in the vertically-stacked SNWTs. The size of the nanowire used is 15 nm of  $W_{Top}$  as shown in Figure 2.10 (b). As a reference, the mobilities of fully-depleted (FD) SOI FET are also shown in Figure 5.17 (b). The FDSOI has a 8 nm channel thickness and the same gate stacks as the vertically-stacked SNWTs. It is clear that the electron mobility dependence on temperature for the vertically-stacked SNWT is much lower than that for FDSOI. In addition, the electron mobility dependence on temperature is also much lower than that for hole (Figure 5.18).

In general, mobility in MOSFETs is limited by three scattering components; coulomb, phonon, and surface roughness as shown in Figure 5.19 (b). The coulomb-limited mobility ( $\mu_{cb}$ ) and phonon-limited mobility ( $\mu_{ph}$ ) have negative and positive contribution at low temperature, respectively. Meanwhile, the surface roughness-limited mobility ( $\mu_{sr}$ ) does not depend on temperature. At low temperature, mobility is limited by only the coulomb scattering only at low  $N_{INV}$  and only by the surface-roughness scattering only at high  $N_{INV}$ . Figure 5.19 (a) shows effective mobility for electron and hole at high  $N_{INV}$  as a function of temperature. The  $\mu_{sr}$  values can be extracted by extrapolating the mobility at 10 K. The  $\mu_{sr}$  values for the vertically-stacked SNWT are much smaller than that for the FDSOI. Phonon-limited mobility can be extracted by using the Matthiessen's rule and the extracted  $\mu_{sr}$ . Figure 5.21 shows

comparison of mobility limiting components at high  $N_{INV}$ . It is clear that electron effective mobility is strongly limited by surface roughness scattering, while hole mobility is limited by both surface roughness and phonon scattering at high  $N_{INV}$ . On the other hand, at low  $N_{INV}$ , the electron mobility is degraded at lower temperatures, while the hole mobility increases as shown in Figure 5.22. This means that electron mobility at low  $N_{INV}$  is limited by coulomb scattering, while phonon scattering is dominant for holes. This may be because that the effect of coulomb scattering is hidden under the strong phonon limitation.

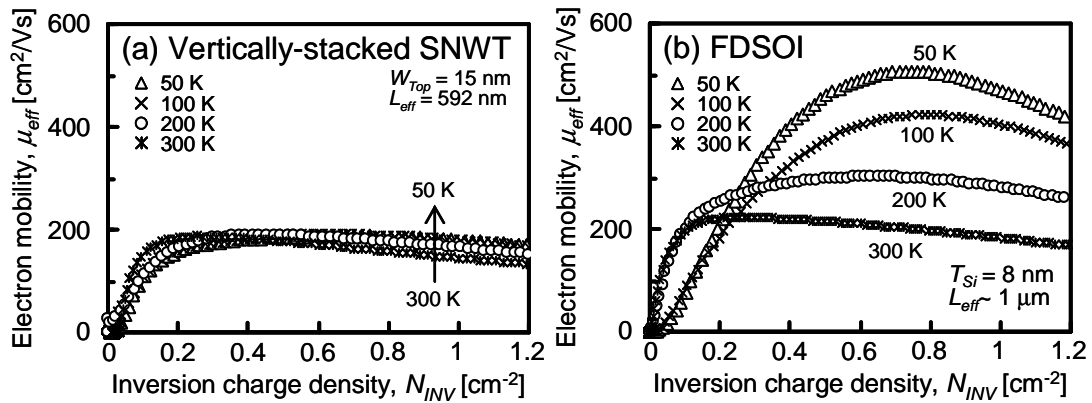


Figure 5.17 Temperature dependence of effective electron mobility in vertically-stacked silicon nanowire FET (a) and in fully-depleted SOI-FET (b).

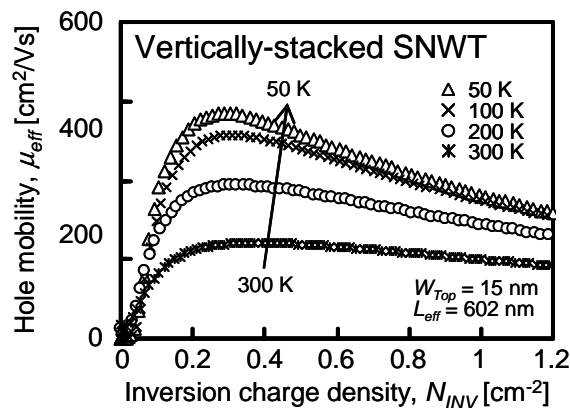


Figure 5.18 Temperature dependence of effective hole mobility in vertically-stacked silicon nanowire FET.

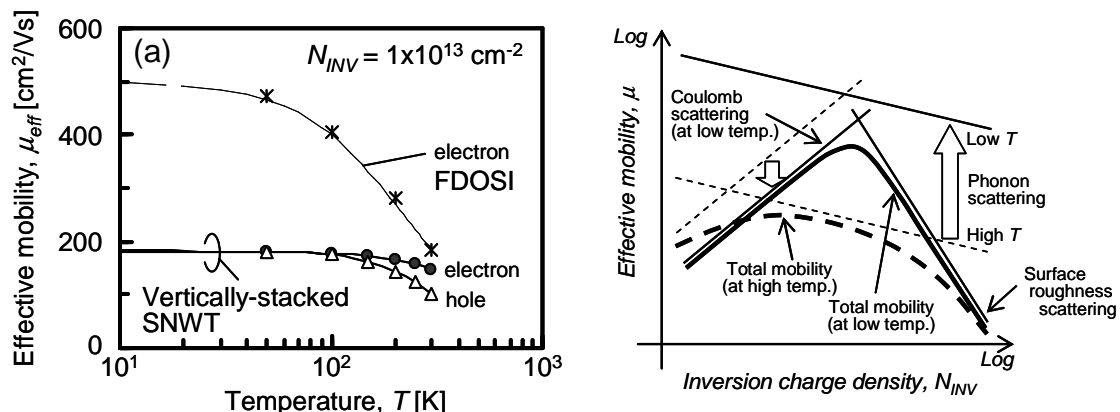


Figure 5.19 (a) Temperature dependence of effective mobility at high inversion charge density ( $N_{INV} = 10^{13}$  cm<sup>-2</sup>). (b) Schematic diagram of mobility limiting components at low temperature.

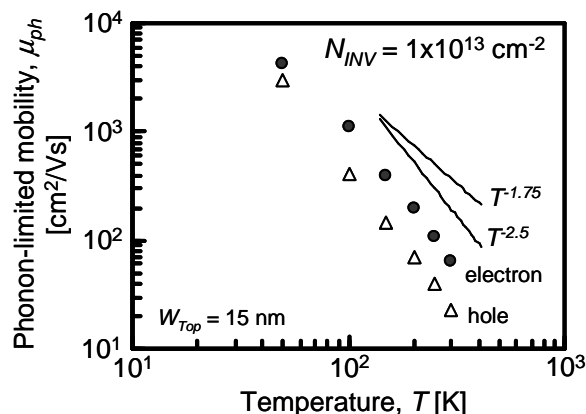


Figure 5.20 Temperature dependence of phonon-limited mobility at high inversion charge density ( $N_{INV} = 10^{13}$  cm<sup>-2</sup>) for vertically-stacked silicon nanowire MOSFETs.

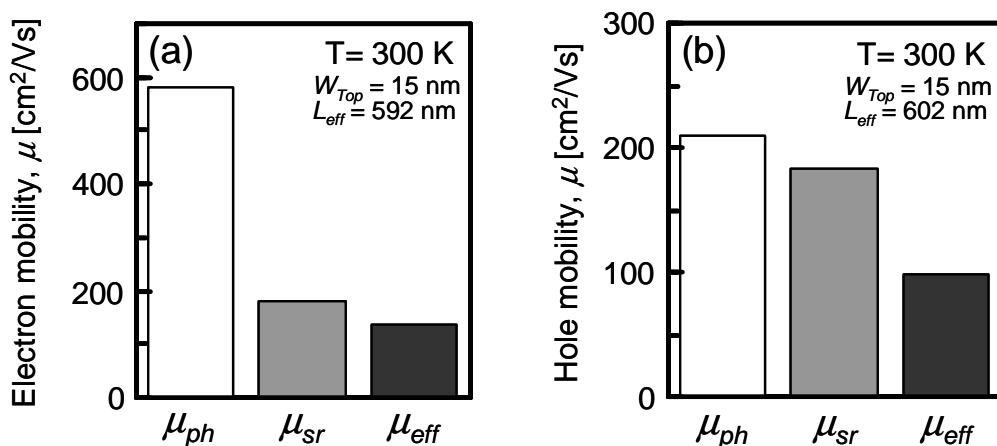


Figure 5.21 Mobility limiting components for electron (a) and hole for vertically-stacked silicon nanowire MOSFETs at 300 K.

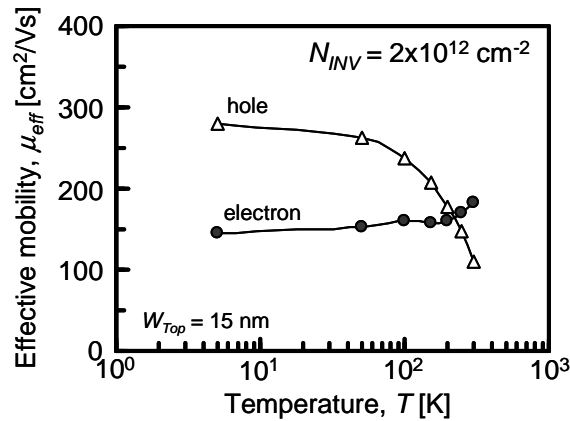


Figure 5.22 Temperature dependence of effective mobility at low inversion charge density ( $N_{\text{INV}}=2 \times 10^{12} \text{ cm}^{-2}$ ).

### 5.3 IMPACT ON PLASMA ETCHING OF SILICON-GERMANIUM SACRIFICIAL LAYERS

In the mobility analysis presented above, we founded that effective mobility for the vertically-stacked SNWTs is strongly degraded due to surface roughness. The surface roughness reduction could be one of the key factors to obtain high performance. One of the possible reasons of degraded surface-roughness limited mobility is some NW surface damage due to the selective SiGe dry and isotropic etching. According to results reported by C. Dupre *et. al.* [5.16], silicon surface is roughened by using an isotropic plasma etching, similar to the one used for our device fabrication process. Figures 5.23 and 5.24 show the impacts of the isotropic plasma etching. Atomic force microscopy (AFM) was used to evaluate the damaged Si surfaces. As a result, the Root Mean Square (RMS) value was increased from 0.15 to 1.4 nm in 46 second. In this section, the impact on isotropic plasma etching of SiGe sacrificial layers to the effective mobility for the vertically-stacked SNWTs is investigated. To compare between the devices with and without the plasma etching, one-level SNWTs were fabricated without the use of SiGe sacrificial layers.

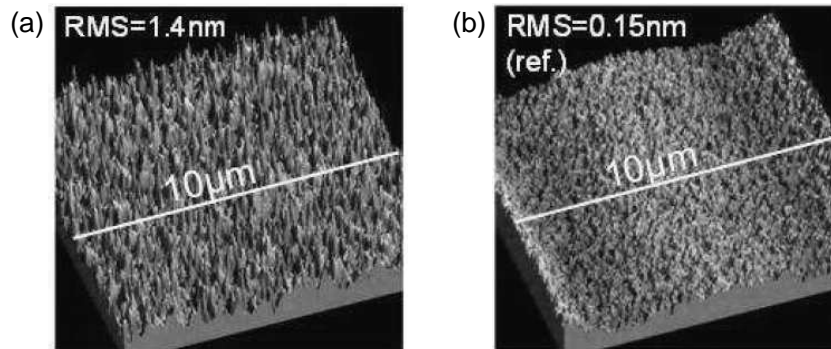


Figure 5.23 Atomic force microscopy images of silicon surface after isotropic SiGe dry etching (a) and the reference sample without the etching (b).

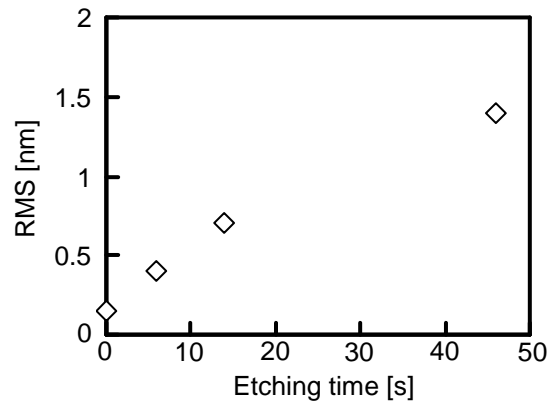


Figure 5.24 Root mean square (RMS) values as a function of isotropic SiGe dry etching.

### 5.3.1 One-Levelled Nanowire MOSFET Fabrication

In order to investigate the impact of the selective SiGe isotropic etching, one-level SNWTs as references were fabricated without SiGe epitaxy and its etching process. The fabrication process is shown in Figure 5.25. First, the nanowires were patterned by e-beam lithography and anisotropic etching of SOI. Then the BOX was isotropically etched by wet etching to obtain the suspended nanowires. The NW diameter is controllable down to 5 nm by self-limited oxidation [5.17] while keeping regularly arrayed NWs as shown in Figure 5.26 (a). After the dimension control of the nanowires, the same process steps as the vertically-stacked SNWTs were used (*e.g.* gate depositions).

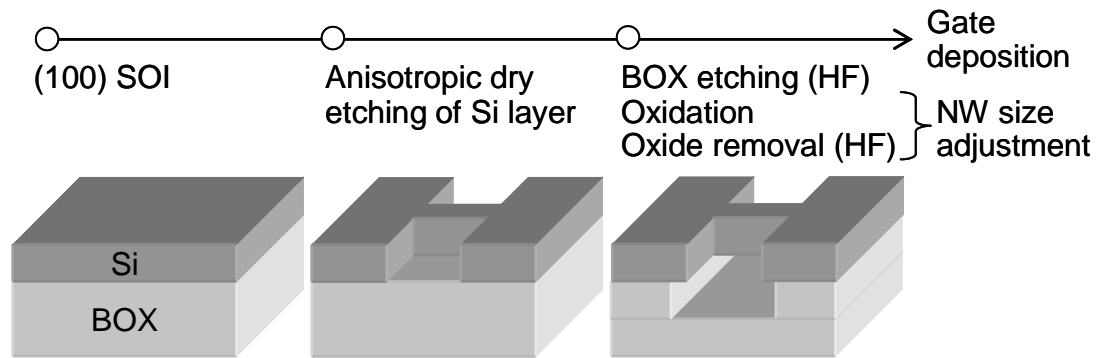


Figure 5.25 Brief process flow of 1-level silicon nanowire MOSFET.

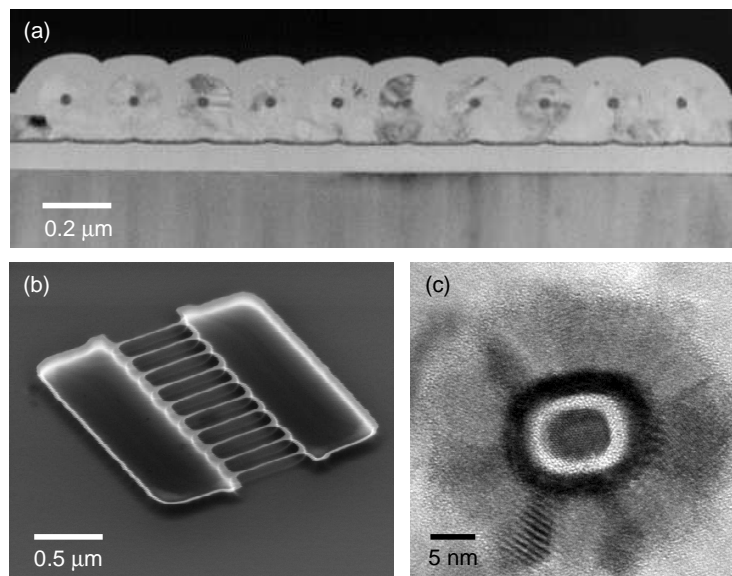


Figure 5.26 Gate-all-around 1-level silicon nanowire MOSFETs fabricated without SiGe epitaxy and selective etching.

### 5.3.2 Carrier Mobility Evaluation

Figure 5.27 shows effective mobility comparisons between the vertically-stacked and the 1-level SNWTs with 15 nm of  $W_{NW}$  at 300 K and 5 K. The 1-level SNWTs show higher mobility than the vertically-stacked ones at both 300 K and 5 K. Figure 5.28 shows the temperature dependence of the effective mobility at high  $N_{INV}$ . It is clear that the mobility of the 1-level SNWTs is largely improved at low temperature. This is because the mobility is strongly limited by phonon scattering at 300 K. In other words, the surface roughness scattering is not a dominant limitation for the 1-level SNWTs.

Figure 5.29 shows the extracted mobility limiting components. The  $\mu_{sr}$  is largely degraded in the vertically-stacked SNWTs, resulting lower total mobility. The use of SiGe sacrificial layers causes the mobility degradation due to the roughened silicon surface during the SiGe etching. Moreover, in the case of the 1-level SNWTs, coulomb scattering is less dominant as shown in Figure 5.30. The reason why stronger coulomb scattering is higher in the vertically-stacked SNWTs may be the degraded interface quality with high- $\kappa$  because of the use of SiGe sacrificial layers. Additional surface treatments thus are needed to recover the damaged surface.

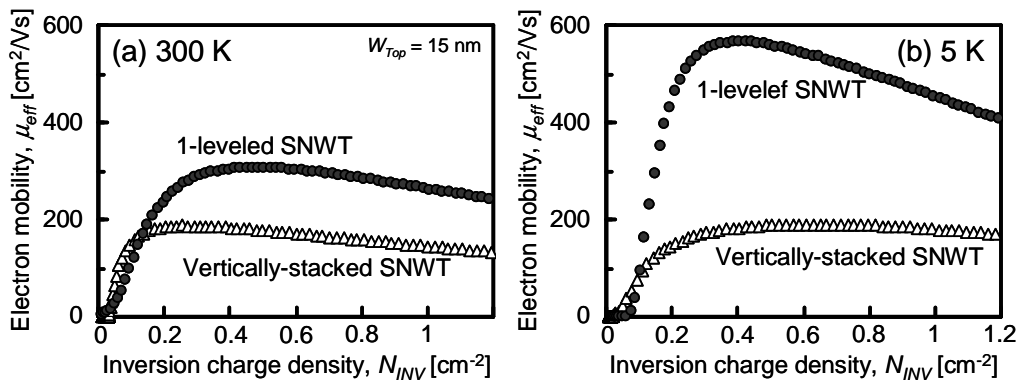


Figure 5.27 Electron mobility comparisons between 1-leveled and vertically-stacked silicon nanowire MOSFET at 300 K (a) and 5 K (b).

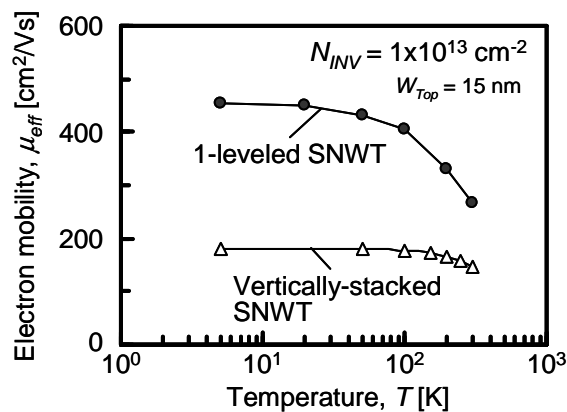


Figure 5.28 Temperature dependence of effective mobility at high inversion charge density ( $N_{INV} = 10^{13} \text{ cm}^{-2}$ ) for 1-leveled and vertically-stacked silicon nanowire MOSFET.



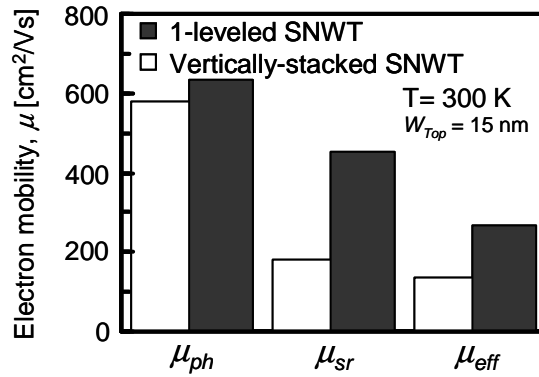


Figure 5.29 Mobility limiting components comparison at high inversion charge density between 1-leveled and vertically-stacked silicon nanowire MOSFETs at 300 K.

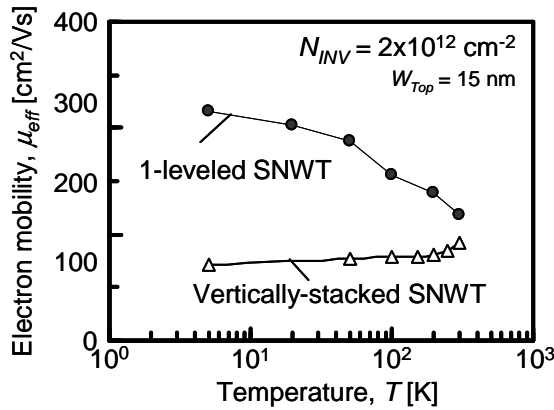


Figure 5.30 Temperature dependence of effective mobility at low inversion charge density ( $N_{INV} = 2 \times 10^{12}$  cm<sup>-2</sup>).

## 5.4 EFFECT OF HYDROGEN ANNEALING

Hydrogen annealing can be used intentionally for three-dimensional profile transformation by rounding sharp corners while diminishing the surface roughness and keeping the active layer crystalline [5.18, 5.19]. In this section, a mobility study was performed in order to highlight the impact of hydrogen annealing on the etched surfaces.

### 5.4.1 Cross-Sectional Shape

Hydrogen annealing (750°C, 2min) was performed on 15 nm wide silicon nanowires (Figure 5.31 (a)). As a result, the silicon nanowires were rounded thanks to

the hydrogen annealing as shown in Figure 5.31 (b).

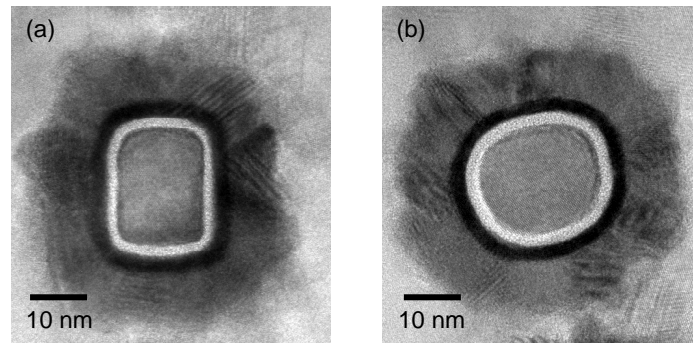


*Figure 5.31 Cross-sectional TEM images of silicon nanowire (a) without and (b) with hydrogen annealing at 750 °C for two minutes.*

#### **5.4.2 Carrier Mobility Evaluation**

First, the impact of hydrogen annealing on silicon nanowire surface quality was investigated by using the 1-leveled SNWTs. Figure 5.32–5.34 show the comparisons of electron effective mobility between with and without hydrogen annealing. We observed the mobility difference at low temperature. It is clear that effective mobility in H<sub>2</sub>-annealed SNWTs is more degraded by coulomb scattering (Figure 5.34), while surface roughness is improved (Figure 5.33). However, the mobility differences are not revealed at 300 K. This is because that these effects are hidden by the strong phonon limitation due to the initially high mobility.

On the other hand, we observed the mobility changes at 300 K on the vertically-stacked SNWTs. Figure 5.35 shows a mobility comparison between with and without hydrogen annealing for the vertically-stacked SNWTs. Improvement of the effective mobility at high  $N_{INV}$  is observed for circular NWs because their surface roughness is reduced by the H<sub>2</sub> annealing. A circular shape formed by hydrogen annealing, however, leads to mobility degradation at low  $N_{INV}$ .

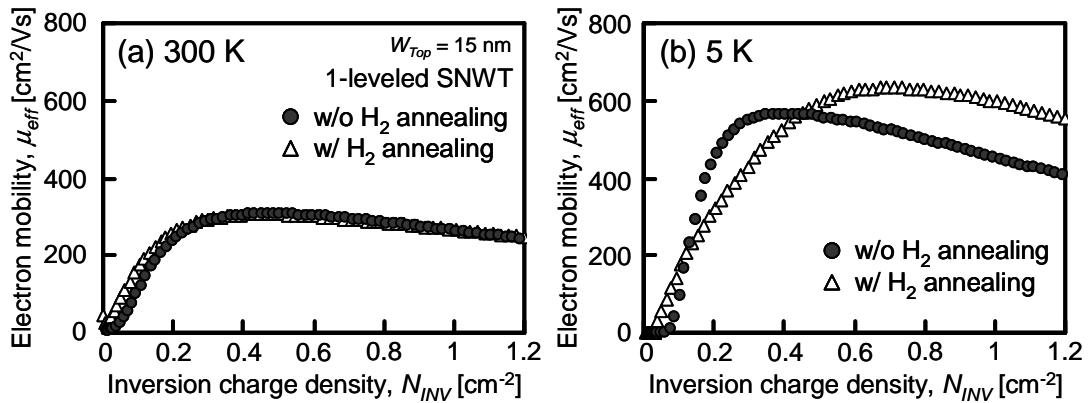


Figure 5.32 Electron mobility comparison of 1-leveled silicon nanowire MOSFETs between with and without hydrogen annealing. The measurement temperatures are 300 K (a) and 5 K (b).

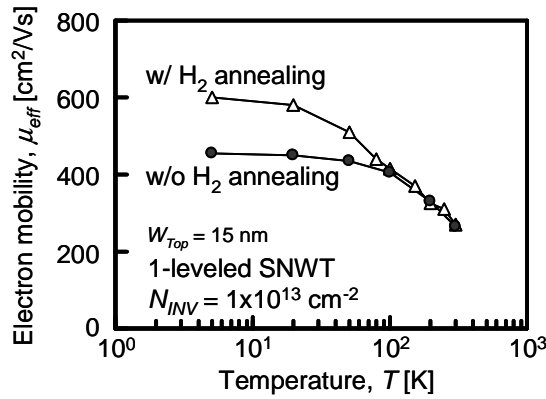


Figure 5.33 Temperature dependence of effective mobility at high inversion charge density ( $N_{INV}=10^{13} \text{ cm}^{-2}$ ) for 1-leveled nanowire MOSFET with and without  $\text{H}_2$  anneal.

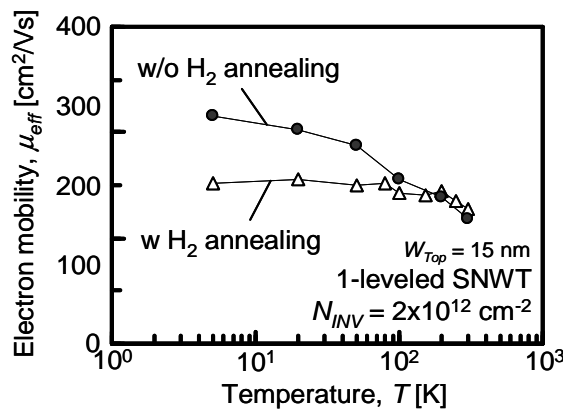


Figure 5.34 Temperature dependence of effective mobility at low inversion charge density ( $N_{INV}=2 \times 10^{12} \text{ cm}^{-2}$ ).

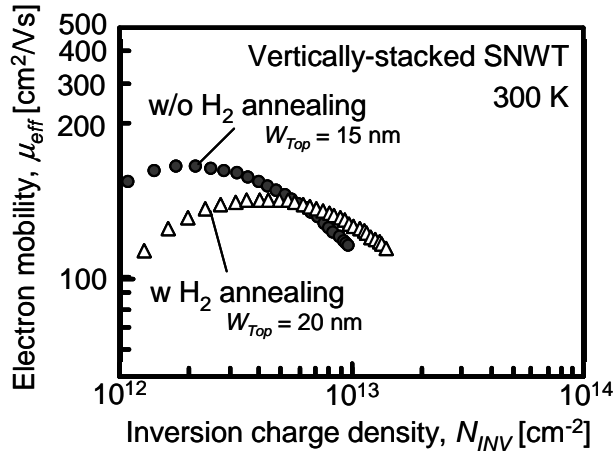


Figure 5.35 Electron mobility comparison of vertically-stacked silicon nanowire MOSFETs between with and without hydrogen annealing.

### 5.4.3 Interface Trap density

Mobility at low  $N_{INV}$  is mainly limited by (remote) coulomb scattering due to interface and oxide charges and/or interface dipoles between high- $\kappa$  and interfacial layer in the case of high- $\kappa$ /metal gate stack. To evaluate the interface quality, the interface trap density ( $D_{it}$ ) have been quantified by adapting the charge pumping method with gated-diode structures as shown in Chapter 3. Figure 5.36 shows the charge pumping current ( $I_{cp}$ ) in the vertically-stacked SNW p-i-n diode which exhibits a typical “hat” shape. The peak  $I_{cp}$ -frequency ( $f$ ) plots shows a good linearity in Figure 5.37. Circular NWs have roughly 3 times higher mean  $D_{it}$  values than rectangular ones.

Figure 5.38 shows the energy profile  $D_{it}(E)$  for, together with the mean value  $D_{it}$  measured at 300K using frequency dependence [5.20]. Wide and long planar SOI MOSFETs as reference devices were also measured to clarify the effect of high- $\kappa$ /metal gate stack on the interface traps density. The mean value ( $\sim 1.1 \times 10^{11} \text{ eV}^{-1} \text{ cm}^{-2}$ ) is reasonably low for this thick nitride metal layer, as the CVD process limits the nitrogen diffusion toward the  $\text{SiO}_2 / \text{Si}$  interface [5.21, 5.22]. Meanwhile the energy profile reveals an asymmetry between the upper half part and the lower half part of the band gap. In the upper part, the trap density is much higher than in the lower part of the band gap, with  $5 \times 10^{11} \text{ eV}^{-1} \text{ cm}^{-2}$  between 0.3 and 0.5 eV, due to dangling bonds (Pb centers)

combined with N-generated defects [5.23]. The latter generally induce a peak density in the upper half part of the band gap [5.21, 5.24]. Near the band edges—for both conduction band (CB) and valence band (VB)—the  $D_{it}$  increases and can reach more than  $10^{13} \text{ eV}^{-1} \text{ cm}^{-2}$  at  $E-E_i = \pm 0.58 \text{ eV}$ . The lower value of  $D_{it}$ , especially in the upper half part of the Si gap, evidences a lower density of interface traps in the middle of the gap. Figure 5.38 also shows the energy profile of  $D_{it}$  for SNWTs with a rectangular and a circular cross section. For both rectangular and circular NWs, the energy profile  $D_{it}(E)$  is modified compared to references as follows: (i) less asymmetry is observed between the upper part and the lower part of the band gap, and (ii) a higher mean density  $D_{it}$  is measured (up to five times more for circular NWs). The lower asymmetry could result from the lower impact of N diffusion in NWs, due to a thicker interfacial oxide ( $\sim 1.5\text{--}2 \text{ nm}$ ) compared to planar devices ( $\sim 1 \text{ nm}$ ), and more Pb centers in SNWTs. The latter point could be explained, especially for the rectangular cross-section, since more dangling bonds are generally measured on (110) plane (i.e, the orientation of the sidewalls of the SNWTs in our case) as reported by Refs. 5.23 and 5.25. Finally, the circular NWs exhibit the highest  $D_{it}$ , roughly two times larger than rectangular NWs. This high value occurs despite the  $\text{H}_2$  annealing, which is known to passivate some defects such as dangling bonds [5.26], and evidences a natural lower quality of the channel interface for circular NWs.

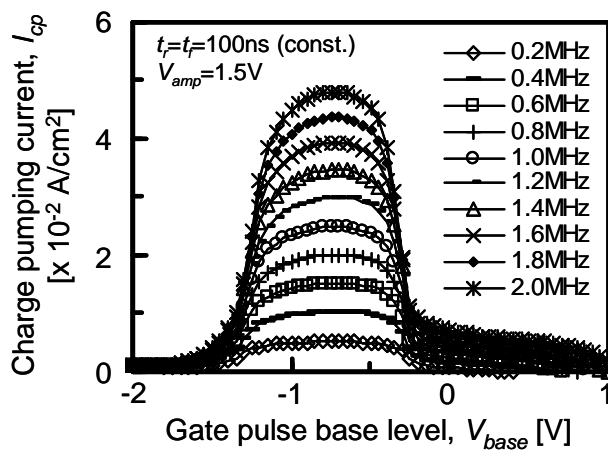


Figure 5.36 Charge pumping currents  $I_{cp}$  obtained base voltage sweep on nanowire gated-diode with  $L_G = 240 \text{ nm}$  and  $W_{NW}/H_{NW} = 20 \text{ nm}/15 \text{ nm}$ . The currents are normalized by  $W_{eff}$  obtained from TEM images.

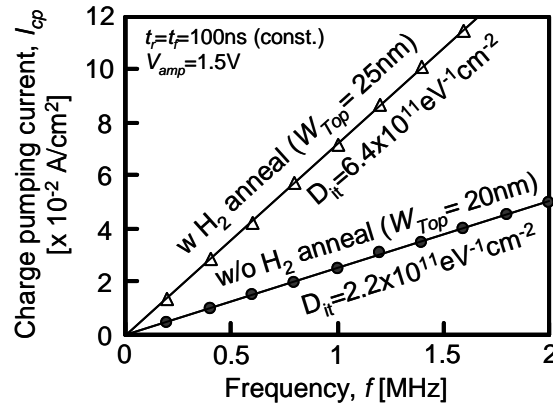


Figure 5.37 Charge pumping currents  $I_{cp}$  as a function of frequency  $f$ .

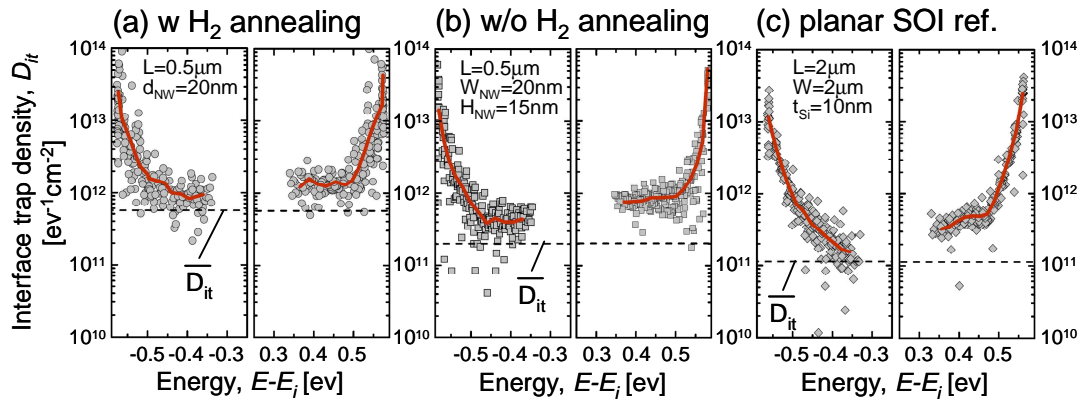


Figure 5.38 Interface trap density as a function of energy for vertically-stacked nanowires with (a) and without (b) hydrogen annealing, and planar SOI devices (c) with the same gate stack (3 nm  $\text{HfO}_2$  ALD/10 nm TiN CVD). The profile is obtained by scanning temperature from 300 K down to 25 K by 25 K steps. The bold line represents the mean value of  $D_{it}(E)$ . The dashed line is the directly measured mean value of interface trap density over the full energy range at 300 K which evidence the lower density of interface traps in the middle of the gap.

## 5.5 SILICON-GERMANIUM NANOWIRE MOSFET

### 5.5.1 Device Fabrication Process

The fabrication process of vertically-stacked SiGe nanowire FETs was changed from Si ones as the following steps. SOI (001) wafers were used for Si and compressively (c)-strained SiGe NWs. Tensile-strained (1.3 GPa) SOI (001) wafers were used for un-strained SiGe NWs, respectively. After anisotropic etching of Si/Si<sub>0.8</sub>Ge<sub>0.2</sub> superlattices, selective isotropic etching of Si layers between Si<sub>0.8</sub>Ge<sub>0.2</sub> layers was performed to obtain the suspended Si<sub>0.8</sub>Ge<sub>0.2</sub> nanowires. In order to achieve better interface quality, a 2 nm-thick-Si cap was grown at 650 °C on the SiGe NWs. Figure 5.39 shows the cross-sectional TEM images and top-viewed SEM images. The cross-sectional shape was hexagonal with {111} faceted sidewalls most likely due to the thermal budget used during the Si capping. Long c-strained SiGe NWs are bended as shown in Figures. 5.39 (a) and (c), while short c-strained SiGe NWs and un-strained SiGe NWs are straight as shown in Figures. 5.39 (d) and (e).

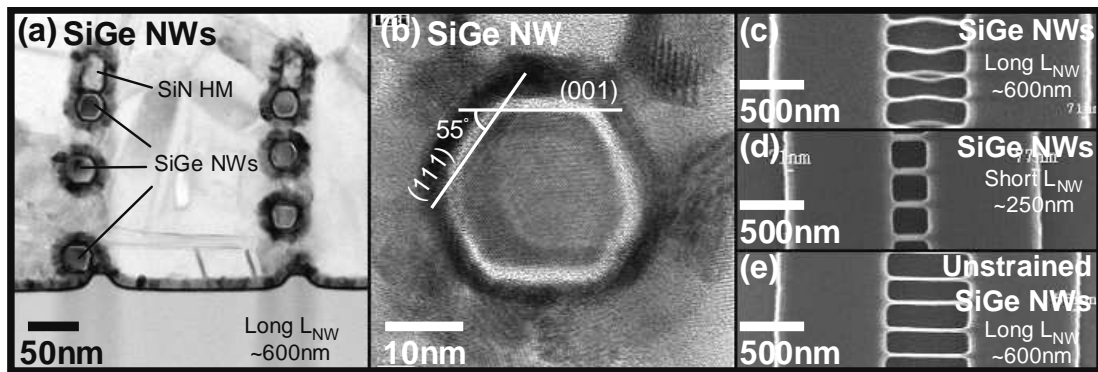


Figure 5.39 (a) Cross-sectional TEM micrographs of 3D-stacked compressively(c)-strained SiGe NWTs, (b) enlarged images of c-strained SiGe NW, (c) top view of bended c-strained SiGe NWs with  $L_{NW}=600\text{nm}$ , (d) top view of c-strained SiGe NWs with  $L_{NW}=250\text{nm}$ , and (e) top view of un-strained SiGe NWs with  $L_{NW}=600\text{nm}$ . Short length SiGe NWs are straight, this whatever their strain state.

### 5.5.2 I–V Characteristics

C-strained SiGe and un-strained SiGe NWs were evaluated in order to boost pFET performances. Figure 5.40 shows  $I_{ON}/I_{OFF}$  characteristics of Si, c-strained and un-strained SiGe NWs. The currents are normalized by the number of wires. Both the SiGe NWTs showed larger off-current than SNWTs. This is due to the lower  $V_T$  for the SiGe NWTs as shown in Figure 5.41. The c-strained SiGe NWTs show higher on-current. However the best  $I_{ON}/I_{OFF}$  performance is obtained for Si NWs.

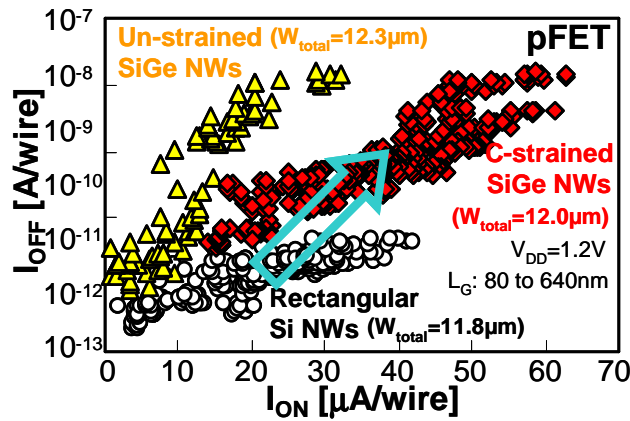


Figure 5.40  $I_{ON}/I_{OFF}$  characteristics of Si, c-strained and un-strained SiGe NWs normalized by the number of wires. The total NW surface  $W_{total}$  is estimated from the cross-sectional TEM images. The  $W_{NW}$  of all NWs is  $\sim 20\text{nm}$ .

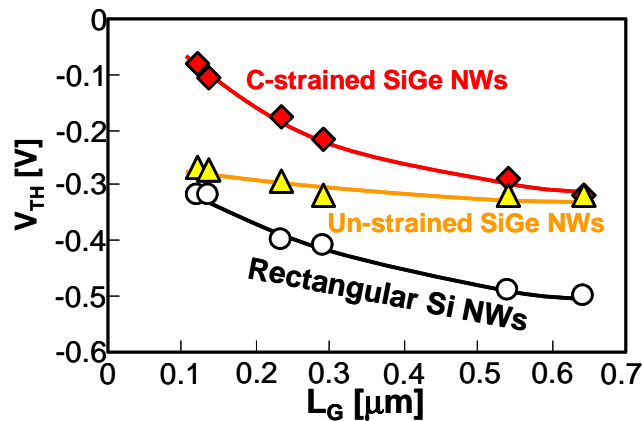


Figure 5.41 Threshold voltage of Si, c-strained and un-strained SiGe NWs as a function of gate length. The  $W_{NW}$  of all NWs are  $\sim 20\text{nm}$ .



### 5.5.3 Carrier Mobility Evaluation

Figure 5.42 shows a mobility comparison. The large enhancement of mobility was obtained in the c-strained SiGe NWTs compared with un-strained ones. This can be due to a compressive strain effect. However, in comparison with SNWTs, a small impact on mobility was observed. The c-strained SiGe NWTs have higher  $\mu_{eff}$  at high  $N_{inv}$  lead to a larger  $I_{ON}$  current than for Si NWTs. The hexagonal cross section of SiGe NWs with (111) sidewalls could also contribute to mobility degradation as shown in Figure 5.44.

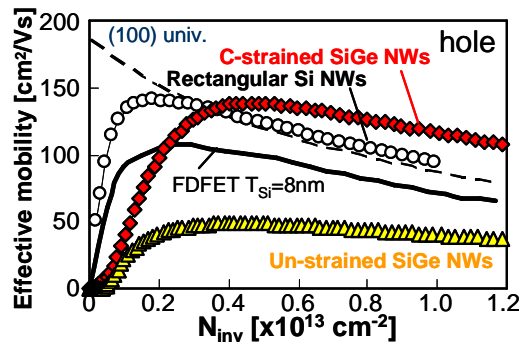


Figure 5.42 Effective hole mobility of Si, c-strained and un-strained SiGe NWs. The  $W_{NW}$  of all NWs are  $\sim 20\text{nm}$ .

### 5.5.4 Noise Measurement

Low-frequency noise measurements performed on the NWs between 10 Hz and 10 kHz at  $V_{DS}=50\text{ mV}$ , show an oxide trap density ( $N_t$ ) for SiGe NWs 3.5 times larger than for Si NWs (Figure 5.45). This higher trap density may reduce the mobility.

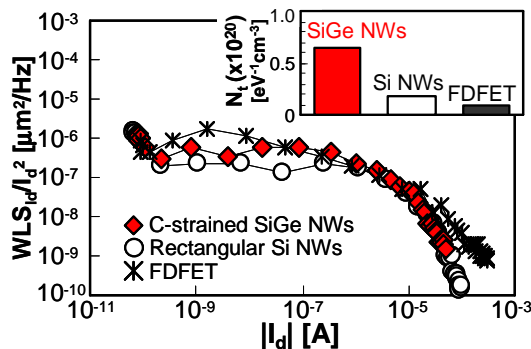


Figure 5.43 Low-frequency noise of Si and c-strained SiGe NWs. Inserted figure is a comparison of oxide trap density ( $N_t$ ).  $L_G$  and  $W_{NW}$  are  $\sim 290\text{nm}$  and  $\sim 20\text{nm}$ , respectively.

## 5.6 CONCLUSIONS

In this chapter, the electrical characteristics of vertically-stacked SNWTs have been investigated. Vertically-stacked nanowire structure can achieve extremely high on-currents per given layout surface with good short-channel effects immunity. This result is expected to achieve high integration and low power consumption. On the other hand, in terms of its performance, the optimisation of short-channel CMOS nanowire drive current will have to take into account specific effects. In particular, the use of SiGe sacrificial layer to make vertically-stacked channels cause the large mobility degradation due to the surface roughness, resulting from the damage of plasma etching. This result can evidence the poor ballisticity in the short channel SNWTs.

The hydrogen annealing can improve the surface-roughness limited mobility on a certain extend. Charge pumping measurements, however, revealed that circular-shaped SNWTs, which are formed by hydrogen annealing, have a higher  $D_{it}$  than rectangular ones, leading to low-field mobility degradation. This high  $D_{it}$  might be caused by the continuously-varying surface orientation. The resulting additional coulomb scattering could partly explain the quite low mobility in 5 nm diameter SNWTs together with the already known transport limitations in NWs.

The vertically-stacked SiGe NWTs have been also investigated. Compressively-strained SiGe showed slightly higher mobility than Si ones. One of the possible reasons of the small mobility enhancement is the higher trap density for SiGe nanowires. Additionally, the hexagonal cross section of SiGe NWs with (111) sidewalls could also contribute to mobility degradation

## 5.7 REFERENCES

- [5.1] S. Bangsaruntip, G.M. Cohen, A. Majumdar, Y. Zhang, S. U. Engelmann, N. C. M. Fuller, L. M. Gignac, S. Mittal, J. S. Newbury, M. Guillorn, T. Barwicz, L. Sekaric, M. M. Frank, and J. W. Sleight, "High performance and highly uniform gate-all-around silicon nanowire MOSFETs with wire size dependent scaling,"

- in *IEDM Tech. Dig.*, 2009, pp. 297–300.
- [5.2] G. Bidal, F. Boeuf, S. Denorme, N. Loubet, J.L. Huguenin, P. Perreau, D. Fleury, F. Leverd, S. Lagrasta, S. Barnola, T. Salvetat, B. Orlando, R. Beneyton, L. Clement, R. Pantel, S. Monfray, G. Ghibaudo, and T. Skotnicki, “High velocity Si-nanodot: a candidate for SRAM applications at 16 nm node and below,” in *VLSI Tech. Dig.*, 2009, pp. 240–241.
- [5.3] M. Li, K.H. Yeo, S.D. Suk, Y.Y. Yeoh, D.-W. Kim, T.Y. Chung, K. S. Oh, and W.-S. Lee, “Sub-10 nm gate-all-around CMOS nanowire transistors on bulk Si substrate,” in *VLSI Tech. Dig.*, 2009, pp. 94–95.
- [5.4] S. D. Suk, M. Li, Y. Y. Yeoh, K. H. Yeo, K. H. Cho, I. K. Ku, H. Cho, W. J. Jang, D.-W. Kim, D. Park, and W.-S. Lee, “Investigation of nanowire size dependency on TSNWFET,” in *IEDM Tech. Dig.*, 2007, pp. 891–894.
- [5.5] M. Saitoh, Y. Nakabayashi, H. Itokawa<sup>1</sup>, M. Murano, I. Mizushima<sup>1</sup>, K. Uchida, and T. Numata, “Short-Channel Performance and Mobility Analysis of <110>- and <100>-Oriented Tri-Gate Nanowire MOSFETs with Raised Source/Drain Extensions,” in *VLSI Tech. Dig.*, 2010, pp. 169–170.
- [5.6] J. Chen, T. Saraya, K. Miyaji, K. Shimizu, and T. Hiramoto, “Experimental Study of Mobility in [110]- and [100]-Directed Multiple Silicon Nanowire GAA MOSFETs on (100) SOI,” in *VLSI Tech. Dig.*, 2008, pp. 32–33.
- [5.7] P. Packan, S. Akbar, M. Armstrong, D. Bergstrom, M. Brazier, H. Deshpande, K. Dev, G. Ding, T. Ghani, O. Golonzka, W. Han, J. He, R. Heussner, R. James, J. Jopling, C. Kenyon, S-H. Lee, M. Liu, S. Lodha, B. Mattis, A. Murthy, L. Neiberg, J. Neiryneck, S. Pae, C. Parker, L. Pipes, J. Sebastian, J. Seiple, B. Sell, A. Sharma, S. Sivakumar, B. Song, A. St. Amour, K. Tone, T. Troeger, C. Weber, K. Zhang, Y. Luo, S. Natarajan, “High Performance 32nm Logic Technology Featuring 2nd Generation High-k + Metal Gate Transistors,” in *IEDM Tech. Dig.*, 2009, pp. 659–662.
- [5.8] K. Tachi, M. Cassé, S. Barraud, C. Dupré, A. Hubert, N. Vulliet, M.E. Faivre, C. Vizioz, C. Carabasse, V. Delaye, J.M. Hartmann, H. Iwai, S. Cristoloveanu, O. Faynot and T. Ernst, “Experimental study on carrier transport limiting

- phenomena in 10 nm width nanowire CMOS transistors,” in *IEDM Tech. Dig.*, p.784, 2010.
- [5.9] D. Fleury, G. Bidal, A. Cros, F. Boeuf, T. Skotnicki and G. Ghibaudo, “New Experimental Insight into Ballistic Transport in Strained Bulk MOSFETs” *VLSI Tech. Dig.*, pp. 16-17, 2009.
- [5.10] C. Jacoboni, C. Canali, G Ottaviani, and A. A. Quaranta, “A Review of Some Charge Transport Properties of Silicon,” *Solid-state Electron.*, 20,77 (1977).
- [5.11] K. Natori, “Ballistic Metal-Oxide-Semiconductor Field Effect Transistor,” *J. Appl. Phys.*, 76,4879 (1994).
- [5.12] M. S. Shur, “Low Ballistic Mobility in Submicron HEMTs,” *IEEE Electron Device Lett.*, vol. 23, no. 9, pp. 511–513, Sep. 2002.
- [5.13] S. M. Sze and Kwok K. Ng, *Physics of Semiconductor Devices*, 3<sup>rd</sup> edition, John Wiley & Sons, Inc., Hoboken, New Jersey, 2007.
- [5.14] V. Barral, T. Poiroux, F. Rochette, M. Vinet, S. Barraud, O. Faynot, L. Tosti, F. Andrieu, M. Casse, B. Previtali, E. Bernard, R. Ritzenthaler, P. Grosgeorges, G. Lecarval, D. Munteanu, J-L. Autran, S. Deleonibus, “Will Strain Be Useful for 10nm Quasi-Ballistic FDSOI Devices? An Experimental Study”, *VLSI Tech. Dig.*, pp.128-129, 2007.
- [5.15] L. Sekaric, O. Gunawan, A. Majumdar, X. H. Liu, D. Weinstein, and J. W. Sleight, “Size-dependent modulation of carrier mobility in top-down fabricated silicon nanowires.” *Appl. Phys. Lett.*, 95, 023113, 2009.
- [5.16] C. Dupre, T. Ernst, S. Borel, Y. Morand, S. Descombes, B. Guillaumot, X. Garros, S. Becu, X. Mescot, G. Ghibaudo, S. Deleonibus, “Impact of Isotropic Plasma Etching on Channel Si Surface Roughness Measured by AFM and on NMOS Inversion Layer Mobility”, *Proceedings of ULIS*, pp. 133-136, 2008.
- [5.17] A. Hubert et al., *ECS Transaction*, 13(1), p.195, 2008.
- [5.18] M.-C. M. Lee and M. C. Wu, “Thermal Annealing in Hydrogen for 3-D Profile Transformation on Silicon-on-Insulator and Sidewall Roughness Reduction,” *Journal of Microelectromechanical systems*, Vol. 15, no. 2, pp.338–343, 2006.
- [5.19] E. Dornel, T. Ernst, J. C. Barbe, J. M. Hartmann, V. Delaye, F. Aussenac, C.

- Vizioz, S. Borel, V. Maffini-Alvaro, C. Isheden, and J. Foucher. “Hydrogen annealing of arrays of planar and vertically stacked Si nanowires”, *Applied Physics Letters*, vol. 91, 233502, 2007.
- [5.20] M. Casse, K. Tachi, S. Thiele and T. Ernst, “Spectroscopic charge pumping in Si nanowire transistors with a high-k/metal gate, ” *Appl. Phy. Lett.* 96, 123506, 2010.
- [5.21] X. Garros, M. Cassé, G. Reimbold, F. Martin, C. Leroux, A. Fanton, O. Renault, V. Cosnier, and F. Boulanger, Dig. Tech. Pap. Symp. VLSI Technol. 2008, 68.
- [5.22] F. Andrieu O. Faynot, X. Garros, D. Lafond, C. Buj-Dufornet, L. Tosti, S. Minoret, V. Vidal, J. C. Barbé, F. Allain, E. Rouchouze, L. Vandroux, V. Cosnier, M. Cassé, V. Delye, C. Carabasse, P. Holliger, A. Vandooren, C. Fenouillet-Béranger, F. Martin, and S. Deleonibus, “Comparative scalability of PVD and CVD TiN on HfO<sub>2</sub> as a metal gate stack for FDSOI cMOSFET down to 25 nm gate length and width,” in *IEDM Tech. Dig.*, 2006, pp. 641–644.
- [5.23] D. K. Schroder, *Microelectron. Reliab.* 47, 841 , 2007.
- [5.24] E.-C. Lee, *Phys. Rev. B* 77, 104108 , 2008.
- [5.25] S. Maeda, J.-A. Choi, J.-H. Yang, Y.-S. Jin, S.-K. Bae, Y.-W. Kim, and K.-P. Suh, in *International Reliability Physics Symposium Proceedings*, 2004, pp. 8–12.
- [5.26] M. L. Reed and J. D. Plummer, *J. Appl. Phys.* 63, 5776, 1988.

# **CHAPTER 6**

## ***THRESHOLD VOLTAGE CONTROL OF VERTICALLY-STACKED NANOWIRE MOSFETS***

# CHAPTER 6 CONTENTS

- 6 Threshold Voltage Control of Vertically-Stacked Nanowire MOSFETs**
  - 6.1 Introduction
    - 6.1.1 Threshold Voltage Control by Independent-Gate FinFET
    - 6.1.2 Vertically-Stacked Nanowire Transistor with Independent Gates
  - 6.2 Optimization of Device Dimensions
  - 6.3 Conclusions
  - 6.4 References

## 6.1 INTRODUCTION

In previous chapter, we discussed the possibility of vertically-stacked SNWTs in terms of  $R_{SD}$  resistance, transport properties, and short channel effect immunity. Another issue for the vertically-stacked SNWTs is how to control the threshold voltage. For various CMOS applications such as HP, LOP, and LSTP, it is important to achieve flexible threshold voltage in a transistor. In this chapter, the possibility of a flexible threshold voltage for vertically-stacked SNWT will be discussed. In particular, the flexibility and the short-channel effects immunity are investigated by numerical simulations.

### 6.1.1 Threshold Voltage Control by Independent-Gate FinFET

In usual case, the threshold voltages are mainly controlled by the gate work function and channel doping level. However, its control by the high- $\kappa$ /metal gate is difficult and complex because of the sensitivity of process conditions and the necessity of the dual metal and/or dual high- $\kappa$ . Furthermore, the use of channel doping technique yields to large  $V_T$  variations within a wafer due to dopants fluctuations. As one of the solutions for three-dimensional devices, independent-gate FinFETs (IG-FinFETs) have been proposed and demonstrated with excellent experimental results of threshold voltage control by the second gate and the synchronized driving mode operation by the double gates [6.1, 6.2]. The independent gates have been successfully fabricated by using a chemical–mechanical-polishing process or an etch-back process [6.1–6.4] as shown in Figure 6.1.

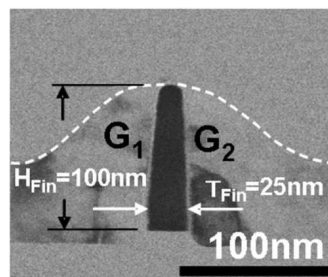


*Figure 6.1 Cross-sectional TEM image of the independent-gate FinFET fabricated by the resist etch back process [6.4].*



### **6.1.2 Vertically-Stacked Nanowire Transistor with Independent Gates**

Vertically-stacked SNWTs with independent gates have been experimentally demonstrated by C. Dupre *et al.* [6.5]. The device has internal spacers between the nanowires as shown in Figure 6.2, named  $\Phi$ FET since its shape is similar to the Greek letter  $\Phi$ . Figure 6.3 summarizes the fabrication process of  $\Phi$ -FET. First, Reduced Pressure- Chemical Vapor Deposition (RP-CVD) was used to epitaxially grow (25nm-Si /25nm-SiGe)x4 superlattice on SOI wafers (Fig.5.3, step 1). A SiN hard-mask was then deposited. After an hybrid DUV/e-beam lithography, the resist was trimmed to define narrow lines (fin width;  $W_{Si} \sim 30\text{nm}$ ). Then, the exposed Si and (Si/SiGe)x4 areas were etched by an anisotropic dry plasma etching (Fig.5.3, step 2). The same RIE reactor was used to remove the SiGe isotropically using a  $\text{CF}_4 + \text{O}_2$  chemistry in order to liberate the suspended Si-nanowires. Then, HTO and SiN were deposited. The partitions between the stacked nanowires were formed by internal spacer obtained by anisotropic and isotropic etchings of SiN selectively to HTO (Fig.5.3, steps 2.1 and 2.2). After chemical cleaning of the channel surface, a  $\text{HfO}_2 / \text{TiN} / \text{Poly-Si}$  gate stack was deposited. The gate stack over the SiN hard mask was removed by Chemical Mechanical Polishing (CMP) (Fig.5.3, step 3). After the gate etching, Source/Drain implantations and spacer formation, dopant atoms were activated and the top of S/D regions were silicided. The fabrication ended with a standard Back-End Of Line (BEOL) process. Figure 6.4 shows the cross-sectional TEM pictures of  $\Phi$ -FET.

This structure is expected to achieve a flexible threshold voltage while keeping better short channel effects immunity due to their partially surrounding gates. Figure 6.5 and 5.6 shows the electrical results. Threshold voltage shift have been demonstrated due to a coupling effect between the two gates for  $\Phi$ FET. Moreover,  $\Phi$ FET's  $I_{\text{OFF}}$  currents are 2-decade lower than IG-FinFET ones thanks to an improved electrostatic control.

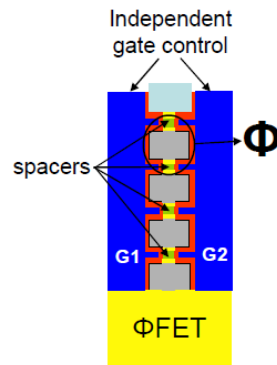


Figure 6.2  $\Phi$ -FET scheme.

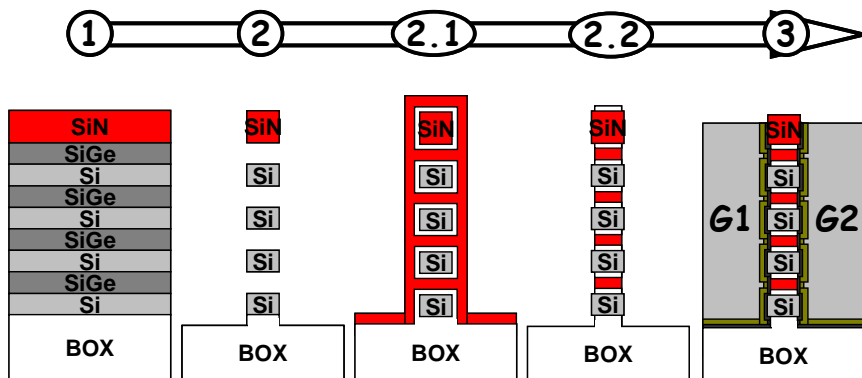


Figure 6.3 Schematic fabrication sequence of  $\Phi$ -FET.

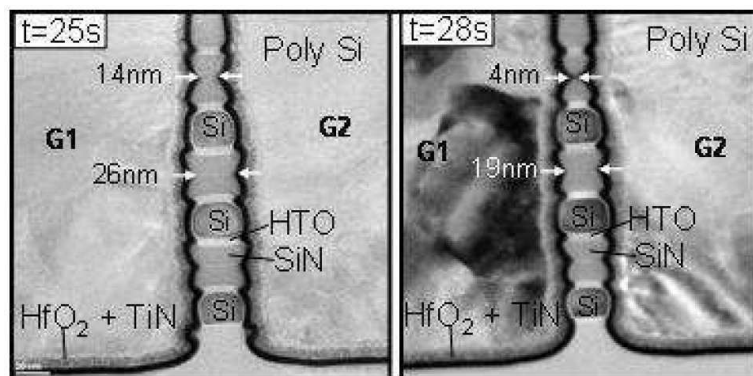


Figure 6.4 Cross-sectional TEM pictures of  $\Phi$ -FET (3 stacked nanowires). Left: 25s SiN isotropic etching Right: 28s SiN isotropic etching.

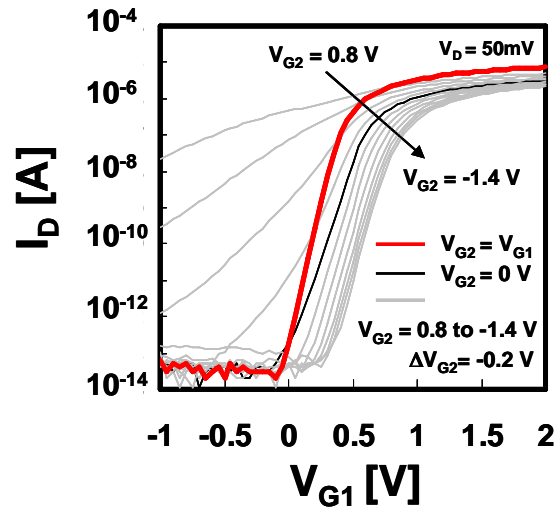


Figure 6.5 Experimental  $I_d$ - $V_{g1}$  characteristics at various  $V_{g2}$  for n-channel  $\Phi$ -FET. The gate length and channel width are 550 nm and 25 nm, respectively.

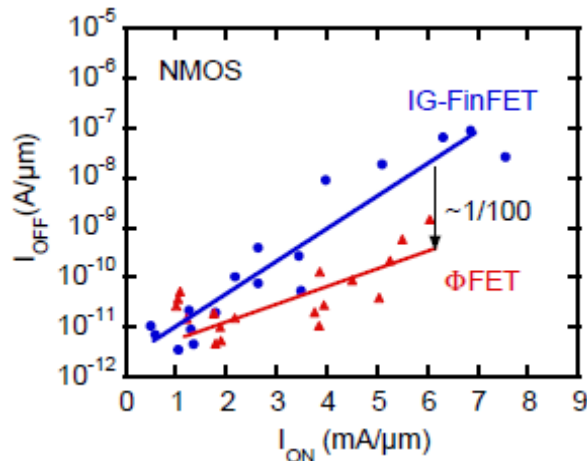


Figure 6.6  $I_{on}$ - $I_{off}$  characteristics comparison between  $\Phi$ -FET and IG-FinFET.

## 6.2 OPTIMIZATION OF DEVICE DIMENTIONS

Although the  $\Phi$ -FETs have been successfully demonstrated, it is necessary to optimize the structure in detail to obtain flexible threshold voltage with better short channel effects immunity. First, we will go through the simulation details. Figure 6.7 shows the simulated  $\Phi$ -FET structure. To extract DIBL associated to the given structure, the currents in the subthreshold regime are determined by using FlexPDF software as

the following procedure.

The source term is detailed as

$$S = \frac{q}{\epsilon} (N_a - N_d + n - p), \quad (6.1)$$

where  $N_a$  is the acceptor density ( $=10^{15} \text{ cm}^{-3}$ ),  $N_d$  the donor density ( $N_d = n_i^2 / N_a$  with  $n_i$  the intrinsic carrier density). Here,  $N_d$  is negligible due to p-type Si.  $n$  and  $p$  are given as a function of the potential  $V$ :

$$n = N_d \exp\left(\frac{qV}{kT}\right), \quad (6.2)$$

$$p = N_d \exp\left(-\frac{qV}{kT}\right). \quad (6.3)$$

The subthreshold current for long-channel MOSFET is given by:

$$I_{Dlong} = \frac{1}{L} \frac{kT}{q} \mu_{eff} Q_{is} \left(1 - e^{-\frac{qV_D}{kT}}\right), \quad (6.4)$$

where  $Q_{is}$  is the inversion charge per surface on the source side which is deduced by integrating  $n$  from the equation (6.2) in the Si volume. The short-channel current thus can be easily rewritten owing to a correction factor C.F [6.6]

$$I_{Dshort} = \frac{I_{Dlong}}{C.F.}, \quad (6.5)$$

$$C.F. = \frac{1}{t_{Si} W_{Si} L} \int \exp\left(\frac{-q(V_{short} - V_{long})}{kT}\right), \quad (6.6)$$

where  $V_{short}$  and  $V_{long}$  are the potentials in short and long channels, respectively. The boundary conditions for a simple nanowire structure as shown in Figure 6.8 are adapted to  $\Phi$ -FET structure as following:  $V_G = 0.6 \text{ V}$  on the gate oxide and the built-in voltage ( $V_{BI}$ ) as each nanowire end as

$$V_{BI} = \frac{kT}{q} \ln\left(\frac{N_a N_d}{n_i^2}\right). \quad (6.7)$$

The long-channel case differs from the short-channel case only by applying Neumann boundary conditions: the gradient of the potential (electric field) is forced to zero at each nanowire end. Once the potential distribution is simulated, we used it to extract the

short-channel effects through the natural length  $\lambda$  [6.7],

$$\lambda = \sqrt{\frac{\epsilon_{Si} t_{Si} t_{ox}}{\epsilon_{ox} \eta}}, \quad (6.8)$$

where  $\eta$  is the empirical parameter which varies as a function of the gate configuration: planar ( $\eta=1$ ), double gate ( $\eta =2$ ), tri-gate ( $\eta =3$ ), and gate-all-around ( $\eta \approx 4$ ). In the long-channel, the potential is constant in the middle of the channel, while in the short-channel, the potential is parabolic as shown in Figure 6.9. In terms of subthreshold currents,  $n$  and  $p$  terms can be removed from equation (6.1). Then the equation (6.1) can be rewritten as follows

$$S = \frac{q}{\epsilon} N_a, \quad (6.9)$$

A quantum correction was introduced to have zero-charge at the Si/SiO<sub>2</sub> interface [6.8]. The Poisson equation (6.10) is then solved:

$$\nabla^2 V = S. \quad (6.10)$$

Figure 6.10 shows the simulated subthreshold currents. From the currents, we extracted the threshold voltage and the DIBL. The threshold voltage was extracted using the current constant method:  $V_T = V_G$  at  $I_D = 10^{-7} L/W$ .

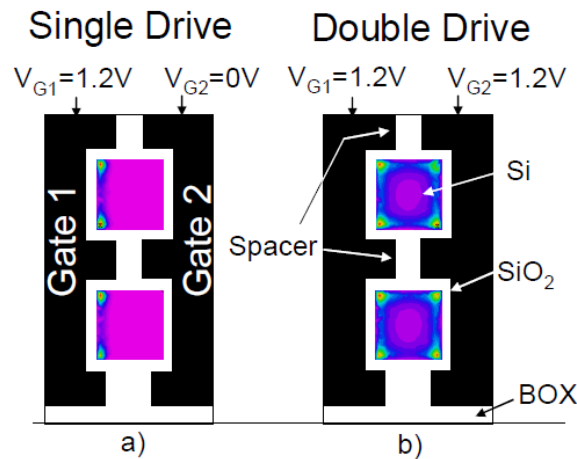


*Figure 6.7 Simulated inversion charge density in a  $\Phi$ FET for (a) one gate activated (single drive mode) and (b) two gates activated (double drive mode).*

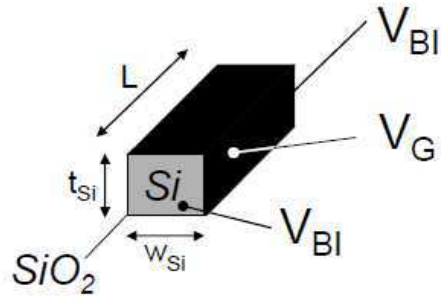


Figure 6.8 Schematic illustration of a SNWT with boundary conditions.

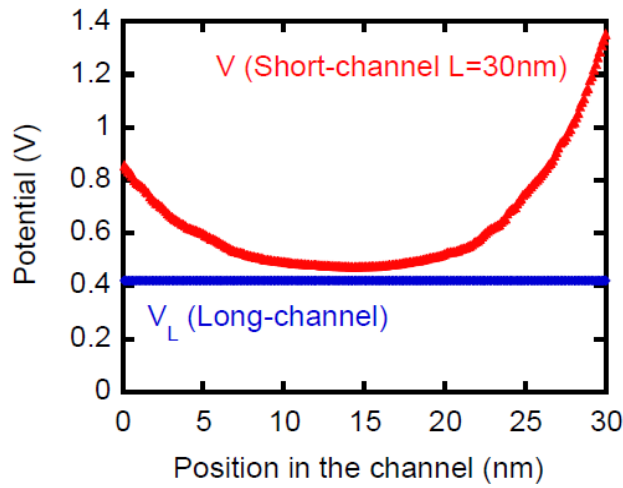


Figure 6.9 Potential along the channel for a long and short-channel transistor.

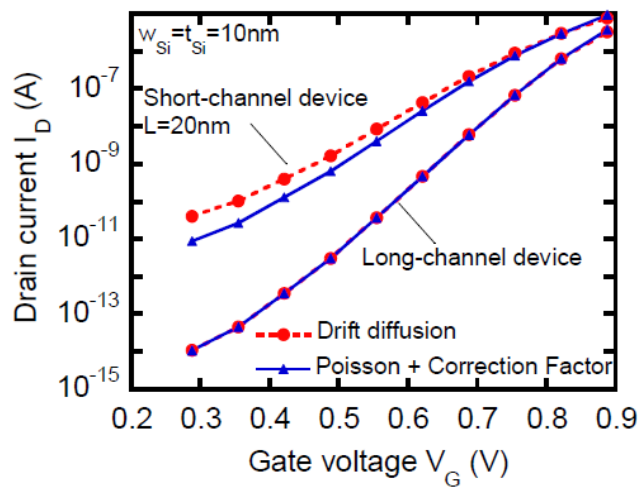


Figure 6.10 Simplified Poisson equation resolution for long-channel with C.F. for short channel is compared to the drift-diffusion model.

As the  $\Phi$ -FET structure is perfectly symmetric, the coupling factor ( $\alpha$ ) can be written as the threshold voltage sensitivity [6.9]:

$$\alpha \equiv \frac{\Delta V_{T1}}{\Delta V_{G2}} \approx \frac{C_{Si}}{C_{ox} + C_{Si} + C_{it}}, \quad (6.11)$$

where  $V_{T1}$  is the threshold voltage on the side of the gate 1, and  $V_{G2}$  is the gate 2 voltage. The coupling factor has been extracted on 2D simulations with long channel. We checked that the coupling is not degraded for shorter gate lengths. For a long-channel, the coupling was evaluated at 0.37 while it is equal to 0.33 at  $L=10$  nm.

From here, the simulation results are discussed. To understand a relationship between flexibility of the threshold voltage and short channel effects immunity, DIBL– $\alpha$  characteristics are plotted as a function of silicon width (Figure 6.11), silicon thickness (Figure 6.12), and spacer width (Figure 6.13). DIBL decreases and  $\alpha$  increases when the Si width is reduced as shown in Figure 6.11. For a given  $W_{Si}$ , DIBL and  $\alpha$  both decrease when changing from an IG-FinFET architecture to a  $\Phi$ -FET. The coupling decrease is understandable considering the rounded gates shape decreasing the gate coupling compared to the IG-FinFET's straight gates. The gate shape immunity to coupling effects has already been studied [6.10]. The lateral gates can screen narrow silicon body from the other gate influence as shown in Figure 6.14. The coupling factor decrease is understandable considering the rounded gates shape decreasing the coupling between the independent gates compared to the IG-FinFET's straight gates. The  $t_{Si}$  variation impact is shown on Figure 6.12. Decreasing the Si thickness improves the architecture electrostatics. The gate coupling is enhanced for the  $t_{Si}$  highest value, reaching the coupling value of IG-FinFET at  $t_{Si} = h_{Si} = 200$ nm. The spacer width  $W_{sp}$  impact is shown on Figure 6.13. For  $W_{sp} = 29$ nm, the spacers are aligned with the Si. This structure is equivalent to an IG-FinFET but with oxide and nitride alternatively with Si. Replacing Si by nitride or oxide decreases slightly the DIBL.  $w_{sp}$  has to be adjusted to have a low DIBL and a satisfying  $\alpha$  value. For  $W_{sp}/W_{Si} \approx 0.5$ , a good DIBL–coupling trade-off is obtained.

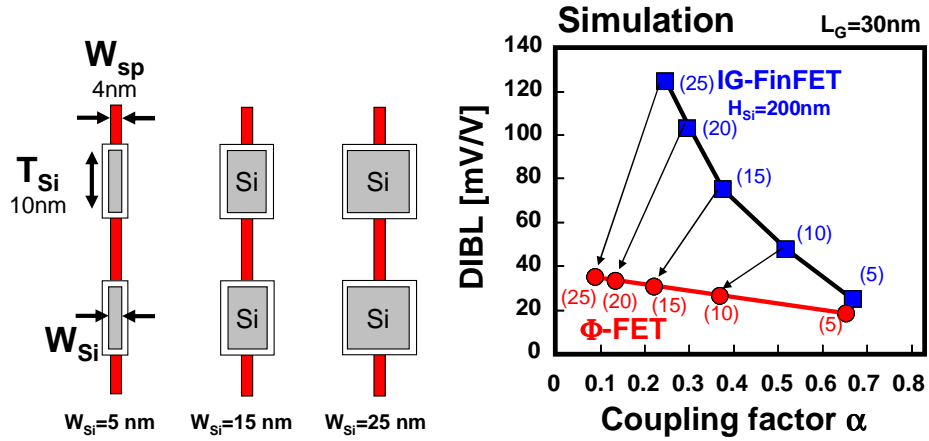


Figure 6.11 DIBL versus coupling factor: Silicon width ( $W_{Si}$ ) dependence.

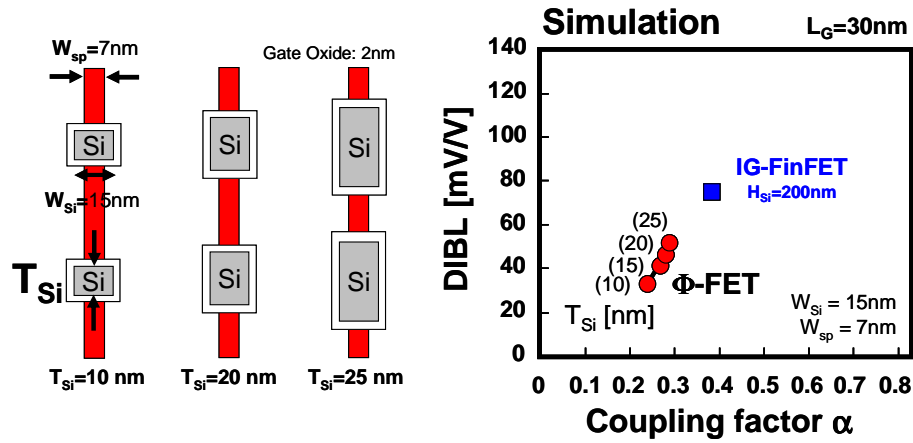


Figure 6.12 DIBL versus coupling factor: Spacer width ( $T_{Si}$ ) dependence.

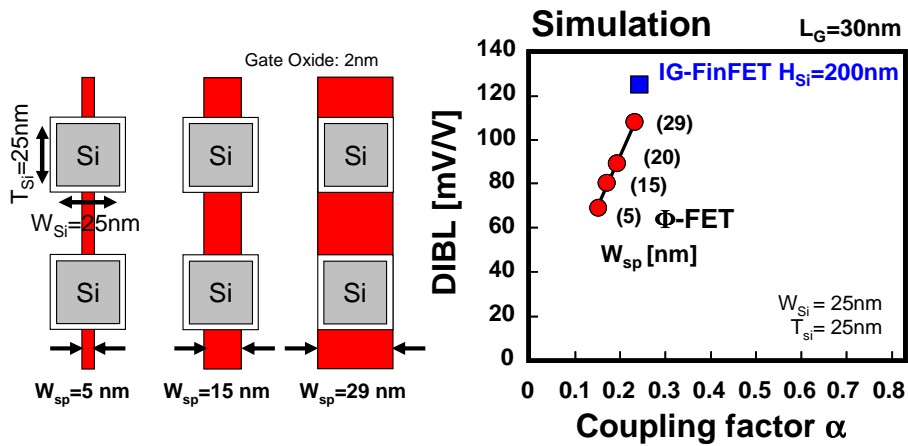


Figure 6.13 DIBL versus coupling factor: Spacer width ( $W_{sp}$ ) dependence.



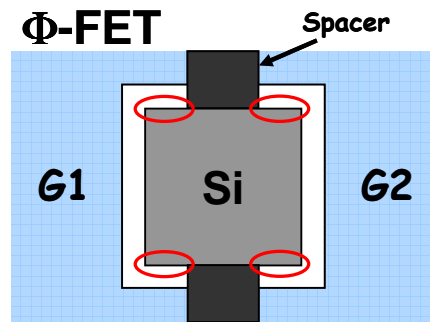


Figure 6.14 Lateral gates can screen narrow silicon body from the other gate influence.

### 6.3 CONCLUSIONS

In this chapter, vertically-stacked SNWTs architectures with independent gate operation ( $\Phi$ -FET) have been evaluated by simulation in terms of the flexibility of the threshold voltage and the short channel effects immunity.  $\Phi$ -FET structure can achieve better short-channel immunity than IG-FinFET owing to the partially surrounded gate structure. On the other hand, the lateral gates screen partially narrow silicon body from the other gate influence. This causes the degradation of coupling factor. However, the change of cross-sectional dimensions can make the threshold voltage flexible.

The proposed architectures can provide solutions for future technological nodes. It enables extremely high integration density and low leakage currents with multi-threshold voltage.

### 6.4 REFERENCES

- [6.1] Y. X. Liu, M. Masahara, K. Ishii, T. Tsutsumi, T. Sekigawa, H. Takahima, H. Yamauchi and E. Suzuki, "Flexible Threshold Voltage FinFETs with Independent Double Gates and an Ideal Rectangular Cross- Section Si-Fin Channel", *IEEE International Electron Devices Meeting IEDM*, p. 986, 2003.
- [6.2] Y. X. Liu, M. Masahara, K. Ishii, T. Sekigawa, H. Takahima, H. Yamauchi and E. Suzuki, "A Highly Threshold Voltage-Controllable 4T FinFET with an

- 8.5-nm-Thick Si-Fin Channel”, *IEEE Electron Device Letter*, vol. 25, no. 7, pp. 510–512, 2004.
- [6.3] D. Fried, J. Duster, and K. Kornegay, “Improved Independent Gate N-Type FinFET: Fabrication and Characterization”, *IEEE Electron Device Letters*, vol. 24, no. 9, p. 592, 2003.
- [6.4] K. Endo, Y. Ishikawa, Y. Liu, K. Ishii, T. Matsukawa, S. O’uchi, M. Masahara, E. Sugimata, J. Tsukada, H. Yamauchi, and E. Suzuki, “Four-Terminal FinFETs Fabricated Using an Etch-Back Gate Separation”, *IEEE Transactions on Nanotechnology*, vol. 6, no. 2, p. 201, 2007.
- [6.5] C. Dupré, A. Hubert, S. Bécu, M. Jublot, V. Maffini-Alvaro, C. Vizioz, F. Aussenac, C. Arvet, S. Barnola, J.-M. Hartmann, G. Garnier, F. Allain, J.-P. Colonna, M. Rivoire, L. Baud, S. Pauliac, V. Loup, T. Chevolleau, P. Rivallin, B. Guillaumot, G. Ghibaudo, O. Faynot, T. Ernst, and S. Deleonibus, “15nm-diameter 3D Stacked Nanowires with Independent Gate Operation: □FET,” in *IEDM Tech. Dig.*, 2008, pp. 749–752.
- [6.6] A. Tsormpatzoglou, C. A. Dimitriadis, R. Clerc, Q. Rafhay, G. Pananakakis and G. Ghibaudo, “Semi-Analytical Modeling of Short-Channel Effects in Si and Ge Symmetrical Double-Gate MOSFETs”, *IEEE Transactions on Electron Devices*, vol. 54, no. 8, p. 1943, 2007.
- [6.7] R.-H. Yan, A. Ourmazd, K. Lee, “Scaling the Si MOSFET: From Bulk to SOI to Bulk”, *IEEE Transactions on Electron Devices*, vol. 39, no. 7, p. 1704, 1992.
- [6.8] W. Hansch, Th. Vogelsang, R. Kircher, M. Orlowski, “Carrier transport near the Si/SiO<sub>2</sub> interface of a MOSFET”, *Solid-State Electronics*, Vol. 32, no.10, p.839, 1989.
- [6.9] H.K. Lim and J. G. Fossum, “Threshold Voltage of Thin-Film Silicon-on-Insulator (Sol) MOSFET’s, *IEEE Transactions on Electron Devices*, vol. 30, no. 10, p. 1244, 1983.
- [6.10] R. Ritzenthaler, S. Cristoloveanu, O. Faynot, C. Jahan, A. Kuriyama, L. Brevard, S. Deleonibus, “Lateral coupling and immunity to substrate effect in sFET devices”, *Solid-State Electronics*, vol. 50, p. 558, 2006.



# **CHAPTER 7**

## *CONCLUSIONS*

# CHAPTER 7 CONTENTS

## **7 Conclusions**

7.1 Summary

7.2 Conclusions and Perspectives

## 7.1 SUMMARY

In this thesis, vertically-stacked silicon nanowire MOSFETs (SNWTs) have been experimentally investigated as one of the possible solutions to various problems related to the CMOS scaling explained in Chapter 1. In particular, they were investigated in order to achieve both high speed and low power consumption with high integration for future LSI applications. Figure 7.1 compares device performance between this study and published SNWT data and Intel’s planar CMOS data. We have successfully demonstrated the suppressed short-channel effects owing to the gate-all-around silicon nanowire structure. The vertically-stacked channel structure has yielded high drive current density per top-viewed channel width compared to planar MOSFETs and one-level SNWTs. Even if the channel surface advantage is removed, our device shows the reasonable drive current density without any mobility enhanced technology as shown in Figure 7.1 (c).

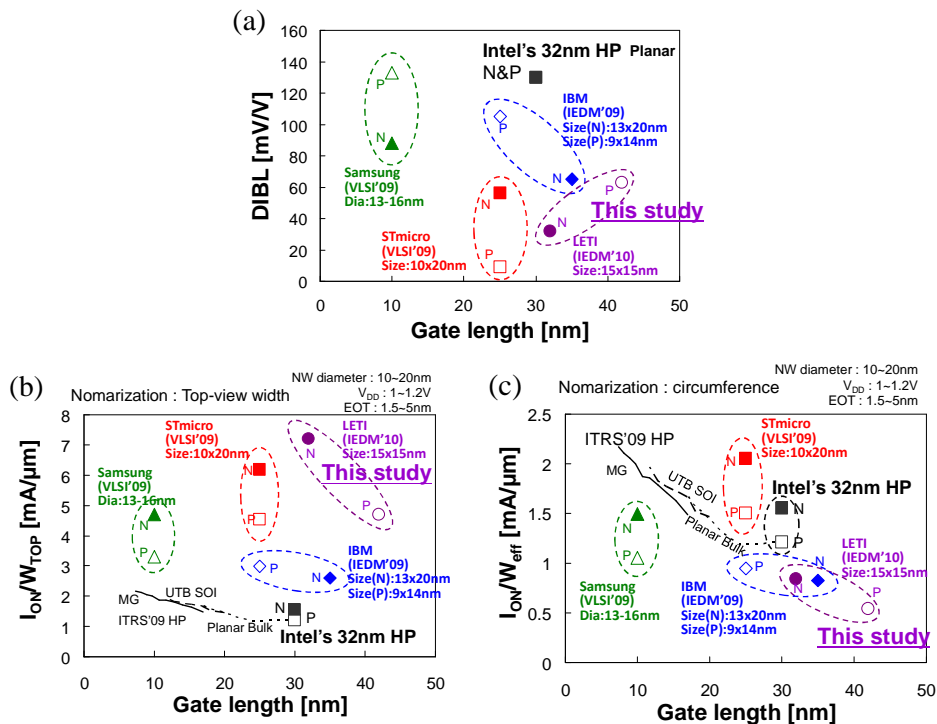


Figure 7.1 Performance benchmark with published SNWT data from other groups. (a) DIBL versus gate length, (b)  $I_{ON}/W_{TOP}$  versus gate length, and (c)  $I_{ON}/W_{eff}$  versus gate length.

The contributions of this work can be divided into three main topics:

- (1) Study of source/drain series resistance for thick source/drain region in vertically-stacked channel MOSFETs (Chapter 4),
- (2) Study of carrier transport in vertically-stacked SNWTs (Chapter 5),
- (3) Study of threshold voltage controllability for vertically-stacked SNWTs with separated gates (Chapter 6).

In Chapter 2, the device fabrication process was described. Vertically-stacked channel MOSFETs have been successfully fabricated by adapting Silicon-On-Nothing technology with sacrificial SiGe layers.

In Chapter 3, the electrical characterization methods were described. In order to analyze the performances of the fabricated devices, the intrinsic parameters extraction methods, Y-function method and Split C–V, were detailed in the latter half.

In Chapter 4, the influence of *in situ* doped SEG source/drain has been examined for vertically-stacked channel MOSFETs. A large enhancement, by a factor of 2 in the drive current, can be obtained when *in situ* doped SEG process is adopted. A detailed parameter extraction from the electrical measurements reveals that the  $R_{SD}$  values can be reduced by 90 and 75% for *n*- and *p*-FETs, respectively, when *in situ* doped SEG is reinforced by adding ion implantation. On the other hand,  $V_T$  roll-off characteristics and the effective mobility behavior are slightly degraded, especially when ion implantation is combined to the SEG process. Mobility analysis has revealed an increase in the Coulomb scattering with  $L_G$  scaling, indicating the diffusion of dopant atoms from S/D regions. These results indicate an avenue to further improve the performance by optimizing the S/D activation annealing step.

In Chapter 5, the carrier transport limiting components for vertically-stacked nanowire MOSFETs have been discussed to obtain better performance with suppressing short channel effects. The optimization of drive currents will have to take into account

specific effects to vertically-stacked SNWTs. In particular, the use of SiGe sacrificial layer to make vertically-stacked channels cause the large mobility degradation due to the surface roughness, resulting from the damage of plasma etching. This result can evidence the poor ballisticity in the short channel SNWTs.

The hydrogen annealing can improve the surface-roughness limited mobility a little. Charge pumping measurements, however, revealed that circular-shaped SNWTs, which are formed by the annealing, have a higher interface trap density ( $D_{it}$ ) than rectangular ones, leading to low-field mobility degradation. This high  $D_{it}$  might be caused by the continuously-varying surface orientation. The resulting additional coulomb scattering could partly explain the quite low mobility in 5 nm diameter SNWTs together with the already known transport limitations in NWs.

In Chapter 6, vertically-stacked SNWTs with independent gates (named  $\Phi$ -FETs), have been evaluated.  $\Phi$ -FETs demonstrated excellent  $V_T$  control by inter-gate coupling effects. As the results of numerical simulations to optimize  $\Phi$ -FETs structures, it has been found that when the spacer width is reduced, the DIBL value can be lowered by a factor of 2 compared to independent-gate FinFETs with the same silicon width. The superior scaling of  $\Phi$ -FETs with narrow spacer results from a better electrostatic control which also attenuates the inter-gate coupling.

## **7.2 CONCLUSIONS AND PERSPECTIVE**

In this thesis, it has been demonstrated that gate-all-around silicon nanowire structure can dramatically suppress short-channel effects. Moreover, the introduction of internal spacers between the nanowires can control threshold voltage. These technologies enable to achieve ultra-low power consumption.

The vertically-stacked channel structure has yielded extremely high drive current



density per top-viewed channel width compared to planer MOSFETs. However, this high current may not induce an intrinsic delay reduction because the parasitic capacitance increases in proportion to the number of channels. A benefit of the structure is a possibility of ultra-high integration per given layout area, that is, gate width scaling. For SNWTs, the optimization of the integration is strongly limited by horizontal spaces between the nanowires. The use of vertically-stacked channel structure without any nanowires in parallel enables to cancel this limitation. To design this structure, it is necessary to increase the number of channels in vertical direction. To do that, various process developments are needed such as (Si/SiGe)  $\times n$  superlattice formation shown in Figure 7.1 and its etching with vertically straight line edge.

In order to obtain higher speed operation, the effective mobility must be recovered and enhanced. Effective mass engineering will be a key technology such as a strained channel, III-V channel and Ge channel.

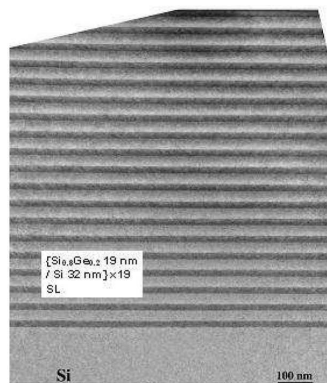


*Figure 7.2 Cross-sectional TEM image of the 19 period superlattice with 19 nm Si<sub>0.8</sub>Ge<sub>0.2</sub> and 32 nm of Si [fabricated by J.M. Hartmann in CEA-Leti].*

*Résumé du travail de thèse en Français*

Chapter 1 Introduction –réduction du MOSFET –

Récemment, l'augmentation de consommation électrique statique due aux effets de canaux courts pour les CMOS sub-50nm est devenue un des problèmes majeurs rencontrés. Les structures multigrilles ont été envisagées comme solution. En particulier, le Gate-All-Around (GAA) nanofils (NW) silicium pourrait permettre un contrôle idéal électrostatiques du canals. De plus, l'empilement vertical des nanofils peut permettre une augmentation de la densité d'intégration. La performance globale du CMOS est généralement évaluée selon 3 facteurs: rapidité de commutation, consommation électrique et densité de l'intégration. Pour profiter au mieux des avantages proposés par l'empilement vertical des nanofils en silicium transistors (SNWTs) pour les prochains CMOS, la vitesse de commutatuion doit également être améliorée. De plus, pour adresser différentes applications, la flexibilité de la tension de seuil ( $V_T$ ) est également requise.

Dans cette thèse, l'empilement vertical SNWTs est étudié de façon expérimentale. Pour augmenter le courant de drain, la technique de réduction de la résistance source/drain ( $R_{SD}$ ) sera débattue dans le troisième chapitre. Dans le chapitre 5, les propriétés de transport électronique des NWs empilées verticalement seront analysées en détail. De plus, des simulations numériques sont effectuées pour examiner les facultés de contrôle de leur tension de seuil utilisant des grilles séparés.

Chapter 2 et 3 Procédés de fabrication basiques et méthodes de caractérisation

La structure aux canaux empilés verticalement est formée en utilisant un super-réseau Si/SiGe sur le Silicium sur Isolant (SOI) et la gravure sélective des couches SiGe en se basant sur la technologie *Silicon-On-Nothing*. Pour l'empilement de grille, ALD-HfO<sub>2</sub> et CVD-TiN sont déposés avec une excellente uniformité pour la structure en trois dimensions.

Chapter 4 Technique de dopage de dopage Source/Drain pour les structures empilées verticalement

L'implantation d'ions sur les régions de source/drain (S/D) épaisses provoque une variation des profils S/D, entraînant une différence dans la longueur des grilles ( $L_G$ ) et la résistance de l'accès entre les canaux inférieurs et supérieurs. La technique dite du dopage *in-situ* de l'épitaxie (*in-situ* doped Selective Epitaxial Growth (SEG)) peut créer des zones S/D avec une uniformité idéale. L'inquiétude principale avec cette technique est la forte résistance due à la densité du dopage pour garder une croissance épitaxiale de qualité supérieure. Fig.1 nous montre un FET multi-canal conçu avec le procédé S/D SEG. Trois types de conditions de dopage sont comparés dans cette étude, comme nous le montre le tableau 1.

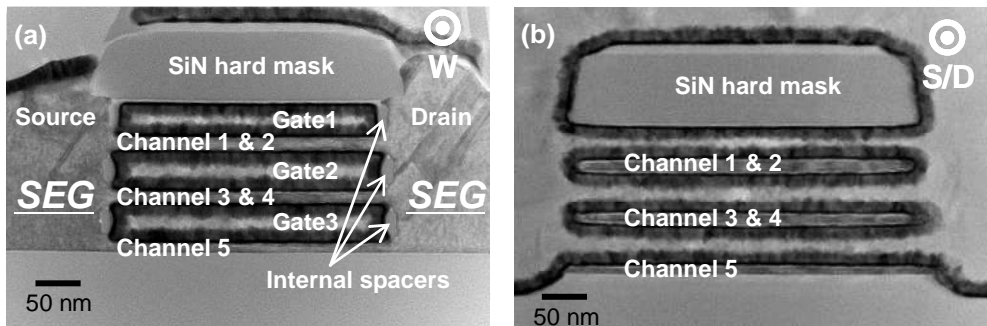


Fig. 1 Cross-sectional TEM images of vertically-stacked channel FET along (a) channel length and (b) width direction.

Table 1 S/D doping conditions. Ion impla.: As,  $BF_2$  ( $10^{15} cm^{-2}$ ), in situ dope: P, B ( $2 \times 10^{19} cm^{-3}$ )

	Control	Process A	Process B
Un-doped SEG	✓		
In-situ doped SEG		✓	✓
Ion implantation	✓		✓

La dépendance du courant à l'état ON ( $I_{ON}$ ) sur le  $L_G$ , pour n- et p-MCFETs est montrée dans la Fig.2. Une forte augmentation de l'alimentation de ce courant avec

respectivement les procédés A et B, peuvent être obtenue grâce au dopage in-situ du procédé SEG, comparé au procédé de contrôle. La dépendance avec le courant  $I_{ON}$  ( $L_G$ ) démontre clairement les réductions obtenues avec le procédé *in-situ* SEG comparés à celles obtenues avec le contrôle MCFETs. En particulier, on peut voir les mérites du procédé de fabrication B, qui permet une nette augmentation du  $I_{ON}$  lorsque  $L_G$  est réduit en dessous de 100 nm. La figure 3 nous montre la comparaison des  $R_{SD}$  extraits. Notez la réduction remarquable de  $R_{SD}$  qui a été obtenue avec succès en combinant dopage *in-situ* SEG avec l'implantation ionique (I/I) pour n- et p- MCFETs (procédé B). L'ajout d'une I/I supplémentaire au dopage in-situ après pour n- et p- MCFETs (procédé B). L'ajout du I/I supplémentaire dans le in-situ doped SEG réduit le  $R_{SD}$  de respectivement 90% pour le n- et de 60% pour le p-MCFET. L'explication d'une telle réduction est toujours inconnue, pourtant, la meilleure uniformité du S/D dopé et la haute densité de dopage peuvent entraîner une baisse du  $R_{SD}$ .

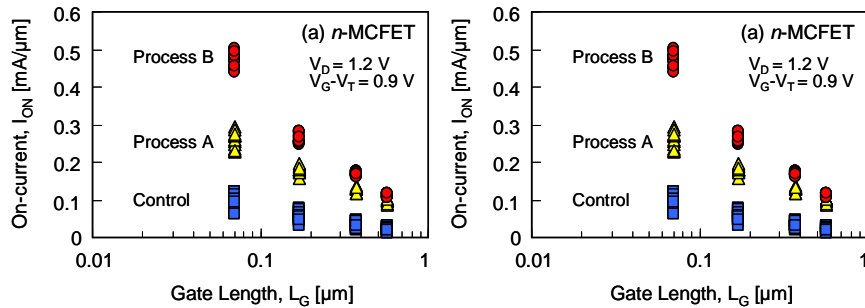


Fig. 2 On-current dependency on the gate length for (a) n- and (b) p- MCFETs. Here, the total width ( $W_{TOT}$ ) of the channels was used for the normalization.

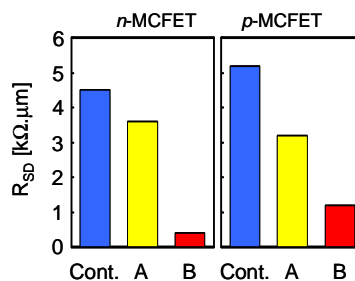


Fig. 3  $R_{SD}$  comparison

La Fig.4 nous montre les courbes des capacités gate-to-channel  $C_{GC}$  ( $V_G$ ) des MCFETs, indiquant qu'il n'y a pas de différence de capacités entre les procédés A et B. Ce qui

signifie que l'addition de l' I/I dans le processus B ne cause pas de variation de  $L_G$  dans les canaux empilés verticalement.

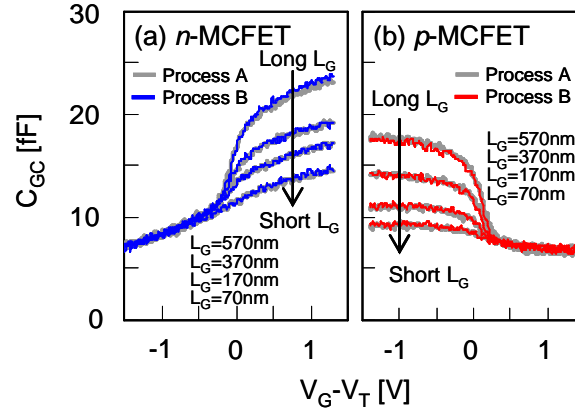


Fig. 4  $C_{GC}(V_G)$  curves of the MCFETs with process A and B.

Chapter 5 Propriétés de transport électrique des MOSFETs à nanofils empilés verticalement

Fig.5 montre une image SEM du SNWTs fabriqué avec 3 niveaux de fils empilés. Les caractéristiques  $I_{DS}-V_{GS}$  avec une largeur de 15 nm NW ( $W_{NW}$ ), de 32 nm de longueur de grille effective ( $L_{eff}$ ) pour le NMOS et de 42 nm pour le PMOS révèlent des caractéristiques tout a fait convenables dans la figure 6. Les courbes  $IPs-VGs$  montrent une excellente descente en dessous du seuil (32 mV/dec pour NMOS et 62 mV/V pour PMOS). Quand le courant est normalisé par la lagueur physique du transistor (vu du dessus) le  $I_{on}$  des NMOS est de 7,2 mA/um pour les nanofils de type 3D-stacked et 2.6 mA/um pour un seul niveau, démontrant l'intérêt de structures 3D pour augmenter la densité de l'alimentation dans un layout donné.

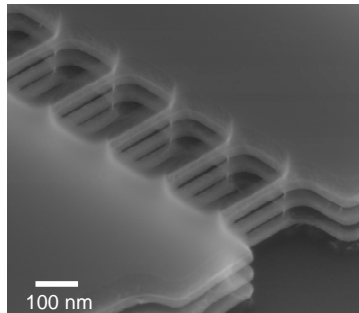


Fig. 5 SEM image of vertically- stacked SNWT.

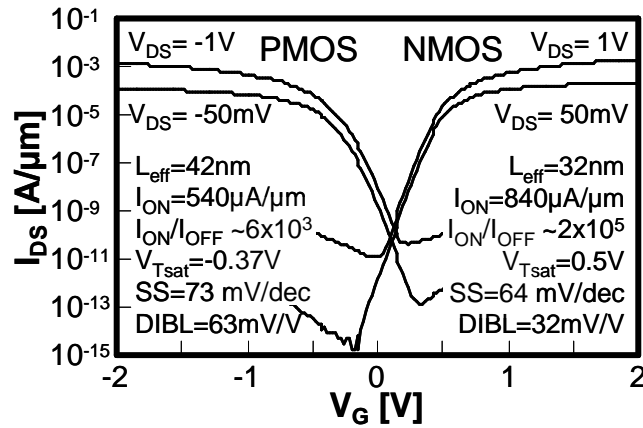


Fig .6  $I_{DS}$ - $V_{GS}$  characteristics with 15 nm  $W_{NW}$  and 32 nm  $L_{eff}$  for NMOS and 42 nm for PMOS.

Pour  $L_G$  inférieure à 50 nm, on s'attend à ce qu'une partie des porteurs de charge agisse ait un comportement balistique. Cependant, le résultat d'une étude sur la dépendance avec la température de la vitesse des porteurs montre que la part du transport limité par la vitesse de saturation (donc hors régime balistique) est dominante dans les nSNWTs comme le montre la Fig.7. Les résultats impliquent la présence de composants fortement éparpillés.

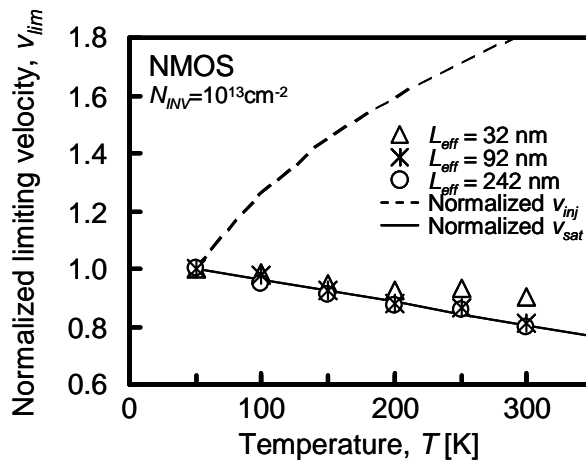


Fig. 7 Temperature dependence of extracted limiting velocity  $v_{lim}$ . The lines are theoretical  $v_{sat}$  and  $v_{inj}$ .

Pour comprendre la cause de ces évènements de collisions empêchant l'avènement d'un régime balistique, la mobilité effective ( $\mu_{eff}$ ) de NWs longs a été évaluée. La figure 8

nous montre  $\mu_{\text{eff}}$  en fonction de température pour une forte densité de charge d'inversion . Une  $\mu_{\text{eff}}$  dégradée pour des SNWTs empilés verticalement comparée au FDSOI planaire est observé a basse température. Cela signifie que le  $\mu_{\text{eff}}$  pour les SNWTs empilés verticalement est fortement limité par les collisions à la surface, rugueuse, du NW. Une des raisons pour expliquer cette dégradation de la surface est les dommages dus à la gravure sélective du SiGe comme montré dans la comme montré dans la Fig.9.

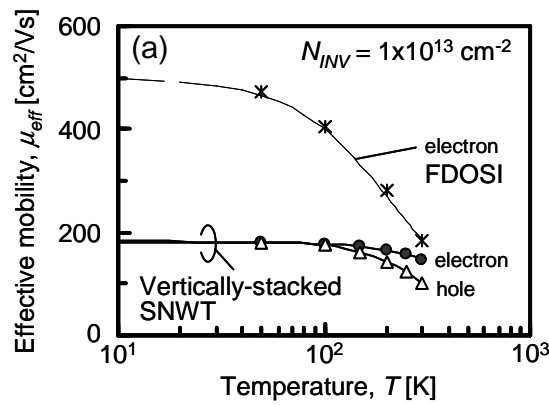


Fig. 8  $\mu_{\text{eff}}$  as a function of temperature as high inversion charge density.

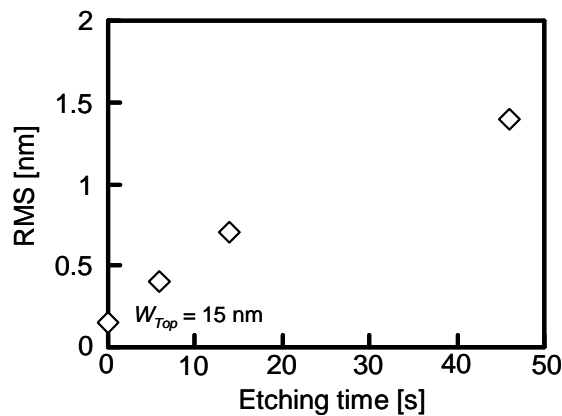
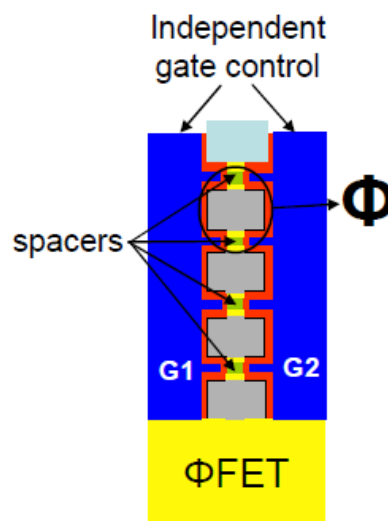


Fig. 9 RMS values as a function of isotropic SiGe dry etching for planar Si surface.



*Chapter 6 Contrôle de la tension de seuil des structures FETs à nanofils empilés verticalement*

Dans ce chapitre, la possibilité d'une flexibilité du seuil d'alimentation pour les SNWT empilés verticalement avec des grilles indépendantes (nommé  $\Phi$ FET) est examinée avec des simulations numériques. La figure 10 montre une structure  $\Phi$ FET qui a des espaceurs internes entre les nanofils. La grille séparée (G2) agit comme la grille arrière d'un FET planaire sur SOI mince complètement déserté. La sensibilité de variation du  $V_T$  en fonction de  $V_{G2}$  est exprimée par le facteur de couplage entre les grilles wsi 1 et 2. Les Fig 11 et Fig 12 montrent le DIBL en fonction du facteur de couplage  $\alpha$  respectivement en fonction de la largeur du Silicium ( $W_{Si}$ ) et de la largeur de l'espaceur ( $W_{Sp}$ ). Le DIBL diminue et  $\alpha$  augmente quand  $W_{Si}$  est réduit. Pour  $W_{Si} = 29$  nm, les espaceurs sont alignés avec les bords du Si. Cette structure est équivalente à une FinFET à grilles indépendantes (IG-FinFET). La structure  $\Phi$ -FET obtient de meilleurs résultats en terme d'immunité aux canaux courts que IG-FinFET grâce à la structure où les grilles sont partiellement enrobées. Cela provoque la dégradation du facteur de couplage. Cependant, le changement de dimensions dans la dimension perpendiculaire au transport peut rendre le seuil d'alimentation flexible.



*Fig. 10  $\Phi$ -FET scheme*

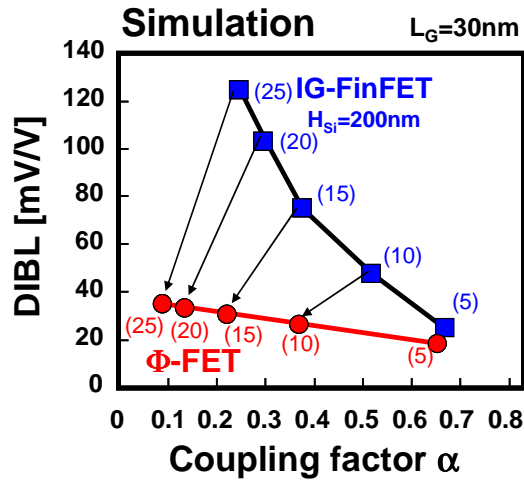


Fig 11 DIBL versus coupling factor: Silicon width ( $W_{Si}$ ) dependence.

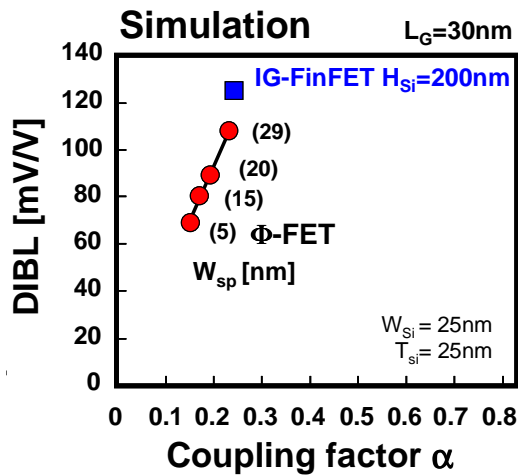


Fig. 12 DIBL versus coupling factor: Spacer width ( $W_{sp}$ ) dependence.

### Chapter 7 Conclusions

Dans cette thèse, il a été démontré que la structure gate-all-around en nanofils de silicium peut radicalement supprimer les effets de canaux courts. De plus, l'introduction d'espaces internes entre ces nanofils peut permettre de contrôler la tension de seuil, à l'aide d'une deuxième grille de contrôle. Ces technologies permettent d'obtenir une consommation électrique extrêmement faible.

Pour obtenir des opérations à haute vitesse, les limitations du transport électronique dans les SNWTs empilés verticalement ont été examinés en détail. Ils sont fortement limités par les phénomènes de collision de porteurs du fait de la rugosité de la surface.

Les structure à canaux empilés verticalement produit des densités de courant extrêmement élevées comparée au planer MOSFETs. Cependant, cette forte alimentation peut ne pas être liée a une réduction intrinsèque du délai à cause de l'augmentation de la capacité parasite par rapport au nombre de canaux. L'avantage de cette structure est la possibilité d'une très grande intégration par unité de surface d'une couche donnée, c'est à dire une réduction de la largeur des grilles. Pour les SNWTs, l'optimisation de l'intégration est fortement limitée par les espaces horizontaux entre les nanofils. L'utilisation parallèle de canaux à structure empilée verticalement permet d'annuler cette limitation. Pour réaliser cette structure, il est nécessaire d'augmenter le nombre de canaux dans le sens de la verticale. Pour y parvenir, différents développements de procédés sont nécessaires, tels que la formation de super-réseaux (Si/SiGe) x n.

## ***Publications and Presentations***

### *Nanowire MOSFETs*

[Publications as 1<sup>st</sup> author]

1. K. Tachi, N. Vulliet, S. Barraud, K. Kakushima, H. Iwai, S. Cristoloveanu and T. Ernst, “Influence of source/drain formation process on resistance and effective mobility for scaled multi-channel MOSFET,” Special Issue of Solid-State Electronics, (accepted for publication)
2. K. Tachi, S. Barraud, K. Kakushima, H. Iwai, S. Cristoloveanu and T. Ernst, “Comparison of low-temperature electrical characteristics of gate-all-around nanowire FETs, Fin FETs and fully-depleted SOI FETs,” *Microelectronics Reliability*, vol. 51, Issue 5, pp. 885-888, 2011.

[Presentations as 1<sup>st</sup> author]

3. K. Tachi, M. Cassé, S. Barraud, C. Dupré, A. Hubert, N. Vulliet, M.E. Faivre, C. Vizioz, C. Carabasse, V. Delaye, J.M. Hartmann, H. Iwai, S. Cristoloveanu, O. Faynot and T. Ernst, “Experimental study on carrier transport limiting phenomena in 10 nm width nanowire CMOS transistors,” *IEDM Tech. Dig.*, p.784, 2010, San Francisco, US.
4. K. Tachi, N. Vulliet, S. Barraud, B. Guillaumot, V. Maffini-Alvaro, C. Vizioz, C. Arvet, Y. Campidelli, P. Gautier, J.M. Hartmann, T. Skotnicki, S. Cristoloveanu, H. Iwai, O. Faynot and T. Ernst, “3D Source/Drain Doping Optimization in Multi-Channel MOSFET,” 40th European Solid-State Device Research Conference (ESSDERC), pp. 368, 2010, Spain.
5. K. Tachi, M. Casse, D. Jang, C. Dupré, A. Hubert, N. Vulliet, V. Maffini-Alvaro, C. Vizioz, C. Carabasse, V. Delaye, J. M. Hartmann, G. Ghibaud, H. Iwai, S. Cristoloveanu, O. Faynot, and T. Ernst, “Relationship between mobility and

high-*k* interface properties in advanced Si and SiGe nanowires,” *IEDM Tech. Dig.*, p.313, 2009, Baltimore, US.

5. K. Tachi, T. Ernst, C. Dupré, A. Hubert, S. Bécu, H. Iwai, S. Cristoloveanu, O. Faynot, “ Transport Optimization with Width Dependence of 3D-stacked GAA Silicon Nanowire FET with High-*k*/Metal Gate Stack,” *2009 IEEE Silicon Nanoelectronics Workshop*, p.11, 2009, Kyoto, Japan.
6. K. Tachi, T. Ernst, C. Dupré, A. Hubert, S. Bécu, H. Iwai, S. Cristoloveanu, O. Faynot, “ F-FET: Electrostatics and influence of spacer thickness,” *5th EUROSIOI*, 2009, Chalmers University of Technology, Sweden.

[Publications as co- author]

7. D. Jang, J. W. Lee, K. Tachi, L. Montes, T. Ernst, G. T. Kim and G. Ghibaudo, “Low-frequency noise in strained SiGe core-shell nanowire p-channel field effect transistors, ” *Appl. Phy. Lett.* 97, 073505, 2010.
8. M. Casse, K. Tachi, S. Thiele and T. Ernst, “Spectroscopic charge pumping in Si nanowire transistors with a high-*k*/metal gate, ” *Appl. Phy. Lett.* 96, 123506, 2010.
9. T. Ernst, K. Tachi, E. Saracco, A. Hubert, C. Dupré, S. Bécu, N. Vulliet, E. Bernard, P. Cherns, V. Maffini-Alvaro (CEA-LETI), J. Damlencourt, C. Vizioz, J. Colonna, C. Bonafos and J. Hartmann, “3D suspended nanowires integration for CMOS and beyond,” *Electrochemical Society (ECS) Transaction*, vol. 25, Issue.7 , pp. 471-478, 2009.

[Presentations as co-author]

10. K-I. Na, W. Van Den Daele, L. Pham-Nguyen, M. Bawedin, K-H. Park, J. Wan, K. Tachi, S-J. Chang, I. Ionica, Y-H. Bae, J.A. Chroboczek, C. Fenouillet-Beranger, T. Ernst, E. Augendre, C. Le Royer, A. Zaslavsky, H. Iwai and S. Cristoloveanu, “(Invited) Selected SOI puzzles and tentative answers, ” 6th SemOI workshop & 1st Ukrainian-French SOI Seminar, 2010, Ukraine.
11. A. Hubert, E. Nowak, K. Tachi, V. Maffini-Alvaro, C. Vizios, C. Arvet, J.-P. Colonna, J.-M. Hartmann, V. Loup, L. Baud, S. Pauliac, V. Delaye, C. Carabasse, G. Molas, G. Ghibaud, B. De Salvo, O. Faynot and T. Ernst, “A stacked SONOS technology, up to 4 levels and 6nm crystalline nanowires, with gate-all-around or independent gates (  $\Phi$  -Flash), suitable for full 3D integration,” *IEDM Tech. Dig.*, p.673, 2009, Baltimore, US.
12. T. Ernst, S. Bécu, P. Cherns, L. Durrafourg, C. Dupré, P. Andreucci, A. Hubert, J.-M. Hartmann, J.-P. Colonna, M. Jublot, G. Delapierre, V. Delaye, K. Tachi, E. Saracco, J.-F. Damlencourt, J. Foucher, and O. Faynot, “A 3D stacked nanowire technology - Applications in advanced CMOS and beyond,” 7th International Conference on Frontiers of Characterization and Metrology for Nanoelectronics, 2009, US.
13. P. D. Cherns, F. Lorut, S. Beçu, C. Dupré, K. Tachi, D. Cooper, A. Chabli, and T. Ernst, “A Study Of Gate-All-Around Transistors By Electron Tomography,” AIP Conf. Proc. 1173, 290, 2009.

*High-k/Metal Gate*

[Publications as 1<sup>st</sup> author]

14. K. Tachi, K. Kakushima, P. Ahmet, K. Tsutsui, N. Sugii, T. Hattori and H. Iwai, “Improvement of interface properties of W/La<sub>2</sub>O<sub>3</sub>/Si MOS structure using Al capping layer,” *Electrochemical Society (ECS) Transaction* Vol.11 No.4 pp.191-198, 2007.
15. K. Tachi, K. Kakushima, P. Ahmet, K. Tsutsui, N. Sugii, T. Hattori and H. Iwai, “Effect of Oxygen for Ultra-Thin La<sub>2</sub>O<sub>3</sub> Film Deposition,” *Electrochemical Society (ECS) Transaction* 3 (3), pp. 425-435, 2006.

[Presentations as 1<sup>st</sup> author]

16. K. Tachi, K. Kakushima, P. Ahmet, K. Tsutsui, N. Sugii, T. Hattori and H. Iwai, “Improvement of interface properties of W/La<sub>2</sub>O<sub>3</sub>/Si MOS structure using Al capping layer,” *212th Electrochemical Society (ECS) Meeting*, Abs#E4-07520, October, 2007, Washington, DC.
17. K. Tachi, K. Kakushima, P. Ahmet, K. Tsutsui, N. Sugii, T. Hattori and H. Iwai, “Effect of Oxygen for Ultra-Thin La<sub>2</sub>O<sub>3</sub> Film Deposition,” *Physics and Technology of High-k Gate Dielectrics 4, 210th Electrochemical Society (ECS) Meeting*, Abs#1128, November, 2006, Cancun, Mexico.

[Publications and Presentations as co-author]

18. K. Kakushima, K. Okamoto, T. Koyanagi, K. Tachi, M. Kouda, T. Kawanago, J. Song, P. Ahmet, K. Tsutsui, N. Sugii, T. Hattori and H. Iwai, “Selection of Rare Earth Silicate with SrO Capping for EOT Scaling below 0.5 nm,” *39th ESSDERC*, pp 403, 2009, Greece.
19. K. Kakushima, K. Tachi, J. Song, S. Sato, H. Nohira, E. Ikenaga, P. Ahmet, K. Tsutsui, N. Sugii, T. Hattori, and H. Iwai, “Comprehensive x-ray photoelectron

- spectroscopy study on compositional gradient lanthanum silicate film,” *Journal of Applied Physics*, vol. 106, 124903, 2009.
20. T. Koyanagi, K. Tachi, K. Okamoto, K. Kakushima, P. Ahmet, K. Tsutsui, N. Sugii, T. Hattori, and H. Iwai, “Electrical Characterization of La<sub>2</sub>O<sub>3</sub>-Gated Metal Oxide Semiconductor Field Effect Transistor with Mg Incorporation,” *Japanese Journal of Applied Physics*, vol. 48, 05DC02, 2009.
21. K. Kakushima, K. Okamoto, K. Tachi, J. Song, S. Sato, T. Kawanago, K. Tsutsui, N. Sugii, P. Ahmet, T. Hattori, and H. Iwai, “Observation of band bending of metal/high-*k* Si capacitor with high energy x-ray photoemission spectroscopy and its application to interface dipole measurement,” *Journal of Applied Physics*, vol. 104, 104908, 2008.
21. M. Kouda, K. Tachi, K. Kakushima, P. Ahmet, K. Tsutsui, N. Sugii, T. Hattori and H. Iwai, “Electrical Properties of CeOX /La<sub>2</sub>O<sub>3</sub> Stack as a Gate Dielectric for Advanced MOSFET Technology,” *Electrochemical Society (ECS) Transaction*, vol. 16, Issue.5 , pp. 153-160, 2008.
22. K. Kakushima, K. Okamoto, M. Adachi, K. Tachi, S. Sato, T. Kawanago, , J. Song, P. Ahmet, K. Tsutsui, N. Sugii, T. Hattori, and H. Iwai, “Impact of Thin La<sub>2</sub>O<sub>3</sub> Insertion for HfO<sub>2</sub> MOSFET,” *Electrochemical Society (ECS) Transaction*, vol. 13, Issue.2 , p. 29, 2008.
23. K. Kakushima, K. Tachi, M. Adachi, K. Okamoto, S. Sato, J. Song, T. Kawanago, P. Ahmet, K. Tsutsui, N. Sugii, T. Hattori, and H. Iwai, “Advantage of La<sub>2</sub>O<sub>3</sub> gate dielectric over HfO<sub>2</sub> for direct contact and mobility improvement,” 38th ESSDERC, p.126, 2008.
24. K. Kakushima, K. Okamoto, K. Tachi, S. Sato, T. Kawanago, J. Song, P. Ahmet, K. Tsutsui, N. Sugii, T. Hattori, and H. Iwai, “Further EOT Scaling below 0.4



- nm for High-k Gated MOSFET,” International Workshop on Dielectric Thin Films for future ULSI devices, p. 9, 2008, Japan.
25. T. Koyanagi, K. Tachi, K. Okamoto, K. Kakushima, P. Ahmet, K. Tsutsui, N. Sugii, T. Hattori, and H. Iwai, “Electrical Characterization of La<sub>2</sub>O<sub>3</sub>-Gated MOSFET with Mg Incorporation,” International Workshop on Dielectric Thin Films for future ULSI devices, p. 73, 2008, Japan.
26. J. Molina, K. Tachi, K. Kakushima, P. Ahmet, K. Tsutsui, N. Sugii, T. Hattori and H. Iwai, “Effects of N<sub>2</sub>-Based Annealing on the Reliability Characteristics of Tungsten/La<sub>2</sub>O<sub>3</sub>/Silicon Capacitors,” *J. Electrochem. Soc.*, Volume 154, Issue 5, pp. G110-G116, 2007
27. T. Kawanago, K. Tachi, J. Song, K. Kakushima, P. Ahmet, K. Tsutsui, N. Sugii, T. Hattori and H. Iwai “Electrical Characterization of Directly Deposited La-Sc Oxide Complex for Gate Insulator Application,” *Microelectronic Engineering*, vol. 84, issue. 9-10, pp. 2235-2238, 2007.
29. S. Sato, K. Tachi, K. Kakushima, P. Ahmet, K. Tsutsui, N. Sugii, T. Hattori and H. Iwai “Thermal-stability improvement of LaON thin film formed using nitrogen radicals,” *Microelectronic Engineering*, vol. 84, issue. 9-10, pp. 1894-1897, 2007.
30. S. Sato, K. Tachi, K. Kakushima, P. Ahmet, K. Tsutsui, N. Sugii, T. Hattori and H. Iwai, “Thermal Stability of Lanthanum Oxynitride Thin Film Fabricated by in-situ Radical Nitridation,” *54th Japan Society of Applied Physics (JSAP) Spring Meeting*, 29p-ZH-13, 2007, Aoyama Gakuin University, Japan.
31. K. Kakushima, P. Ahmet, J.-A. Ng, J. Molina, H. Sauddin, Y. Kuroki, K. Nakagawa, A. Fukuyama, K. Tachi, Y. Shiino, J. Song, K. Tsutsui, N. Sugii, T.

- Hattori and H. Iwai, "Study of La<sub>2</sub>O<sub>3</sub> Gate Dielectric Suitability for Future MIM and MOSFETs", *2006 IEEE Silicon Nanoelectronics Workshop*, 12th June 2006, Hawaii, USA.
32. H. Nohira, T. Matsuda, K. Tachi, Y. Shiino, J. Song, Y. Kuroki, J. Ng, P. Ahmet, K. Kakushima, K. Tsutsui, E. Ikenaga, K. Kobayashi, H. Iwai and T. Hattori, "Effect of Deposition Temperature on Chemical Structure of Lanthanum Oxide/Si Interface Structure," *2006 International Workshop on Dielectric Thin Films for Future ULSI Devices (IWDTF)*, pp.29-30, November, 2006, Kawasaki, Japan
33. J. Molina, K. Tachi, K. Kakushima, P. Ahmet, K. Tsutsui, N. Sugii, T. Hattori and H. Iwai, "Effects of N<sub>2</sub>-Based Annealing on the Reliability Characteristics of Tungsten/La<sub>2</sub>O<sub>3</sub>/Silicon Capacitors," *Electrochemical Society (ECS) Transaction 3 (3)*, pp. 233, 2006.
34. H. Nohira, T. Matsuda, K. Tachi, Y. Shiino, J. Song, Y. Kuroki, J. Ng, P. Ahmet, K. Kakushima, K. Tsutsui, E. Ikenaga, K. Kobayashi, H. Iwai and T. Hattori, "Effect of Deposition Temperature on Chemical Structure of Lanthanum Oxide/Si Interface Structure," *Electrochemical Society (ECS) Transaction 3 (2)*, pp. 169, 2006.
35. H. Nohira, T. Matsuda, K. Tachi, Y. Shiino, J. Song, Y. Kuroki, J. Ng, P. Ahmet, K. Kakushima, K. Tsutsui, E. Ikenaga, K. Kobayashi, H. Iwai and T. Hattori, "Thermal Stability of LaOX/Si Interfacial Transition Layer", *53rd Japan Society of Applied Physics (JSAP) Spring Meeting*, 23p-V-2, 2006, Musashi Institute of Technology, Japan.
36. K. Nakajima, K. Kimura, K. Tachi, K. Kakushima and H. Iwai, "Hydrogen Depth Profiling in La<sub>2</sub>O<sub>3</sub>/Si(001) by High-resolution Erastic Recoil Detection",

*53rd Japan Society of Applied Physics (JSAP) Spring Meeting, 23p-V-5, 2006,  
Musashi Institute of Technology, Japan.*

***Awards***

*2010 IEEE EDS Japan Chapter Student Award*

*2009 IEEE EDS Japan Chapter Student Award*